Possibility of increasing the thermal stability of Si by doping with transition or rare-earth metals

V. M. Glazov, G. G. Timoshina, and M. S. Mikhaĭlova

Moscow Institute of Electronics, 103498 Moscow, Russia

A. Ya. Potemkin

Moscow Aviation Institute, 125871 Moscow, Russia

(Submitted February 2, 1997; accepted for publication March 17, 1997)
Fiz. Tekh. Poluprovodn. **31**, 1025–1028 (September 1997)

It is pointed out that the degradation of Si single crystals after heating is due primarily to structural transformations associated with a partial transformation of diamond–like Si into silicon with the structure of white tin. These transformations, which are observed at high pressures, occur as a result of the appearance of numerous zones of stress concentration due to the anisotropy of thermal expansion of differently oriented microvolumes of the crystal. The high pressures required for the indicated phase transition to occur can be reached in these zones. It is pointed out that the structural transformations leading to the degradation of the electrical properties of Si can be prevented by doping it with transition or rare–earth metals, which increase the interatomic interaction energy and, as a result, decrease the thermal expansion. The choice of dopant is made on the basis of calculations of the binding energy and charge density based on a system of unpolarized ionic radii. © *1997 American Institute of Physics.* [S1063-7826(97)00109-9]

The problem of increasing the thermal stability of Si has existed nearly since the time it was used as the main material of semiconductor electronics.[1,2] It still exists today, despite the fact that it is long–standing. To decrease the degradation of the material after it is heated and then cooled, heat treatment involving annealing at a definite temperature followed by slow cooling is used.[1–4]

Heat treatment decreases but does not completely eliminate the degradation. It is therefore profitable to try to resolve this problem by doping Si with specially selected dopants. In the present paper we examine the basis for choosing dopants for the purpose of increasing the thermal stability of Si.

The approach proposed for choosing dopants which would increase the thermal stability of silicon is based on ideas which we advanced concerning the reasons why the electrical properties of silicon are degraded after heating and cooling. In our view, the comparatively recently observed structural transformations occurring in Si when it is heated are due mainly to degradation of the material after heating (Refs. 5–10).$^{1)}$ It is well known[11] that polymorphous transformations occur in Si under high pressures.

When Si is heated, as a result of the anisotropy of thermal expansion, zones of stress concentration appear at locations where differently oriented sections of the single crystal (subgrains, blocks) meet and high pressures develop in these local sections of the crystal. Structural transformations associated with the precipitation of Si with the structure of white tin occur in such high–pressure regions. These ideas are supported by the results obtained in previous investigations of the stressed state of a Si single crystal before and after heat treatment.[12] The formation of a high–pressure phase in the sections of the crystal that were discussed above results in stress relaxation and further growth of the precipitates stops. However, the single–crystal nature of the material after heating and cooling in accordance with the appropriate stages of the technological process is substantially disturbed. This results in the formation of numerous lattice defects together with thermal donors associated with them (see Refs. 1–4), which lead to the degradation of the electrical properties of the material. Therefore, doping is used to introduce dopants into silicon that would suppress these transformations and thereby increase the thermal stability of silicon.

It is obvious that substances which on dissolving in Si increase the strength of the interatomic bonds, thereby strengthening the lattice as a whole, can play the role of such additives. A consequence of this process should be a decrease in the thermal expansion and therefore a decrease in the probability of formation of high–pressure regions which lead to the phase transformation accompanied by a precipitation of a different modification of Si (high–pressure phase). To provide a basis for choosing dopants which are distinguished by the indicated properties, we employed the principles of the metal chemistry of complex doping which are based on a system of unpolarized ionic radii.[13,14] A scheme for calculating the parameters that determine the character of the interatomic interaction of the dopant atoms with the solvent (in this case with Si) is presented in Refs. 15 and 16 . To estimate the interatomic interaction in the case of doping of a material, according to Ref. 15 it is necessary to

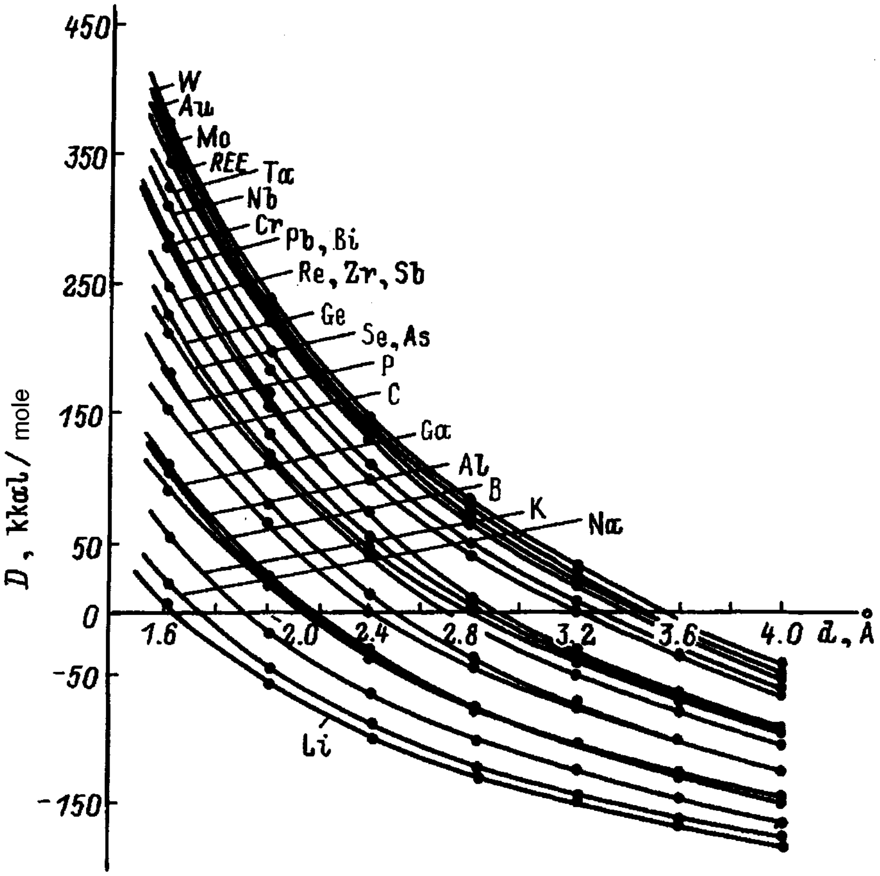

FIG. 1. Binding energy D versus interatomic distance d between interacting particles in binary systems of Si atoms with elements from the periodic table.

pay special attention to the directionality of the interatomic bonds and the covalence, hybridization, and anisotropy of the electronic distribution which accompany it. The semiempirical approach, which makes it possible to take into account these effects, is based on the use of a system of unpolarized ionic radii.[14] According to Refs. 14 and 15, we have

$$\log R_i^{(z_i)} - \log R_i^{(0)} + z_i \tan \alpha_i = 0, \tag{1}$$

where z_i is the effective charge of the dopant atom, the index i denotes the type of atom, $R_i^{(z)}$ and $R_i^{(0)}$ are, respectively, the radii of the ions and atoms, α_i is the slope angle of the function $\log R_i = f(n)$, and n is the number of identifiable electrons.[14] The interaction of Si and dopant atoms can be represented schematically as an interaction of ions A and B at a fixed distance d. The effective charges and ionic radii of the interacting particles are determined, according to Ref. 5, by solving the system of equations

$$R_{\mathrm{A}}^{(z_{\mathrm{A}})} + R_{\mathrm{B}}^{(z_{\mathrm{B}})} = d, \tag{2}$$

$$\log R_{\mathrm{A}}^{(z_{\mathrm{A}})} = \log R_{\mathrm{A}}^{(0)} - (z_{\mathrm{A,min}} + \Delta l/2) \tan \alpha_{\mathrm{A}}, \tag{3}$$

$$\log R_{\mathrm{B}}^{(z_{\mathrm{B}})} = \log R_{\mathrm{B}}^{(0)} - (z_{\mathrm{B,min}} + \Delta l/2) \tan \alpha_{\mathrm{B}}. \tag{4}$$

The quantity Δl characterizes the degree of deformation of the electronic clouds of the interacting particles, $z_{i,\min}$ is the charge of the reagents for a purely ionic interaction and a point contact of the interacting particles and is determined from the condition that the charge density and electronegativities of the interacting particles equalize at the point of contact.[17] As a result, the effective charges of the interacting particles are determined for a specific direction of the interaction and include as constituent parts a spherical component ($z_{i,\min}$) and a directed component ($\Delta l/2$): [15]

$$z_{\mathrm{A}} = z_{\mathrm{A,min}} + \Delta l/2; z_{\mathrm{B}} = z_{\mathrm{B,min}} + \Delta l/2. \tag{5}$$

It follows from the solution of the system of equations (2)–(4) that the effective charges and radii of the atoms of the interacting substances vary in conformity with the intermolecular distances and depend on the chemical individuality of the bonding partners. According to Ref. 15, this is taken into account by a set of parameters $\tan \alpha_i$ and $R_i^{(0)}$ of the system of unpolarized ionic radii.[13,14]

This approach does not postulate the value of the effective charge of the interacting substances or that their electronic shells are spherical, and it gives a clear representation of the directed character of the interatomic bonds.[15,17]

A special feature of the computational procedure described above is that the conditions of equality of the directed charge density ρ_l hold for any value of the effective charges of the interacting particles when ions with charges z_A and z_B come into contact and, according to Ref. 13, is determined from the relation

$$\rho_{l_{\mathrm{A}}}[e/\text{Å}] = \frac{0.434}{R_{\mathrm{A}}[\text{Å}] z_{\mathrm{A}} \tan \alpha_{\mathrm{A}}}, \tag{6}$$

where the index $l = l_A$ signifies the directional nature of the charge density. The correctness of this approach to estimating the charge density is confirmed by comparing this quantity with different physicochemical properties of the ions and the corresponding compounds.[17] The most important consequence of this approach is establishing a direct correlation between the experimental values of the binding energy and the results of a calculation of the charge density using Eq. (6).[15,16] According to Ref. 16 , this correlation can be represented by the empirical equation

$$D\left[\frac{\text{kcal}}{\text{mole}}\right]=85\rho_l[e/\text{Å}]-310. \tag{7}$$

The relation (7) makes it possible to estimate, on the basis of calculations of the charge density from the relation (6), the binding energy of a pair of atoms separated by a certain distance. The effect of the interatomic distances of the interacting substances is expressed in terms of Eq. (2), which is part of the system of equations whose solution gives an expression for the directed charge density (6).

On the basis of the ideas examined above, we performed calculations of the binding energy in the case of the dissolution of different simple substances in silicon.[2)] The results of these calculations are presented in Fig. 1 in the form of a plot of $D=f(d)$. We see that as the distance between the interacting particles increases, the binding energy decreases nearly exponentially. Figure 1 shows the curves $D=f(d)$ not for all elements in the periodic table but rather only for the most important donor- and acceptor-type dopants, which are employed for obtaining silicon with the required electrical properties, as well as for some transition metals and rare-earth elements (REE). Moreover, the binding energy depends strongly on the physical-chemical nature of the interacting substances. The highest binding energies occur for pair interactions in binary Si systems with transition metals W, Ni, Ta, Cr, and others, as well as with rare-earth elements. The family of curves which lie in the region of high binding energies also includes a curve for the silicon–gold system.[3)] Therefore, when these substances dissolve in Si, the thermal stability of Si should increase as a result of an increase in the strength of the interatomic bonds in the crystal lattice of the solid solution.

It is well known that as the strength of interatomic bonds increases, the thermal expansion coefficient decreases. This behavior should primarily lead to a decrease in the number of zones of stress concentration and, correspondingly, high-pressure regions in the crystal when it is heated. Furthermore, because of the decrease in the thermal expansion, coefficient, the effect of the anisotropy of thermal expansion should decrease substantially. As a result, the pressures developing in the zones of stress concentration are not be high enough to induce a phase transition of Si with diamond structure into Si with white-tin structure. Thus, it follows from the curve shown in Fig. 1 that the energetics of the interatomic interaction depends substantially on the interatomic distances, and therefore on the chemical nature of the interacting particles. However, in our specific case, when the problem of the nature of the interaction of the dopant atoms with the Si atoms is being solved, it is desirable to establish a relation between the binding energy D and the charge density at distance $d=1.4$ Å, which approximately corresponds to the interatomic distance in the silicon lattice.[4)] This dependence is essentially obvious, considering the sequence of calculations and the constant spacing of the curves $D=f(d)$. Indeed, the dependence of the binding energy on the charge density (Fig. 2) is found to be linear, and the rectilinear section in the region of high binding energies agrees with the tabulated data.[18] This shows that our prediction is reliable and gives hope that doping of Si with transition or rare-earth metals will lead to a solution of the problem of the thermal stability of Si.

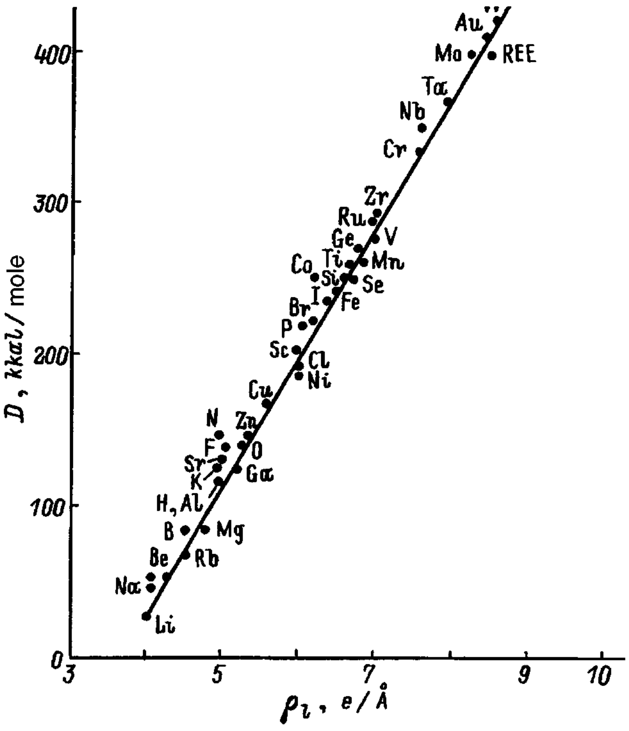

FIG. 2. Relation between the binding energy D and the charge density ρ_l for interatomic distance $d=1.4$ Å corresponding to the silicon lattice.

[1)] In Ref. 6 ribbon precipitates of hexagonal Si with microindentations of diamond-like Si were observed in the temperature interval 400–500 °C. The microindentations were attributed to a martensite transformation process.

[2)] We thank É. V. Prikhod'ko for a discussion of this problem and for assisting in the calculations.

[3)] According to Refs. 1 and 2, when Si is doped with gold, the lifetime of the nonequilibrium charge carriers drops sharply. For this reason, doping with gold is not recommended, since the cost is also taken into account.

[4)] The shortest interatomic distance between the (100) planes in the Si lattice equals 1.3577 Å (Ref. 4), but this distance can change when dopants dissolve in the lattice. This is why an approximate value is used in the text.

---

[1] A. Ya. Potemkin and I. E. Satsevich, *The Effect of Heat Treatment on the Physical Properties of Silicon* [in Russian], ONTI GIREDMET, Moscow (1962).
[2] A. Ya. Potemkin, Izv. Akad. Nauk SSSR, Neorg. Mater. **8**, 1353 (1972).
[3] I. T. Bagraev, L. S. Vlasenko, V. M. Volle *et al.*, Zh. Tekh. Fiz. **54**, 917 (1984) [Sov. Phys. Tech. Phys. **29**, 547 (1984)].
[4] V. M. Glazov and V. S. Zemskov, *The Physicochemical Principles of Semiconductor Doping* [in Russian], Nauka, Moscow (1967).
[5] Yu. N. Taran, V. Z. Kutsova, and K. I. Uzlov, Dokl Akad. Nauk Ukr. SSR, Fiz.-Mat. Tekhn. Nauki **6**, 74 (1987).
[6] P. Pirous, R. Chaim, U. Dahmen, and K. H. Westmacott, Acta Metall. Mater. **38**, 313 (1990).

[7] V. M. Glazov, V. B. Kol'tsov, V. Z. Kutsova, A. R. Regel', Yu. N. Taran, G. G. Timoshina, K. I. Uzlov, and É. S. Fal'kevich, Élektron. Tekhn. Ser. 6 — Materialy, No. 4(249), 53 (1990).

[8] V. M. Glazov, V. B. Kol'tsov, V. Z. Kutsova, A. R. Regel', Yu. N. Taran, G. G. Timoshina, K. I. Uzlov, and É. S. Fal'kevich, Fiz. Tekh. Poluprovodn. **25**, 588 (1991) [Sov. Phys. Semicond. **25**, 355 (1991)].

[9] V. M. Glazov, V. B. Kol'tsov, V. Z. Kutsova, A. R. Regel', S. V. Sirotyuk, Yu. N. Taran, and É. S. Fal'kevich, Fiz. Tekh. Poluprovodn. **27**, 1080 (1993) [Semiconductors **27**, 594 (1993)].

[10] V. M. Glazov, V. I. Pil'din, A. M. Zubkov, and V. B. Kol'tsov, Fiz. Tekh. Poluprovodn. **27**, 1605 (1993) [Semiconductors **27**, 886 (1993)].

[11] E. Yu. Tonkov, *Phase Diagrams of the Chemical Elements at High Pressures* [in Russian], Nauka, Moscow (1979).

[12] V. V. Dobrobenskiĭ and A. Ya. Potemkin, Fiz. Met . Metalloved. **17**, 83 (1964).

[13] É. V. Prikhod'ko, *Metallochemistry of Multicomponent Systems* [in Russian], Metallurgiya, Moscow (1995).

[14] É. V. Prikhod'ko, *System of Unpolarized Ionic Radii and Its Application for the Analysis of the Structure and Properties of Materials* [in Russian], Nauk. Dumka, Kiev (1973).

[15] É. V. Prikhod'ko, Izv. Akad. Nauk SSSR, Ser. — Metally, No. 6, 208 (1981).

[16] É. V. Prikhod'ko and L. I. Garmash, Izv. Akad. Nauk SSSR, Ser. — Metally, No. 1, 59 (1992).

[17] É. V. Prikhod'ko, K. Yu. Sidorenko, and V. B. Kol'tsov, Zh. Fiz. Khim. **62**, 62 (1988).

[18] *Handbook of Chemistry and Physics,* CRC Press Inc., Boca Raton, Florida (1989−1990), p. F197.

Translated by M. E. Alferieff

Optical spectroscopy of excitonic states in zinc diarsenide

A. V. Mudryĭ, V. M. Trukhan, A. I. Patuk, I. A. Shakin, and S. F. Marenkin

Institute of Solid-State and Semiconductor Physics, Bellorussian Academy of Sciences,
220072 Minsk, Belarus

(Submitted December 20, 1996; accepted for publication December 25, 1996)
Fiz. Tekh. Poluprovodn. **31**, 1029–1032 (September 1997)

The luminescence and transmission of zinc diarsenide single crystals near the fundamental absorption edge have been investigated in the temperature range 4.2–300 K. Intense luminescence and absorption lines at 1.0384, 1.0488, and 1.0507 eV, referring to the ground state ($n=1$) and excited states ($n=2$, $n=3$) of a free exciton were observed at low temperatures. The free-exciton binding energy was found to be ~13.9 meV on the basis of the hydrogen-like model and the direct band gap was found to be 1.0523, 1.0459, and 0.9795 eV at 4.2, 78, and 300 K, respectively. © *1997 American Institute of Physics.* [S1063-7826(97)01208-8]

The compound $ZnAs_2$ is a II–V semiconductor which crystallizes in a monoclinic structure.[1] The arsenic atoms form chain structures which are oriented along the principal crystallographic axis **C**. As a result, the physical (electrical, optical, and other) properties of this material are strongly anisotropic.[2–6] Until now, among the compounds in this group of semiconductors, $ZnAs_2$ has been studied in greatest detail, but many of its properties, primarily the optical properties, have not been adequately studied. In most cases the data on the fundamental parameters and band structure of this material are inconsistent.[3–5] Furthermore, no one has investigated the luminescence near the intrinsic absorption edge. Since optical spectroscopy is an effective method for determining band-structure parameters, in the present work measurements of the optical transmission and luminescence were performed near the fundamental absorption edge in a wide range of temperatures in order to establish the fundamental parameters of this material — the exciton binding energy and an accurate value of the width of the band gap.

The investigations were performed on structurally perfect $ZnAs_2$ single crystals, grown by Bridgman's method of vertical directed crystallization, and on crystals obtained from the gas phase. The initial samples exhibited, as a rule, *p*-type conductivity and possessed a carrier density $\sim 10^{14}$ cm^{-3} and Hall mobility 150 $cm^2/(V\cdot s)$. The dislocation density in the crystals was less than 5×10^2 cm^{-2}. The optical spectra were recorded in unpolarized light in the temperature interval 4.2–300 K. The spectral dependence of the absorption coefficient $\alpha(h\nu)$ was determined from the transmission spectra according to the ratio

$$T_0=\frac{(1-R)^2\,\exp(-\alpha d)}{1-R^2\,\exp(-2\alpha d)}, \tag{1}$$

where T_0 and R are the reflectance and transmittance, and d is the thickness of the sample. It was determined that the transmittance T_0 in the spectral region 0.7–0.9 eV does not depend on $h\nu$ and equals 50–55% for all samples studied, i.e., $\alpha d \ll 1$ (transmission region). The reflectance R for this energy interval was determined from the relation $T_0=(1-R)/(1+R)$. The luminescence spectra were recorded by the method described in Ref. 7. The spectral position of the lines in the optical spectra was determined to within ± 0.2 meV.

A typical absorption spectrum of one sample of zinc diarsenide ($d\simeq 60$ μm) at 4.2 K is shown in Fig. 1. Three lines with maxima at 1.0384, 1.0488, and 1.0507 eV, which merge in the short-wavelength region, are clearly seen in the spectrum. The half-width of these lines equals ~0.54 meV, i.e., ~1.5 kT. It should be noted that the energy position of the lines is virtually identical for crystals grown by Bridgman's method or synthesized from the gas phase and remains unchanged from sample to sample in the range ± 0.2 meV. The stability of the energy position of the spectral lines and the quality of the half-widths in samples cut from different ingots or parts of the same ingot shows that the single crystals synthesized by Bridgman's method and the crystals grown from the gas phase were structurally perfect. The structure of the absorption spectrum displayed in Fig. 1 is characteristic of direct-gap materials and can be interpreted as a manifestation of the ground state ($n=1$) and two excited states ($n=2$, $n=3$) of a free exciton — the lines 1.0384, 1.0488, and 1.0507 eV, respectively. If the hydrogen-like model describing the energy of the excitonic states is taken as a basis, the exciton binding energy E_{ex} can be calculated and the direct gap E_g can be estimated. According to this model the energy E_n of the excitonic states is determined from the formula

$$E_n=E_g-\frac{E_{ex}}{n^2}. \tag{2}$$

Using the experimentally determined values of the energy position of the ground state (1.0384 eV) and excited excitonic states (1.0488 and 1.0507 eV), we estimated the exciton binding energy as 13.9 meV and obtained a direct gap of 1.0523 eV at 4.2 K.

Figure 2 shows the transmission spectra of a $\simeq 300$ μm-thick-sample at 4.2, 78, and 300 K. One can see that as the measurement temperature increases, the excitonic series shifts into the long-wavelength region of the spectrum, the corresponding $n=1$, 2, and 3 lines are broadened, and the components referring to the excited states gradually vanish.

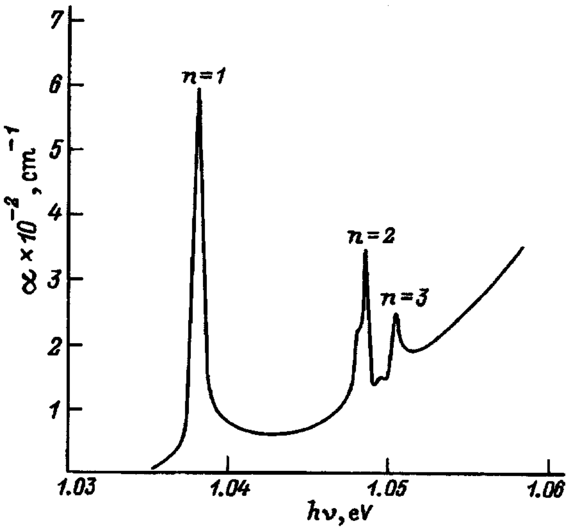

FIG. 1. Absorption spectrum of zinc diarsenide at 4.2 K. The spectral resolution is 0.1 meV.

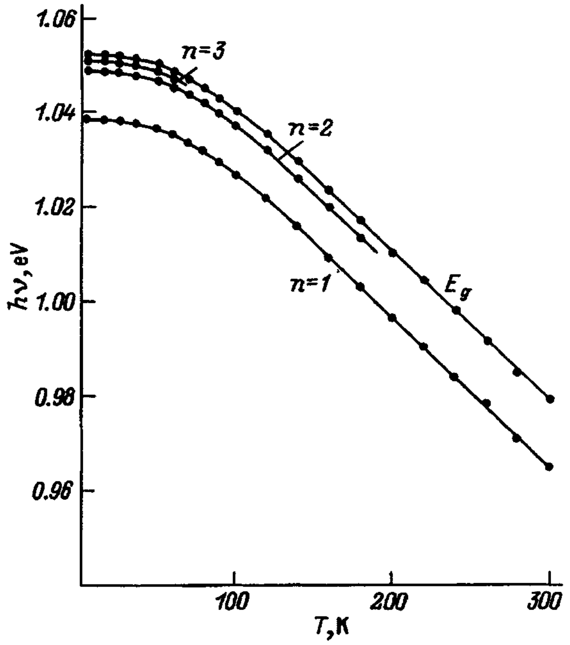

FIG. 3. Temperature dependence of the energy position of the excitonic states and band gap in zinc diarsenide.

The experiments showed that the relative energy splitting between the lines does not depend on the temperature and remains constant. Lines with $n=3$ and $n=2$ are present in the transmission spectra up to temperatures of 70 and 180 K, respectively. At room temperature only the exciton ground state $n=1$ is seen (Fig. 2c).

As follows from Figs. 1 and 2a, besides the excitonic absorption peaks corresponding to the ground and two excited states, the $n=2$ line possesses a fine structure, which consists of two additional components 1.0482 and 1.0498 eV. These components are observed in the spectra up to temperatures ~35 K, and at higher temperatures they are not resolved because of temperature broadening. One reason for the appearance of a fine structure in the first excited state will be given below.

The temperature dependence of the variation of the energies of the ground state and two excited states, as well as the gap width, are shown in Fig. 3. It follows from our experiments that the exciton binding energy does not depend on the measurement temperature. In accordance with Eq. (2), the temperature dependence of the band gap can therefore be obtained by adding the exciton binding energy of 13.9 meV to the experimentally measured value of the ground-state energy (the line $n=1$). An estimate of the temperature coefficient of the variation of the band gap in the region 110–300 K gives 3.1×10^{-4} eV/K.

Figure 4 shows the luminescence spectra of zinc diarsenide single crystals at different temperatures. A doublet structure (1.0384 and 1.0396 eV) with a 3:1 intensity ratio is observed near the absorption edge (Figs. 4a and 4b). This structure is due to the recombination of free excitons in the ground state. A large increase in sensitivity of the measuring apparatus (by a factor of $\sim 10^3$) makes it possible to record in the emission spectra a line at 1.0788 eV due to the annihilation of excitons in the first excited state ($n=2$). The experiments showed that the energy positions of the absorption and luminescence peaks for excitonic states are the same. The 1.0344-eV (*M*5) luminescence line, which we observed previously, is attributable it to the radiative recombination of excitons localized at impurity–defect complexes.[8]

The half-width of the excitonic luminescence lines with $n=1$ and $n=2$ at 4.2 K is equal to ~0.48 meV, i.e., 1.3 kT.

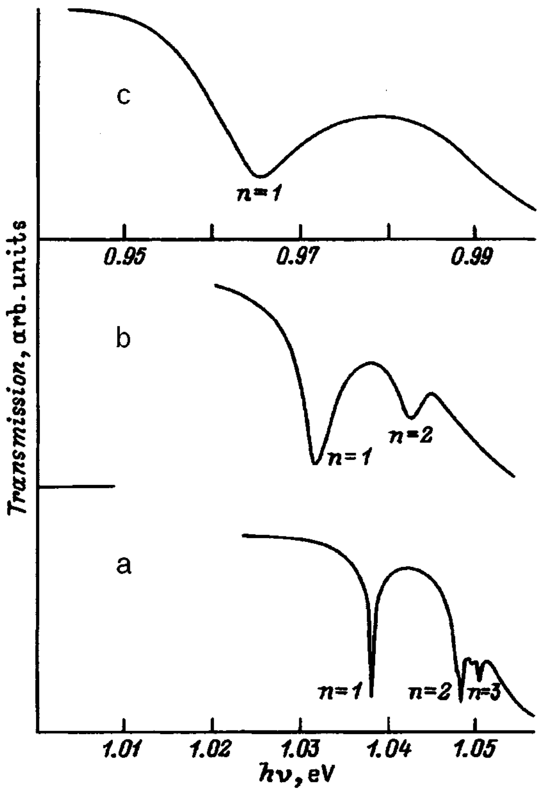

FIG. 2. Transmission spectra of zinc diarsenide. The spectral resolution is 0.1 meV. *T*, K: a — 4.2, b — 78, c — 300.

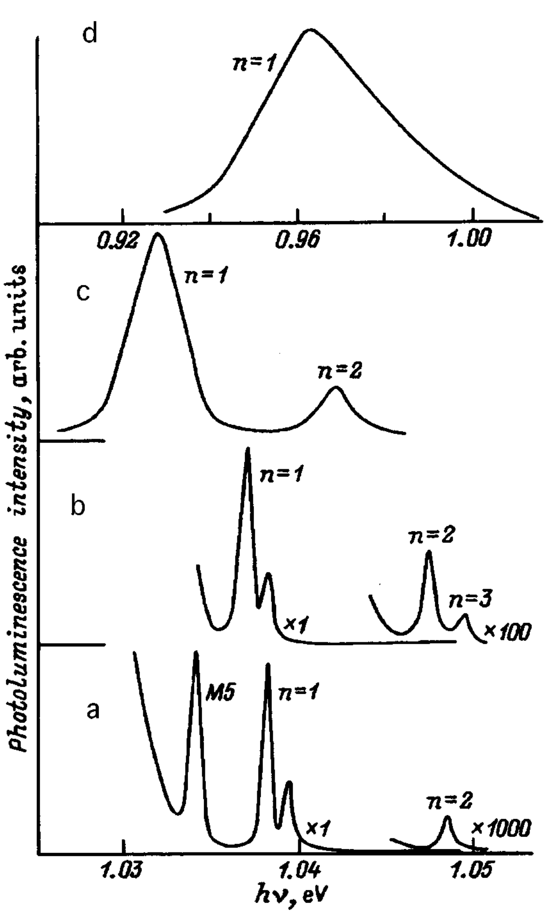

FIG. 4. Luminescence spectra of zinc diarsenide, the spectral resolution is 0.3 meV. a — 4.2, b — 48, c — 78, d — 3000.

As the temperature increases, these lines broaden and shift into the low-energy region. At $T\sim48$ K (Fig. 4b), together with the $n=1,2$ lines, a line referring to the second excited state $n=3$ is clearly seen in the luminescence spectra and it remains up to temperatures of ~65 K. The excitonic state with $n=2$ is seen in the luminescence up to temperatures ~180 K.

As liquid-nitrogen temperature is approached, the doublet structure of the split exciton ground state becomes impossible to resolve and at 78 K (Fig. 4c) a line with $n=1$, which broadens up to 4.5 meV, is observed.

A line at 0.963 eV, which corresponds to the excitonic ground state with $n=1$, dominates the room-temperature luminescence spectra.

We note especially the existence of splitting (~1.2 meV, Figs. 4a and 4b) of the excitonic ground state in luminescence and the first excited state in absorption (Fig. 1). In our opinion, this could be due to the spin-orbit or exchange interactions, as well as splitting of the energy bands. Effects of this kind have also been observed for other semiconductor compounds.[9,10]

It was determined that the temperature shift of the ground and excited states in luminescence is the same as in transmission. The exciton binding energy, which turned out to be 13.9 meV, in agreement with the absorption data, was determined on the basis of the energy position of the luminescence lines $n=1$, 2 at 4.2 K and $n=1$, 2, and 3 at 48 K in the hydrogen-like model.

The equation $1/m^*=1/m_e+1/m_h$, together with the known expressions for the electron and hole effective masses $m_e=0.345m$ and $m_h=2.45m$ (m is the free-electron mass), give for the reduced mass of the exciton $m^*=0.3m$. Taking into account the permittivity $\varepsilon_0=15$, we can define the binding energy of the exciton in the ground state in the hydrogen-like approximation as

$$E_{\text{ex}}=\frac{m^*e^4}{2h^2\varepsilon_0^2}. \tag{3}$$

Equation (3) gives the value $E_{\text{ex}}=18.3$ meV, which agrees satisfactorily with the experimental value.

It should be noted that the lines 1.0375 and 1.0475 eV, which refers to the $n=1$ and $n=2$ states of a free exciton, were observed previously in Ref. 3 in the transmission and reflection spectra at 4.2 K. The binding energy estimated from these data equals 12 meV, and the gap width equals ~1.049 eV at 4.2 K. However, the results obtained by us give different values for E_{ex} and E_g.

In our opinion, the observation of a state with $n=3$ in absorption and states with $n=1$, 2, and 3 in luminescence at different temperatures made it possible to obtain more accurate values for the direct band gap and the binding energy.

In summary, our experiments, which were performed for the first time, on the observation of the characteristic luminescence of zinc diarsenide with high spectral resolution, supplemented by measurements of the optical transmission, made it possible to determine to a high degree of accuracy the binding energy of a free exciton (~13.9 meV) and the band gap in the temperature interval 4.2–300 K.

This work was supported by the Fund for Fundamental Research of the Republic of Belorus.

[1] V. B. Lazarev, V. Ya. Shevchenko, Ya. Kh. Grinberg, and V. V. Sobolev, *II–V Semiconductor Compounds* [in Russian], Nauka, Moscow, 1978.
[2] V. V. Sobolev and N. N. Syrbu, Phys. Status Solidi B **51**, 863 (1972).
[3] V. V. Sobolev and A. I. Kozlov, Phys. Status Solidi B **126**, K59 (1984).
[4] S. F. Marenkin, A. M. Raukhman, D. I. Pishchikov, amd V. B. Lazarev, Neorg. Mater. **28**, 19813 (1992).
[5] V. A. Morozova, D. I. Pishchikov, V. M. Loseva, O. R. Koshelev, and S. F. Marenkin, Fiz. Tekh. Poluprovodn. **25**, 1664 (1991) [Sov. Phys. Semicond. **25**, 1005 (1991)].
[6] K. Khakimov, V. S. Vavilov, S. F. Marenkin, M. Yu. Khukhryanskiĭ, and V. M. Chukichev, Fiz. Tekh. Poluprovodn. **21**, 1447 (1987) [Sov. Phys. Semicond. **21**, 878 (1987)].
[7] S. F. Marenkin, D. I. Pishchikov, V. A. Leont'ev, A. V. Mudryĭ, V. G. Solov'eva, A. I. Patuk, and I. A. Shakin, Neorg. Mater. **29**, 607 (1993).
[8] A. V. Mudryi, A. I. Patuk, I. A. Shakin, A. E. Kalmykov, S. F. Marenkin, and A. M. Raukhman, Mater. Chem. and Phys. **44**, 151 (1996).
[9] J. Z. Wan, J. L. Brevner, R. Leonelli, G. Zhao, and J. T. Graham, Phys. Rev. B **48**, 5197 (1993).
[10] R. P. Seĭsyan and M. P. Abdulaev, Fiz. Tekh. Poluprovodn. **7**, 811 (1973) [Sov. Phys. Semicond. **7**, 554 (1973)].

Translated by M. E. Alferieff

The valence band structure in chalcopyrite Cu(In,Ga)Se_2 films

A. S. Kindyak and V. V. Kindyak

Institute of Physics of Solid State and Semiconductors, Belorussian Academy of Sciences,
220072 Minsk, Belarus

Yu. V. Rud'

A.F. Ioffe Physico-technical Institute, Russian Academy of Sciences, 194021 St. Petersburg, Russia

Fiz. Tekh. Poluprovodn. **31**, 1033–1036 (September 1997)

The structure of the valence band at the Γ point of the Brillouin zone of Cu(In,Ga)Se_2 films is investigated on the basis of interference spectrophotometry data and an analysis of the structure of edge absorption within the framework of the quasicubic model of valence-band $p-d$ hybridization in chalcopyrite compounds. The fundamental parameters of the quasicubic model associated with splitting of the valence band under the action of the tetragonal lattice field (Δ_{cf}), the spin–orbit interaction (Δ_{so}), and the degree of adulteration (hybridization) of the upper p-levels of the chalcogen by copper d states in Cu(In,Ga)Se_2 chalcopyrite films are determined. The dependence of the direct allowed transitions E_A, E_B, E_C on the composition of $CuIn_xGa_{1-x}Se_2$ solid solutions (for $0 \leqslant x \leqslant 1$) is established. © *1997 American Institute of Physics.* [S1063-7826(97)01808-5]

1. INTRODUCTION

Complex semiconductor I–II–VI_2 compounds and solid solutuions based on them are unique objects for the study of the fundamental properties of chalcopyrite semiconductors and for practical use in photo-energetics and opto-electronics.[1–6] In recent years thick-film structures based on I–III–VI_2 compounds have attracted much attention in connection with the possibility of using them to build solar cells with efficiencies as high as $16-17\%$ (Refs. 2–6). A special place among them is occupied by Cu(In,Ga)Se_2 (CIGS) chalcopyrite thick films possessing high absorption coefficient ($10^4-10^5\,\mathrm{cm}^{-1}$) and optimal bandgap width ($1.0-1.7$ eV). In this regard, the frequency region near the absorption edge is the most important segment of the spectrum for obtaining qualitative and quantitative information about the band structure near the energy extrema. However, it should be noted that there have been practically no systematic, detailed studies of CIGS thick films in this regard, while the information available in the literature is quite contradictory.[2–5] The energy transitions in CIGS films are interpreted differently, and not all the transitions have been identified. This has to do, first of all, with the fact that the optical properties of CIGS thick films are especially critical to the conditions of preparation of these films, and besides for the most part only the transmission spectra have been studied.

Previously, we published data on the structure of the edge absorption in laser-deposited, stoichiometric $CuInSe_2$ and $CuGaSe_2$ films, solid solutions based on them, and on the observed splittings of the valence band connected with the tetragonal lattice field and with the spin–orbit interaction.[7–11] The goal of the present work is to generalize these earlier data and to examine the structure of the valence band of CIGS thick films at the Γ point of the Brillouin zone using both reflection and transmission interference spectra and an analysis of the structure of the edge absorption within the framework of the quasicubic model of $p-d$ hybridization of the valence bands in chalcopyrite compounds.

2. SAMPLES

A study of the structure of the edge absorption was carried out on $CuIn_xGa_{1-x}Se_2$ films ($0 \leqslant x \leqslant 1$), obtained by pulsed laser evaporation, which allowed us to grow multicomponent layers whose composition reproduces the composition of the target thanks to the high evaporation rate and the high degree of supersaturation. Deposition of CIGS films was carried out using a YAG⟨Nd⟩ laser operating in the free lasing regime (wavelength $\lambda = 1.06\,\mu$m, pulse duration $\tau = 10^{-3}$ s, $E = 150-180$ J) on glass substrates at substrate temperature $T_s = 350$ °C (Refs. 11 and 12).

With the help of an x-ray diffractometer we determined that the obtained films possessed chalcopyrite structure and were oriented in the ⟨112⟩ direction. The degree of disorientation of the crystallites in the (112) plane as inferred from the rocking curves for the better samples did not exceed $2.0-2.5°$ (Refs. 11 and 12). A determination of the composition of the films by energy-dispersion x-ray analysis (EDAX) and Rutherford backscattering (RBS) showed that the composition of the films corresponds to that of the original material within the limits of measurement error ($\pm 2\%$).

3. EXPERIMENT AND CALCULATIONS

The optical constants and absorption coefficients of the CIGS films were determined from the reflection interference spectra $R(\lambda)$ and transmission interference spectra $T(\lambda)$ in the visible and near-infrared region of the spectrum ($400-1700$ nm) at room temperature. The spectral distribution of the reflection coefficient $R(\lambda)$ was measured on a Beckman-5240 spectrophotometer using a KSVU-3M spectral computational complex. To make these measurements, we used a special attachment which has symmetric ray-paths for near-normal incidence of light on its surface. The error in the amplitude, ΔR, was $\sim 2\%$. The transmission spectra were taken on a Perkin–Elmer-280 spectrophotometer. The thickness of the films was $0.6-0.7\ \mu$m.

It is well known that allowing for all the optical phenomena in the system film–substrate, including multiple reflection and interference, leads to complicated transcendental equations that couple the refractive index n_2 and the absorption coefficient k_2 of the film with the measurements of $R(\lambda)$ and $T(\lambda)$.[7–10] However, although the solution of these equations may cause some difficulties, it allows one to obtain the most accurate and complete information about the complex structure of the edge absorption in CIGS thick films and about the band structure of chalcopyrite compounds.

The system of equations is

$$T_{14}=\frac{1-R_{12}}{1-R_{12}R_a^1}T_a,$$

$$R_{14}=\frac{R_{12}T_a^2}{1-R_{12}R_a^1}. \tag{1}$$

Here $R_{12}=(n_2-1)^2/(n_2+1)^2$ is the Fresnel coefficient of reflection at the film–air boundary, $R_a=\mathrm{C}/\mathrm{A}$; $R_a^1=\mathrm{B}/\mathrm{A}$; $T_a=16n_3(n_2^2+k_2^2)/A$; T_{14} and R_{14} are the measured transmission coefficient and reflection coefficient of the system film–substrate;

$$\mathrm{A}=\rho\tau\exp(\gamma k_2)+\delta\sigma\exp(-\gamma k_2)+2S\cos(n_2\gamma)$$
$$+2t\sin(n_2\gamma),$$
$$\mathrm{B}=\rho\sigma\exp(\gamma k_2)+\delta\tau\exp(-\gamma k_2)+2q\cos(n_2\gamma)$$
$$+2r\sin(n_2\gamma),$$
$$\mathrm{C}=\tau\sigma\exp(\gamma k_2)+\sigma\rho\exp(-\gamma k_2)+2q\cos(n_2\gamma)$$
$$+2r\sin(n_2\gamma),$$
$$\sigma=(n_2-n_3)^2+k_2^2,\quad \rho=(n_2+1)^2+k_2^2,$$
$$\tau=(n_2+n_3)^2+k_2^2,\quad r=2k_2(n_3-1)(n_2^2+k_2^2+n_3),$$
$$\delta=(n_2-1)^2+k_2^2,\quad t=2k_2(n_3+1)(n_2^2+k_2^2-n_3),$$
$$S=(n_2^2+k_2^2)(n_3^2+1)-(n_2^2+k_2^2)^2-n_3^2+4n_3k_2^2,$$
$$q=(n_2^2+k_2^2)(n_3^2+1)-(n_2^2+k_2^2)^2-n_3^2-4n_3k_2^2,$$
$$\gamma=4\pi d_2/\lambda.$$

The solution of system of equations (1) was found iteratively. It was assumed that the refractive index of the initial phase (n_1) and of the final phase (n_4) both equal unity, and that the refractive index of the substrate $n_3=1.5\pm0.01$. The accuracy of determination of n_2 and k_2 was ±0.001. The absorption coefficient α was determined from the expression $\alpha=2\pi k/\lambda$. The spectral dependence $\alpha(\hbar\omega)$ of the CIGS films is shown in Fig. 1.

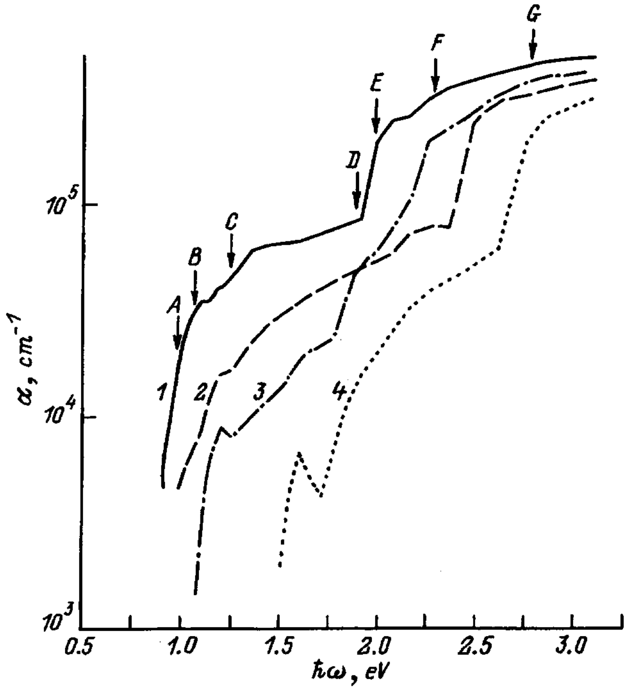

FIG. 1. Spectral dependence of the absorption coefficient of $\mathrm{CuIn}_x\mathrm{Ga}_{1-x}\mathrm{Se}_2$ thick films for x equal to 1.0 (*1*), 0.8 (*2*), 0.5 (*3*), 0.9 (*4*).

4. ANALYSIS AND DISCUSSION OF RESULTS

It is well known that the peculiarities of I–III-VI_2 compounds with chalcopyrite structure, in particular, tetragonal distortion of the crystalline lattice, have a substantial effect on the formation of the levels of the valence band.[13] Since the volume of the unit cell of chalcopyrite is four times greater than the volume of the unit cell of sphalerite, the valence band of chalcopyrite compounds consists of not three, but 12 branches, and in the case of I–III-VI_2 compounds, of 16 branches. The transformation from sphalerite to chalcopyrite can be represented as the result of substitution of the metal atoms by metal atoms of two sorts. As a result of such a substitution, the symmetry of the lattice is lowered and the branches of the sphalerite valence band are deformed and partly split off, one from another. The top of the valence band, as in sphalerite, is located at the Γ point of the Brillouin zone. At this point the representation Γ_6 or Γ_7 develops in chalcopyrite (Fig. 2).

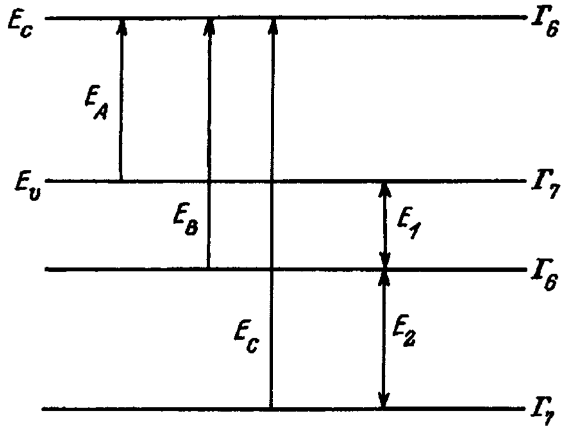

FIG. 2. Energy level diagram in the center of the Brillouin zone of CIGS chalcopyrite films.

TABLE I. Valence band parameters of $CuIn_xGe_{1-x}Se_2$ thick films

x	E_A	E_B	E_C	E_D	E_E	E_F	E_G	$-\Delta_{ef}$	Δ_{so}	hybridization, %
0.00	1.68	1.78	1.98	2.60	2.80	–	–	0.13	0.23	36
0.20	1.48	1.57	1.74	1.99	2.09	2.21	–	0.12	0.20	41
0.50	1.25	1.35	1.50	2.15	2.23	2.60	–	0.13	0.18	45
0.80	1.08	1.17	1.28	2.23	2.43	2.60	–	0.11	0.13	54
1.00	0.99	1.04	1.22	1.90	2.00	2.35	2.80	0.07	0.20	41

Note: All values of the energy parameters are given in eV.

Here it should be noted that the results of band-structure calculations for I–III–VI_2 compounds differ from the data obtained experimentally.[14–16] The hypothesis of $p-d$ hybridization was in fact advanced to explain these differences. In I–III-VI_2 compounds the upper p-like valence bands are subject to the influence of the near-lying d level of the group-I metal. The Hopfield quasicubic model satisfactorily explains the observed splitting of the valence band in chalcopyrite compounds associated with the tetragonal lattice field (Δ_{cf}) and spin–orbit interaction (Δ_{so}), in terms of $p-d$ hybridization of the valence band under the action of the tetragonal distortion of the chalcopyrite crystalline lattice, which leads to an adulteration of the upper p levels of the chalcogen in the valence band by the copper d level.[14–16]

An analysis of the dependence $\alpha(\hbar\omega)$ (Fig. 1) of CIGS thick films within the framework of the quasicubic model shows that a substantial contribution to the structure of the edge absorption of CIGS films comes from direct, allowed transitions defined by the relations $(\alpha\hbar\omega)^2=A^2(\hbar\omega-E_g)$ (E_g is the bandgap and A is a coefficient) in different energy intervals: $E_A=0.99-1.68$ eV for the transition valence band–conduction band ($\Gamma_7^v-\Gamma_6^c$); $E_B=1.04-1.78$ eV for the transition due to splitting of the valence band under the action of the tetragonal lattice field ($\Gamma_6^v-\Gamma_7^c$); and $E_C=1.22-1.98$ eV for the transition associated with spin–orbit splitting of the valence band ($\Gamma_7^v-\Gamma_6^c$). The high-energy structure (E_D, E_E, E_F, E_G), which leads to an increase of α by nearly an order of magnitude, is due to transitions of electrons from the copper d levels mixed into the upper chalcogen p levels in the valence band to the conduction band under the action of the tetragonal distortion of the crystalline lattice. The degree of mixing (hybridization) of the copper d levels into the chalcogen p levels in the valence band is defined by the expression[14]

$$\Delta_{so}^{\exp}=\beta\Delta_c+(1-\beta)\Delta_d,$$

where Δ_c are the calculated values $\Delta_{so}^{\text{theor}}$, Δ_d is the negative spin–orbit splitting of the d levels (for copper compounds it is assumed to be equal to 0.13 eV), and $1-\beta$ is the percent content of copper d levels in the valence band.

For CIGS films the degree of adulteration of the chalcogen p levels by the copper d levels amounts to 36−41% (see Table I), which is in good agreement with the data for copper compounds reported in Ref. 14.

The main parameters of the quasicubic model, i.e., the crystal field (Δ_{cf}) splitting and spin–orbit (Δ_{so}) splitting, were determined from the data of the observed splittings of the valence band via the relations[17]

$$E_{1,2}=\frac{1}{2}(\Delta_{so}+\Delta_{cf})\pm\frac{1}{2}\left[(\Delta_{so}+\Delta_{cf})^2-\frac{8}{3}\Delta_{so}\Delta_{cf}\right]^{1/2},$$

where $E_1=E_B-E_A$ and $E_2=E_B-E_C$. Thus we determined the energies of the Γ_7 valence bands relative to the top of the Γ_6 band. The calculated values of Δ_{cf} and Δ_{so} for CIGS films, shown in Table I, are in good agreement with the Δ_{cf} and Δ_{so} data for single crystals.[14]

We have also established that the concentration dependences of the E_A, E_B, and E_C transitions have a nonlinear form and are described by the quadratic equations (Fig. 3):

$$E_A=1.678-1.003x+0.317x^2;$$

$$E_B=1.772-0.966x+0.244x^2;$$

$$E_C=1.978-1.168x+0.401x^2.$$

The nonlinearity parameter for the E_A transition, equal to 0.317, differs from the value given in Ref. 5 (0.160), but agrees well with the results of Ref. 18 (0.298).

The values of the energy transitions in CIGS thick films obtained in the region of the fundamental absorption edge agree well with the experimental values for bulk crystals and corroborate the valence-band $p-d$-hybridization model in chalcopyrite compounds.

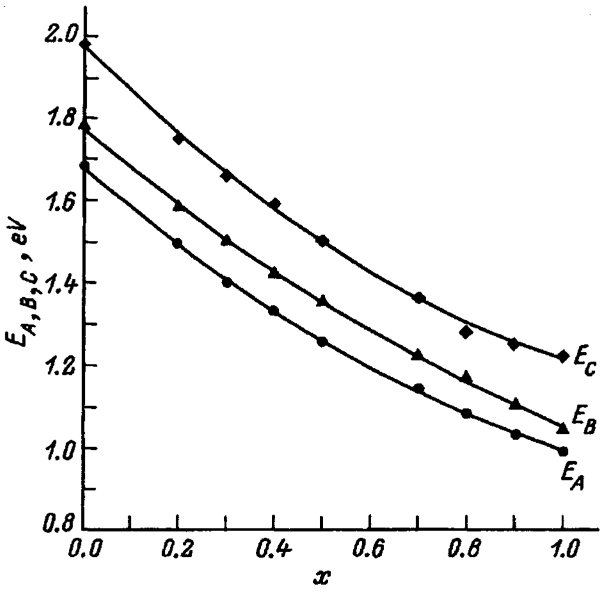

FIG. 3. Concentration dependence of the E_A, E_B, E_C transitions in $CuIn_xGa_{1-x}Se_2$ thin films.

In summary, we have identified the complex structure of the edge absorption in CIGS thick films. On the basis of an analysis of the structure of the edge absorption within the framework of the quasicubic $p-d$ hybridization model, we have examined the structure of the valence band of CIGS thick films at the Γ point of the Brillouin zone. We have determined the main parameters of the quasicubic model associated with splitting of the valence band under the action of the tetragonal lattice field, the spin–orbit interaction, and the degree of hybridization of copper d states with the upper chalcogen p levels in the valence band of the CIGS chalcopyrite films.

The authors express their gratitude to V. F. Gremenok for preparing the films, and M. Ya. Yakushev (Selford University, England) for providing data on reversible Rutherford scattering of CIGS films.

These studies were supported financially, in part, by the Belorussian Fund for Fundamental Research (Grant No. F94-289) and the INTAS program (Grant No. 94-3998).

[1] *Current Topics in Photovoltaics*, Vol. 1, edited by T. J. Coutts and J. O. Meakin (Academic Press, Orlando, 1985)
[2] H. Neumann, B. Perlt, N.A.K. Abdul-Hussein, R.D. Tomlinson, and A.E. Hill, Cryst. Res. Technol. **27**, 469 (1982).
[3] J.R. Tuttle, D. Albin, R.I. Matson, and R. Noufi, J. Appl. Phys. **66**, 4408 (1989).
[4] Y. Aparma, R.S. Reddy, M.B. Srinivasulu, and Reddy P. Jayarama, Physica Scripta **44**, 310 (1991).
[5] T. Yamaguchi, J. Matsufusa, and A. Yoshida, Jpn. J. Appl. Phys. **31**, L603 (1992).
[6] J. Hedstrom, H. Ohlsen, M. Bodegard *et al.*, *Twenty-third IEEE Photovol. Spec. Conference*, Louisville (1993), p. 364.
[7] V.V. Kindyak, A.S. Kindyak, V.F. Gremenok, I.V. Bodnar', Yu.V. Rud', and G.A. Medvedkin, Fiz. Tekh. Poluprovodn. **27**, 1154 (1993) [Semiconductors **27**, 636 (1993)].
[8] V.V. Kindyak, A.S. Kindyak, V.F. Gremenok, I.V. Bodnar, Yu.V. Rud', and G.A. Medvedkin, Thin Solid Films **250**, 33 (1994).
[9] V.V. Kindyak, A.S. Kindyak, V.F. Gremenok, and A.A. Kutas, Thin Solid Films **240**, 114 (1994).
[10] A.S. Kindyak, V.V. Kindyak, and V.F. Gremenok, Mater. Lett. **28**, 273 (1996).
[11] V.F. Gremenok, V.V. Kindyak, E.P. Zaretskaya, A.S. Kindyak, I.A. Viktorov, I.V. Bodnar', and Yu.V. Rud', Fiz. Tekh. Poluprovodn. **29**, 1692 (1995) [Semiconductors **29**, 881 (1995)].
[12] V.F. Gremenok, E.P. Zaretskaya, I.V. Bodnar, and I.A. Victorov, Jpn. J. Appl. Phys. **32**, Suppl. 3, 90 (1993).
[13] V.A. Chaldyshev and G.F. Karavaev, Izv. Vuzov. Fizika, No. 5, 103 (1963).
[14] J.L. Shay, B. Tell, H.M. Kasper, and L.M. Schiavone, Phys. Rev. B **5**, 5003 (1972).
[15] J.L. Shay and H.M. Kasper, Phys. Rev. Lett. **29**, 1162 (1972).
[16] J.E. Rowe and J.L. Shay, Phys. Rev. B **3**, 451 (1971).
[17] J.L. Shay, E. Buecher, and J.H. Wernick, Phys. Rev. B **2**, 4104 (1970).
[18] A. Zegadi, M.A. Slifkin, M. Diamin, A.E. Hill, and R.D. Tomlinson, Phys. Status Solidi **133**, 533 (1992).

Translated by Paul F. Schippnick

Electronic structure of the Er–O_6 complex in silicon

N. P. Il'in and V. F. Masterov

St. Petersburg State Technical University, 195251 St. Petersburg, Russia

(Submitted January 4, 1997; accepted for publication January 22, 1997)
Fiz. Tekh. Poluprovodn. **31**, 1037–1044 (September 1997)

The energy diagram of the Er–O_6 complex in silicon is calculated. The square amplitudes of the wave functions of the complex on the erbium atom are determined. The results of our calculations show that the Er–O_6 complex is an acceptor in silicon. In addition, it is possible that the electron trap energy level is located in the energy gap of silicon. On the whole, the results of our calculations correspond to the Er–O quantum dot model proposed previously. © *1997 American Institute of Physics.* [S1063-7826(97)01908-X]

1. INTRODUCTION

A great deal of attention by researchers worldwide has been given in recent years to the study of the physical—especially optical—properties of erbium-doped silicon. This interest has been motivated, first of all, by the fact that this material exhibits electroluminescence and photoluminescence at 1.54 μm due to the $^4I_{13/2}-^4I_{15/2}$ intracenter transitions of the Er^{3+} ion. As is well known, optical-fiber transmission lines have minimum losses and minimal dispersion at $\lambda \approx 1.5$ μm.

Numerous studies[1,2] have shown that the optically active center in erbium-doped silicon is a complex formed as a result of the interaction of erbium with oxygen. The authors of Ref. 3 used the EXAFS method to identify the optically active complex consisting of an Er^{3+} ion with a six-oxygen environment (the Er–O_6 complex). The most symmetric configuration of the six oxygen atoms corresponds to an octahedral complex. However, by virtue of the fact that $f-f$ transitions are forbidden by parity in this case, intracenter luminescence of the Er^{3+} ions cannot be observed. Therefore, it is natural to assume that the symmetry of the Er–O_6 complex in erbium-doped silicon is lower than cubic, as is the case, for example, for the erbium sites in Er_2O_3 (Ref. 4), where two Er^{3+} ion sites are observed with symmetries C_2 and C_{3i}. Furthermore, the authors of Ref. 5 suggested on the basis of an analysis of structural studies of Si : Er, O crystals that the optimal radiating objects in erbium-doped silicon are Er_2O_3 clusters having dimensions of 1×2.5 nm. Recent studies of amorphous doped silicon *a*-Si : H(Er) by Mössbauer emission spectroscopy[6] indicate that the optically active center is the low-symmetry complex Er–O in amorphous erbium-doped silicon as well.

Obviously, the problem of determining the electronic structure of such complexes is of vital interest since it plays an important role in the excitation mechanism of $f-f$ luminescence. The authors of Ref. 7 proposed a quantum-dot model of Er_2O_3 in silicon, where the quantum dot is approximated by a spherical square well of the second type. The well parameters were estimated from the parameters of the band spectra of silicon and erbium oxide. It was assumed that the excitation of intracenter luminescence is effected by Auger recombination of the ''indirect'' exciton formed as a result of trapping of an electron at a level in the potential well, which interacts with a silicon band hole.

In this paper we present results of a calculation of the energy spectrum of the octahedral Er$-O_6$ complex in silicon, obtained within the framework of the cluster–band method. We have consciously chosen the symmetric octahedral complex in order to be able to solve the problem analytically, understanding that the result so obtained is of an approximate nature. However, we believe that the main features of the electronic structure of the center are preserved in the transition to a low-symmetry cluster with the difference that here we have additional splittings of the individual levels which are degenerate in our problem.

2. MODEL OF THE $[ErO_6]^Q$ IN A SILICON MATRIX

According to the available experimental data,[3] it may be assumed that an atom is located at an interstice with distorted octahedral configuration of the nearest sites of the tetrahedral lattice.[8] At these sites the silicon atoms are replaced by oxygen atoms. As a result, an ErO_6 complex which is imbedded in the silicon matrix is formed. Since the formal valence of oxygen is equal to two, each oxygen atom bonded with an Er atom retains a bond with only one silicon atom.1) It may be assumed that the remaining tetrahedral bonds of the silicon atoms, having been broken, close back up with each other (Fig. 1), by analogy with the formation of an *A* center in silicon.

Disregarding distortion, we will treat the ErO_6 complex as a complex of octahedral type; Fig. 2 indicates the oxygen orbitals which take part in the formation of the bonds with Er (sp_z, p_x, p_y) and Si ($\overline{sp_z}$). Next, we will show that the calculation of the electronic states of such a system can be reduced to a calculation of an ErO_6 complex possessing total electrical charge Q, where the quantum-chemical parameters of this complex are renormalized with allowance for the O bonds with the Si matrix. The symmetry of the system of levels of the octahedral complex is described in the literature (see, e.g., Ref. 9) and contains two levels each with symmetry a_{1g} (the bond of the 6s-orbitals of Er with the sp_z-orbitals of O), a level with symmetry e_g [the $5d(\mathrm{Er})-sp_z(\mathrm{O})$ bonds] and a level with symmetry t_{2g} [the $5d(\mathrm{Er})-p_x, p_y(\mathrm{O})$ bonds], and also a group of nonbinding levels, which can be subdivided into two subgroups: 1) oxygen levels with symmetry $t_{1u}/sp_z/\mathrm{f}$ and symmetry

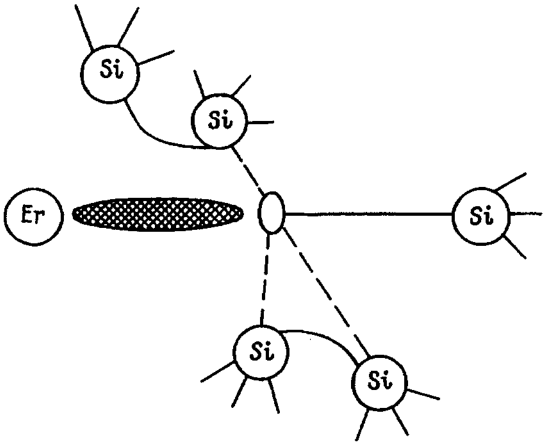

FIG. 1. Nature of the chemical bonds near an oxygen site in the system ‘‘ErO_6 complex in a Si matrix.’’

t_{1u}, t_{2u}, t_{1g}/p_x, p_y/;2) 2) the $4f$-levels of Er, whose splitting into levels with symmetry a_{2u}, t_{1u}, t_{2u} we disregard in light of the weak influence of the crystal field on this shell.[10] Finally, in addition to the $4f$ levels, there are the ten levels of the ErO_6 complex, on which the ‘‘valence’’ electrons of Er and the O electrons are located, with the exception of those that participate in the bonds with Si.

Let us now determine the total number of ‘‘inner’’ electrons of the complex filling the above-enumerated levels. Toward this end, we take as our starting point the $Er^{+3}O_6^{-2}$ complex and then introduce corrections associated with the deviation from pure ionicity of the Er–O and O–Si bonds. In the approximation of complete polarization of these bonds the valence shell of the oxygen ion takes the form $2s^2 2p^6$; of the eight electrons here, six are localized on the ‘‘inner’’ sp_z, p_x, p_y orbitals and two on the ‘‘outer’’ $\overline{sp}_z$ orbitals. Thus the $[ErO_6]^{-9}$ complex includes 36 electrons formally assigned to the oxygen ions plus 11 electrons of the ion in a shell of $4f$. The first group of electrons must be assigned to the ten levels of different symmetry indicated above. Taking into account the data on the structure of rare-earth oxides,[11] it may be assumed that these electrons occupy the lower (binding) levels a_{1g}, e_g, t_{1g}, and also nonbinding oxygen π-levels (t_{1u}, t_{2u}, t_{1g}) and σ-level (t_{1u}). The upper (unbinding) levels $a^*_{1g}, e^*_g, t^*_{2g}$ remain empty and constitute an analog of a conduction band. This situation is shown schematically in Fig. 3. We have excluded the $4f$-levels from consideration since in what follows we will disregard their hybridization with the states of the O atoms. This automatically means that the f-states, both filled and empty, do not take part in the process of charge transfer. Therefore, these levels are not shown in Fig. 3, but it is noted that the Er atom gives back three electrons to the formation of the bond—two $6s$ electrons and one $4f$ electron.

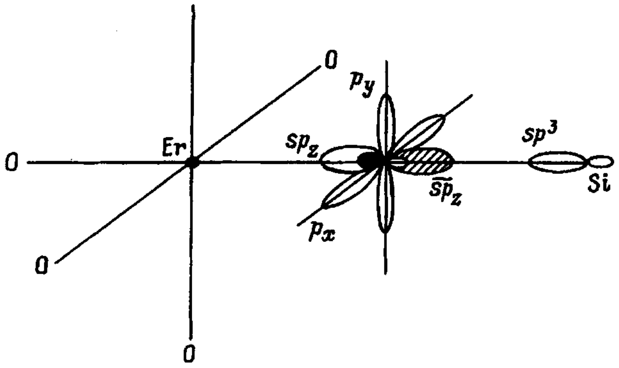

FIG. 2. Octahedral ErO_6 complex; the oxygen orbitals which form the ‘‘inner’’ and ‘‘outer’’ oxygen bonds are shown.

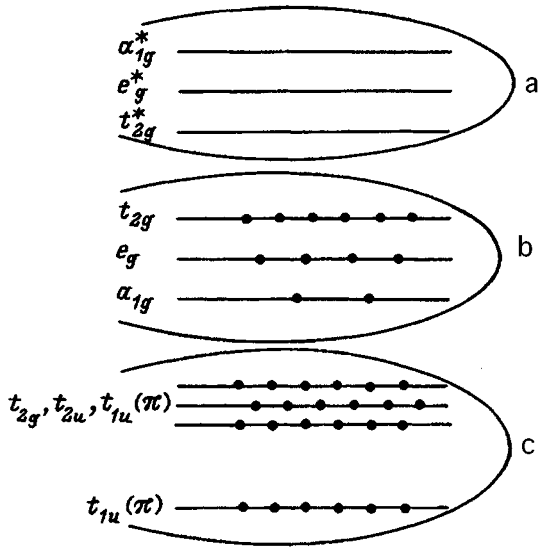

FIG. 3. Filling diagram of the one-electron levels in the $[ErO_6]^Q$ complex $(Q<0)$; a — unbinding levels, b — binding levels, c — nonbinding levels.

What will happen if we reject the hypothesis of complete polarization of the bonds? As for the Er–O bonds, a redistribution of the inner electrons of the complex will only affect the effective charges of the Er and O ions, which now must be written in the form $q=3-\chi$ and $q_0=-2+\chi/6$, respectively. The total charge of the complex $Q=q+6q_0$, of course, will not vary.

The matter is somewhat different with the O–Si bonds. It is clear that a redistribution of electrons on these bonds will have no effect on the number of ‘‘inner’’ electrons.

In any case we take for granted that in the formation of the complex the O atoms give back a total of three electrons to the outer bonds with three electrons from the Er atom compensating this loss. Here it is understood that the Si matrix contributes nine electrons to the bond with the complex (and not six, as one might assume by simply ‘‘cutting the Si–Si bond in two at the middle and replacing the neutral Si atom by a neutral O atom). In other words, we assume that the electronegativity of the O atom (electron affinity) is manifested already in the very process of complex formation, and not only by the charge number, in the distribution on the O–Si bond of the electrons obtained from O and Si for parity reasons (one from each atom). Obviously, this must lead to the appearance of holes in the silicon matrix. In this sense, such a complex should play the role of an acceptor.

However, this redistribution affects the total charge of the complex due to the change in the effective charge of the

O atom, which should now be written in the form $q_0=-2+\chi/6+\delta$, where δ is equal to the fraction of electrons forming the O–Si bond, which effectively belongs to the Si atom. To estimate δ, we may make use of data on the Si–O bond in Si oxides. It is well known that the mean bond energy here is equal to approximately 8 eV, where the fraction of the ionic and covalent contributions are roughly equal.[12] We denote the effective energies of the sp^3 orbitals of Si and the sp orbitals of O by E_1 and E_2, respectively, and their overlap integral (interaction integral) by β. From elementary quantum-mechanical arguments we then obtain a system of binding and unbinding levels:

$$E_{a,b}=\frac{1}{2}(E_1+E_2)\pm\sqrt{\frac{1}{4}(E_1-E_2^2+\beta^2)}.$$

The bond energy is defined, in the first approximation, as the distance between these levels, i.e.,

$$E_b=\sqrt{(E_1-E_2)^2+4\beta^2}.$$

Hence, taking the above into account we find $\beta^2=8$ eV. The square amplitude of the wave function of the lower binding level E_b on the sp-orbital of O is given by

$$C_0^2=\left[1+\frac{(E_b-E_2)^2}{\beta^2}\right]^{-1}\cong 0.85.$$

Thus, on the O atom is effectively located an electronic charge numerically equal to 1.7, i.e., $\delta=0.3$. Consequently, in a more accurate description the initial ErO_6 cluster has total charge $Q=q+6g_0=-7.2$, and the Er and O charges are equal, respectively, to $q=3-\chi$ and $q_0=-1.7+\chi/6$. The correction χ, associated with the redistribution of electrons the Er atom and the six O atoms, will be estimated below.

3. CALCULATIONAL METHOD AND RESULTS

Within the framework of the cluster–band method, various aspects of which were considered by us in a number of publications (see, e.g., Refs. 13 and 14), the main characteristics of the electronic structure of the impurity center may be obtained with the help of the one-electron Green's function represented as

$$G_{il}(E)=\left[E-E_i-\frac{b_{il}^2}{E-E_l-b_{lm}^2G_m(E)}\right]^{-1}, \tag{1}$$

where E_i and E_l are the effective energies of the orbitals of the central atom (Er) and the orbitals of the ligands (in the present case, the O atoms), b_{il} and b_{lm} are the hybridization integrals (of the covalent bond) between the Er and O orbitals, and also O and Si; $G_m(E)$ is the model Green's function for the Si matrix. The poles of $G_{il(E)}$ determine the position of the localized levels of the impurity center with respect to the Si bands prescribed by $G_m(E)$. Expression (1) allows us also to calculate the square amplitude of the wave function of the corresponding impurity levels on the Er orbitals, and also the local density of states in the allowed bands.

TABLE I. Values of the intraatomic parameters for Er and O.

	Er	O
E_f^c	−222.69	–
E_d^c	−117.41	–
E_s^c	−106.34	−140.62
E_p^c	–	−117.64
U_{ff}	20.00	–
U_{sf}	7.87	–
U_{df}	8.77	–
U_{dd}	9.40	–
U_{sd}	7.44	–
U_{ss}	5.79	24.22
U_{sp}	–	21.98
U_{pp}	–	20.02

Note: Values of the energies are given in eV (relative to the vacuum).

The structure of the function $G_m(E)$ for ideal semiconductors with tetrahedral bonds was considered in detail in Ref. 15. Without discussing the details, we note only the following. Setting $b_{lm}=0$, we obtain the pure cluster approximation for the ErO_6 complex. However, expanding $G_m(E)$ near the center of the Si band gap, given by E_m (Ref. 13), we can write $G_{il}(E)$ in quasicluster form:

$$G_{il}(E)=\left[E-E_i-\frac{\tilde{b}_{il}^2}{E-\tilde{E}_l}\right], \tag{2}$$

where the parameters b_{il} and E_l have been renormalized with allowance for the effect of the matrix; specifically,

$$\tilde{E}_l=(E_l+\gamma E_m)/(1+\gamma), \tag{3}$$

$$\tilde{b}_{il}=\frac{b_{il}}{\sqrt{1+\gamma}},$$

where $\gamma=b_{lm}^2/(b_1^2-b_2^2)$; the quantities b_1 and b_2 characterize the band structure of Si, and are uniquely determined by the width of the band gap and the width of the conduction band. An estimate using the data on the Si–O bond considered above gives $\gamma=0.40$.

Let us now consider the effective energies of the $6s$ and $5d$ orbitals of Er and the $2s$ and $2p$ orbitals of O in the ErO_6 complex. We will start with the situation corresponding to purely ionic bonds inside the complex ($b_{il}^2=0$, $\chi=0$, $Q=0$, $q=-1.7$). In this case we obtain, to start with, unoccupied levels of the $6s$ and $5d$ orbitals in the Er^{+3} ion; their effective energies can be represented in the form

$$\begin{aligned}E_s&=E_s^c+11U_{sf}+\rho Q,\\ E_d&=E_d^c+11U_{df}+\rho Q,\end{aligned} \tag{4}$$

where E_s^c and E_d^c are the contributions of the Er shell (with charge $Q_c=14.0$) to the corresponding orbitals; U_{sf} and U_{df} are the intraatomic interaction integrals with participation of the electrons in the $4f$ shell (their values together with the values of other intraatomic parameters were obtained by the method described in Ref. 16 and are given in Table I); the number 11 in expressions (4) corresponds to the number of f electrons, and ρ is a parameter of the electrostatic interaction. The last term, whose fundamental importance for the stabilization of the states of rare-earth ions in semiconductors was considered in Ref. 17, formally takes into account the total electrostatic interaction with the environment. But since the system ''ErO_6 + matrix'' as a whole is electrically neutral, the given term in fact determines the contribution to the effective energy from the Er electrons that have been shifted over onto the O ions; the effective number of these electrons is equal to the effective charge of the Er ions. Utilizing the data given in Table I, we obtain for the $Er_6^{+3}O_6^{-1.7}$ complex

$$E_s = -19.77 + 3\rho; \quad E_d = -20.94 + 3\rho. \tag{5}$$

The effective energies of the $2s$ and $2p$ orbitals of the O ion are determined in an analogous way with the one difference that here we are dealing with occupied states and, consequently, it is necessary to exclude the ''self-action'' of the electron in the corresponding orbital. Taking this fact into account, we write

$$\begin{aligned} \overline{E_s} &= \overline{E_s^c} + \overline{U_{ss}}(\overline{N_{ss}} - 1) + \overline{U_{sp}}\,\overline{N_p} + \overline{\rho q}, \\ \overline{E_p} &= \overline{E_p^c} + \overline{U_{pp}}(\overline{N_p} - 1) + \overline{U_{sp}}\,\overline{N_s} + \overline{\rho q}. \end{aligned} \tag{6}$$

The overplaced bar in expressions (6) is needed to distinguish the O parameters from the corresponding Er parameters. Above for the ion with effective charge $q = -1.7$ we determined values of the effective occupation numbers $\overline{N_s} = 1.85$ and $\overline{N_p} = 5.85$. Using the data of Table I, we find

$$\begin{aligned} \overline{E_s} &= 8.55 - 1.7\overline{\rho}, \\ \overline{E_p} &= 20.12 - 1.7\overline{\rho}. \end{aligned} \tag{7}$$

Let us turn our attention now to the role of the ''outer'' electrostatic field, which is taken into account by the parameters ρ (for Er) and $\overline{\rho}$ (for O). The loss by the Er atom of three electrons will lead to an abrupt drop in the effective energies of the $6s$ and $5d$ orbitals since attraction to the ionic shell now substantially dominates over the Coulomb interaction with the $4f$ shell. This is reflected in the significant negative value of the first terms in Eq. (5). In contrast, in the O ion, which has acquired almost maximally negative charge, the reverse phenomenon occurs: neglecting the electrostatic interaction with the environment, we would obtain here an abrupt increase in the effective energies [the first terms in Eq. (7)]. Taking this interaction into account makes it possible to stabilize the states of the corresponding ions in the sense of decreasing their deviation from the states in the neutral atom.

Naturally, it is impossible to estimate ρ and $\overline{\rho}$ from data for free atoms and ions. Therefore, we use data on the state of the Er and O ions in semiconductors. In this regard it should be noted that as a result of the interaction with the matrix the energies of the O orbitals are renormalized and the energies that figure in the calculation are, in fact, the energies $\overline{E_l}$ $(l = s,p)$ defined above [Eq. (3)]. The value of E_m can be determined, departing from the fact that data on the photoionization threshold in Si give the position of the top of the valence band $E_v = -5.20$ eV (Ref. 18); consequently, $E_m = -4.64$ eV (all values of energies are given relative to the vacuum). From Eqs. (5) and (7) it is clear that the lower level for the Er^{+3} ion is the E_d level, and the upper level for the O ion is the $\widetilde{E}_p$ level. Using the value of the band gap in Er_2O_3 (Refs. 7 and 11), the distance between these levels can be set equal to 5.4 eV. On the other hand, to estimate the position of the $\widetilde{E}_p$ level we can make use of the data of Ref. 19 on the position of the $2p$ level of fluorine relative to the top of the valence band of Si. This gives $\widetilde{E}_p = -12.2$ eV (relative to the vacuum), and finally, transforming from $\widetilde{E}_p$ to $\overline{E_p}$, we find $\rho = 4.87$ eV and $\overline{\rho} = 20.46$ eV.

TABLE II. Energy parameters of Er and O for the free atoms and in the ErO_6 cluster.

Er	E_d	2.71	−6.33
	E_s	−6.11	−5.16
	E_f	−6.95	−28.08
O	E_p	−13.62	−14.66
	E_{sp}	−21.05	−20.44

Note: Values of the energies are given in eV (relative to the vacuum).

This radical difference in the values of the electrostatic interaction parameter for the Er and O ions is in some sense understandable. Both ρ and $\overline{\rho}$ are close to the values of the corresponding intraatomic Coulomb integrals in these ions (see Table I). It is just this similarity that accounts for the stabilization effect: by losing (or acquiring) electronic charge in the crystal, the impurity ion ''feels'' a charge of opposite sign located at the surrounding atoms, and therefore does not deviate strongly from the electrically neutral state. Note that this does not pertain to the effective energy of the $4f$ orbitals; for them the difference between the values of ρ and U_{ff} is very substantial and therefore the levels of the $4f$ electrons lie significantly lower in the Er^{+3} ion than in the free atom. The system of levels for the free Er and O atoms and for the corresponding ions in the $Er^{+3}O_6^{-1.7}$ complex are given in Table II. Finally, the estimate we used for the parameters ρ and $\overline{\rho}$ are of a qualitative character, like the proposed model as a whole.

Let us now consider the hybridization of the Er and O orbitals $(b_{il} \neq 0, \chi \neq 0)$, taking into account the main symmetry aspects of the problem. In each irreducible representation (IR) of the group O_h, where hybridization occurs, the equation $[G_{il}^{\alpha}(E)]^{-1} = 0$ gives the pair of levels

$$E_{1,2}^{\alpha} = \frac{E_i + \widetilde{E}_l}{2} \pm \sqrt{\left(\frac{E_i - \widetilde{E}_l}{2}\right)^2 + \widetilde{b}_{il}^2}, \tag{8}$$

where α is the index of the irreducible representation; naturally, different values of α correspond, in general, to different i and l. In particular, for the irreducible representation a_{1g} the index $i = s$, and the index l corresponds to the ''hybrid'' sp_z orbital of O (see Fig. 2), whose effective energy is given by $\widetilde{E}_{sp} = (1/2)(\widetilde{E}_s + \widetilde{E}_p)$. For the irreducible representation e_g the index $i = d$, and the index l also corresponds to the sp_z orbital. For the irreducible representation t_{2g} the index $i = d$, but $l = p$ since the corresponding $5d$ orbitals of Er hybridize here with the molecular π orbitals constructed from the p_x and p_y orbitals of O.

TABLE III. Self-consistent values of the effective parameters of the ErO_6 complex in Si.

	Er	O
E_f	-27.52	–
E_d	-5.68	–
E_s	-5.00	-26.94
E_p	–	-15.18
N_f	11.0	–
N_d	0.21	–
N_s	0.06	1.83
N_p	–	5.83
Q	2.73	-1.66

Note: Values of the energies are given in eV (relative to the vacuum).

In each of these irreducible representations the square amplitude of the wave function corresponding to the level E_k^α $(k=1,2)$ on the Er orbital is given by

$$C_{k\alpha}^2=\left[1+\frac{(E_k^\alpha-E_i)^2}{\tilde{b}_{il}^2}\right]^{-1}. \tag{9}$$

Here the normalization condition $C_{1\alpha}^2+C_{2\alpha}^2=1$ is satisfied, which allows us from here on to consider only the quantities $C_{1\alpha}^2$ for the lower (binding) level in the irreducible representation α. From expressions (8) and (9), with allowance for Eq. (2), it is not hard to obtain a relation linking the quantities $C_{1\alpha}^2$ directly with the effective energies E_i and $\tilde{E}_l$:

$$E_i-\tilde{E}_i=|\tilde{b}_{il}|\frac{1-2C_{1\alpha}^2}{\sqrt{(1-C_{1\alpha}^2)C_{1\alpha}^2}}. \tag{10}$$

Note the simple meaning of this relation. If in the given irreducible representation the effective energy of the Er orbital lies above (below) the effective energy of the O orbital, then localization of an electron on the Er orbital is less (greater) than 0.5. The case of complete localization $(C_{1\alpha}^2=1)$ or complete delocalization $(C_{1\alpha}^2=0)$ implies that the hybridization parameter $\tilde{b}_{il}=0$. Finally, the homeopolar bond $(C_{1\alpha}^2=0.5)$ corresponds to equality of the effective energies $E_i=\tilde{E}_l$. Since partial filling of the Er ''valence'' orbitals takes place for $\tilde{b}_{il}\neq 0$, the effective energy of the latter is now written in the form (numerical energy values are given in eV)

$$\begin{aligned} E_s&=-19.77+U_{ss}N_s+U_{sd}N_d+\rho Q;\\ E_d&=-20.94+U_{dd}N_d+U_{sd}N_s+\rho Q, \end{aligned} \tag{11}$$

where $Q=3-N_s-N_d$, N_s, and N_d are the effective occupation numbers. As for the valence orbitals of O, the expressions for the effective energies of the latter remains, as before, (6), but the quantities $\overline{N_s}$ and $\overline{N_p}$ change. In this case, the condition

$$N_s+N_d=-6(\Delta\overline{N_s}+\Delta\overline{N_p}), \tag{12}$$

is satisfied since a redistribution of the electronic charge takes place between the orbitals of the Er ion and the six O ions. To simplify the notation, we write the quantities $C_{1\alpha}^2$ for the irreducible representations a_{1g}, e_g, and t_{2g} in terms of C_{11}^2, C_{12}^2, and C_{13}^2, respectively. Thus, allowing for the number of electrons on the lower (filled) levels (Fig. 3), we obtain the following expression for erbium:

$$N_s=2C_{11}^2,\quad N_d=4C_{12}^2+6C_{13}^2. \tag{13}$$

In order to write similar expressions for O, it is necessary to take the following two points into account: 1) the distribution of the electron occupying the corresponding molecular orbital in the irreducible representation α between the orbitals of the six O ions; and 2) participation in the formation of molecular orbitals for the irreducible representations a_{1g} and e_g of the ''hybrid'' O sp orbital; we assume the electronic charge localized at such an orbital to be distributed equally between the $2s$ and $2p_z$ orbitals. We thus obtain

$$\begin{aligned} \overline{N_s}&=1.85-\frac{1}{6}C_{11}^2-\frac{1}{3}C_{12}^2,\\ \overline{N_p}&=5.85-\frac{1}{6}C_{11}^2-\frac{1}{3}C_{12}^2-C_{13}^2. \end{aligned} \tag{14}$$

It is not difficult to guess that the condition of conservation of total charge of the ErO_6 complex [Eq. (12)] is satisfied in this case.

The calculation of the quantities $C_{1\alpha}^2$, according to Eq. (10) has, by virtue of the expressions for the effective energies [Eqs. (6) and (11)] and the effective occupation numbers [Eqs. (13) and (14)], a self-consistent character if the values of the hybridization integrals b_{il} are known. To estimate these latter, we may use the relations obtained by Harrison based on the pseudopotential method.[20] Taking into account the interatomic distances in the ErO_6 complex and the characteristic mean radii of the $5d$ shells for the rare-earth ions obtained by the same author, we find that the values of b_{il}^2 in the irreducible representations a_{1g}, e_g, and t_{2g} are equal to 5.66, 3.39. and 0.34 $(\mathrm{eV})^2$, respectively. Obviously, in the first approximation hybridization of the $5d$ orbitals of Er and the $2p$ orbitals of O in the irreducible representation t_{2g} can be ignored; i.e., we can set $C_{13}^2=0$. The self-consistent values of C_{11}^2 and C_{12}^2 here are equal to 0.03 and 0.05, respectively. The final values of the effective energies and occupation numbers for Er and O in the ErO_6 complex are given in Table III.

The values of the energies of the binding and unbinding orbitals a_{1g}, a_{1g}^* and e_g, e_g^* can be obtained from Eq. (8); as for the t_{2g} and t_{2g}^* levels, by virtue of the approximation made above they are assumed to be nonbinding, where the empty level t_{2g}^* corresponds to the energy E_d, and the filled level t_{2g} corresponds to the energy $\tilde{E}_p$. We also have a system of nonbinding oxygen levels in the irreducible representations t_{1g}, t_{2u}, and t_{1u}, and in the last case two levels with energies $\tilde{E}_p$ and $\tilde{E}_{sp}$, which are calculated as described above.

In addition, we have two levels, which correspond to an occupied state and an empty state in the $4f^{11}$ shell. The energy of the occupied levels is given by

$$E_f=E_f^c+10U_{ff}+U_{st}N_s+U_{dt}N_d+\rho Q, \tag{15}$$

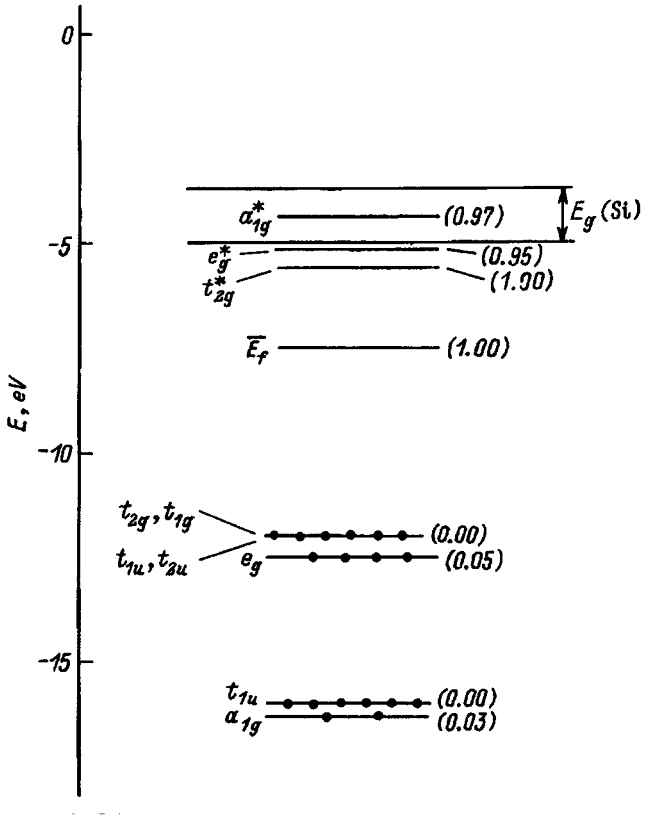

FIG. 4. Energy spectrum of the $\mathrm{Er}^{+2.74}\mathrm{O}_6^{-1.66}$ complex; positions of levels and band gap of Si are given relative to the vacuum. The filled level $E_f(4f^{11})$, located substantially lower, is not indicated.

where we have made note of the absence of ''self-action'' of the electron (or the presence of a ''Coulomb hole'' in Anderson's terminology[21]). The energy of the empty level is defined here as $\overline{E_f} = E_f + U_{ff}$. The final system of levels for an ErO_6 complex imbedded in a Si matrix is shown in Fig. 4, with the degree of localization of each level on the corresponding orbitals of the Er ion indicated.

4. DISCUSSION

Let us consider the energy spectrum of an Er–O_6 cluster, as shown in Fig. 4. As was already noted, the $4f$ states of the Er ion, by virtue of their lack of hybridization with the states of the O ions, do not participate in charge transport processes even inside the complex, and this is not to speak of Si. Obviously, such a statement can be made regarding the t_{2g}^* states, which are genetically related to the $5d$ states of the Er atom since the square of their wave function on the Er ion is essentially equal to 1.

Thus, we have two systems of levels—the upper empty levels a_{1g}^* and e_g^*, which are genetically related to the $6s$ and $5d$ states of the Er atom, and the filled, delocalized energy levels located deep in the valence band of Si, the upper ones of which t_{1g}, t_{1u}, t_{2g}, t_{2u}, and e_g are genetically related to the $2p$ states of the O atoms. The energy spectrum of the Er–O_6 complex so obtained corresponds to the band structure of the rare-earth oxides (see, e.g., Ref. 11), in which the bottom of the conduction band is formed by the $5d$ states of the rare-earth atoms and the top of the valence band is formed by the $2p$-states of the O atoms.

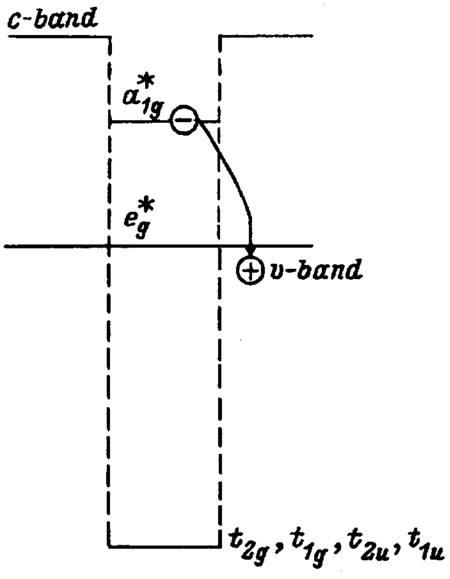

FIG. 5. Energy structure of an ErO_6 cluster in silicon in the ''well'' representation.

It should be noted that in the given calculation the Si matrix was taken into account only by ''renormalization'' of the parameters of the Green's function for a cluster; therefore, the energy spectrum shown in Fig. 4 does not contain levels which may arise due to the rearrangement of the bonds of the Si atoms on the boundary of the cluster, in particular, the formation of Si–Si double bonds shown in Fig. 1.

The energy spectrum of the Er–O_6 complex, we believe, confirms the main points of the model of a quantum well created by the $\mathrm{Er}_2\mathrm{O}_3$ cluster in Si. Indeed, the bottom of the electron well formed by the e_g^* states is located near the top of the valence band (Fig. 5), while the energy level of symmetry a_{1g}^*, located in the middle of the band gap, plays the role of a quantum-well level in the potential well. For the holes there exists a ''potential barrier'' with height of about 8 eV. Thus, an electron excited in the Si matrix can get trapped at an empty level of symmetry a_{1g}^* and, interacting via the Coulomb interaction with a hole from the valence band of Si, it can form an indirect exciton bound to the Er$-\mathrm{O}_6$ complex. Auger recombination of this exciton is accompanied by excitation of a $4f$ electron of erbium.

We note once more that the results obtained in the approximation of a symmetric octahedral Er–O_6 complex should be considered as qualitative, which give a faithful picture of the electronic structure of the Er–O complex in silicon, the order of the energy levels, their symmetry, and their arrangement relative to the energy bands of silicon.

5. CONCLUSIONS

The results of our calculation of the electronic structure of the octahedral Er–O_6 complex in Si support the main points of the model of a spherical square well proposed in Ref. 7 to explain the excitation of $f-f$ luminescence in

Er–O clusters in Si. In this case excitation is effected via trapping of an electron from the conduction band of Si to a localized level of the complex with subsequent formation of an indirect exciton bound to the complex followed by its Auger recombination.

The Er–O_6 complex is an acceptor in Si. This statement is valid only for such a complex, but not for the Er_2O_3 cluster, which is most probably responsible for the optical properties of Si : Er, O.

Finally, we note that analogous complexes can be formed in other semiconductors (e.g., III–V semiconductors doped with rare-earth atoms and also with oxygen.

This work was supported by the international program INTAS and the Russian Fund for Fundamental Research within the scope of INTAS–RFBR Grant No. 95-0531.

[1)] The bonds of the erbium atoms with their oxygen environments, of course, have a ''diffuse'' character substantially different from that of the O–Si bond.

[2)] Wherever we indicate oxygen atomic orbitals, we have in mind the symmetrized σ and λ orbitals constructed from them.

[1] *Rare-Earth Doped Semiconductors,* edited by G.S. Pomrenke, P.B. Klein, and D.W. Langer. MRS Symp. Proc. (Pittsburg, MRS, 1993) V. 301.

[2] *Rare-Earth Doped Semiconductors* II, edited by A. Polman, S. Coffa, and R.N. Schwartz. MRS Symp. Proc. (Pittsburg, MRS, 1996) V. 422.

[3] D.I. Adler, D.C. Jacobson, M.A. Marcus, J.L. Benton, J.M. Poate, and P.H. Citrin. Appl. Phys. Lett., **61**, 2181 (1992).

[4] K.M. Moon, W.C. Kochler, H.K. Child, and I.J. Raubenheimer. Phys. Rev., **176**, 722 (1968).

[5] J.C. Phillips. J. Appl. Phys., **76**, 5896 (1994).

[6] V.F. Masterov, F.S. Nasredinov, P.P. Seregin, V.Kh. Kudoyarova, A.N. Kuznetsov, and E.I. Terukov, Pis'ma Zh. Tekh. Fiz. **22**, 25 (1996) [Tech. Phys. Lett. **22**, 26 (1996)].

[7] V.F. Masterov and L.G. Gerchikov, in *Rare-Earth Doped Semiconductors*, edited by A. Polman, S. Coffa, R.N. Schwartz. MRS Symp. Proc. (Pittsburg, MRS, 1996), Vol. 422, p. 227.

[8] J. Bourgoin and M. Lanno, *Point Defects in Semiconductors* (Springer-Verlag, New York, 1983) [in Russian trans. Mir, Moscow (1984)] p. 19.

[9] I.B. Bersuker, *Electronic Structure and Properties of Coordination Compounds* (Khimiya, Leningrad, 1976), p. 120.

[10] V.F. Masterov, Fiz. Tekh. Poluprovodn. **27**, 1435 (1993) [Semiconductors **27**, 791 (1993)].

[11] A.A. Samokhvalov, in *Rare-Earth Semiconductors* [in Russian], edited by V.P. Zhuze and I.A. Smirnov (Nauka, Leningrad, 1977), pp. 5–47.

[12] V.I. Gavrilenko, A.M. Grekhov, A.V. Korbutyak, and V.G. Litovchenko, *Handbook of Optical Properties of Semiconductors* [in Russian], Naukova Dumka, Kiev (1987), p. 465.

[13] N.P. Il'in, V.F. Masterov, and A.É. Vasil'ev, Fiz. Tekh. Poluprovdn. **26**, 1866 (1992) [Sov. Phys. Semicond. **26**, 1046 (1992)].

[14] N.P. Il'in and V.F. Masterov, in *Spectroscopy of Crystals Activated by Rare-Earth and Transition Metal Ions*, edited by A. Ryskin and V. Masterov, SPIE **2706**, 226 (1996).

[15] N.P. Il'in, V.F. Masterov, and A.É. Vasil'ev, Fiz. Tekh. Poluprovdn. **25**, 185 (1991) [Sov. Phys. Semicond. **25**, 111 (1991)].

[16] A.É. Vasil'ev, N.P. Il'in, and V.F. Masterov, Fiz. Tekh. Poluprovdn. **25**, 1253 (1988) [Sov. Phys. Semicond. **22**, 793 (1988)].

[17] N.P. Il'in and V.F. Masterov, Semicond. Sci. Technol. **8**, 1253 (1993).

[18] A. Zunger. Solid State Phys., **39**, 275 (1986).

[19] T. Tiedje, K.M. Colbow, J. Gao, J.K. Kahn, J.N. Reimers, and D.C. Houghton, Appl. Phys. Lett., **61**, 1296 (1992).

[20] W. Harrison, *The Electronic Structure and Properties of Solids* [Russian trans.], Mir, Moscow (1993).

[21] R.W. Anderson. Phys. Rev., **124**, 41 (1961).

Translated by Paul F. Schippnick

Quenching of *EL*2 defect-induced luminescence in gallium arsenide by copper atoms

F. M. Vorobkalo, K. D. Glinchuk,[a)] and A. V. Prokhorovich

Institute of Semiconductor Physics, Ukrainian National Academy of Sciences, 252028 Kiev, Ukraine

(Submitted June 10, 1996; accepted for publication December 25, 1996)
Fiz. Tekh. Poluprovodn. **31**, 1045–1048 (September 1997)

It is shown that the introduction of copper atoms into gallium arsenide crystals containing $EL2$ antisite defects results in virtually complete vanishing of the $EL2$–induced luminescence bands with radiation maxima at $h\nu_m = 0.63$ and 0.68 eV. This occurs as a result of the deactivation of the $EL2$ defects as a result of their interaction with copper atoms, which account for the formation of electrically inactive $EL2$-Cu complexes. *© 1997 American Institute of Physics.* [S1063-7826(97)00509-7]

1. INTRODUCTION

It is well known that in GaAs $EL2$ defects, which are binary donors with levels ε_1 lying 0.75 eV below the conduction band bottom E_c and ε_2 levels lying 0.54 eV above the valence band top E_v and consist of antisite defects $\mathrm{As_{Ga}}$, which are either isolated or bound in pairs with interstitial arsenic atoms As_i or gallium vacancies V_{Ga}, initiate the appearance of luminescence bands with maxima at $h\nu_m = 0.63$ and 0.68 eV (Refs. 1–7).[1] The first band is due to a transition of free electrons to filled hole levels $\varepsilon_1 = E_c - 0.75$ eV, i.e., positively charged defects $EL2^+$. The second band is due to a transition of free holes into the energy levels ε_1 filled with electrons, i.e., neutral defects $EL2^0$. We shall show below that the introduction of copper atoms into gallium arsenide leads to complete quenching of the $EL2$-induced luminescence as a result of the formation of electrically inactive complexes $EL2$–Cu.

2. INVESTIGATION PROCEDURE

The initial crystals consisted of semi-insulating, undoped gallium arsenide crystals with resistivity $\rho = 2\times10^8\ \Omega\cdot\mathrm{cm}$ at 300 K and $EL2$ defect density $N = 1.6\times10^{16}\ \mathrm{cm}^{-3}$. The conductivity decreased with temperature T exponentially with activation energy 0.75 eV. This shows that the electric properties of the initial crystals are determined by the partially compensated levels $\varepsilon_1 = E_c - 0.75$ eV of $EL2$ defects — the Fermi level in the experimental crystals was fixed near the level ε_1, i.e., $N = N^+ + N^0$ and N^0, $N^+ \neq f(T)$. The shallowest acceptors in GaAs — carbon atoms with density $N_{\mathrm{C}} \simeq 3\times10^{15}\ \mathrm{cm}^{-3}$, which produce levels with energy $\varepsilon_{\mathrm{C}} = E_v + 0.026$ eV — were the main compensating impurity for $EL2$ defects.[8] The equilibrium density of positively charged $EL2^+$ defects in the experimental semi-insulating undoped crystals was $N^+ = 3\times10^{15}\ \mathrm{cm}^{-3} \simeq N_{\mathrm{C}}$, the density of neutral defects $EL2^0$ was $N^0 = 1.3\times10^{16}\ \mathrm{cm}^{-3}$, and the lifetime of the minority current carriers (electrons), which was controlled by defects other than $EL2$, is $\tau_n \simeq 10^{-10}$ s at 77 K.

The copper atoms, which upon replacement of the gallium atoms become double acceptors and form deep levels with energies in the experimental crystals $\varepsilon_1^* = E_v + 0.14$ eV and $\varepsilon_2^* = E_v + 0.44$ eV,[8] were diffused into semi-insulating GaAs crystals to density $N_{\mathrm{Cu}} \simeq 10^{17}\ \mathrm{cm}^{-3} \gg N$ at 750 °C in 4.5 h, which was followed by quenching. Diffusion was conducted in sealed quartz cells. The diffusion time was adequate for uniform saturation of the crystals with copper atoms. Quenching made it possible to avoid the precipitation of copper atoms from the solid solution when the crystals were cooled. The crystals obtained in this manner were of *p*-type and their resistivity was low compared with that of the initial crystals. The equilibrium hole density in the crystals at 300 K was $p_0 \simeq 8\times10^{16}\ \mathrm{cm}^{-3}$ — it was determined by the ionization of the carbon and copper atoms, $p_0 \simeq N_{\mathrm{C}} + N_{\mathrm{Cu}}$, and at 77 K $p_0 \simeq 3\times10^{15}\ \mathrm{cm}^{-3}$, determined by the ionization of the copper atoms, $p_0 \simeq N_c$. It follows from the relation $p_0 \simeq N_c$ established experimentally at 77 K that the carbon atoms in the crystals (just as in the initial semi-insulating undoped crystals) were the dominant shallow impurity (see also Ref. 8).

The Fermi level in the copper-doped crystals at low temperatures ($T \leqslant 77$ K) was located near the carbon level. Therefore the $EL2$ defects in the crystals could be primarily in the positively charged state $EL2^{++}$ ($N^{++} = N$, $N^+ = N^0 = 0$), and the copper atoms could be in the neutral state $\mathrm{Cu_{Ga}^0}$ with energy level $\varepsilon_1^* = E_v + 0.14$ eV; the equilibrium concentration of neutral copper atoms is $N_{\mathrm{Cu}}^0 \simeq N_{\mathrm{Cu}}$. The diffusion of copper atoms into the semi-insulating GaAs crystals has virtually no effect on the lifetime τ_n of the excess electrons (i.e., the copper atoms do not produce a recombination channel for the excess current carriers that is more efficient than the channels existing in the initial crystals) or on the density of the electrically active carbon atoms N_{C}.

Annealing of the control crystals (no copper atoms on the surface) had virtually no effect on the characteristics of the initial semi-insulating crystals (ρ, N_C, τ_n, and the intensities of the luminescence bands with $h\nu_m = 0.63$ eV — $I_{0.63}$ and $h\nu_m = 0.68$ eV — $I_{0.68}$).

The photoluminescence (PL) of the gallium arsenide crystals was excited by the strongly absorbed 1.96-eV radiation from a helium-neon laser. The light absorption coeffi-

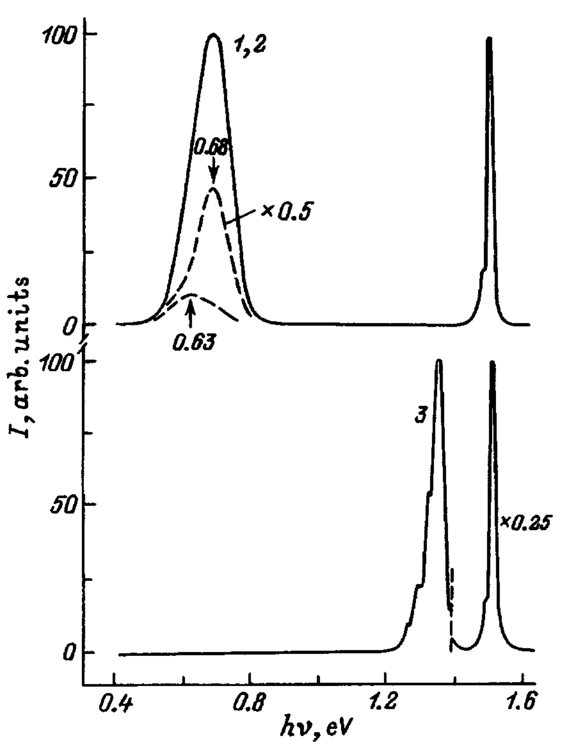

FIG. 1. PL spectra of gallium arsenide crystals: Initial semi–insulating undoped crystals (*1*), crystals after being heated at 750 °C for 4.5 h without (*2*) and with (*3*) a copper film on the surface. The measurement temperature is 77 K. Dashed lines — decomposition of the $EL2$–induced PL spectrum into components with radiation maxima at 0.63 and 0.65 eV.

cient was equal to 4×10^4 cm^{-1}, the intensity of the excitation photon flux was $L\simeq10^{18}$ cm$^{-2}\cdot$s^{-1}, and the number of excess electrons generated per cm^2 of the crystal surface was $\delta\mathcal{N}= L\tau_n$. Excitation changed only slightly the density of $EL2^+$ and $EL2^0$ defects in the initial crystals and $\mathrm{Cu}_{\mathrm{Ga}}^0$ copper atoms in the copper-doped crystals: The $EL2^+$ and $\mathrm{Cu}_{\mathrm{Ga}}^0$ states dominated in the radiative electron recombination processes and the state $EL2^0$ dominated in the case of hole recombination processes. The intensities I of the $EL2$- and Cu-induced luminescence bands increased linearly with the number of excess electrons. The PL spectra were measured at 77 K.

3. RESULTS

Figure 1 shows data illustrating the effect of copper atoms on the $EL2$–induced luminescence in gallium arsenide crystals. The following points are of interest.

1. The luminescence bands with $h\nu_m=0.63$ and 0.68 eV, which are due to radiative recombination of current carriers on the $EL2$ defects, dominate in the initial crystals.

2. Annealing of the control crystals (no copper layer on their surface) does not change the form of the initial spectra or the PL band intensities.

3. The introduction of copper atoms into the semi–insulating undoped crystals, as expected, leads to the appearance of a luminescence band with $h\nu_m=1.35$ eV. This band is associated with the transition of free electrons to neutral copper atoms $\mathrm{Cu}_{\mathrm{Ga}}^0$.[2] However, in this case the luminescence bands due to $EL2$ defects unexpectedly vanished completely. Emission bands other than the bands due to copper atoms are not observed in the PL spectra. The difference in the intensities of the characteristic luminescence bands ($h\nu_m\simeq1.51$ eV) between the initial undoped and copper–doped crystals is due mainly to the difference in free–hole density in the crystals.[2]

4. DISCUSSION

The quenching of the $EL2$–induced luminescence is undoubtedly due completely to the copper atoms, since annealing of the seminsulating undoped control crystals had virtually no effect on the PL spectrum (see Fig. 1).

As follows from the most general considerations (see, for example, Ref. 2), in the case under discussion the intensities $I_{0.63}$ and $I_{0.68}$ of the $EL2$–induced photoluminescence bands are

$$I_{0.63}=\eta^+u_1=c_n^+(N^++\delta N^+)\delta\mathcal{N}$$
$$=c_n^+(\varphi^++\delta\varphi^+)N\delta\mathcal{N}, \tag{1}$$

$$I_{0.68}=\eta^0u_1=(\eta^0/\eta^+)I_{0.63}, \tag{2}$$

where η^+ is the fraction of the electrons which recombine through the $EL2^+$ defects with emission of photons, η^0 is the fraction of holes which recombine through the $EL2^0$ defects with the emission of photons, u_1 is the intensity of recombination of excess electrons and holes via the level ε_1, c_n^+ is the radiative capture of electrons by $EL2^+$ defects, and $\varphi^+=N^+/N$ and $\delta\varphi^+=\delta N^+/N$ are the equilibrium and nonequilibrium fractions of $EL2$ defects in the state $EL2^+$.

As follows from Eqs. (1) and (2),

$$I_{0.63}=c_n^+N^+L\tau_n=c_n^+\varphi^+NL\tau_n=(\eta^+/\eta^0)I_{0.68} \tag{3}$$

in the initial semi-insulating GaAs crystals (in these crystals the illumination changes the initial density of defects in the $EL2^+$ state very little) and

$$I_{0.63}=c_n^+\delta N^+L\tau_n=c_n^+\delta\varphi^+NL\tau_n=(\eta^+/\eta^0)I_{0.68} \tag{4}$$

in the low-resistivity copper-doped *p*-GaAs crystals (in these crystals the equilibrium density of defects in the state $EL2^+$ is low — the latter appear mainly under illumination).

As follows from Eqs. (3) and (4), the substantial decrease in the intensity of the $EL2$–induced luminescence observed experimentally after the copper atoms are diffused could be due to the following factors:

1) Decrease in the lifetime τ_n of the excess electrons, since new efficient electron recombination centers appear; as a result, the number of carriers recombining through the $EL2$ defects decreases;

2) Change in the fraction of $EL2$ defects in the state $EL2^+$: $\varphi^++\delta\varphi^+\simeq\varphi^+\simeq0.2$ in the initial semi-insulating crystals and very likely $\varphi^++\delta\varphi^+\simeq\delta\varphi^+\ll0.2$ in the copper-doped, low-resistivity crystal;

3) Passivation of $EL2$ defects as a result of the formation of electrically inactive complexes $EL2$–Cu.

The first explanation is very unlikely, since as noted above, the diffusion of copper atoms has virtually no effect on the lifetime τ_n of the nonequilibrium electrons.

The second explanation is also unlikely. Indeed, in this case, as a result of the decrease in the density of defects in the state $EL2^{+}$ and the increase in the density of defects in the state $EL2^{++}$, one would expect that luminescence bands with $h\nu_m = 0.63$ and 0.68 eV would transform into different bands with maxima near 0.9 and 0.5 eV, induced by a transition of free electrons and holes to a second donor level of the $EL2$ defects $\varepsilon_2 = E_v + 0.54$ eV. However, in the experiment no impurity luminescence bands other than the one due to copper atoms was observed (see Fig. 1).

The latter explanation is the most likely one, since it is known that copper atoms can bind with $EL2$ defects to form electrically inactive complexes $EL2$–Cu, thereby substantially decreasing the density of isolated $EL2$ defects.[8,9] This is confirmed by the copper-atom-induced transformation observed at 77 K of semi-insulating GaAs crystals into ''conducting'' crystals. Evidently, this occurs when the density of $EL2$ defects decreases from the value $N > N_C$ to $2N < N_C$. Hence it follows that if $N = 1.6 \times 10^{16}$ cm^{-3} in the initial crystals, then $N > 1.5 \times 10^{15}$ cm^{-3} after the diffusion of copper atoms.

Therefore, the copper–atom–induced quenching of the $EL2$-induced luminescence bands is due mainly to a large decrease in the density of isolated $EL2$ defects as a result of the interaction of these defects with highly mobile interstitial copper atoms Cu_i (the copper atoms $\mathrm{Cu}_{\mathrm{Ga}}$ occupying lattice sites are immobile at the annealing temperatures employed). As noted above, some authors believe that the $EL2$ centers studied consist of isolated $\mathrm{As}_{\mathrm{Ga}}$ defects,[1,2,4,5] whereas other authors believe that they consist of the complexes $\mathrm{As}_{\mathrm{Ga}}V_{\mathrm{Ga}}$[6,7] or $\mathrm{As}_{\mathrm{Ga}}\mathrm{As}_i$.[1–3,5] Then the observed copper–atom–induced passivation of $EL2$ defects is due to the formation of complexes of $EL2$ defects with copper atoms $\mathrm{As}_{\mathrm{Ga}}\mathrm{Cu}_i$ or $\mathrm{As}_{\mathrm{Ga}}\mathrm{Cu}_{\mathrm{Ga}}$ or the associates $\mathrm{As}_{\mathrm{Ga}}\mathrm{As}_i\mathrm{Cu}_i$, whose electrical properties differ substantially from those of $EL2$ defects.

Undoubtedly, the quenching effect discussed in this paper can occur if the density of copper atoms is equal to or higher than the initial density of $EL2$ defects. Then most $EL2$ defects become bound with copper atoms (the density of the $EL2$–Cu complexes produced is of the order of the initial density of $EL2$ defects). As a result, the density of isolated $EL2$ defects decreases substantially and the $EL2$–induced luminescence is almost completely quenched. This is the case realized in our experiments.

5. CONCLUSIONS

Copper atoms in gallium arsenide play a dual role in the radiative recombination of excess current carriers. First, they are centers of luminescence in gallium arsenide, inducing the appearance of different luminescence bands which are due to a transition to them of free electrons and electrons bound on shallow donors. Second, they can be luminescence quenching centers, specifically, the luminescence due to antisite defects $EL2$, as a result of the formation of electrically inactive complexes $EL2$–Cu.

[a] Fax: (044) 265-83-42; electronic-mail: mickle@semicond.kiev.us

[1] The $EL2$ defects in the neutral state ($EL2^0$) and positively charged state ($EL2^{+}$) correspond to the level $\varepsilon_1 = E_c - 0.75$ eV and defects in the positively charged states ($EL2^{+}$ and $EL2^{++}$) correspond to the level $\varepsilon_2 = E_v + 0.54$eV. Obviously, the total density of $EL2$ defects is $N = N_0 + N^{+} + N^{++}$ and $\delta N^0 + \delta N^{+} + \delta N^{++} = 0$, where N^0, N^{+}, and N^{++} are the equilibrium densities of $EL2$ defects in the neutral and singly- and doubly-charged states, and δN^0, δN^{+}, and δN^{++} are the corresponding excess densities with respect to equilibrium.

---

[1] A. N. Georgibiani and I. M. Tiginyanu, Fiz. Tekh. Poluprovodn. **22**, 3 (1988) [Sov. Phys. Semicond. **22**, 1 (1988)].

[2] K. D. Glinchuk, V. I. Guroshev, and A. V. Prokhorovich, Optoélektron. Poluprovodn. Tekhn., No. 24, 66 (1992).

[3] D. J. Chadi, Phys. Rev. B **46**, 15053 (1992).

[4] Q. M. Zhang and J. Bernholc, Phys. Rev. B **47**, 1667 (1993).

[5] C. Y. Chang and F. Kai, *GaAs High-Speed Devices: Physics, Technology, and Circuit Applications*, New York (1994), p. 48.

[6] R. A. Morrow, J. Appl. Phys. **78**, 3843 (1995).

[7] R. A. Morrow, J. Appl. Phys. **78**, 5166 (1995).

[8] W. J. Moore, R. L. Henry, S. B. Saban, and J. S. Blakemore, Phys. Rev. B **46**, 7229 (1992).

[9] B. H. Yang and H. P. Gislason, in *Proceedings of the 18th International Conference Def. Semicond.*, Sendai, Japan, 1995, p. 713 [Mater. Sci. Forum, **196–201**, 713 (1995)].

Translated by M. E. Alferieff

Investigation of the parameters of deep centers in *n*-6*H*SiC epitaxial layers obtained by gas-phase epitaxy

A. A. Lebedev and D. V. Davydov

A. F. Ioffe Physicotechnical Institute, Russian Academy of Sciences, 194021 St. Petersburg, Russia

(Submitted November 28, 1996; accepted for publication February 13, 1997)
Fiz. Tekh. Poluprovodn. **31**, 1049–1051 (September 1997)

Epitaxial layers of 6*H*-SiC obtained by gas–phase epitaxy have been investigated by capacitance spectroscopy methods. It is shown that deep centers are present in the test samples. Such centers were previously observed in SiC epitaxial layers obtained by sublimation epitaxy. However, the total density of deep acceptors in structures prepared by gas-phase epitaxy is two to three orders of magnitude lower than in epitaxial films obtained by sublimation epitaxy with the same value of N_d-N_a. It is suggested that the conditions of growth of the epitaxial layers influence the density and the type of defects formed in them. © *1997 American Institute of Physics.* [S1063-7826(97)00609-1]

1. INTRODUCTION

Sufficiently pure epitaxial films ($N_d-N_a\approx10^{13}-10^{14}$ cm^{-3}) have been obtained in recent years by gas phase epitaxy (GPE). This has made it possible to produce on the basis of such films diode structures with a breakdown voltage U_{br} up to several kilovolts.[1,2] At the same time, record-high values of U_{br} have been attained in structures with small working areas ($\sim10^{-4}$ cm^2). Breakdown in these structures has been observed at substantially lower voltages than expected for a critical electric field strength in layers with such values of N_d-N_a. It was shown earlier that the dislocation density is, as a rule, high in layers prepared by GPE ($\sim10^3-10^4$ cm^{-2}), i.e., one to two orders of magnitude higher than in epitaxial layers prepared by sublimation epitaxy (SE).[3] It is also known that centers with deep levels (DCs) can have a large effect on the magnitude and temperature dependence of the breakdown voltage of SiC-based *p–n* structures.[4] Thus, the investigation of the parameters of compensating DCs in lightly doped silicon carbide layers obtained by GPE is a pressing problem.

2. EXPERIMENTAL PROCEDURE

Samples. The *p–n* junctions investigated in the present work were formed on the (0001) face of single–crystal 6*H* silicon carbide substrates. The junctions were fabricated by gas phase epitaxy by the CREE Company (USA) (GPE *p–n* structures) and structures obtained by sublimation growth of a p^+ emitter on *n*-type layers made by the CREE Company[5] (GPE–SE *p–n* structures) were investigated.

In both cases, Al (*p*-type) and N (*n*-type) served as the dopant. The *p*-type epitaxial layers were 1–2 μm thick and the *n*-type layers were 5–10 μm thick. Ohmic contacts to *n*-type layers were formed by depositing Ni metal films and ohmic contacts to *p*–type layers were formed by depositing films of the system [Al + Mo + Au] followed by fusing at temperatures of 1000 and 1900 °C, respectively.

Capacitance–voltage characteristics. The density of the uncompensated donor impurity and the magnitude of the contact potential difference U_d were determined by the method of capacitance–voltage characteristics. For the case of a sharply nonsymmetric *p–n* junction the capacitance cutoff voltage U_c is determined by extrapolating the linear curve $C^{-2}-U$ to $C^{-2}=0$, where C is the differential capacitance of the *p–n* junction and U is the voltage on the structure. The quantity U_c is related to the contact potential difference U_d by the relation[6] $U_c=U_d-2kT/e$, where k is Boltzmann's constant, and T is the temperature. It was found that the experimental value of the uncompensated donor impurity density N_d-N_a was equal to the value of N_d-N_a obtained from measurements of the capacitance of Schottky barriers formed on the surface of the *n* layer prior to growth of the p^+ emitter or to the value of N_d-N_a taken from the specifications. The $C-U$ characteristics constructed in $C^{-2}-U$ coordinates were linear in the experimental voltage interval.

The values obtained for U_d are shown in Fig. 1. The computed curves $U_d=F(N_d-N_a)$ for two values of the

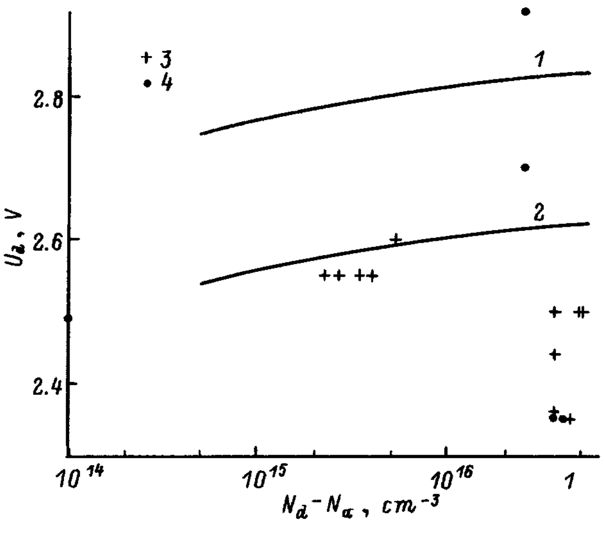

FIG. 1. Contact potential difference for 6*H*-SiC *p–n* structures versus the density N_d-N_a in the base at $T=300$ K. Computed curves for E_g, eV: *1* — 3.07, *2* — 2.86. Experimental values for *p–n* structures prepared different methods: *3* — gas-phase epitaxy and *4* — GPE together with sublimation epitaxy.

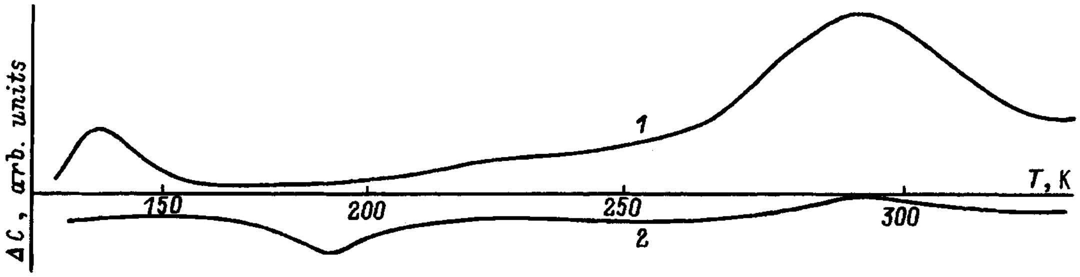

FIG. 2. Typical DLTS spectrum of a *p–n* structure prepared by gas-phase epitaxy (for spectrum parameters $t_1 = 10$ ms, $n = 3$). The spectrum was measured *1* — after injection of holes through the metallurgical boundary of the *p–n* junction and *2* — without injection.

band gap, 2.86 and 3.07 eV, are also plotted in the figure. In Ref. 7 it was shown that the computed value of U_d for 6*H*-SiC *p–n* structures obtained by different technological methods agree better with experiment if the band gap of 6*H*-SiC is assumed to be $E_g = 2.86$ eV. As one can see from Fig. 1, this correspondence also holds for GPE and GPE–SE *p–n* structures.

3. RESULTS AND DISCUSSION

Deep levels. The parameters of deep centers in the experimental *p–n* structures were determined by deep-level transient spectroscopy (DLTS) and *i*-DLTS[8,9] (Fig. 2). Essentially the same deep levels that were previously observed in films fabricated by GPE were observed in the GPE *p–n* structures. The total density of the observed deep acceptor centers with energy E_{na} was approximately an order of magnitude higher than the density of deep donors.

Earlier it was shown that the density of DCs with activation energy E_{na} in SE *p–n* structures, in which $N_d - N_a = 10^{17}$ cm^{-3}, was equal to 10–30% of $N_d - N_a$.[10] As $N_d - N_a$ in the epitaxial layer was varied, the density of DCs with energy E_{na} also varied negligibly: For $N_d - N_a = 10^{18}$ cm^{-3} the compensation caused by them was less than 3% and overcompensation of the epitaxial layers was observed at $N_d - N_a = 10^{16}$ cm^{-3}. This made it difficult to obtain epitaxial layers with $N_d - N_a \leqslant 10^{16}$ cm^{-3}. We observed a similar dependence of centers with energy E_{na} on $N_d - N_a$ in GPE *p–n* structures (Fig. 3). However, the density of the observed deep acceptor centers in GPE *p–n* structures was two to three orders of magnitude lower than in SE structures with the same value of $N_d - N_a$. There was no overcompensation of the GPE layers right up to $N_d - N_a \simeq 10^{14}$ cm^{-3}.

Discussion. In the experimental GPE structures, the *i* centers and the *D* centers, whose parameters and properties were close to those of the *i* centers, had the highest density. Previously, *i* centers were observed in 6*H*-SiC crystals, which were irradiated with Al ions, and in SE layers of SiC which were not doped separately.[11] The introduction of scandium also led to the formation of such a center in 6*H*-SiC and to the appearance of ‘‘defect’’ luminescence (DEL) ($h\nu_{\max} \sim 2.35$ eV).[12] It was shown that all characteristics of the DEL can be described on the basis of a donor–acceptor recombination model: <nitrogen inpurity>–*i* center.[13] It is also known that irradiation of SiC with electrons, neutrons, and some types of ions can also result in the appearance of DEL.[14] Therefore, the formation of *i* centers is not associatd with any one type of impurity, but rather it can be caused by different factors including irradiation. This points to a purely defect nature of the center.

In Ref. 15 it was found in x-ray investigations of SiC–based *p–n* structures obtained by different technologies on the basis of SE layers that the minimum half–widths of the x–ray peaks mainly occur in samples with maximum DEL intensity (high density of *i* centers). It was assumed there that the centers — DEL activators — are formed as stresses in the epitaxial layer relax, for example, during growth of a layer or during irradiation followed by annealing.

GPE SiC layers grow at much lower temperatures (1500 °C) than SE layers (2000 °C). This suggests that the conditions for stress relaxation via the formation of *i*–centers and other analogous defects of an acceptor nature still do not exist during gas–phase epitaxy. In the present case such relaxation can occur, for example, as a result of the formation of many dislocations. This assumption explains the observed low density of deep acceptor levels and the high density of

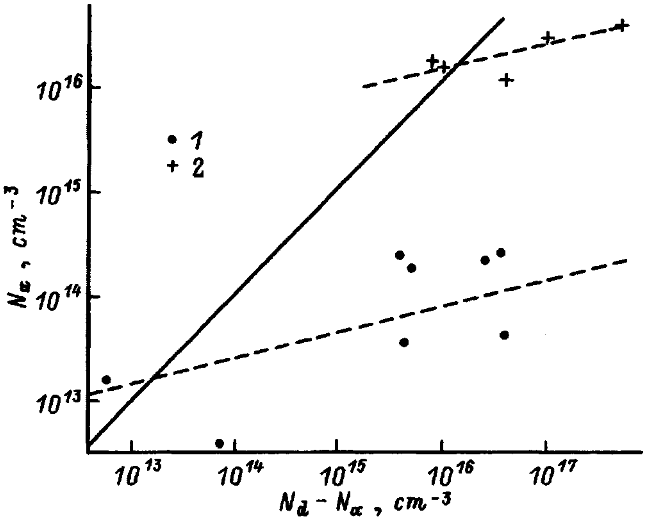

FIG. 3. Total density of deep acceptors versus $N_d - N_a$ in the epitaxial layers of *p–n* structures prepared by different methods: *1* — gas-phase epitaxy and *2* — sublimation epitaxy. The solid line corresponds to an acceptor density when $N_a = 0.5 N_d$.

dislocations in GPE SiC layers as compared with layers obtained by sublimation epitaxy.

4. CONCLUSIONS

The following conclusions can be drawn from this study.

1. The computed value of the contact potential difference obtained for GPE $p-n$ structures using a band gap of 2.86 eV for 6*H*-SiC agrees better with the experimental value, just as for other types of SiC–based $p-n$ structures investigated earlier.

2. Deep acceptor levels, which were previously observed in SE structures, were observed in GPE $p-n$ structures. However, the total density of deep acceptors in GPE structures is two to three orders of magnitude lower than in SE structures with a similar value of $N_d - N_a$.

This work was supported, in part, by the University of Arizona (USA) and INTAS Grant No. 93-543.

[1] J. W. Palmor, J. A. Edmond, H. S. Kong, and C. H. Carter, Jr., Physica B **185**, 461 (1993).

[2] O. Kordina, J. P. Bergman, A. Henry, E. Jansen, S. Savage, J. Andre, L. P. Ramberg, U. Lindefelt, W. Hermansson, and K. Bergman, Appl. Phys. Lett. **67**, 1561 (1995).

[3] A. A. Lebedev, A. S. Tregubova, A. A. Glagovskii, M. P. Scheglov, and V. E. Chelnokov in *Abstracts E-MRS Conference*, June 4–7, (1996), Strasbourg, France, p. A-15.

[4] A. A. Lebedev, A. M. Strel'chuk, S. Ortolland, C. Raynaud, M. L. Locatelli, D. Planson, and J. P. Chante, in *Inst. Phys. Conference*, IOP, Bristol, (1996), No. 142, Chap. 4, p. 701.

[5] N. S. Savkina, A. A. Lebedev, M. G. Rastegaeva, A. M. Strel'chuk, A. A. Mal'tsev, V. E. Chelnokov, and N. K. Poletaev, *Inst. Phys. Conference*, IOP, Bristol, (1996), No. 142, Chap. 3, p. 501.

[6] G. G. B. Garret and W. H. Brattain, Phys. Rev. B **19**, 376 (1970).

[7] A. A. Lebedev, D. V. Davydov, and K. I. Ignat'ev, Fiz. Tekh. Poluprovodn. **30**, 1865 (1996) [Semiconductors **30**, 975 (1996)].

[8] D. V. Lang, J. Appl. Phys. **45**, 3023 (1974).

[9] N. I. Kuznetsov, Prib. Tekh. Éksp., No. 6, 163 (1990).

[10] A. A. Lebedev and V. E. Chelnokov, Diamond films and Related Mater. **3**, 1393 (1994).

[11] M. M. Anikin, A. A. Lebedev, A. L. Syrkin, and A. V. Suvorov, Fiz. Tekh. Poluprovodn. **19**, 114 (1985) [Sov. Phys. Semicond. **19**, 69 (1985)].

[12] V. L. Balandovich, Fiz. Tekh. Poluprovodn. **25**, 287 (1992) [Sov. Phys. Semicond. **25**, 174 (1992)].

[13] A. N. Andreev, M. M. Anikin, A. A. Lebedev, N. K. Poletaev, A. M. Strel'chuk, A. L. Syrkin, and V. E. Chelnokov, Fiz. Tekh. Poluprovodn. **28**, 729 (1994) [Semiconductors **28**, 430 (1994)].

[14] V. V. Makarov and N. N. Petrov, Fiz. Tverd. Tela (Leningrad) **8**, 1602 (1966) [Sov. Phys. Solid State **8**, 1272 (1966)].

[15] A. A. Lebedev, M. P. Shcheglov, and T. V. Sokolova, Pis'ma Zh. Tekh. Fiz. **16**, 49 (1995) [Tech. Phys. Lett. **16**, 225 (1995)].

Translated by M. E. Alferieff

Anomalous magnetic properties of the solid solutions $(InSb)_{1-x}(CdTe)_x$ at low temperatures

A. V. Brodovoĭ, V. A. Brodovoĭ, L. M. Knorozok, V. G. Kolesnichenko, and S. P. Kolesnik

Institute of Materials Engineering Problems, 252680 Kiev, Ukraine

(Submitted July 8, 1996; accepted for publication March 18, 1997)
Fiz. Tekh. Poluprovodn. **31**, 1052–1054 (September 1997)

The magnetic susceptibility of the solid solutions $(InSb)_{1-x}(CdTe)_x$ has been investigated. It has been established that for the composition $x = 0.05$ a tenfold anomalous increase in diamagnetism is observed with decreasing temperature. This anomaly can be explained by the appearance of metallic superconducting modifications in the volume of the crystal.
[S1063-7826(97)00709-6]

It is well known that a number of atomic semiconductors and some semiconductor compounds under hydrostatic pressure undergo a phase transition into a metallic state. As a rule, the metallic phases that are formed are superconducting.

According to Ref. 1 , indium antimonide possesses several polymorphous metallic modifications, and in Ref. 2 it was established that under hydrostatic pressure of close to 23 kbar at room temperature the semiconductor compound InSb undergoes an insulator–metal transition, which makes it possible to obtain a metallic state at quite low temperatures by gradually decreasing the pressure. Resistivity measurements have shown that the metallic state in InSb is superconducting with a transition temperature in the range[3] 2.1–5.1 K. It is also known that the transition into a metallic state under hydrostatic pressure is accompanied a change in the volume and the lattice parameters of the crystal. A strong local distortion of the crystal lattice similar to the effect of a high pressure can be obtained by forming a system of three solutions on the basis of semiconducting compounds whose interacting elements possess different atomic and ionic radii. This suggests the possibility of forming a metallic state in InSb crystals by complex doping.

In the present work we investigated the magnetic susceptibility (MS) of single crystals of the solid solutions (SSs) $(InSb)_{1-x}(CdTe)_x$ in the temperature range 4.2–300 K and magnetic fields $H \simeq 0.1-5$ kOe. The SS samples were prepared by directioned crystallization of an InSb melt with the addition of Cd and Te. The total impurity density ranged from 1.5×10^{19} cm^{-3} ($x=0.001$) up to 7.5×10^{20} ($x=0.05$). Synthesis was performed in quartz cells evacuated to a pressure of 10^{-3} Pa. The melt was homogenized at a temperature of 1100 °C for 100 h. The ingots obtained were additionally subjected to a homogenizing anneal at 500 °C for 100–150 h. Equilibrium was considered to have been achieved when the microstructure and microhardness no longer changed and were the same over the entire ingot. All samples were *n*-type. The homogeneity and chemical composition of the ingots was monitored by Auger spectroscopy and x–ray crystallographic and chemical analyses.

The MS measurements were performed by the relative Faraday method using electronic microbalances with automatic compensation according to the procedure described in Ref. 4 . The MS of all experimental specimens at $H=4$ kOe is diamagnetic with $\chi = -(1-3.5)\times10^{-7}$ cm^3/g and is virtually independent of temperature in the interval 77–300 K (Fig. 1).

It is well known that the MS of crystals which do not possess an intrinsic magnetic moment consists of a sum of the contributions of the MS of the crystal lattice and the Pauli paramagnetism of electrons. The MS of electrons and its dependence on density and composition of the SS have been examined in detail in Ref. 5 on the basis of the Zawadski theory.[6] The results of the calculations of the MS of the electrons in $(InSb)_{1-x}(CdTe)_x$ for compositions in the range $0 \leqslant N_{\mathrm{CdTe}} \leqslant 5$ mole % gave a susceptibility of the order of 10^{-9} cm^3/g, which is two orders of magnitude less than the experimentally observed value of χ. This suggests that the magnetic susceptibility of $(InSb)_{1-x}(CdTe)_x$ is determined mainly by the lattice component of χ.

As the temperature decreases $T<77$ K, the paramagnetism of MS is observed to increase for solid solutions with $x=0.001$, 0.01, and 0.02. This is apparently due to the paramagnetism of lattice defects, which was observed in narrow–gap semiconductors during investigations of electron spin resonance (ESR) at temperatures below[7] 20 K.

Figure 2 shows a typical curve of χ versus the magnetic field H for $(InSb)_{1-x}(CdTe)_x$ single crystals. As one can see from the figure, for the composition $x=0.05$ the magnetic susceptibility increases rapidly for low values of H, changing from diamagnetic into paramagnetic state, which is characteristic of substances possessing magnetic order. It can be assumed that in the experimental crystals disarranged regions which can form around clusters of impurity atoms are responsible for the field dependence of the magnetic susceptibility. These disarranged regions are apparently produced by the high elastic stresses that appear in the cooling crystal because of the difference of the thermal expansion coefficients of the main material and an impurity cluster. As the x–ray crystallographic analysis has shown, the maximum compression of the InSb lattice, which reaches 6.2×10^{-2} % with respect to the pure InSb lattice, is observed for the solid solution $(InSb)_{0.95}(CdTe)_{0.05}$. This apparently leads to the appearance of metallic modifications in the volume of the crystal.[2]

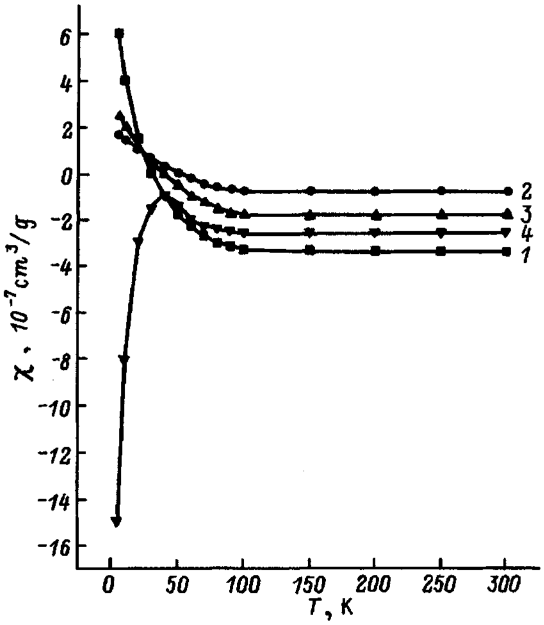

FIG. 1. Temperature dependences of the magnetic susceptibility of crystals of the solid solutions $(InSb)_{1-x}(CdTe)_x$ for different values of x: *1* — 0.001, *2* — 0.01, *3* — 0.02, *4* — 0.05.

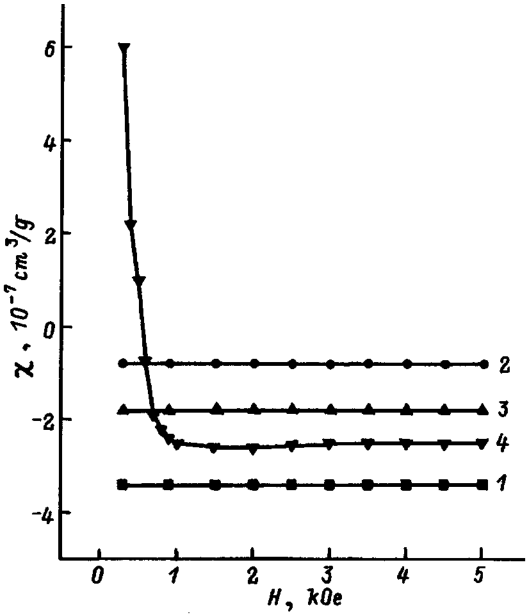

FIG. 2. Field dependences of the magnetic susceptibility of crystals of the solid solutions $(InSb)_{1-x}(CdTe)_x$ at $T=300$ K for different values of x: *1* — 0.001, *2* — 0.01, *3* — 0.02, *4* — 0.05.

Measurements at 78 K showed that the character of the dependence $\chi(H)$ remains unchanged. The paramagnetism of the test samples, however, increases slightly (of the order of 5–10%). An anomalous tenfold increase in diamagnetism is observed in the temperature dependence of the magnetic susceptibility of $(InSb)_{0.95}(CdTe)_{0.05}$ (Fig. 1, curve *4*) in the region $T=4.2-30$ K. This is apparently due to the appearance of superconductivity of a metallic modification formed as a result of local lattice deformations accompanying doping. The measurements of the magnetic susceptibility correlate well with ESR investigations performed at $T\leqslant 77$ K. In the course of the investigation of superconductivity by the ESR method, it was discovered that this method offers a unique capability which has been called microwave diagnostics.[8,9] This is the nonresonance microwave response of a superconductor that depends on the external magnetic field. This response is detected with high sensitivity by means of an ESR spectrometer. The response is observed only when the sample makes a transition into the superconducting state.

A SE/X-2544 ‘‘Radiopan’’ 3-cm radiospectrometer especially equipped for measurements near zero magnetic fields in a wide temperature interval was used for the ESR investigations.[10] In $(InSb)_{1-x}(CdTe)_x$ crystals no microwave absorption signal was observed in $H=0$, while for a composition with $x=0.05$ at $T<77$ K a ‘‘hysteresis’’ microwave response signal does appear. The latter signal was previously observed in high-T_c superconducting materials.[10]

In summary, it has been shown in the present work that metallic phases form in the solid solution $(InSb)_{0.95}(CdTe)_{0.05}$ as a result of local lattice deformations. This results in a sign change in the magnetic susceptibility from negative to positive in weak magnetic fields. These phases apparently become superconducting at liquid–helium temperatures.

[1] M. D. Banus and M. S. Lavin, J. Appl. Phys. **40**, 409 (1969).
[2] A. Jayaraman, R. C. Newton, and G. C. Kennedy, Nature **191**, 1288 (1961).
[3] H. E. Bommel, A. J. Darnell, W. F. Libry, and B. R. Tittman, Science **139**, 1301 (1963).
[4] G. V. Lashkarev, D. F. Migley, A. D. Shevchenko, and K. D. Tovstyuk, Phys. Status Solidi B **63**, 663 (1974).
[5] A. V. Brodovoĭ, V. A. Brodovoĭ, N. G. Vyalyĭ, L. M. Knorozok, and A. L. Mirets, Nauch. Zap. Nezhinsk. Ped. Institut, Ser. Fiz.-Mat. Nauk **14**, 73 (1994).
[6] W. Zawadski, Phys. Status Solidi B **3**, 1421 (1963).
[7] Yu. A. Bratashevskiĭ, V. D. Prozorovskiĭ, and Yu. O. Kharionovskiĭ, Fiz. Nizk. Temp. **3**, 120 (1977) [Sov. J. Low Temp. Phys. **3**, 58 (1977)].
[8] D. L. Lyfar’, D. P. Moiseev, and A. A. Motuz, Fiz. Nizk. Temp. **13**, 876 (1987) [Sov. J. Low Temp. Phys. **13**, 503 (1987)].
[9] A. A. Bugaĭ, B. M. Bulakh, and I. M. Zaritskiĭ, in *Problems of High-T_c Superconductivity* [in Russian], Sverdlovsk, (1987), Pt. 1, p. 213.
[10] I. M. Zaritskiĭ, A. A. Konchits, and S. P. Kolesnik, Preprint No. 4–91, Institute of Semiconductors, Kiev (1991).

Translated by M. E. Alferieff

Luminescence spectra of blue and green light-emitting diodes based on multilayer InGaN/AlGaN/GaN heterostructures with quantum wells

K. G. Zolina, V. E. Kudryashov, A. N. Turkin, and A. É. Yunovich[a)]

M. V. Lomonosov Moscow State University, 119899 Moscow, Russia

(Submitted 27 September 1996; accepted for publication 18 March 1997)
Fiz. Tekh. Poluprovodn. **31**, 1055–1061 (September 1997)

The luminescence spectra of blue and green light–emitting diodes based on $In_xGa_{1-x}N/Al_yGa_{1-y}N/GaN$ heterostructures with a thin (2–3 nm) $In_xGa_{1-x}N$ active layer have been investigated in the temperature and current intervals 100–300 K and $J=0.01$-20 mA, respectively. The spectra of the blue and green light-emitting diodes have maxima in the interavals $\hbar\omega_{\max}=2.55-2.75$ eV and $\hbar\omega_{\max}=2.38-2.50$ eV, respectively, depending on the In content in the active layer. The spectral intensity of the principal band decreases exponentially in the long–wavelength region with energy constant $E_0=45-70$ meV; this is described by a model that takes into account the tails of the density of states in the two–dimensional active region and the degree of filling of the tails near the band edges. At low currents radiative tunneling recombination with a voltage-dependent maximum in the spectrum is observed in the spectra of the blue diodes. A model of the energy diagram of the heterostructures is discussed. © *1997 American Institute of Physics.* [S1063-7826(97)00809-0]

1. INTRODUCTION

In the last three years substantial progress has been made in the development of emitting heterostructures based on GaN and GaN–based solid solutions. The work performed on the problem was presented at the First International Seminar on GaN and Similar Materials at a meeting of the Society of Materials Engineering (December 1995, Ref. 1) and the First European Seminar on GaN.[2] Record results on the development of light–emitting diodes (LEDs) for the short-wavelength part (violet, blue, green) of the visible spectrum were achieved by a group from the Nichiya Company using organometallic compound-hydride method.[3,4] In Ref. 4 it was shown that LEDs emitting in the indicated spectral region with a high quantum yield, reaching 4–9%, can be developed on the basis of multilayer InGaN/AlGaN/GaN heterostructures with a thin (2–3 nm) InGaN active layer (see also the review in Ref. 5).

The electroluminescence spectra (EL) of these LEDs have been investigated as a function of the current J and temperature T.[4,6] In our on going study we investigated the EL spectra of these LEDs in a wide range of currents J. We also analyzed in detail the characteristic features of the spectra. The spectral features are of interest for understanding the radiative recombination mechanisms and the factors influencing the quantum yield of radiation in InGaN/AlGaN/GaN heterostructures. Quantum-well and tunneling effects, fluctuations of the potentials in the quantum wells, and doping of adjoining wide-gap regions are important in structures with a thin active layer.

2. EXPERIMENTAL PROCEDURE

Ten LEDs made of structures, grown by hydride MOCVD and described in Ref. 4, were investigated (Fig. 1). A n-GaN:Si ($t=5$ μm) layer was grown on a sapphire substrate and a GaN buffer layer (≈ 300 Å). An thin ($d\approx 20-30$ μm) $In_xGa_{1-x}N$ active layer was grown on this layer. The wavelength at the maximum of the spectrum changes from the blue to the green region as the composition x of the active layer varies in the range 0.2–0.43; the wavelength also depends on the thickness of the layer. This is followed by a wide-gap p-$Al_{0.1}Ga_{0.9}N$:Mg layer (≈ 1000 Å) — a barrier for electrons, which is necessary for hole injection and for lattice matching the active layer with the top p-GaN:Mg (≈ 0.5 μm) contact layer. The p-$Al_{0.1}Ga_{0.9}N$:Mg layer prevents the evaporation of the active layer during the growth of the comparatively thick top layer. A Ni–Au metal contact is deposited on p-GaN:Mg. A Ti–Al metal contact to n–GaN layer was produced after part of the structure was etched off. The area of the crystal with the p–n heterojunction was $S=350\times 350$ μm^2. For comparison, the spectra of two blue and two green LEDs, containing two additional epitaxial layers between n-GaN:Si and the active layer

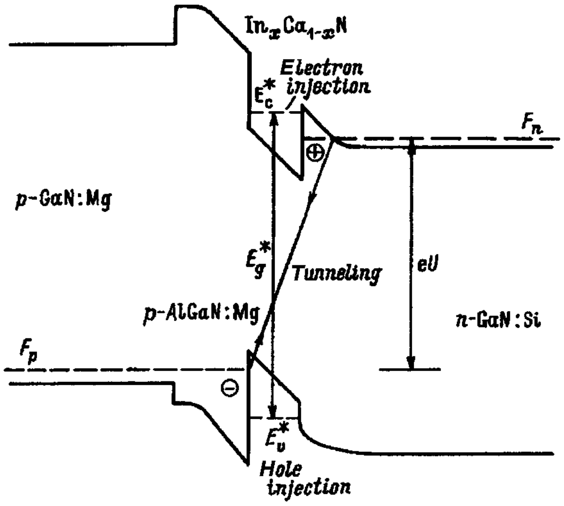

FIG. 1. Energy diagram of $In_xGa_{1-x}N/Al_yGa_{1-y}N/GaN$ heterostructures described in Ref. 4.

TABLE I. Parameters of group I and group II diodes.

Group	Diode	$\hbar\omega_{\max}$, eV	E_0 meV	m	ΔF_H, eV	E_g^*, eV	$\Delta(\hbar\omega)_{1/2}$, eV	ν_e,%*
I	G3	2.435	68.2	1.105	−0.125	2.584	0.152	
	G2	2.445	69.9	1.108	−0.166	2.646	0.152	4.1
	G4	2.446	66.8	1.123	−0.123	2.559	0.151	4.0
II	B3	2.709	54.5	1.005	−0.141	2.853	0.133	0.86
	B2	2.732	44.3	1.059	−0.089	2.824	0.131	
	B5	2.752	49.1	1.104	−0.091	2.851	0.134	0.70

Note: *The measurements of the external quantum yield η_e are described in Ref. 13.

— n-$Al_{0.1}Ga_{0.9}N$:Si (100 nm) and n-$In_{0.05}Ga_{0.95}N$:Si (50 nm), from previous work by the Nichiya Company[3] were also investigated.

The radiation was observed in the standard LED construction through a plastic focusing bowl above the crystal with the structure.

The radiation spectra were investigated in the KSVU–12 system, the signal from which was fed into a IBM PC-486 computer through ADCs and an interface. A QBASIC program was developed to control the spectral system. The mathematical analysis was performed with the ORIGIN and EASYPLOT programs.

3. EXPERIMENTAL RESULTS

3.1. General form of the spectra. The room-temperature electroluminescence spectra of several diodes (Table I) with a dc current $J=10$ mA are shown in Fig. 2. The maxima in the spectra of the light–blue and blue–violet diodes (group II) lie in the interval $\hbar\omega_{\max}=2.55-2.75$ eV, depending on the In content in the active layer ($x=0.20-0.25$). For the green diodes (group I) $\hbar\omega_{\max}=2.38-2.45$ eV ($x=0.40-0.44$). The diodes in the third group were fabricated by a technology with additional heterolayers;[3] they correspond to the blue-green and greenish-blue $\hbar\omega_{\max}=2.46-2.60$ eV. Therefore, the LEDs, made with the InGaN/AlGaN/GaN heterostructures, cover the entire short–wavelength range of the visible region in accordance with Refs. 1–4. For brevity, we shall call the group–II diodes light–blue diodes.

3.2.Dependence of the spectra on the current and spectral band shape. The emission spectra for $J=20-0.2$ mA and at room temperature T are shown in Fig. 3. The dropoff of these spectra is described by the exponentials $I\sim\exp(\hbar\omega/E_1)$ and $\sim\exp(-\hbar\omega/E_0)$ in the short– and long–wavelength regions, respectively. The decay constant E_1 in the exponential function is of the order of $1.0-1.3kT$;

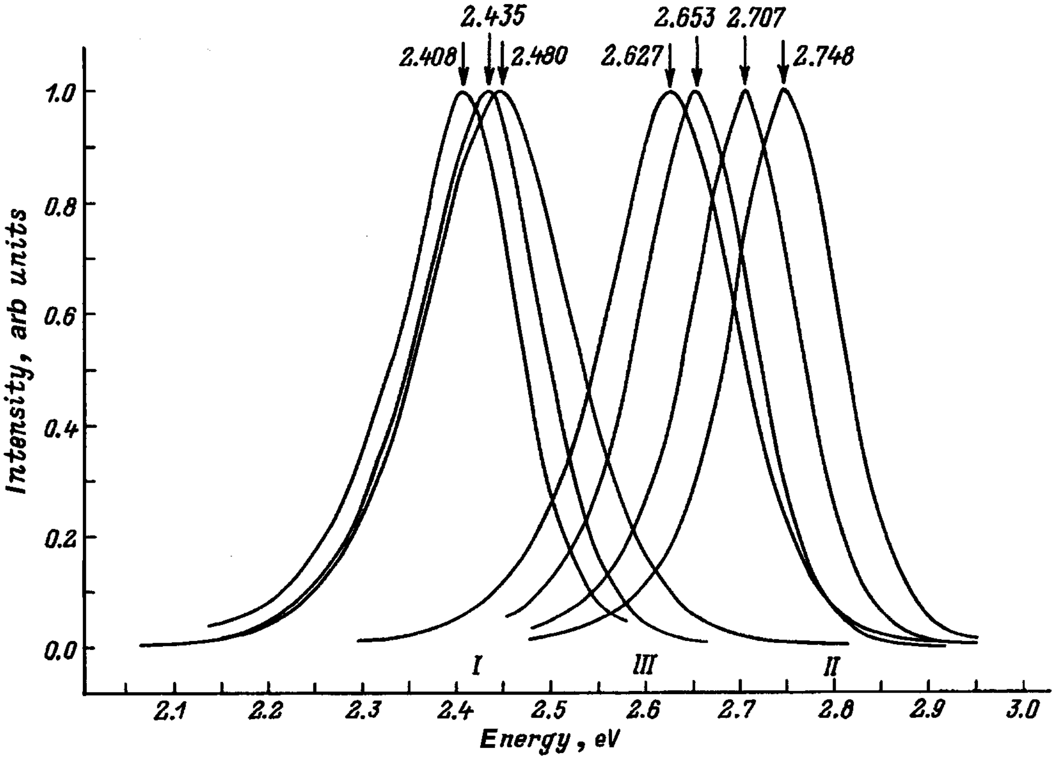

FIG. 2. Electroluminescence spectra of LEDs consisting of $In_xGa_{1-x}N/Al_yGa_{1-y}N/GaN$ heterostructures with quantum wells at temperature T and $J=10$ mA; I — first group, II — second group, III — third group (see Table I).

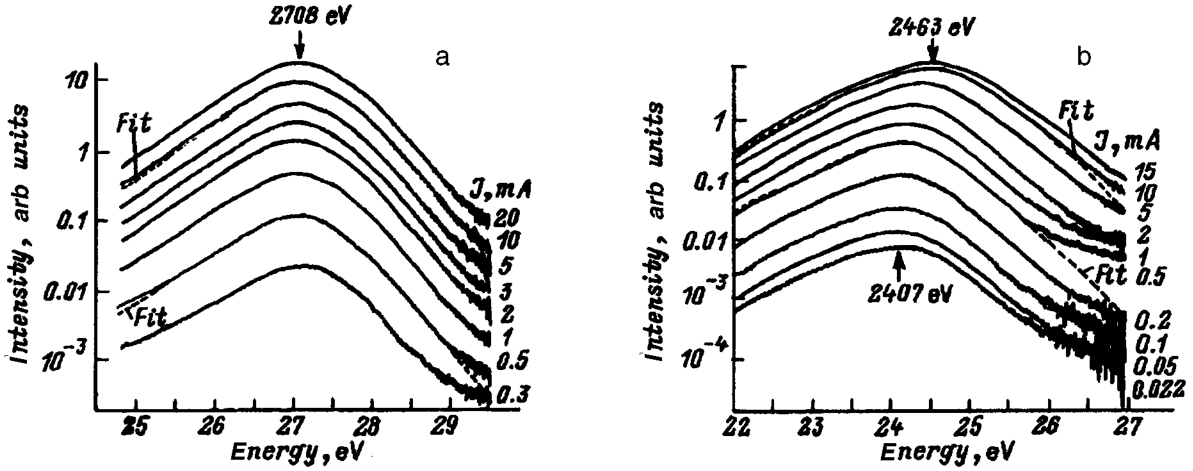

FIG. 3. Emission spectra of LEDs as a function of current (the numbers in the column are J in mA) at room temperature; a — light-blue N3 diode from group I; b — green N2 diode from group II. The arrows mark the position of the maxima. Dashed curves — approximation by Eqs. (5)–(8).

$E_0 \gg kT$ and does not depend on T. The maximum in the spectra of the light-blue diodes is virtually independent of current in this interval. The maximum in the spectra of the green diodes shifts with increasing current into the short–wavelength direction by ≈ 60 meV.

For the light–blue diodes the intensity dropped rapidly at $J < 0.7 - 0.2$ mA. This is seen in Fig. 3a as a change in the distance between the curves on a logarithmic scale. For low currents the long–wavelength part of the spectra of the light–blue diodes deviates from an exponential function. For green LEDs a sharp drop in $I(J)$ is not observed, and spectra could be investigated down to $J = 10$ μA with a resolution up to ≈ 0.5 meV (Fig. 3b). The widths of the spectra were virtually independent of current and varied in the range $\Delta(\hbar\omega)_{1/2} = 130 - 150$ meV for different diodes (see Table I). This made it possible to investigate the dependence of the radiation intensity Φ on J with constant T according to measurements of $I_{\max}(J)$.

3.3. Interference-determined structure of the spectra. The high intensity of the radiation made it possible to investigate spectra with resolution down to 0.2 meV and an accuracy of up to 0.1% and to observe the structure shown in Fig. 4. The periodic structure was clearly resolved when a smooth approximation of the band (dotted line) was extracted from the experimental spectrum. This structure is explained by the interference of the radiation reflected from the boundaries of

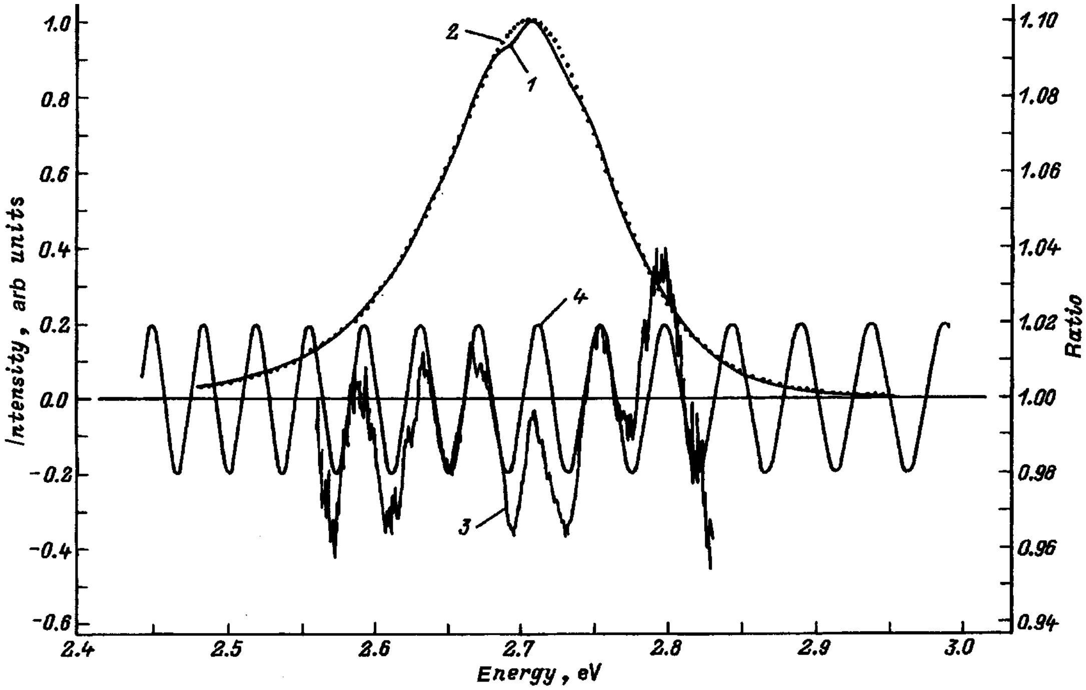

FIG. 4. Structure of the EL spectrum (1) of a light–blue LED (N2, see Table I) resulting from interference in the GaN layer. Dotted line *2* — smooth approximation with Eqs. (5)–(8); *3* — ratio of the approximation spectrum (2) to the experimental (1) spectrum; *4* — the factor $(1 + a \cdot \cos(2p(\lambda - \lambda_0)/\Delta\lambda))$; $a = 0.020 \pm 0.001; \Delta\lambda = 7.02 \pm 0.07$. The ordinate for curves *3* and *4* is on the right-hand side.

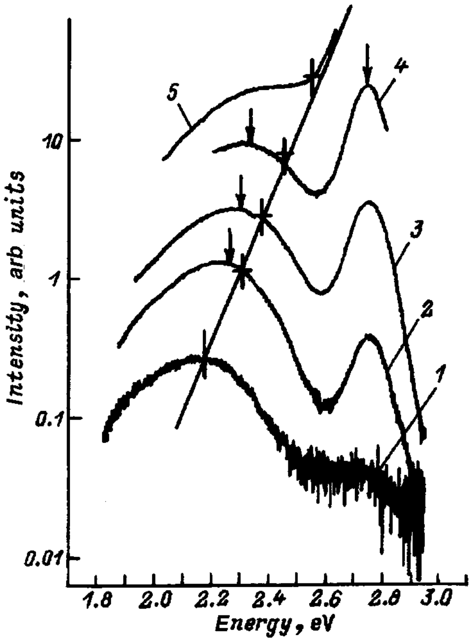

FIG. 5. Luminescence spectra of a light-blue LED (N5) at low currents and room temperature. The intersections of the straight line and the spectra indicate the energy corresponding to the voltage on the diode. J, mA; *1* — 0.025, *2* — 0.01, *3* — 0.075, *4* — 0.1, *5* — 0.15. The position of the maxima of the tunneling radiation band, eV: *1* — 2.13, *2* — 2.21, *3* — 2.27, *4* — 2.33. Energy of the maximum of the short-wavelength band — 2.75 eV.

the transparent n–GaN layer (thickness $t\pm\delta t=5\pm0.5$ μm).[6,7] The values of $n[1+(\lambda/n)(dn/d\lambda)]$ (n is the refractive index, and $dn/d\lambda$ is the dispersion), calculated from the equation

$$n[1+(\lambda/n)(dn/d\lambda)]=(\lambda/2)(1+\lambda/\Delta\lambda)/t \qquad (1)$$

($\Delta\lambda$ is the period) at $t=5.0$ μm, are in the range 2.48 – 3.03. Since $\delta t\approx0.5$ μm, this value agrees with the index of refraction of GaN ($n=2.5$).

3.4. Radiative tunneling recombination. A spectral band with a maximum ranging in the interval $\hbar\omega_{\max}=2.16-2.39$ eV as the voltage on the p–n junction $\hbar\omega_{\max}\simeq eU$ (Fig. 5) was observed in the luminescence spectra of the light–blue LEDs at low currents ($J=0.02-0.2$ mA). The quantum yield of the prinicpal spectral band drops by four orders of magnitude in this region. The observed band corresponds to tunneling radiation, which was previously investigated and described theoretically for other direct-gap III–V compounds.[8] This band was not observed in the green LEDs, which correlates with their large serial resistance and absence of a tunneling current component.

3.5. Temperature dependence of the spectra. As the temperature decreased, the long-wavelength decay of the spectrum in the principal band remained nearly constant, the short–wavelength decay became appreciably steeper, and the parameter E_1 decreased and became current-dependent. Measurements of the temperature T performed with a thermocouple attached to the plastic cap of the diode showed that T changes appreciable when the diode is heated by a current exceeding 1 mA. For this reason, the variation of the spectra of one of the light–blue diodes as a function of T with $J=1$ mA, for which the heating is weak, is shown in Fig. 6. The integrated radiation intensity Φ was virtually independent of T, varying at this current by not more than a factor of 2.

3.6.Current and voltage dependences of the intensity. The integrated intensity Φ depended linearly on the current J

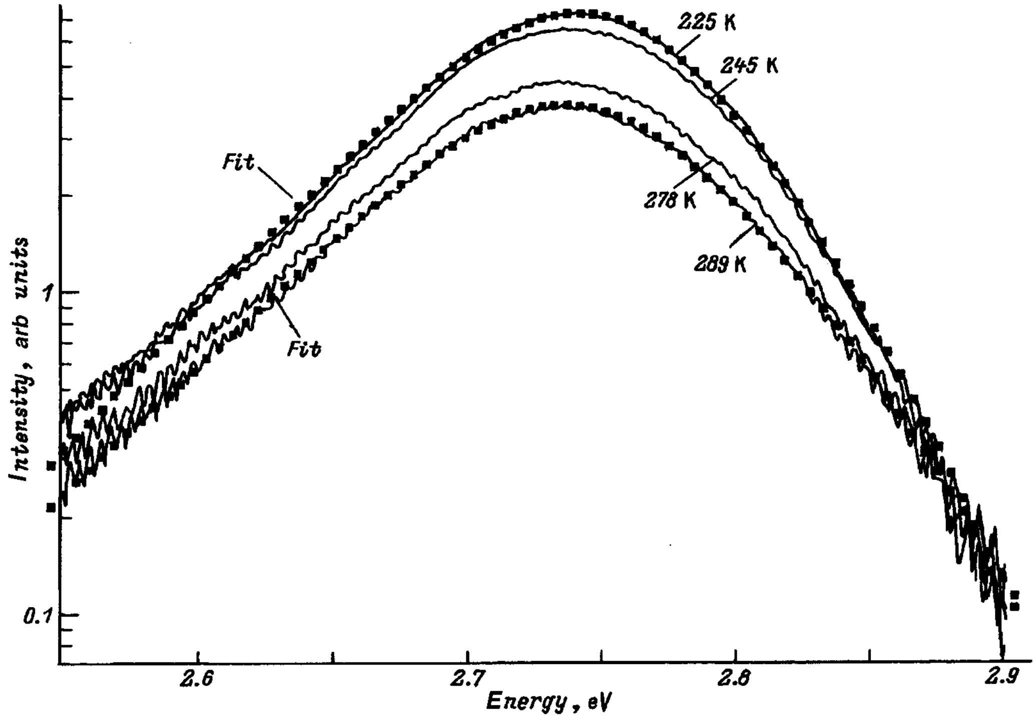

FIG. 6. Luminescence spectra of a light-blue diode (N2, see Table I) at different temperatures. Dots — approximation using the Eqs. (5)–(8).

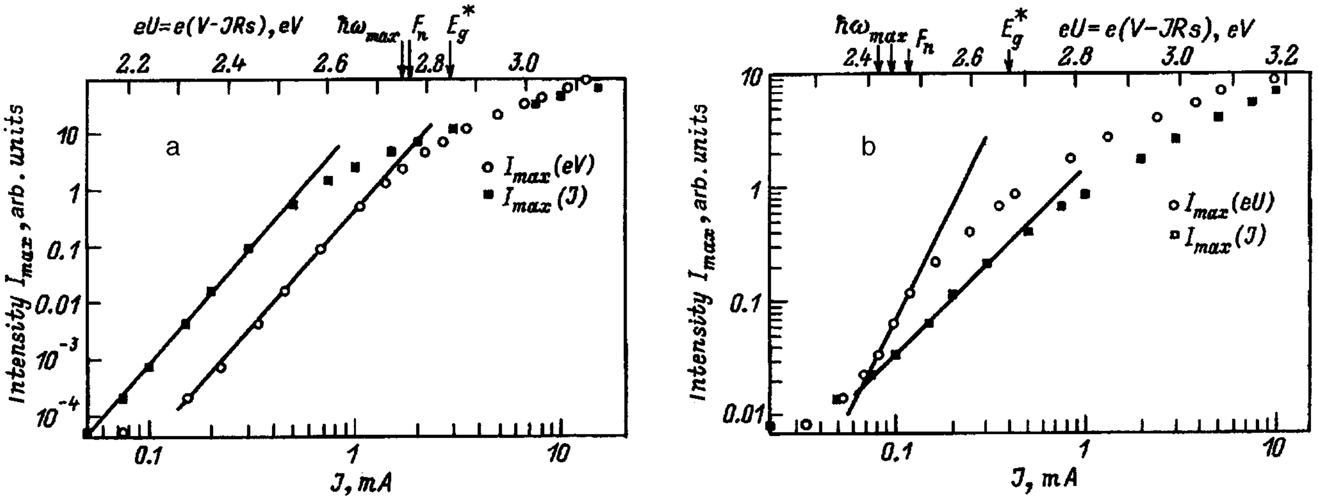

FIG. 7. Radiation intensity versus voltage (top scale) and current (bottom scale) for the light-blue (a) and green (b) LEDs. The straight lines correspond to Eqs. (2) and (3). The parameters of the approximation using Eqs. (5)–(8) are indicated on the top scale; Room temperature.

for $J=1-10$ mA (Fig. 7), it grew sublinearly with J for $J>10$ mA, and it dropped superlinearly with decreasing J ($J<0.7-0.3$ mA). This drop can be described by the law

$$\Phi\sim J^p. \tag{2}$$

For light–blue diodes the exponent p varied in the range $p=4.5-5.2$. Such a sharp dependence is due to the change in the ratio of the nonradiative and radiative recombination in the structure. For green diodes the drop in I was less sharp, $p\approx 1.5$. This is due to the difference in the mechanisms of current flow in the diodes investigated. At low currents for light-blue diodes $U\approx V$ (V is the voltage on the diode), so that

$$I_{\max}=\text{const}\cdot\exp(eU/E_1), \tag{3}$$

where E_1 is the decay constant for the radiation intensity. At high currents a serial resistance appears: $V=U+JR_s$. The electric properties of diodes are studied in Ref. 9.

4. DISCUSSION

4.1.Energy level diagram. Let us examine the energy level diagram of the heterostructure (Fig. 1).

The effective band gap E_g^* in the active layer is

$$E_g^*=E_g(x,T)+\Delta E_{1c}+\Delta E_{1v}+\Delta E_p-E_{\text{exc}}-\Delta E_{D,A}, \tag{4}$$

where $E_g(x,T)$ is the band gap in the layer, ΔE_{1c} and ΔE_{1v} are the quantum wells in the conduction bands, ΔE_p is the change in E_g as a result of deformations due to differences in the lattice constants in the layers of the heterostructure, E_{exc} is the binding energy of a two–dimensional exciton, and $\Delta E_{D,A}$ are the shifts produced in the edges of the effective band gap by the potential of the donors and acceptors.[10,11] For calculations it is necessary to know how $E_g^*(x,T)$, $m_{c,v}(X,T)$, ΔE_{1c}, and ΔE_{1v} depend on the band offsets $\Delta E_{c,v}$ at the two heteroboundaries and on the thickness d of the active layer. It is necessary to know the tensors of the elastic constants, the deformation potentials, and the ionization energies (E_D, E_A) and densities (N_D, N_A) of the donors and acceptors, and their fluctuations in the quantum well. It is necessary to estimate the fluctuation of the potential as a function of the well thickness and the impurity density. Since the electric field $\mathbf{E}$ in the p–n junction is large, E_g^*, ΔE_{1c}, and ΔE_{1v} can depend on $\mathbf{E}$.

Calculations of E_g^* are complicated and they contain specific parameters which are not always known.

4.2. Model describing the luminescence spectra. Here restrict the analysis to spectra in the principal band, proceeding from the following model. Efficient radiative recombination occurs when current carriers of both signs are injected into the active layer — into a quantum well. For low currents the tunneling component can be substantial. For high currents some of the voltage falls across the serial resistance, giving rise to heating. Let us examine the emission spectra in a quantum well in the current and voltage ranges that correspond to efficient radiation emission.

We assume that optical transitions occur between the edges of two-dimensional conduction and valence bands, which possess tails of the density of states as a result of different fluctuations of the potential (Coulomb field of the impurities, quantum-well levels, composition of the solid solution, boundary roughness). In this case we apply a formula for the $2D$ density of states $N^2(\hbar\omega-E_g^*)$ that was used in Refs. 11 and 12 to describe the luminescence of GaAs/AlGaAs quantum wells:

$$I(\hbar\omega)\sim N^2D(\hbar\omega-E_g^*)f_c(\hbar\omega,kT,F_n)\times(1-f_v(\hbar\omega,kT,F_p)); \tag{5}$$

$$N^{2D}(\hbar\omega-E_g^*)=(1+\exp(-(\hbar\omega-E_g^{\text{eff}})/E_0))^{-1}. \tag{6}$$

The energy parameter E_0 characterizes the exponential decay of the density of states in the long-wavelength region. In Eq. (5) f_c and $1-f_v$ are the filling functions of the states near the band edges:

$$f_c(\hbar\omega,kT,F_n)=[1+\exp(((1/m)\times(\hbar\omega-E_g^*)-\Delta F_n)/kT)]^{-1}, \tag{7}$$

TABLE II. Parameters in Eqs. (5)–(8) obtained by fitting the experimental spectra of the light-blue and green LEDs. The number of significant figures corresponds to the accuracy of the fit.

N Diode	J, mA	$V-JR_s$, V	$\hbar\omega_{\max}$, eV	E_0, eV	m	ΔF_H, eV	E_g^*, eV
$B3$	0.2	2.464	2.708	79.5	0.96	−0.176	2.899
	0.5	2.615	2.707	60.4	0.99	−0.143	2.858
	1	2.692	2.709	56.5	1.00	−0.132	2.845
	2	2.772	2.708	55.5	0.99	−0.138	2.848
	5	2.880	2.709	54.8	0.99	−0.140	2.850
	10	3.080	2.709	54.5	1.01	−0.141	2.853
	20	3.028	2.708	54.6	1.02	−0.144	2.858
$G4$	0.022	2.285	2.409	65.9	1.05	−0.238	2.672
	0.05	2.351	2.409	65.9	1.04	−0.236	2.668
	0.1	2.422	2.409	70.1	1.02	−0.241	2.670
	0.2	2.480	2.410	70.0	1.00	−0.254	2.678
	0.5	2.597	2.416	69.6	0.96	−0.303	2.722
	1	2.683	2.423	69.0	0.94	−0.293	2.712
	2	2.791	2.426	68.6	0.94	−0.370	2.790
	5	2.955	2.435	68.3	1.00	−0.212	2.666
	10	3.078	2.446	66.8	1.12	−0.123	2.599
	20	3.188	2.460	67.7	1.23	−0.106	2.602

$$(1-f_v(\hbar\omega,kT,F_p))=[1+\exp(((1(1/m))\times(\hbar\omega-E_g^*)-\Delta F_p)/kT)]^{-1}, \tag{8}$$

where $\Delta F_n=(F_n-E_c^*)$ and $\Delta F_p=(E_v^*-F_p)$ are the Fermi quasilevels for electrons and holes in the active region and are related by the relations

$$F_n-F_p=eU;\Delta F_p=eU-E_g^*-\Delta F_n,E_g^*+E_c^*-E_v^*, \tag{9}$$

where U is the voltage drop across the active region which, in general, can be less than the voltage drop across the p–n junction.

The parameters $1/m$ and $(1-1/m)$ characterize the fractions of the energy $(\hbar\omega-E_g^*)$ that an electron possesses above the effective conduction band edge E_c^* and a hole possesses below the effective valence band top E_v^*. For direct transitions $m=(1+m_c^*/m_v^*)$ in the case of parabolic bands and $m=1$ for transitions between the conduction band and an acceptor level. In the model proposed m is a phenomenological parameter. If the diode temperature is not measured directly, an increase in the parameter m with increasing current could indicate heating of the diode.

The experimental spectra were normalized to 1 at the maximum and were described by Eqs. (5)–(8) with the aid of the ORIGIN and EASYPLOT programs by fitting the parameters $\hbar\omega_{\max}$, E_g^*, m, E_0, and ΔF_n so as to obtain the best description of the spectra as functions of the voltage U and temperature T.

The results are presented in Figs. 3–5 and in Table II. We see that as the current varies over wide limits and as the intensity varies, in each spectrum the approximation describes the spectra well up to two decimal places. The rms deviations over 2000 points did not exceed 7×10^{-3} for the spectra normalized to unity at the maximum; more than 50 spectra were analyzed. The values of the parameters are presented in Table II, and their variation with current for two diodes is shown.

The energy in the argument of the exponential function describing the short–wavelength decay of the spectral band — the parameter E_0 — is virtually independent of J for each diode until (for light-blue LEDs) the tunneling radiation comes into play. The value of E_0 increases from diode to diode from 49 to 70 meV as the maximum $\hbar\omega_{\max}$ shifts in the long–wavelength direction. Therefore, it can be concluded that the fluctuations of the potential in the quantum wells increase with increasing In content in the active layer of the diodes. In the publications with which we are familiar, the characteristic fluctuations of the potential in the quantum wells of the structures studied were not analyzed.

The parameter m, which characterizes the difference in the energy in the argument of the exponential functions in Eqs. (7) and (8) from the value kT (in the calculations in Table II it was assumed that kT corresponds to room temperature), almost equals 1 for all diodes, until heating starts as the current increases. This increase is greatest for green diodes, for which $R_s=27-30\ \Omega$. If it is assumed that the apparent change in m is completely due to heating, then with a dc current of 20–30 mA the temperature of the active region of the diode can reach $T\approx390$ K. The value $m\approx1$ could mean that radiative transitions proceed from the tail of the density of states in the conduction band into local acceptor levels. This assumption needs to be checked.

The value obtained for the Fermi quasilevel ΔF_n for electrons by the fitting procedure varies at low currents from -0.11 to -0.36 eV (from violet to green diodes). The deeper position of the Fermi level in green diodes correlates with large values of R_s and with the absence of tunneling radiation. An increase in ΔF_n by $1-2kT$ with increasing current corresponds to double injection of carriers into the active region.

The values of $E_g^*=\hbar\omega_{\max}+\Delta$ should be compared with estimates of E_g^* using Eq. (4). The fit was made for spectra normalized to unity at the maximum. The dependence of the radiation intensity on the voltage U and on the approximation parameters requires a simultaneous analysis of the spectra and electric properties of the diodes. This falls outside the scope of this paper.

5. CONCLUSIONS

1. The luminescence spectra of LEDs based on heterostructures with $In_xGa_{1-x}N$/ $Al_yGa_{1-y}N$/ GaN quantum wells with a thin $In_xGa_{1-x}N$ active layer have maxima in the visible region ranging from the violet to green part of the spectrum, depending on the In content in the active layer. The spectrum drops off exponentially in the short- and long-wavelength parts.

2. A structure due to reflection of radiation from the substrate and interference in the GaN layer appears in the spectra of the diodes. This shows that the optical yield of the radiation from the diodes can be controlled.

3. Radiative tunneling recombination is observed in the spectra of light-blue diodes at low currents. The maximum in the spectrum of this radiation shifts in proportion to the voltage drop across the p–n junction.

4. The current and voltage dependences of the radiation intensity have three sections: The nonradiative tunneling component of the current is important in light-blue diodes at low currents; the quantum yield of radiation is greatest in the intermediate current and voltage ranges, which depends on the In content in the active layer ($\hbar\omega_{\max} \leqslant eU \leqslant E_g^*$); and at high currents heating of the diodes is substantial and the quantum yield drops.

5. The shape of the principal spectral band in the indicated region of maximum quantum yield is described well by a model of recombination in a two-dimensional quantum well, with allowance for the exponential decay of the tail of the reduced density of states due to the fluctuations of the potential.

6. The parameter in the exponential function describing in the model the decay of the spectra in the long-wavelength region is in the range $E_0 = 45-70$ meV. This characterizes the fluctuations of the potential which arise for different reasons (roughness of the heterstructures, nonuniformity of the composition of the solid solution, Coulomb potential of the impurities, etc.).

7. The energy decay constant in the exponential for the short-wavelength dropoff of the spectra is close to kT. Its variation gives an estimate of the heating of the region up to 100 °C with a current $J \approx 20$ mA.

We are deeply grateful to Dr. S. Nakamura for the LED specimens which he sent to Moscow State University, A. E. Kovalev for assisting in the computerization of the apparatus, S. S. Shumilov for assisting in the computer software development, and A. N. Kovalev and F. I. Manyakhin for performing the electric measurements.

---

[a] Electronic-mail: yunovich@scon175.phys.msu.su

[1] *First International Symposium on Gallium Nitride and Reelated Materials,* Abstracts of Mater Res. Soc. (1995) Fall Meeting, Symp. AAA, Boston, (1995).

[2] *Abstracts of First European GaN Workshop,* Rigi, Switzerland (1996).

[3] S. Nakamura, M. Senoh, N. Iwasa, and S. Hagahama, J. Appl. Phys. **34**, Part 2, 797 (1995).

[4] S. Nakamura, M. Senoh, N. Iwasa, S. Hagahama, T. Yamada, and T. Mukai, Jpn. J. Appl. Phys. **34**, Part 2, L1332 (1995).

[5] A. É. Yunovich, Svetotekh., No. 5/6, 2 (1996).

[6] K. G. Zolina, V. E. Kudryashov, A. N. Turkin, A. E. Yunovich, and A. Nakamura, MIJ-NSR **1**, Article 11 (1996), http://nsr. mij. mrs. org/1/11/.

[7] S. Nakamura, Jap. J. Appl. Phys. **30**, 1620 (1991).

[8] A. É. Yunovich and A. B. Ormont, Zh. Éksp. Teor. Fiz. **51**, 1292 (1966) [Sov. Phys. JETP **24**, 869 (1967)].

[9] A. N. Kovalev, F. I. Manyakhin, and A. É. Yunovich, Fiz. Tekh. Poluprovodn. [Semiconductors], in press.

[10] M. Herman, *Semicinductor Superlattices* [Russian trans., Mir, Moscow (1984)].

[11] B. R. Vardanyan and A. É. Yunovich, Fiz. Tekh. Poluprovodn. **29**, 1976 (1995) [Semiconductors **29**, 1030 (1995)].

[12] R. Chingolani, W. Stolz, and K. Ploog, Phys. Rev. B **40**, 2950 (1989).

Translated by M. E. Alferieff

Polarization photoluminescence study of the complex $V_{Ga}Te_{As}$ in *n*-type GaAs in the temperature range 77–230 K

A. A. Gutkin, M. A. Reshchikov, and V. E. Sedov

A. F. Ioffe Physicotechnical Institute, Russian Academy of Sciences, 194021 St. Petersburg, Russia

(Submitted March 18, 1997; accepted for publication March 20, 1997)
Fiz. Tekh. Poluprovodn. **31**, 1062–1070 (September 1997)

The polarization of the photoluminescence band with a maximum near 1.18 eV, which is formed as a result of the resonance excitation of $V_{Ga}Te_{As}$ complexes by polarized light, is investigated for GaAs:Te with various electron densities in the temperature range 77–230 K. Based on a previously developed model of these defects, theoretical equations for the polarization of their luminescence are derived in the one-dipole approximation, taking into account the possible reorientation of Jahn–Teller distortions of the complexes. It is shown that the temperature dependence of the polarization of the investigated band is well described by these equations, and the parameters characterizing the optical dipoles of the complexes are estimated. A decrease in the degree of polarization at temperatures above ∼120 K is explained by the transfer of excitation to complexes with any possible orientations of the initial axis and by Jahn–Teller distortion (owing to thermal-field emission and retrapping of holes by the photoexcited complexes). The decrease in polarization can also be partially linked to the reorientation of distortions during the lifetime of the emitting state of the complex. The height of the energy barrier for such reorientation is at least ∼200 meV. [S1063-7826(97)00909-5]

1. INTRODUCTION

Complexes containing a gallium vacancy (V_{Ga}) and a shallow donor and occupying nearest-neighbor lattice sites excite a broad photoluminescence band in *n*-type GaAs, with a maximum at the photon energy ($\hbar\omega_{em}$)∼1.18 eV (Ref. 1). This band is attributable to the radiative recombination of an electron from a state near the bottom of the conduction band with a hole localized in a deep state of the complex.[1,2] The complex can form a radiative state in *n*-typeGaAs by trapping a hole produced in the generation of electron-hole pairs or by emitting an electron into the conduction band or into shallow states as a result of the absorption of a photon by the complex in resonance excitation.

Investigations of such a defect in GaAs:Te have shown that the complex does not have trigonal symmetry in the radiative (excited) state, but is distorted and can exist in one of several equivalent configurations with different orientations of the distortion.[3–5] The application of pressure to the crystal along the [111] or [110] direction with the recombination of electron-hole pairs through the complex at low temperatures (∼2 K) has the effect of aligning these distortions.[3–5] If pressure is applied in the [100] direction, the distortions of the excited state align more slowly as the pressure is increased. These patterns have suggested a model of the excited state of the $V_{Ga}Te_{As}$ complex whereby the distortion of the initial trigonal symmetry of the complex is associated with the Jahn–Teller effect, i.e., with interaction between a hole trapped by the complex and partially symmetrical vibrations of the atoms surrounding V_{Ga} atoms (Refs. 5 and 6). In this case the complex acquires monoclinic symmetry, and for each defect there are three equivalent configurations corresponding to the three possible orientations of the Jahn–Teller distortion (Fig. 1), as in the case of the vacancy-donor complexes binding three holes in Si (Refs. 7–9). It follows from the results of an investigation of the polarization of emission from the $V_{Ga}Te_{As}$ complex in resonance polarized excitation[10,11] that its symmetry is also no higher than monoclinic in the ground (absorbing) state. The corresponding required additional distortion of the initially trigonal complex in the ground state could be a result of the pseudo Jahn–Teller effect (or the Jahn–Teller effect if the ground state binds one hole and the emitting state binds two holes).

For this model to be qualitatively consistent with the results of investigations of polarized photoluminescence from the complex,[10] it must also be assumed, as indicated in Ref. 12, that reorientation of the Jahn–Teller distortion cannot take place at low temperatures within the lifetime of the excited state. The observed alignment of these distortions under uniaxial pressure and in the presence of recombination of electron-hole pairs[3–5] can take place in the ground state and be preserved (at least partially) upon transition to the emitting state (hole trapping).[11] This process is possible because the barrier between equivalent configurations in the ground state can be lower than in the radiative state, and the complex has a long residence time in this state at lower excitation levels. The absence of variations in the polarization diagrams of the complex when the temperature is raised to 77 K (Ref. 10) indicates that the characteristic reorientation time, even at 77 K, greatly exceeds the lifetime of the excited state. With a further increase in temperature, however, the reorientation process in the excited state can become significant, because the lifetime of this state is comparatively long (∼10^{-6} s; Ref. 13).

Here we report an investigation of $V_{Ga}Te_{As}$ by polarized photoluminescence methods[14] at elevated temperatures. The

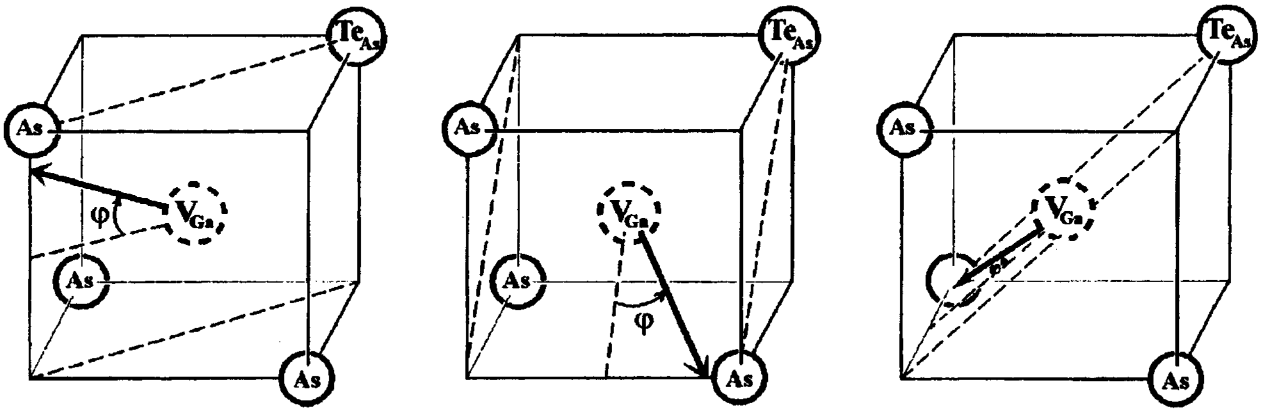

FIG. 1. $V_{Ga}Te_{As}$ in *n*-type GaAs. The arrows show the direction of the axis of the optical dipole, and the dashed lines indicate the symmetry plane of the complex.

polarization of photoluminescence from $V_{Ga}Te_{As}$ complexes excited by polarized light from the impurity absorption band of GaAs:Te is calculated within the framework of the above-indicated model. Possible reorientation of the Jahn–Teller distortion in the excitated state is taken into account, along with the thermal-field emission and retrapping of holes by the complexes. The relative influence of the Jahn–Teller effect and the donor on the initial states of a hole localized at the complex is assumed to be arbitrary in the analytical model. The results of the calculations are compared with experimental data for $V_{Ga}Te_{As}$ complexes in *n*-GaAs in the temperature range 77–230 K. Certain parameters characterizing the states of the defect are estimated on the basis of this comparison, and it is shown that the investigated laws do not conflict with previously proposed[5,6,12] models of the $V_{Ga}Te_{As}$ complex.

2. CHARACTERISTICS OF THE PHOTOLUMINESCENCE OF A SYSTEM OF MONOCLINIC COMPLEXES WITH A FIXED AXIS OF THE ⟨111⟩ TYPE AND REORIENTED DISTORTION

In accordance with the above-described model of the $V_{Ga}Te_{As}$ complex,[5,6,12] if the temperature is not too high, the Jahn–Teller effect is static, and a single complex can have three equivalent configurations of monoclinic symmetry (Fig. 1). A symmetry plane of the type {110} containing the initial axis of the complex, i.e., the lattice sites corresponding to the initial positions of both components of the complex, exists in each configuration. The reorientation of the Jahn–Teller distortion of the complex reduces to the rotation of this plane about the initial axis through an angle ±120°. In crystals of III-IV semiconductors there are four equiprobable orientations of the initial axis and, accordingly, four groups of the investigated defects; within each group a single defect admits three equivalent configurations, between which transitions are possible, inducing reorientation. The axis of the elementary dipole (linear oscillator or rotator) characterizing the emission and absorption of light by a defect lies in the symmetry plane of the defect and changes its direction as it rotates. We describe the position of this axis below by the angle φ measured from an axis of the type ⟨110⟩ situated in the symmetry plane of the defect (Fig. 1).

To analyze the experimental data, we calculate the temperature dependences of the linear polarization of luminescence from such defects in the case of resonance excitation by polarized light. We make the following assumptions:

1. The distortion of the complex in the ground state is similar to the distortion of the complex in the radiative state, and the directions of the axes of the emitting and absorbing dipoles coincide (one-dipole approximation).
2. Each complex resides in the ground state for a sufficiently long time (low excitation intensity), and the reorientation time in this state is short enough for all possible configurations of the complex in the ground state (possible directions of the axis of the absorbing dipole) to be equiprobable in the excitation of photoluminescence.

In the classical dipole approximation the optical characteristics of a point defect in a crystal are described by the superposition of an oscillator and a rotator, which can be regarded as incoherent.[15] We introduce the parameter μ, which characterizes the relative contributions of the oscillator and the rotator to the absorption of light by the defect. The values of μ range from 0 for the ‘‘pure’’ oscillator to 1 in the case of the ‘‘pure’’ rotator. The probability of optical excitation of a single defect in the *i*th group ($i=1$, 2, 3, 4 for the initial axis of the complex directed along the [111], [1 11], [11 1], and [111] axes of the crystal, respectively) in the *j*th configuration ($j=1$, 2, 3) can be represented by the expression

$$A_{i,j}=\sigma_0[(1-\mu)\cos^2\gamma_{i,j}+\mu\ \sin^2\gamma_{i,j}]N_{\hbar\omega}, \tag{1}$$

where σ_0 is a constant characterizing the photon absorption cross section, $\gamma_{i,j}$ is the angle between the dipole axis and the direction of the electric vector of the light wave, and $N_{\hbar\omega}$ is the photon flux density of the exciting light.

For defects of the *i*th group the concentrations of the various configurations of the excited state under stationary conditions are related to the characteristics of the exciting light and the parameters of the defect by the equations

$$\frac{\partial n_{i1}}{\partial t}=\left(\frac{N}{4}-\sum_{j=1}^{3} n_{ij}\right)A_{i1}-\frac{n_{i1}}{\tau_0}-\frac{n_{i1}}{\tau}+\frac{n_{i2}+n_{i3}}{2\tau}$$

$$-n_{i1}c_p p_1+\alpha_{i1}=0,$$

$$\frac{\partial n_{i2}}{\partial t}=\left(\frac{N}{4}-\sum_{j=1}^{3} n_{ij}\right)A_{i2}-\frac{n_{i2}}{\tau_0}-\frac{n_{i2}}{\tau}+\frac{n_{i1}+n_{i3}}{2\tau}$$

$$-n_{i2}c_p p_1+\alpha_{i2}=0,$$

$$\frac{\partial n_{i3}}{\partial t}=\left(\frac{N}{4}-\sum_{j=1}^{3} n_{ij}\right)A_{i3}-\frac{n_{i3}}{\tau_0}-\frac{n_{i3}}{\tau}+\frac{n_{i1}+n_{i2}}{2\tau}$$

$$-n_{i3}c_p p_1+\alpha_{i3}=0. \tag{2}$$

Here N is the number density of complexes, n_{ij} is the density of excited complexes with the ith initial axis in the jth configuration, τ is a characteristic distortion reorientation time in the excited state, which depends on the height of the barrier between configurations and on the temperature, τ_0 is the lifetime of the excited state, which is determined by the recombination of a localized hole with an electron, $c_p p_1$ is the rate of thermal-field emission of holes into the valence band (c_p is the rate of capture of holes by the complex), p_1 is the density of holes in the valence band when the Fermi level coincides with the level of the complex, and α_{ij} is the stationary number of hole-trapping events per unit time at a complex with the ith initial axis that lead to the formation of the jth configuration.

For weak excitation (when the photoluminescence intensity is proportional to $N_{\hbar\omega}$) the density of excited centers is small in comparison with N and can be disregarded in the first term of Eqs. (2). Under these conditions we have

$$\alpha_{i,j}=\alpha_{k,l}=\frac{m}{12}c_p p_1\sum_{i=1}^{4}\sum_{j=1}^{3} n_{ij}(i,j\neq k,l), \tag{3}$$

where m is the ratio of the capture rate of holes by the investigated complexes to the total rate of departure of holes from the valence band (as a result of trapping by all deep centers and interband recombination). Solving the system represented by the set of equations (2) for $i=1, 2, 3, 4$, we can evaluate n_{ij}/τ_0 for any direction and polarization of the exciting light and then determine the intensity and linear polarization of the emission for any direction of observation of photoluminescence. It is necessary here to know the relative contribution of the rotator to the emission of light by a defect. In our calculations we assume that this quantity is equal to the relative absorption contribution of the rotator.

In the polarized photoluminescence experiments we used an orthogonal arrangement with mutually perpendicular directions of the exciting light and observation of photoluminescence. The direction of the electric vector of the exciting light wave was specified by the angle η measured from the axis perpendicular to the directions of the incident light flux and observation of photoluminescence. The degree of polarization of the photoluminescence $\rho(\eta)$ was measured:

$$\rho(\eta)=\frac{I_{\parallel}(\eta)-I_{\perp}(\eta)}{I_{\parallel}(\eta)+I_{\perp}(\eta)}, \tag{4}$$

where $I_{\parallel}(\eta)$ and $I_{\perp}(\eta)$ are the photoluminescence intensities with the electric vector of the light wave parallel and perpendicular to the axis from which the angle η is measured. For the most part two orientations of the crystal relative to the directions of the exciting light and observation of photoluminescence were used: [110]–[001] and [100]–[010] (the first and second of each pair give the direction of the exciting light and the direction of observation, respectively). In these cases $\rho(\eta)$ has extrema at $\eta=0$ and at $\eta=90°$.

Calculations under the above-stated assumptions give

$$\rho(\eta=0)=\rho_1=\frac{1+(1-m)\tau_0 c_p p_1}{1+\tau_0 c_p p_1}\times\frac{f_1+\frac{\tau}{\tau_0}(1+\tau_0 c_p p_1)f_2}{f_3+\frac{\tau}{\tau_0}\left[(1+\tau_0 c_p p_1)f_4-\frac{1}{3}m\tau_0 c_p p_1 f_5\right]} \tag{5}$$

for the orientation [110]–[001] and

$$\rho(\eta=0)=\rho_2=\frac{1+(1-m)\tau_0 c_p p_1}{1+\tau_0 c_p p_1}\times\frac{\frac{\tau}{\tau_0}(1+\tau_0 c_p p_1)f_5}{f_3+\frac{\tau}{\tau_0}\left[(1+\tau_0 c_p p_1)f_4-\frac{1}{3}m\tau_0 c_p p_1 f_5\right]} \tag{6}$$

for the orientation [100]–[010]. Here $f_1,\ldots,f_5$ are quantities that depend only on the parameters of the dipole and not on the temperature:

$$f_1=(1-2\mu)^2(\cos\varphi-2\sqrt{2}\sin\varphi)^2\cos^2\varphi,$$

$$f_2=2(1-2\mu)^2(\cos^2\varphi+4\sin^2\varphi)\cos^2\varphi,$$

$$f_3=4(1+\mu)^2,$$

$$f_4=(\cos^2\varphi+2\sin^2\varphi+2\mu\cos^2\varphi)^2$$

$$+2(\cos^2\varphi+2\mu\sin^2\varphi)^2,$$

$$f_5=(1-2\mu)^2(\cos^2\varphi-2\sin^2\varphi)^2.$$

On the other hand, for the same orientations we have

$$\rho(\eta=90°)\equiv 0. \tag{7}$$

Equations (5) and (6) show that the temperature dependence of the luminescence polarization can be formed both by a variation of the probability of direct reorientation of distortion in the excited state [variation of $(\tau/\tau_0)(1+\tau_0 c_p p_1)$] and by the emergence of excited centers of any group with any possible direction of the distortion due to the emission of holes from photoexcited complexes and their retrapping by any unexcited complexes of the same nature (transfer of excitation).

The thermal–field emission of holes from complexes into the valence band also tends to lower the photoluminescence intensity of these complexes,[2,16] which is described by the following expression in the case of photoluminescence excitation by light from the fundamental absorption band of the semiconductor:

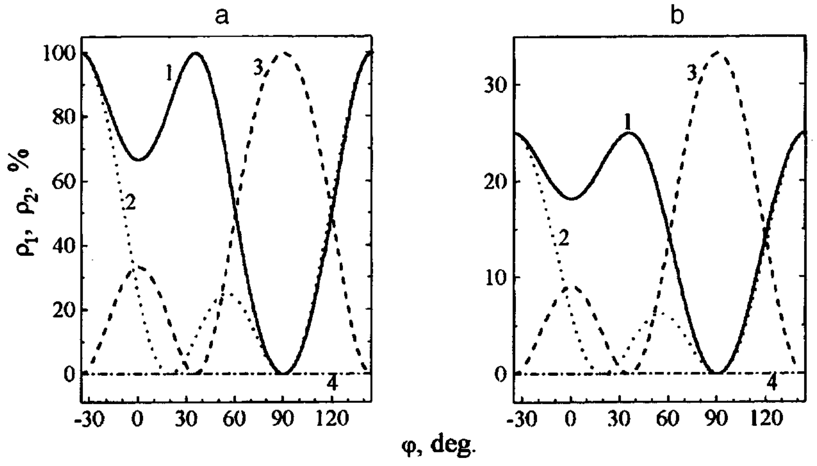

FIG. 2. Degree of polarization of photoluminescence versus angle φ. a) Oscillator; b) rotator; *1)* ρ_1, $\tau/\tau_0 \to \infty$; *2)* ρ_1, $\tau/\tau_0 \to 0$; *3)* ρ_2, $\tau/\tau_0 \to \infty$; *4)* ρ_2, $\tau/\tau_0 \to 0$.

$$I = mN_{e-h}\frac{1}{1+(1-m)\tau_0 c_p p_1}, \tag{8}$$

where N_{e-h} is the number of electron-hole pairs generated by the photoluminescence-exciting light per unit time. The quantity m appearing in Eqs. (5), (6), and (8) can be estimated, as in Ref. 16, from the variation of the intensity of quasi-interband recombination accompanying the decrease of I due to the thermal-field emission of holes from the complex.

If processes of emission and retrapping of holes in resonance excitation do not occur, i.e., if the defect creates a deep level and the temperature is not too high ($c_p p_1 \to 0$), the polarization of the emission for the chosen geometry of the experiment and $\eta = 0$ depends only on the direction and type of radiator and on the possibility of reorientation in the excited state, i.e., on φ, μ, and τ/τ_0. Figure 2 shows the dependence of ρ_1 and $d\rho_2$ on φ for limiting values of μ ($\mu = 1$ and $\mu = 0$) and τ/τ_0 ($\tau/\tau_0 \to \infty$ and $\tau/\tau_0 \to 0$).

It is evident from Fig. 2 that reorientation of the distortions of the complex in the excited state produces a very large absolute variation of $\rho(\eta = 0)$ in at least one of the two investigated configurations for almost any direction of the dipole (except close to the initial axis of the complex). This conclusion is equally valid for the superposition of an oscillator and a rotator except in cases where the values of μ are in the neighborhood of $\mu = 0.5$. We also note that, according to (5) and (6), φ and μ can be found analytically from the values of ρ_1 and ρ_2 at low temperature, when $\tau/\tau_0 \to \infty$:

$$\varphi = \pm \arctan\left(\sqrt{\frac{1}{2} + \frac{\rho_2}{\rho_1}\left(1 \pm \frac{3\rho_1}{2\rho_2}\right)}\right), \tag{9}$$

$$\mu = \frac{1}{2} - \frac{\pm\sqrt{(3\rho_1 + 2\rho_2)(3-\rho_2)} - \frac{1}{2}(3\rho_1 + 2\rho_2)}{4 - \rho_1 - 2\rho_2}. \tag{10}$$

3. EXPERIMENTAL RESULTS

The investigated samples were cut from several GaAs:Te crystals grown by the Czochralski method in the [100] direction. They had various electron densities (n) in the range $\sim(2\times10^{17}$–$2\times10^{18})$ cm^{-3} and were in the form of wafers with dimensions ~3×15×20 mm. The procedure for measuring the intensity, polarization, and excitation spectra of photoluminescence was similar to that used in Ref. 10. The investigated sample was placed in a Dewar flask and pressed tightly against a thick copper holder to ensure a uniform temperature distribution over the area of the sample, and a regulated flow of liquid nitrogen vapor was circulated around it. The temperature was measured by two copper-constantan thermocouples clamped to the upper and lower ends of the sample. The readings of these thermocouples did not differ by more than 0.2 K at any time during the experiment. Control measurements showed that the degree of polarization of the light transmitted through the sample and the Dewar flask did not exceed 1%.

In the photoluminescence spectra of all the investigated samples at low temperature and with interband excitation we observe a band with a luminescence maximum at a photon energy close to 1.18 eV, which is associated with the investigated complexes, and edge luminescence with a maximum at a photon energy ~1.51 eV (Fig. 3). As the temperature is raised, the edge luminescence spectra shift toward lower photon energies and broaden. The luminescence band of the investigated defects changes very little at temperatures below

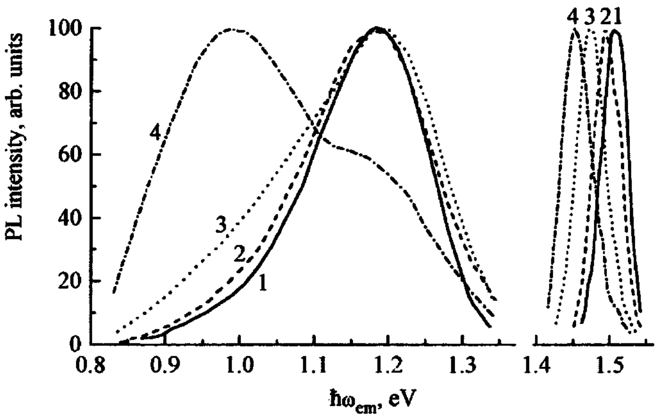

FIG. 3. Photoluminescence spectra of a sample with $n = 5\times10^{17}$ cm^{-3} for excitation by light from the fundamental absorption band. *1)* $T = 80$ K; *2)* 150 K; *3)* 180 K; *4)* 230 K. The intensities of "quasi-interband" and impurity photoluminescence for each temperature are shown in arbitrary units.

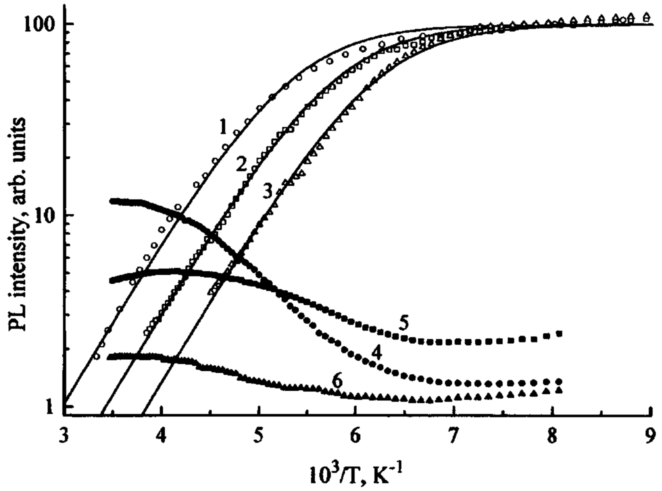

FIG. 4. Total intensity versus temperature for: *1–3*) the luminescence spectral band of the $V_{\mathrm{Ga}}\mathrm{Te}_{\mathrm{As}}$ complex; *4–6*) quasi-interband luminescence. *1, 4*) Electron density in the samples $n=10^{18}$ cm^{-3}; *2, 5*) 5×10^{17} cm^{-3}; *3, 6*) 2×10^{17} cm^{-3}. The solid curves are calculated according to Eqs. (8) and (12) for the following values of the parameters: $E_T=170$ meV; *1*) $(1-m)\tau_0 c_p^0 N_v=3.6\times10^4$; *2*) 8.7×10^4; *3*) 2×10^5.

$\sim$140 K, but then with increasing temperature its intensity decreases, heightening the relative intensity of the band with a maximum near 0.95 eV, which is attributed to complexes having a deeper energy level[17] (Fig. 3). Here the ratio of the intensities of bands with maxima at 0.95 eV and at 1.18 eV at the given temperature vary from one sample to the next and, as a rule, decrease as the density of free electrons in the sample increases. The 0.95–eV band is predominant in the spectra of samples with concentrations $\sim2\times10^{17}$ cm^{-3}, even at low temperatures. The temperature dependence of the total intensities of ''edge luminescence'' (I_{cv}) and luminescence from the investigated complexes (I) in interband excitation is shown in Fig. 4. It has been observed previously[16] that the drop in intensity of the 1.18–eV band is accompanied by an increase in the edge-luminescence intensity.

The excitation spectra of the 1.18–eV band are shown in Fig. 5a. It is evident from the figure that an increase in temperature causes the long-wavelength edge to broaden and shift toward lower photon energies. The excitation of photoluminescence by polarized light with a photon energy ($\hbar\omega_{\mathrm{exc}}$) smaller than the width of the band gap, as first discovered in Ref. 18, induces polarization of the photoluminescence. According to the results of the calculations discussed in Sec. 2, it is observed that $\rho(\eta=90°)\equiv0$ for both of our crystal orientations ([110]–[001] and [100]–[010]).

The values of $\rho(\eta=0)$ for these orientations depend on $\hbar\omega_{\mathrm{exc}}$ and on the temperature. The dependence of $\rho(\eta=0)$ on $\hbar\omega_{\mathrm{exc}}$ has the same form at various temperatures for either orientation and is shown in Fig. 5b for [110]–[001]. It is evident from Fig. 5 that $\rho(\eta=0)$ is independent of $\hbar\omega_{\mathrm{exc}}$ for sufficiently small values of the latter. The existence of such a region in the photoluminescence polarization spectra indicates that only resonance excitation of the investigated complexes takes place in it.[1)] The values of $\rho(\eta=0)$ in this region are independent of $\hbar\omega_{em}$ within the measurement error limits and are a characteristic of these centers. For the orientations [110]–[001] and [100]–[010] they should correspond to ρ_1 and ρ_2 [see Eqs. (5) and (6)]. When the temperature is increased from 77 K to $\sim$120 K, the experimental values of ρ_1 and ρ_2 remain essentially constant and the same as at 2 K: 0.28 ± 0.02 and 0.08 ± 0.01, respectively.[10] A further increase in the temperature causes ρ_1 and ρ_2 to decrease significantly. The experimental temperature curves of the parameter ρ_1, which is determined with a lower relative error than ρ_2, have been compared with the results of the calculations. These curves are shown in Figs. 6 and 7.

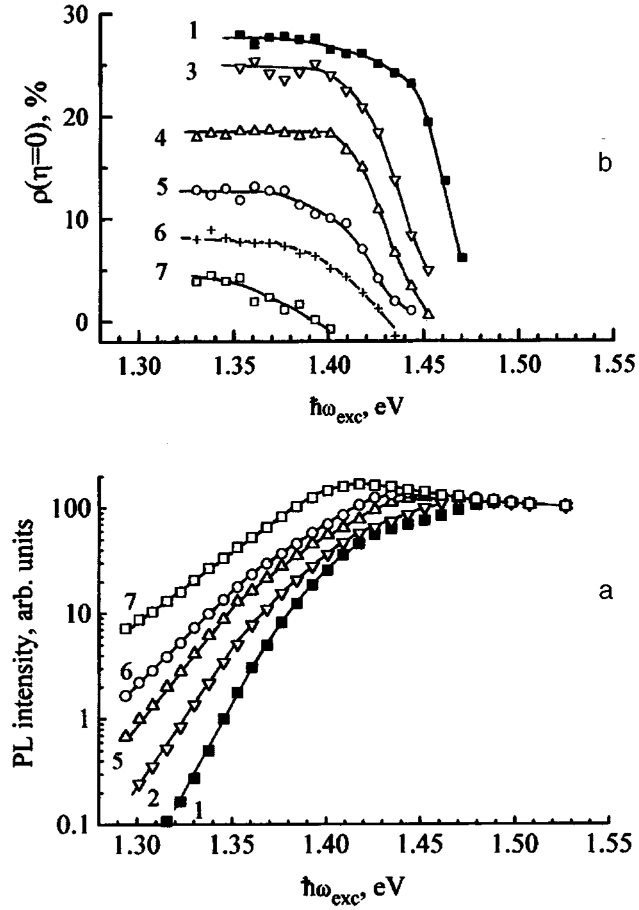

FIG. 5. a) Spectral distributions of the intensity of excitation of photoluminescence in the 1.18-eV band; b) polarization spectra of this band for excitation by polarized light in the crystal orientation [110]–[001]. *1*) $T=80$ K; *2*) 120 K; *3*) 130 K; *4*) 150 K; *5*) 165 K; *6*) 180 K; *7*) 230 K.

4. DISCUSSION

A. Low-temperature region

The invariance of the polarization of the investigated photoluminescence band over a wide range of temperatures (2–120 K) shows that neither the thermal-field emission and trapping of holes by a $V_{\mathrm{Ga}}\mathrm{Te}_{\mathrm{As}}$ complex nor the reorientation of distortions takes place directly in the radiative state in this region. In this case, according to Eq. (9), the ratio ρ_1/ρ_2 depends only on the angle φ characterizing the position of the axis of the elementary radiator in the symmetry plane of the defect. The values of this angle, which are consistent with the experimental value of ρ_1/ρ_2, are equal to $\pm15°$ and

$\pm 51°$. On the other hand, in the model postulating weak splitting of the t_2-state of V_{Ga} by the donor in the complex[6] the angle φ can be linked to the ratio of this splitting, as described in Ref. 6 by the parameter α, to the energy of Jahn–Teller stabilization (E_{JT}). In this model, in fact, the direction of the radiating dipole in real coordinates x,y,z (Fig. 1) coincides with the direction of the radius vector of the point at which the adiabatic potentials of the vacancy complex are a minimum in the space of mutually orthogonal generalized coordinates Q_4,Q_5,Q_6, which are associated with F_2 vibrations of the atoms surrounding V_{Ga}. In the first approximation of perturbation theory with respect to α/E_{JT} this alignment yields the following relation between φ, α, and E_{JT}:

$$\sqrt{3}\,\sin\varphi = 1 - \frac{2\alpha}{3E_{JT}}. \tag{11}$$

Here $\alpha > 0$ (Ref. 6). It follows from Eq. (11) that only the angle $\varphi \approx 15°$ concurs with the postulated relatively weak influence of the donor on the state of the vacancy in the $V_{\mathrm{Ga}}\mathrm{Te}_{\mathrm{As}}$ complex.[6] Using the above-indicated values of ρ_1 and ρ_2, it can also be inferred from Eq. (10) that $\mu \approx 0.16$. Consequently, the relative contribution of the linear oscillator to the absorption and luminescence of the complex is far greater than that of the rotator.

B. Temperature dependence of the photoluminescence intensities with interband excitation

We now consider the temperature variation of the photoluminescence intensity of the complexes in the presence of interband excitation, as shown in Fig. 4. As mentioned previously,[2,16] these temperature curves are attributable to the thermal-field emission of defect-trapped holes into the valence band and can be described by Eq. (8), in which

$$c_p p_1 = c_p^0 N_v \exp(-E_T/kT), \tag{12}$$

where c_p^0 (rate of capture of holes by the complex in the high-temperature limit), N_v (effective density of states in the valence band), and E_T (activation energy of hole emission) are identical constants for all samples. According to Refs. 2, 13, 16, and 19, the parameters τ_0 and m are practically independent of the temperature in the region of strong variation of I, but differ for different samples.

The approximation of the experimental $I(T)$ graphs by Eqs. (8) and (12) is shown in Fig. 4 and is attained for $E_T = 170$ meV. The quantities $(1-m)\tau_0 c_p^0 N_v$ obtained in this approximation are given in the caption to Fig. 4 for samples with various electron densities.

As mentioned in Sec. 2, the range of possible values of m can be determined from the variation of the intensity of quasi-interband luminescence I_{cv} as I decreases with increasing temperature (Fig. 4). Indeed, the observed increase of I_{cv} in the region of the abrupt drop in the luminescence intensity of the complexes in interband excitation is associated with an increase of the nonequilibrium hole density in the valence band due to the thermal-field emission of holes trapped by the complexes.[2,16] Here the intensity I_{cv} varies for the value I_{cv}^0, which corresponds to the total absence of hole emission from the complexes, to the value I_{cv}^{em} corresponding to the almost complete return of holes trapped by the complexes to the valence band. Using the model discussed in Ref. 16, we can readily show that m is related to the relative variation of I_{cv} by the following equation in the case of weak excitation of photoluminescence (linear dependence of I and I_{cv} on the excitation intensity):

$$m = 1 - I_{cv}^0 / I_{cv}^{em}. \tag{13}$$

The experimental value of I_{cv}^{em} is determined by the maximum of I_{cv} (Fig. 4). The intensity I_{cv}^0 can be obtained by extrapolating the experimental $I_{cv}(T^{-1})$ curve from the low-temperature region, where the thermal-field emission of holes from the complexes does not take place, to the temperature at which I_{cv}^{em} is determined. The extrapolation error determines the interval of possible values of m calculated according to relation (13). These values of m are 0.85–0.95, 0.7–0.9, and 0.4–0.6 for samples with $n = 10^{18}$, 5×10^{17}, and 2×10^{17} cm^{-3}, respectively.

C. Reduction of the induced polarization of photoluminescence of the complexes at elevated temperatures

It is evident from a comparison of Figs. 6, 7, and 4 that the polarization of the investigated photoluminescence band decreases with increasing temperature in approximately the same temperature range as that in which its intensity decreases. Consequently, the processes of emission and retrapping of holes by defects can play a significant role in the temperature depolarization of the luminescence and must be taken into account in analyzing the experimental plots of $\rho_1(T)$ by means of Eq. (5). In order for the influence of reorientation of the centers in the excited state on the temperature depolarization of photoluminescence to be observed under these conditions, it is necessary to investigate samples having the smallest possible parameter m; this condition is met by samples with a low electron density. However, such samples are weak radiators in the investigated photoluminescence band, and the intensity of this band begins to diminish at lower temperatures. Moreover, the very strong photoluminescence band with its maximum at a photon energy of 0.95 eV precludes any sufficiently accurate determination of the polarization of the investigated band for these samples. Consequently, a detailed comparison with theory is made for samples with $n = 5\times 10^{17}$ cm^{-3}. The results of this comparison are shown in Fig. 6. While the decrease in the polarization is associated entirely with the thermal-field emission and retrapping of holes ($\tau/\tau_0 \to \infty$), according to Eqs. (5) and (6), the temperature dependence of ρ_1 and ρ_2 is determined entirely by the temperature dependence of $\tau_0 c_p p_1$. The latter can be determined from the dependence $I(T)$ (Fig. 4) for given m. Graphs of $\rho_1(T)$ calculated in this way for various values of m are shown in Fig. 6a and for reasonable values of m are close to the experimental curve. The agreement between the experimental and calculated curves can be improved if reorientation of the distortions of a complex in the excited state is taken into account together with the emission

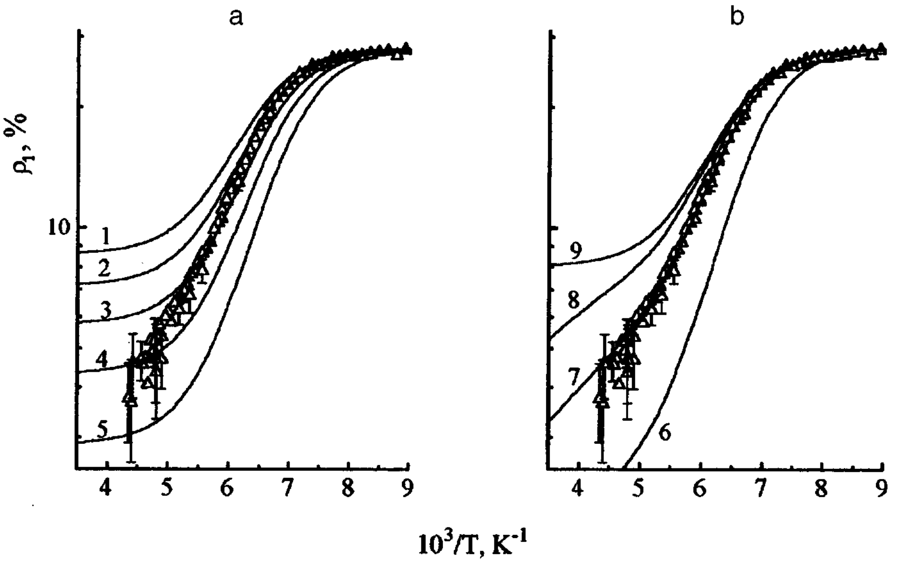

FIG. 6. Degree of polarization ρ_1 versus temperature for the luminescence band of $V_{\mathrm{Ga}}\mathrm{Te}_{\mathrm{As}}$ complexes ($\hbar\omega_{\mathrm{exc}}=1.35$–$1.36$ eV, $\hbar\omega_{em}=1.20$–1.25 eV) in a sample with $n=5\times10^{17}$ cm^{-3}. The solid curves are calculated according to Eqs. (5) and (14): a) in the case $\tau/\tau_0\to\infty$; b) in the general case. The following parameters are used in the calculations: $\varphi=15°$, $\mu=0.16$, $\tau_0=10^{-6}$ s, $E_T=170$ meV, $c_p^0N_v=3.1\times10^{-5}$ s^{-1}; *1)* $m=0.7$, $E_B=\infty$; *2)* $m=0.75$, $E_B=\infty$; *3)* $m=0.8$, $E_B=\infty$; *4)* $m=0.85$, $E_B=\infty$; *5)* $m=0.9$, $E_B=\infty$; *6)* $m=0.72$, $E_B=200$ meV; *7)* $m=0.72$, $E_B=225$ meV; *8)* $m=0.72$, $E_B=250$ meV; *9)* $m=0.72$, $E_B=\infty$.

and retrapping of holes. Assuming that the characteristic time of such reorientation depends on the temperature according to the equation

$$\tau=\nu^{-1}\exp(E_B/kT), \tag{14}$$

where E_B is the height of the barrier between equivalent configurations, and ν is the frequency of collisions with the walls of the barrier, we obtain good agreement between the calculations and experiment (Fig. 6b) for $E_B=200$–260 meV and $\nu^{-1}=10^{-11}$–10^{-13} s. These same parameters also give satisfactory agreement of the calculations with the experimental polarization curve for samples with other electron densities (Fig. 7). The quantity τ_0, which is needed for approximating the experimental data, varies from 0.6 μs to 1.3 μs for samples with electron densities of 10^{18} cm^{-3} and 2×10^{17} cm^{-3}, in good agreement with the values of τ_0 obtained in Ref. 13. As the electron intensity increases, *m* increases approximately from 0.4 to 0.9 and is consistent with estimates based on Eq. (13). However, as mentioned above, the deviation of the calculated curves obtained without the reorientation of distortion in the excited state from the experimental curves is slight (Fig. 6a). In this regard, the existing measurement error and the simplicity of the model based on the assumptions of temperature independence of *m* and the absence of thermal-field emission of holes generated in the absorption of light by uncontrollable acceptors rule out the unequivocal assertion that this reorientation plays an appreciable role in the depolarization of radiation at $T=130$–230 K. Consequently, the agreement of the calculations with the experimental data, as demonstrated in Figs. 6b and 7, merely implies that the barrier for reorientation in the excited state cannot be lower than ~200 meV.

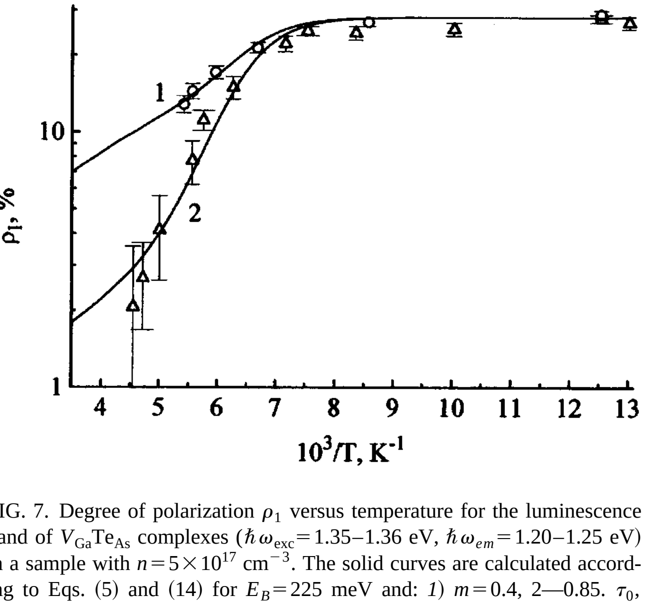

FIG. 7. Degree of polarization ρ_1 versus temperature for the luminescence band of $V_{\mathrm{Ga}}\mathrm{Te}_{\mathrm{As}}$ complexes ($\hbar\omega_{\mathrm{exc}}=1.35$–$1.36$ eV, $\hbar\omega_{em}=1.20$–1.25 eV) in a sample with $n=5\times10^{17}$ cm^{-3}. The solid curves are calculated according to Eqs. (5) and (14) for $E_B=225$ meV and: *1)* $m=0.4$, 2—0.85. τ_0, 10^{-6} s: 1 — 1.07, 2 — 0.77. The remaining parameters are the same as in Fig. 6.

5. CONCLUSIONS

The foregoing analysis shows that the polarization of the photoluminescence band with a maximum near 1.18 eV in *n*-type GaAs:Te with resonance excitation by polarized light over a broad range of temperatures (2–230 K) is well described by the one-dipole approximation within the framework of a previously developed[5,6,11,12] model of a $V_{\mathrm{Ga}}\mathrm{Te}_{\mathrm{As}}$ complex inducing such photoluminescence. At temperatures above ~120 K the reduction of the polarization of this band induced as a result of excitation by polarized light is mainly attributable to the transfer of excitation to complexes with any possible orientations of the initial axis and Jahn–Teller distortion (owing to the thermal-field emission of holes by the photoexcited complexes and their retrapping), and it can also be partially associated with the reorientation of distortions during the lifetime of the excited state of the complex. The height of the energy barrier for such reorientation is at least ~200 meV.

This work has received partial support from the Russian Fund for Fundamental Research (Grant No. 95-02-04146-a).

[1)] Our observations that $\rho(\eta=0)$ is constant and $\rho(\eta=90°)$ is equal to zero in this region, along with the invariance of $\rho(\eta=0)$ over the spectrum of the investigated photoluminescence band, also indicate that the influence of scattering of the exciting light and the 0.95–eV luminescence band can be disregarded in the ranges of $\hbar\omega_{\rm exc}$ and $\hbar\omega_{em}$ used in our work.

---

[1] E. W. Williams, Phys. Rev. **168**, 922 (1968).
[2] K. D. Glinchuk, A. V. Prokhorovich, and V. I. Vovnenko, Phys. Status Solidi A **34**, 777 (1976).
[3] N. S. Averkiev, A. A. Gutkin, E. B. Osipov, M. A. Reshchikov, and V. R. Sosnovskiĭ, Fiz. Tekh. Poluprovodn. **26**, 1269 (1992) [Sov. Phys. Semicond. **26**, 708 (1992)].
[4] A. A. Gutkin, M. A. Reshchikov, V. E. Sedov, and V. R. Sosnovskii, Proc. Estonian Acad. Sci. Phys. Math. **44**, 212 (1995).
[5] A. A. Gutkin, N. S. Averkiev, M. A. Reshchikov, and V. E. Sedov, in *Defects in Semiconductors 18*, edited by M. Suezawa and H. Katayama-Yoshida (*Materials Science Forum*, Vol. 196–201, Part 1) (Trans. Tech. Publ., Zurich, 1995), p. 231.
[6] N. S. Averkiev, A. A. Gutkin, M. A. Reshchikov, and V. E. Sedov, Fiz. Tekh. Poluprovodn. **30**, 1123 (1996) [Semiconductors **30**, 595 (1996)].
[7] G. D. Watkins and J. W. Corbett, Phys. Rev. **134A**, A1359 (1964).
[8] E. L. Elkin and G. D. Watkins, Phys. Rev. **174**, 881 (1968).
[9] X.-Q. Fan, S.-G. Shen, and D.-X. Zhang, Phys. Rev. B **42**, 9501 (1990).
[10] N. S. Averkiev, A. A. Gutkin, E. B. Osipov, M. A. Reshchikov, V. E. Sedov, and V. R. Sosnovskiĭ, Fiz. Tekh. Poluprovodn. **25**, 50 (1991) [Sov. Phys. Semicond. **25**, 28 (1991)].
[11] A. A. Gutkin, M. A. Reshchikov, and V. E. Sedov, Z. Phys. Chem. (to be published in 1997).
[12] A. A. Gutkin, M. A. Reshchikov, and V. R. Sosnovskiĭ, Fiz. Tekh. Poluprovodn. **27**, 1516 (1993) [Semiconductors **27**, 838 (1993)].
[13] K. D. Glinchuk, A. V. Prokhorovich, and V. E. Rodionov, Fiz. Tekh. Poluprovodn. **11**, 35 (1977) [Sov. Phys. Semicond. **11**, 18 (1977)].
[14] P. P. Feofilov, *Polarized Luminescence of Atoms, Molecules, and Crystals* [in Russian], Gos. Izd. Fiz. Mat. Lit, Moscow (1959).
[15] E. E. Bukks, N. N. Grigor'ev, and M. V. Fok, Tr. Fiz. Inst. Akad. Nauk SSSR **79**, 108 (1974).
[16] K. D. Glinchuk and A. V. Prokhorovich, Phys. Status Solidi A **44**, 777 (1977).
[17] A. A. Gutkin, M. A. Reshchikov, and V. R. Sosnovskii, Semicond. Sci. Technol. **9**, 2247 (1994).
[18] I. A. Buyanova, S. S. Ostapenko, and M. K. Sheĭnkman, Fiz. Tverd. Tela (Leningrad) **27**, 748 (1985) [Sov. Phys. Solid State **27**, 461 (1985)].
[19] V. I. Vovnenko, K. D. Glinchuk, K. Lukat, and A. V. Prokhorovich, Fiz. Tekh. Poluprovodn. **14**, 1003 (1980) [Sov. Phys. Semicond. **14**, 596 (1980)].

Translated by James S. Wood

The problem of intermediate temperatures or electric fields in the scattering of hot electrons by acoustic phonons

Z. S. Kachlishvili and L. G. Kukutariya

I. Dzhavakhishvili Tbilisi State University, 380028 Tbilisi, Georgia

(Submitted November 27, 1995; accepted for publication April 21, 1997)
Fiz. Tekh. Poluprovodn. **31**, 1071–1073 (September 1997)

An approximate expression is derived for the momentum relaxation time in the quasielastic scattering of hot electrons by acoustic phonons as a function of the electron energy and the lattice temperature. The mobility and the dependence of the impurity breakdown electric field on the degree of compensation are calculated in the electron-temperature approximation. The results of the calculations are in good agreement with the experimental for n-type Ge. © *1997 American Institute of Physics.* [S1063-7826(97)01009-0]

The so-called intermediate-temperature problem arises when the momentum of hot electrons is lost in scattering by acoustic phonons. The problem stems from the following situation. The momentum relaxation time in quasielastic acoustic scattering can be written in the form[1,2]

$$\frac{1}{\tau}=\frac{(16k_0T)^{1/2}}{m^{1/2}l_{ae}}\left(\frac{k_0T}{ms^2}\right)^{1/2}\frac{1}{x^3}\int_0^x\chi^4\cot\chi d\chi, \tag{1}$$

where $x=(2ms^2\varepsilon)^{1/2}/k_0T$, ε is the electron energy, m is the effective electron mass, T is the temperature of the crystal lattice, s is the sound velocity, and l_{ae} is the mean free path in the ''high-temperature'' approximation.

It is a well-known fact that a solution of the integral in Eq. (1) does not exist for an arbitrary degree of excitation of lattice acoustic modes. A simple solution of the integral is obtainable only in the high-temperature and low-temperature approximations, when the laws of equidistribution of phonons or zero-point lattice vibrations are valid.[1,2] Appropriate energy distribution functions have been found by Davydov[3] and Streton.[4] The criteria of the high-temperature and low-temperature approximations impose restrictions on the average electron energy, which depends on the applied electric field. Consequently, in the steady state, when the energy acquired from the field is restored to the system of phonons, the average electron energy can be determined as a function of the electric field, and the criteria of the high-temperature and low-temperature approximations can therefore be written in terms of the electric field strength:[5]

$$E_1\gg E \quad\text{and}\quad E_1\ll E, \tag{2}$$

where, in the case of germanium for example, $E_1\approx0.11T^{5/2}$ V/cm (Ref. 5).

In the impurity breakdown range the electric field depends strongly on the degree of compensation of the sample and weakly on the lattice temperature. In this field range, therefore, the asymptotic behavior of the distribution function is determined by the ratio between the degree of compensation of the sample and the lattice temperature. It is readily verified that the range of intermediate temperatures or electric fields covers a fairly broad interval, which increases rapidly with the temperature. The behavior of the kinetic coefficients is unknown in this interval, because neither the Davydov nor the Streton distribution functions are valid in it. In many problems, including the applied kind, it is very important to know how the kinetic coefficients behave in the indicated interval. The custom, therefore, is to make various interpolations between the values obtained in the high-temperature and low-temperature approximations. The major role of the intermediate-field problem in the investigation of the kinetic coefficients in the presence of acoustic scattering becomes all the more obvious in view of the complex dependence of the pump electric field on the applied field in the presence of a magnetic field when the direction of the current is specified.

In this note we give the results of an investigation of the problem of intermediate temperatures (between the high-temperature and low-temperature approximations) or electric fields. The corresponding mobility and electron temperature as functions of the applied electric field are calculated by means of an analytical approximation of the expression for the momentum relaxation time (1). The dependence of the breakdown field on the degree of compensation is also calculated, and it is shown in a specific example that this essentially nonlinear problem cannot be satisfactorily described by the high-temperature or low-temperature approximations. A comparison with experiment reveals good agreement between the theoretical and experimental results.

Calculations have shown that relation (1) is well approximated by the expression

$$\frac{1}{\tau}=\frac{(16k_0T)^{1/2}}{m^{1/2}l_{ae}}\left(\frac{k_0T}{ms^2}\right)^{1/2}\left[\frac{x^2}{5}+\frac{x}{4}\exp(-0.95x)\right]. \tag{3}$$

The discrepancy between the values of τ obtained by means of Eqs. (1) and (3) does not exceed 3.5% over the entire range of variation of x. Equation (3) is used to calculate the mobility in the electron-temperature approximation:[6]

$$\mu=\frac{4esl_{ae}}{3\pi^{1/2}k_0T}\frac{1}{x_e}[1-\exp(-1.2/x_e)], \tag{4}$$

where $x_e=(2ms^2/k_0T)^{1/2}(T/T_e)^{1/2}$.

These results enable us to calculate the dependence of the electron temperature T_e/T on the applied electric field. From the energy balance equation we obtain

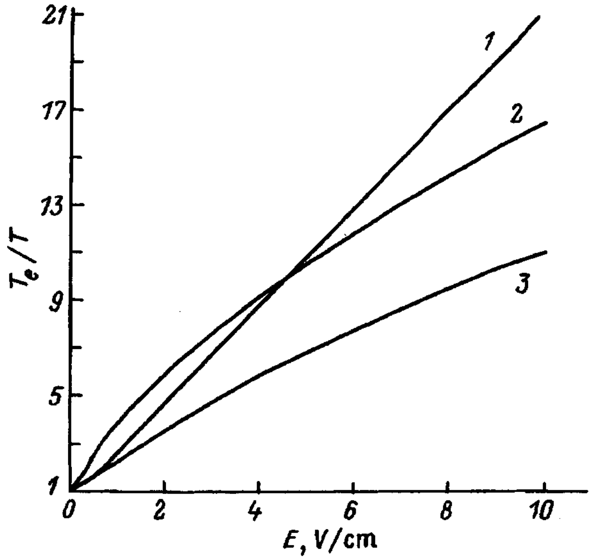

FIG. 1. Electron temperature T_e versus applied electric field E at a lattice temperature $E=4.2$ K. 1) In the high-temperature approximation; 2) in the low-temperature approximation; 3) according to Eq. (5).

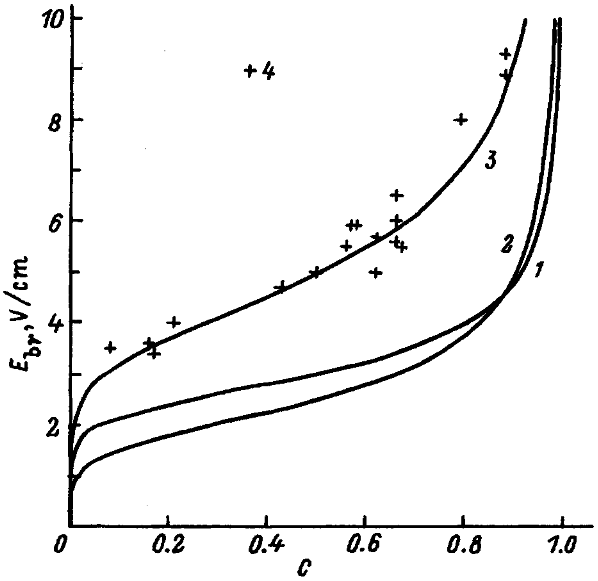

FIG. 2. Impurity breakdown electric field E_{br} versus degree of compensation C. 1) In the high–temperature approximation; 2) in the low-temperature approximation; 3) according to Eqs. (5) and (6); 4) experimental results from Refs. 10 and 11.

$$\left(\frac{E}{E_0}\right)^2=\frac{T_e}{T}\left(\frac{T_e}{T}-1\right)\frac{x_e}{1-\exp(-1.2/x_e)}\left\{\frac{3}{2}\sqrt{\pi}+\frac{15}{2^{9/4}x_e}\right.$$
$$\left.\times\exp\left[\frac{(0.95x_e)^2}{8}\right]W_{-\frac{11}{4},-\frac{1}{4}}\left[\frac{(0.95x_e)^2}{4}\right]\right\}, \qquad (5)$$

where $E_0=(6ms^2k_0T)^{1/2}/el_{ae}$, and $W_{ik}(z)$ is the Whittaker function.

A graph of $T_e(E)/T$ for n-type Ge ($m=0.22m_0$ and $T=4.2$ K) is shown in Fig. 1. Also shown in the figure are curves corresponding to the high-temperature and low-temperature approximations. It is readily apparent that both approximations underestimate the electric field for each fixed value of the electron temperature. This disparity is strongly manifested in the dependence of the breakdown electric field E_{br} on the degree of compensation. In fact, it is evident from the plot of $E_{\mathrm{br}}(C)$ in Fig. 2 that the breakdown fields are too low in the indicated approximations for the same degree of compensation C. An expression for the differential capture cross section derived previously[7] on the basis of the results of the corrected theory of Lax[8] has been used in calculating the thermal capture coefficient. The impact ionization coefficient is calculated by means of the differential cross section obtained on the basis of the generalized Born method:[9]

$$\sigma=\pi a_0^2\left(\frac{N_e}{\varepsilon_i^2}\right)\left(\frac{\eta-1}{\eta}\right)^{3/2}\frac{b}{\eta-1+\varphi}, \qquad (6)$$

where ε_i is the impurity ionization energy in units of $\mathrm{Ry}=m_0e^4/2\hbar^2$, $\eta=\varepsilon/\varepsilon_i$, a_0 is the Bohr radius of a hydrogen-like center, N_e is the number of electrons in the shell from which ionization takes place, $b=9.3$, and $\varphi=2.5$ (Ref. 9).

Previous experimental results[10,11] are also shown in Fig. 2. It is evident from the figure that the experiment is well described by curve 3 over the entire range of electric fields, including the intermediate-field interval.

[1] E. M. Conwell, in *Solid State Physics*, Suppl. 9 (Academic Press, New York, 1967) [Russian trans., Mir, Moscow, 1970].

[2] B. F. Gantmakher and I. B. Levinson, *Carrier Scattering in Metals and Semiconductors* [in Russian], Nauka, Moscow (1984).

[3] B. I. Davydov, Zh. Éksp. Teor. Fiz. **7**, 1069 (1937).

[4] R. Streton, Proc. R. Soc. London Ser. A **246**, 406 (1958).

[5] Z. S. Kachlishvili, Fiz. Tekh. Poluprovodn. **2**, 580 (1968) [Sov. Phys. Semicond. **2**, 478 (1968)].

[6] Z. S. Kachlishvili and L. G. Kukutariya, Tr. Tbilis. Gos. Univ. **313**, 93 (1992).

[7] T. O. Gegechkori, V. G. Dzhakeli, and Z. S. Kachlishvili, Soobshch. Akad. Nauk Gruz. SSR **163**, 565 (1981).

[8] V. N. Abakumov and I. N. Yassievich, Zh. Éksp. Teor. Fiz. **71**, 657 (1976) [Sov. Phys. JETP **44**, 345 (1976)].

[9] I. I. Sobelman, L. A. Vainshtein, and E. A. Yukov, *Excitation of Atoms and Broadening of Spectral lines* (Springer-Verlag, Berlin, 1981) [Russian original, Nauka, Moscow, 1979].

[10] V. F. Bannaya, L. I. Veselova, E. M. Gershenzon, and V. R. Grinberg, Fiz. Tekh. Poluprovodn. **5**, 155 (1971) [Sov. Phys. Semicond. **5**, 131 (1971)].

[11] V. F. Bannaya, L. I. Veselova, E. M. Gershenzon, and V. A. Chuenkov, Fiz. Tekh. Poluprovodn. **7**, 1972 (1973) [Sov. Phys. Semicond. **7**, 1315 (1973)].

Translated by James S. Wood

SEMICONDUCTOR STRUCTURES, INTERFACES, AND SURFACE

Mechanisms of current flow in zinc telluride–zinc selenide heterojunctions

V. E. Baranyuk and V. P. Makhniĭ

Yu. Fed'kovich Chernovtsy State University, 274012 Chernovtsy, Ukraine

(Submitted March 22, 1996; accepted for publication November 14, 1996)
Fiz. Tekh. Poluprovodn. **31**, 1074–1076 (September 1997)

The electrical properties of zinc telluride–zinc selenide heterojunctions prepared by solid-phase substitution reactions are investigated. It is established that the forward current is governed by tunneling-recombination processes at low biases and by above-barrier carrier diffusion at high biases. The initial segments of the reverse branches of the *I–V* characteristics are described on the basis of the model of tunneling carrier transmission with the participation of deep levels. For high reverse biases the current was found to increase abruptly as a result of impact ionization. © *1997 American Institute of Physics.* [S1063-7826(97)01109-5]

Variable-zincgap heterojunctions in the zinc telluride–zinc selenide system are already finding applications in various optoelectronic devices.[1,2] It will be impossible to further refine their operational parameters without gaining a deeper understanding of the physical processes governing the characteristics of heterojunctions. In this note we give the results of experimental studies of the electrical properties of *p*-ZnTe/*n*-ZnSe heterostructures with a view toward clarifying the mechanisms of current flow.

The technology used to prepare the heterojunctions is described in Refs. 3 and 4. The current cutoff voltage V_I at 300 K lies within the limits 1.2–1.4 V, and the temperature coefficient of its variation is $\gamma\approx 3.5\times 10^{-3}$ V/K. The density of surface states N_S at the interface, determined from capacitance measurements, is $\approx 5\times 10^{11}$ cm^{-2}, which is several orders of magnitude lower than the calculated value ($N_S\approx 1.5\times 10^{14}$ cm^{-2}; Ref. 5). The investigated heterojunctions therefore have a sufficiently perfect interface and correspond to Anderson's model.

For such structures, in general, the forward current is the sum of the above-barrier current I_d, the recombination current in the space-charge region I_{gr}, and the tunneling current I_t (Ref. 5):

$$I=I_d+I_{gr}+I_t=I_0\exp(eV/kT)+I^0_{gr}\exp(eV/2kT)+I^0_t\exp(\alpha V+\beta T), \tag{1}$$

where I_0, I^0_{gr}, ad I^0_t are the cutoff currents at the barrier voltage $V=0$, α and β are parameters independent of the voltage and the temperature, and all other notation is standard.

It follows from Fig. 1 that the recombination current is dominant at low biases. The temperature dependence of I^0_{gt} in coordinates $\{\ln I^0_{gr},\ 10^3/T\}$ is approximated by a straight line, and the activation energy determined from its slope is $E_a=0.65\pm 0.05$ eV. This value is considerably lower than expected on the basis of the Cah–Neyse–Shockley theory,[6] according to which $E_a=E_g/2\approx 1.05$ eV if recombination is assumed to take place in a layer of the solid solution ZnTe$_x$Se$_{1-x}$, even with a bandgap of the minimum width $E_g\approx 2.1$ eV (Ref. 7). As the forward bias is increased, the recombination current is superseded by the tunneling current, and the experimental values of the parameters α and β are equal to 5 V^{-1} and 2.5×10^{-2} K^{-1}, respectively.

An analysis of the plots of $I(V,T)$ leads to the conclusion that the forward current in the investigated range of V and T is attributable to successive tunneling-recombination transitions through a series of levels in the space-charge region of the structure. According to the model adopted here, the total current (for any given pair of values of V and T) is limited by whichever process, tunneling or recombination, has the lower probability. Since $I^0_t\gg I^0_{gr}$ in our case, the forward current is controlled by recombination in the space-charge region for small values of V. When the voltage is increased, because I_{gr} depends more strongly on V, the recombination current is limited by the tunneling current, as observed in experiment (Fig. 1). The given model therefore provides a fairly good qualitative description of the observed

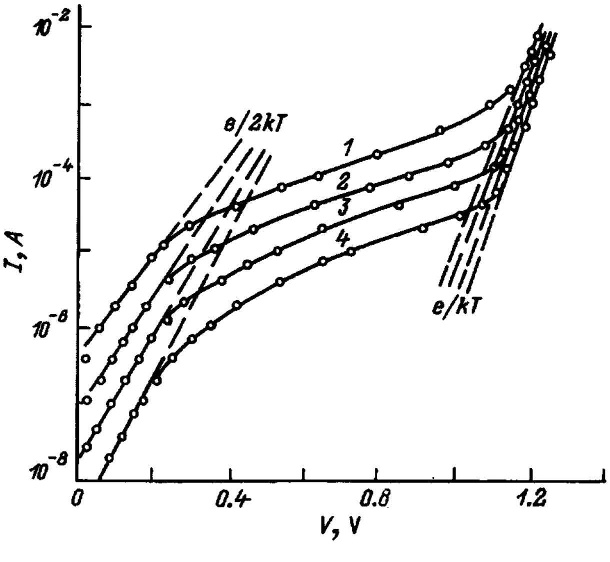

FIG. 1. Forward branches of the *I–V* curves at various temperatures. *1)* $T=410$ K; *2)* 380 K; *3)* 340 K; *4)* 300 K.

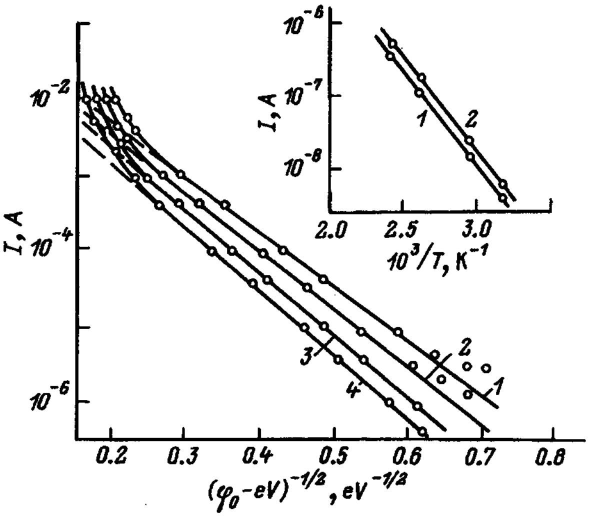

FIG. 2. Comparison of $I_R(V)$ curves with Eq. (3). *1)* $T=410$ K; *2)* 380 K; *3)* 340 K; *4)* 300 K. Inset: at $V=-0.2$ V, temperature dependence of: *1)* the forward cutoff current I_g^0; *2)* the reverse current.

current-voltage characteristics in the low-bias range.

With a further increase in the forward voltage, the above-barrier transmission of carriers becomes dominant (Fig. 1). The experimental dependence of $ln I_S$ on $10^3/T$ is approximated by a straight line with slope $eV_0 \approx 2.4$ eV, consistent with the energy E_g for zinc telluride at 0 K (Ref. 7). At 300 K (taking into account the experimental value of γ) the diffusion potential is $V_0 \approx 1.35$ eV, which is close to the experimental value of the current cutoff voltage at room temperatures. According to Ref. 5, the saturation current is described by the expression

$$I_S = SPN_{d2}(D_{n1}/\tau_{n1})^{1/2}\exp(-eV_0/kT), \tag{2}$$

where S is the area of the diode, N_{d2} is the density of donors in the *n*-type semiconductor, P is the carrier transmissivity across the interface, D_{n1} and τ_{n1} are the diffusion coefficient and lifetime of electrons in the *p*-type material. Assuming for the investigated structures that $S \approx 0.1$ cm^2, $N_{d2} \approx 10^{16}$ cm^{-3}, $D_{n1} \approx 1$ cm^2/s, $\tau_{n1} \approx 10^{-8}$ s, and $V_0 \approx 1.4$ eV, we obtain $I_S \approx P \cdot 10^{-19}$ A at 300 K. The experimental value of the saturation current is approximately 10^{-19} A. It follows from these estimates that $P \approx 1$; i.e., the influence of the potential ''spike'' at the heterojunction on the carrier transmissivity can be disregarded. We also note that the potential barrier is much lower on the ZnSe side than on the ZnTe side, so that the above-barrier current is primarily an electron current.

It is logical to assume that the current-flow mechanisms discussed above in the presence of forward bias can also operate in the presence of reverse bias. An analysis of the mechanisms leads to the following conclusions. First, in above-barrier carrier transmission the reverse current I_R is of the same order of magnitude as I_S. In the investigated temperature range, however, I_S does not exceed 10^{-15} A, which is many orders of magnitude lower than the measured value (Fig. 2). For this reason the contribution of the above-barrier component to the reverse current is negligible and can be ignored. Second, as mentioned previously, the low-V tunneling-emission current must be determined by the less probable emission process in the space-charge region. In this case we have $I_R \approx I_{gr}^0 \sim \exp(E_a/2kT)$, which is corroborated by experiment (see the inset to Fig. 2). With a further increase in the voltage, the measured value of I_R increases far more rapidly than is required for the emission current, since the functional relation $I_R \sim \sqrt{V_0 - V}$ must be observed for the latter.[5] Now the reverse branches of the *I-V* characteristics are described over a broad range of V by the characteristic expression for the tunneling current[5]

$$I = a_1\exp(-b_1/\sqrt{\varphi_0 - eV}), \tag{3}$$

where $\varphi_0 = eV_0$, and b_1 is a parameter independent of V, whose value is determined by the parameters of the heterojunction and the form of the tunneling transitions. The parameter a_1 takes into account the degree of filling of the energy levels from which tunneling originates. The T-independence (within the experimental error limits) of the parameter a_1 suggests that electron tunneling transitions take place from within the valence band of ZnTe into the conduction band of ZnSe. However, since the calculated values of b_1 for forward interband tunneling in the given heterojunctions are much higher than the experimental values, it must be assumed that deep impurity levels are involved in the tunneling transitions. Unfortunately, a lack of information about their parameters is a hindrance to quantitative calculations. Moreover, the given model qualitatively explains the observed plots of $I_R(V)$ in the ranges of V and T where tunneling processes are predominant. The deviation of the experimental *I-V* curves from the relation (3) in the low-V range is associated with the contribution of the emission current to I_R.

The steeper rise of I_R in comparison with (3) for high V is associated with avalanche carrier multiplication as a result of impact ionization. This assertion is further confirmed by photocurrent multiplication. An analysis of the multiplication factor M as a function of the reverse voltage indicates a pronounced difference between the impact ionization for electrons and that for holes. Since the current introduced in the strong-field region is an electron current, ionization takes place predominantly by virtue of electrons in zinc selenide. The experimental impact ionization threshold energy E_i, determined from graphs of $M(V)$, is equal to 3 eV at 300 K. For a direct-gap semiconductor, on the other hand, E_i is given by the expression[8]

$$E_i = E_g[1 + m_n^*/(m_n^* + m_p^*)]. \tag{4}$$

Substituting the known values of E_g, m_n^*, and m_p^* for zinc selenide[7] into Eq. (4), at 300 K we obtain $E_i \approx 3.2$ eV, which is close to the experimental threshold energy for impact ionization.

The authors are grateful to V. D. Ryzhikov for furnishing the zinc selenide crystals.

[1] O. P. Verbitskiĭ, L. A. Kosyachenko, V. P. Makhniĭ, and V. D. Ryzhikov, Pis'ma Zh. Tekh. Fiz. **14**, 702 (1988) [Sov. Tech. Phys. Lett. **14**, 311 (1988)].
[2] L. A. Kosyachenko and V. P. Makhniy, J. Cryst. Growth **110**, 523 (1991).
[3] V. P. Makhniĭ, Izv. Akad. Nauk SSSR Neorg. Mater. **27**, 619 (1991).
[4] V. P. Makhniĭ, Élektron. Tekh. Ser. Mater. **4**, 30 (1991).

[5] B. L. Sharma and R. K. Purohit, *Semiconductor Heterojunctions* (Pergamon Press, Oxford-New York, 1974) [Russian trans., Sov. Radio, Moscow, 1979].
[6] C. Cah, R. Neyse, and W. Schockley, Proc. IRE **45**, 1228 (1957).
[7] N. N. Berchenko, V. E. Kreve, and V. G. Sredin, *Semiconductor Solid Solutions and Their Application* [in Russian], Vosnizdat, Moscow (1982).
[8] I. K. Vereshchagin, *Electroluminescence of Crystals* [in Russian], Nauka, Moscow (1974).

Translated by James S. Wood

Resonant interaction of electrons with an rf electric field in asymmetric double-barrier structures

E. I. Golant and A. B. Pashkovskiĭ

Scientific-Research Institute ''Istok'', 141120 Fryazino, Russia

(Submitted June 10, 1996; accepted for publication January 20, 1997)
Fiz. Tekh. Poluprovodn. **31**, 1077–1082 (September 1997)

Analytical expressions for the electron wave functions, the low-signal, high-frequency conductance, and the widths of the energy levels (minibands) in a asymmetric double-barrier structure with thin barriers are obtained under conditions of coherent electron tunneling strictly along the centers of the energy levels and with the electron energies deviating from exact resonance. It is shown that an electron transmittance equal to 1 and a substantial increase in the integrated (taking into account the energy distribution of the electrons incident on the structure) rf conductance of the structure can be obtained by choosing the appropriate arrangement of the minibands of the structure relative to the conduction band bottom of the semiconductor materials to the left and right of the structure. © *1997 American Institute of Physics.* [S1063-7826(97)01209-X]

1. INTRODUCTION

Interest in double- and many-barrier resonant tunneling structures has greatly increased in recent years as a result of the development of a unipolar quantum cascade infrared (IR) laser operating on intersubband electronic transitions.[1,2] The theory and calculation of lasers of this type are ordinarily constructed under the assumption of successive tunneling of electrons; i.e., it is assumed that a substantial portion of the electrons passing through the structure undergoes collisions with phonons, destroying the coherence of the electron wave functions.[3] At the same time, as shown in Ref. 4 , efficient lasing on intersubband transitions can be done by using structures with coherent tunneling, where the tunneling time of the electrons out of a quantum well is shorter than the phonon scattering time.

The characteristic features of the resonant interaction of coherently tunneling electrons with an rf field in symmetric, double-barrier, resonant-tunneling structures (DBRTS) and in structures with barriers of different strength but the same level of the conduction band bottom inside and on both sides of the structure were investigated in Ref. 5. Analytic expressions were obtained there, in the approximation of strong barriers, for the dynamic conductivity and width of the resonance levels of a symmetric DBRTS as a function of the well width and barrier height. This made it possible to estimate the working characteristics of DBRTS as an active element of terahertz-range devices with electron injection into an arbitrary energy level of the symmetric structure. However, the use of structures with a uniform profile of the conduction band bottom implies the presence of an injector in the form of a barrier, a double-barrier structure, or a potential jump, all of which give a strongly nonequilibrium electron energy distribution in the electron flux incident on the DBRTS.[6,7] The use of DBRTS with different levels of the conduction band bottom at the entrance and exit of the structure makes it possible to produce the required distribution without using an injector, thereby greatly simplifying the fabrication process and expanding the spectrum of possible applications of such structures. It is therefore desirbale to extend the computational method proposed in Ref. 5 to asymmetric DBRTSs with different levels of the conduction band bottom in order to analyze the possibility of increasing in such structures the dynamic conductivity and the intensity of radiative transitions, which is proportional to it.

2. STRICTLY RESONANT TUNNELING OF ELECTRONS

Let us assume that a uniform low-amplitude rf field varying in time as $E(t)=E(e^{i\omega t}+e^{-i\omega t})$ is applied to a structure with thin (δ-like) barriers. For definiteness, we assume that the electrons move from left to right, that there is no field outside the structure, and that the space charge can be ignored. Then, under the assumptions made above, the nonstationary Schrödinger equation has the form

$$i\hbar\frac{\partial\psi}{\partial t}=-\frac{\hbar^2}{2m^*}\frac{\partial^2\psi}{\partial x^2}+H(x)\psi+H(x,t)\psi, \tag{1}$$

$$H(x)=-U[\theta(x)-\theta(x-a)]-U_1\theta(x-a)+\alpha\delta(x)\psi+\gamma\alpha\delta(x-a),$$

$$H(x,t)=-qE\{x[\theta(x)-\theta(x-a)]+a\theta(x-a)\}\times(e^{i\omega t}+e^{-i\omega t}).$$

Here q and m^* are the electron charge and mass, $\alpha=\varphi_b b$; φ_b and b are the height and width of the first barrier, respectively; $\theta(x)$ is a unit step function, γ is a numerical factor characterizing the asymmetry of the barriers, and U and U_1 are the jumps of the conduction band bottom at the barriers (see Fig. 1). Three basic situations are possible here.

1. Transitions occur between the levels which lie above the conduction band bottoms of the semiconductor materials to the left and right of the structure (Fig. 1a).

2. Electrons are injected into a level lying above the conduction band bottom in the material on the left-hand side (entrance) and pass into a level lying below the conduction band bottom of this material (Fig. 1b).

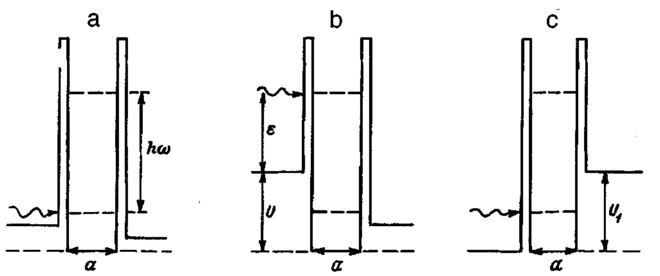

FIG. 1. Schematic representation of the band diagram of the double-barrier structures.

3. Electrons are injected into a level lying below the conduction band bottom in the material on the right-hand side (exit) and pass into a level lying above the conduction band bottom of this material (Fig. 1c).

The ground-state wave function ψ_0, normalized to one electron, is

$$\psi_0(x)=\begin{cases}\exp ik_0x+D_0\exp(-ik_0x), & x<0;\\ A_0\sin kx+B_0\cos kx, & 0<x<a;\\ C_0\exp ik_1(x-a), & x>a.\end{cases}\tag{2}$$

In the first case the correction ψ_1 to ψ_0 in the low-signal approximation is[8,9]

$$\psi_1=\psi_+(x)e^{-i(\omega_0+\omega)t}+\psi_-(x)e^{-i(\omega_0-\omega)t},$$

where $\omega_0=\varepsilon/\hbar$, ε is the energy of the electrons incident on the structure,

$$k_0=(2m^*\varepsilon/\hbar^2)^{1/2},\quad k=[2m^*(\varepsilon+U)/\hbar^2]^{1/2},$$

$$k_1=[2m^*(\varepsilon+U_1)/\hbar^2]^{1/2}$$

are the wave numbers of the electrons. The functions $\psi_\pm$ for this structure have the form

$$\psi_\pm(x)=\begin{cases}D_\pm\exp-ik_{0\pm}x, & x<0;\\ A_\pm\sin k_\pm x+B_\pm\cos k_\pm x+\chi_\pm(x), & 0<x<a;\\ C_\pm\exp ik_{1_\pm}(x-a)+P_\pm\exp ik_1(x-a), & x>a,\end{cases}\tag{3}$$

where

$$k_{0\pm}=[2m^*(\varepsilon\pm\hbar\omega)/\hbar^2]^{1/2},$$

$$k_\pm=[2m^*(\varepsilon+U\pm\hbar\omega)/\hbar^2]^{1/2},$$

$$k_{1\pm}=[2m^*(\varepsilon+U_1\pm\hbar\omega)/\hbar^2]^{1/2},\quad P_{1\pm}=\mp\frac{qEa}{\hbar\omega}\psi_0(a)$$

the functions

$$\chi_{1\pm}(x)=\mp qEx\psi_0(x)/\hbar\omega+qE\psi_0'(x)/m^*\omega^2$$

are the partial solutions of the corresponding equation for $\psi_\pm$,[8] and the system of equations for the coefficients $A_{1\pm}$, $B_{1\pm}$, $C_{1\pm}$, and $D_{1\pm}$ is found from the conditions for matching the wave function and its derivatives at the barriers at each instant of time; this system of equations is

$$\begin{pmatrix}1 & 0 & -1 & 0\\ ik_{0\pm}-y & k_\pm & 0 & 0\\ 0 & \sin k_\pm a & \cos k_\pm a & -1\\ 0 & -k_\pm\cos k_\pm a & k_\pm\sin k_\pm a & ik_{1\pm}-\gamma y\end{pmatrix}\times\begin{pmatrix}D_\pm\\ A_\pm\\ B_\pm\\ C_\pm\end{pmatrix}=\begin{pmatrix}f_1\\ f_2\\ f_3\\ f_4\end{pmatrix},\tag{4}$$

where

$$f_1=\chi_\pm(0),\quad f_2=-\chi_\pm'(0),\quad f_3=P_\pm-\chi_\pm(a),$$

$$f_4=(\gamma y-ik_1)P_\pm+\chi_\pm'(a),\quad y=2m^*\alpha/\hbar^2.$$

Equations (4) can be easily solved analytically, but the formulas obtained are quite complicated and inconvenient for investigation. However, they can be substantially simplified under certain conditions. It is well known that the transmittance in a DBRTS has a pronounced resonant character, and in symmetric structures with thin barriers and the same height of the conduction band bottom inside and outside the structure, the electron wave number, for which the electron transmittance equals 1 (resonant tunneling), is found from the solution of the transcendental equation[10]

$$\tan ka=-\frac{k\hbar^2}{\alpha m^*}=-\frac{2k}{y}.\tag{5}$$

Let us assume that the transmittance (and also the interaction probability) are maximum when

$$\tan ka=-\beta k/y.\tag{6}$$

in the case of an asymmetric structure as well. It can be shown in a manner similar to Ref. 10 that this holds when

$$\beta=(1+\gamma)/\gamma.\tag{7}$$

Under resonant tunneling conditions the coefficients of the unperturbed wave function assume the form

$$D_0=\frac{\gamma^2k_0-k_1}{\gamma^2k_0+k_1},B_0=\frac{2\gamma^2k_0}{\gamma^2k_0+k_1},\tag{8}$$

$$A_0=\frac{2\gamma^2k_0}{\gamma^2k_0+k_1}\frac{y}{k}+i\frac{2k_1k_0}{k(\gamma^2k_0+k_1)},$$

$$C_0=\frac{2\gamma k_0}{\gamma^2k_0+k_1}(-1)^{N+1}.$$

It thus follows that for such a structure the reflection coefficient vanishes for $k_1=\gamma^2k_0$.

Let a monoenergetic electron flux pass through the Nth resonant level and let the frequency of the electric field correspond to transitions to the Lth resonance level ($L=1, 2,\ldots$). For $y\gg k_\pm$ and wave number corresponding to the resonant level, the determinant of the system (4) becomes small:

$$\Delta \approx \frac{ik_\pm}{\gamma}(k_{1\pm}+\gamma^2 k_{0\pm})(-1)^{L+1}, \tag{9}$$

and for transitions to a nonresonant level $\Delta \approx k_\pm y$. For this reason, for narrow resonant levels the probability of transitions between only two levels is substantial. However, in the case of wide levels with large numbers transitions to the bottom and top levels become important. For $y \gg k_\pm$ the determinants for finding $C_\pm$ and $D_\pm$ have the form

$$\Delta_{D\pm} \approx \frac{qE}{m^*\omega^2}\frac{2\gamma^2 k_0}{\gamma^2 k_0 + k_1}(ik_1+y)(ik_{1\pm}-\gamma y) \times k_\pm(\cos k_\pm a - \cos ka), \tag{10}$$

$$\Delta_{C\pm} \approx \frac{qE}{m^*\omega^2}\frac{2\gamma^2 k_0}{\gamma^2 k_0 + k_1}(ik_1+y)(ik_{0\pm}-y)k_\pm \times (\cos k_\pm a \cos ka - 1). \tag{11}$$

Using Eq. (6), we see that, just as in a symmetric structure, we have

$$|\cos k_\pm a - \cos ka| \approx |\cos k_\pm a \cos ka - 1| \approx 2$$

for transitions in which the change in the level number is an odd number, and we have

$$|\cos k_\pm a - \cos ka| \approx |\cos k_\pm a \cos ka - 1| \approx 0$$

when the change is an even number. This well-known parity selection rule is explained by the symmetry of the wave functions and the perturbation.

For wave functions of the form (3) the low-signal dynamic conductivity at frequency ω is determined by the difference in the fluxes of electrons which have absorbed and emitted an energy quantum $\hbar\omega$ and leave the DBRTS:[8]

$$\sigma = \frac{\hbar^2\omega}{2aE^2 m^*}[k_+(|C_+|^2+|D_+|^2) - k_-(|C_-|^2+|D_-|^2)]. \tag{12}$$

For monoenergetic electrons with density n and transitions between resonant levels Eqs. (9)–(12) yield the following expression for the conductance of a DBRTS, taking into account that $ak_\pm \approx \pi L$:

$$\sigma \approx \sigma_{\text{sim}} \frac{8\gamma^6 k_0^2 k_\pm}{(\gamma^2 k_0 + k_1)^2(\gamma^2 k_{0\pm}+k_{1\pm})}, \tag{13}$$

where σ_{sim} is the resonant conductivity of a symmetric DBRTS with a constant height of the conduction band bottom inside and outside the structure with barrier strength α (Ref. 5)

$$\sigma_{\text{sim}} \approx \pm \frac{8q^2 m^* \alpha^4 n}{\pi L \hbar^6 \omega^3}[1-(-1)^{N-L}]. \tag{14}$$

Here the plus and minus signs correspond to transitions to the top and bottom resonant levels, respectively.

It is interesting to note that for $\gamma \to \infty$ and $k_0 = k$ (for the case in which the barrier is an infinite-wall type section with a localized field) $\sigma = 8\sigma_{\text{sim}}$.

The second case, in which the resonant level into which an electron passes lies below the conduction band bottom on the left-hand side of the structure, is of greatest interest for applications. In this case the ground-state wave function has the same form as in the preceding case, and the function ψ_- assumes the form

$$\psi_-(x) = \begin{cases} D_1 \exp \varkappa x, & x<0, \\ A_- \sin k_- x + B_- \cos k_- x + \chi_-(x), & 0<x<a; \\ C_- \exp ik_{1-}(x-a) + P_- \exp ik_1(x-a), & x>a, \end{cases} \tag{15}$$

where $\varkappa = [2m^*(\hbar\omega - \varepsilon)/\hbar^2]^{1/2}$. The system of equations for determining the coefficients of the perturbed wave functions has the form

$$\begin{pmatrix} 1 & 0 & -1 & 0 \\ -(\varkappa+y) & k_- & 0 & 0 \\ 0 & \sin k_- a & \cos k_- a & -1 \\ 0 & -k \cos k_- a & k_- \sin k_- a & -\gamma y + ik_{1-} \end{pmatrix} \times \begin{pmatrix} D_- \\ A_- \\ B_- \\ C_- \end{pmatrix} = \begin{pmatrix} f_1 \\ f_2 \\ f_3 \\ f_4 \end{pmatrix}. \tag{16}$$

It is interesting that the determinant of this system is small almost under the same conditions as in the preceding case:

$$\beta = \frac{(\gamma+1)y+\varkappa}{\gamma(y+\varkappa)} \approx \frac{1+\gamma}{\gamma} - \frac{\varkappa}{y}. \tag{17}$$

Here

$$\Delta \approx \frac{ik_- k_{1-}}{\gamma}(-1)^{L+1}, \tag{18}$$

$$\Delta_{C_-} \approx \frac{qE}{m^*\omega^2}\frac{2k_0}{\gamma^2 k_0 + k_1}(ik_1+\gamma y)(\varkappa y)k_- \times (1-\cos k_- a \cos ka). \tag{19}$$

We thus have, as in the preceding case, the same selection rules as for a symmetric structure, and we obtain for the conductivity

$$\sigma \approx \sigma_{\text{sim}} \frac{8\gamma^6 k_0^2 k_-}{(\gamma^2 k_0 + k_1)^2 k_{1-}}. \tag{20}$$

In the third case, in which transitions occur from a level lying below the conduction band bottom on the right-hand side to a level lying above the conduction band bottom, the ground-state wave function has the form

$$\psi_0(x) = \begin{cases} \exp ik_0 x + D_0 \exp(-ik_0 x), & x<0, \\ A_0 \sin kx + B_0 \cos kx, & 0<x<a, \\ C_0 \exp[-\varkappa(x-a)], & x>a. \end{cases} \tag{21}$$

Here $\varkappa = [2m^*(U_1 - \varepsilon)/\hbar^2]^{1/2}$. For this case the resonant conditions are

$$\beta=\frac{(\gamma+1)y+\varkappa}{\gamma y+\varkappa}\approx\frac{1+\gamma}{\gamma}-\frac{\varkappa}{\gamma^2 y},\tag{22}$$

and the coefficients D_0, A_0, B_0, and C_0 assume the values

$$D_0=1,\quad B_0=2,\quad A_0=\frac{2y}{k},\quad C_0=\frac{2}{\gamma}(-1)^{N+1}.\tag{23}$$

The correction to the ground state is described by Eq. (3). Using the system of equations (4), we obtain

$$\Delta_{D_+}\approx\frac{qE}{m^*\omega^2}2\gamma y(ik_{1+}-\gamma y)k_+(\cos k_+a-\cos ka).\tag{24}$$

$$\Delta_{C_+}\approx\frac{qE}{m^*\omega^2}2y(ik_{0+}-y)k_+(\cos k_+a\ \cos ka-1)\tag{25}$$

and, finally,

$$\sigma\approx\sigma_{\text{sim}}\frac{8\gamma^2k_+}{\gamma^2k_{0+}+k_{1+}}.\tag{26}$$

3. PASSAGE OF ELECTRONS NEAR THE CENTERS OF THE RESONANT LEVELS

In accordance with Eqs. (13), (20), and (26), the monoenergetic conductivity σ is directly proportional to the fourth power of the barrier strength α. It would seem that arbitrarily large values of the resonant conductivity of a DBRTS can be obtained by increasing α. However, as indicated in Ref. 5 , this possibility is limited by narrowing of the resonant levels of the DBRTS, which results in a higher average residence time of an electron in the well and therefore a greater role of scattering processes which destroy the coherence of the electron tunneling. Furthermore, the integrated conductivity and working current of a DBRTS depend strongly on the width of the energy levels. For this reason, to estimate the potential possibilities of asymmetric DBRTSs it is necessary to determine the width of the energy levels for the above-indicated variants of the arrangement of the levels relative to the conduction band bottom in the left- and right-hand contact layers and to determine the intensity of the transitions between arbitrary allowed electronic states with small deviations of the electron energy from the centers of the levels.

In Ref. 5 it was shown that the width Γ_M^{sim} of the Mth level (Mth energy miniband), which is determined by tunneling through identical δ barriers with the same level of the conduction band bottom inside and on both sides of the structure, is inversely proportional to α^2:

$$\Gamma_M^{\text{sim}}=\left(\frac{\hbar^2\pi M}{m^*}\right)^3\frac{1}{\alpha^2a^4}.\tag{27}$$

For a resonant wave vector k at the level M and small deviations from it $\delta k\ll k$, it follows from Eq. (6) that

$$\tan(k+\delta k)a=-\frac{\beta k}{y}-\delta ka.\tag{28}$$

Let us consider the case in which the levels between which transitions occur lie above the conduction band bottom of the semiconductor material on the right- and left-hand sides of the structure. Retaining in the determinant of the system (4) the correction with the maximum power of y, we obtain

$$\Delta(k+\delta k)\approx\left(\frac{ik}{\gamma}(k_1+\gamma^2k_0)-\gamma y^2\delta ka\right)(-1)^{M+1}.\tag{29}$$

If the half-width of a level in a nonsymmetric structure is assumed to be the distance from the resonance at which the intensity of the transitions (in the static case — the transmittance) decreases by a factor of 2 [analysis of the determinants for finding the coefficients $C_\pm$ and $D_\pm$ and the expression (29) shows that this corresponds to doubling of the squared modulus of the determinant (9)], then expressing δk in terms of $\delta\varepsilon$, we obtain from Eq. (29) the expression

$$\Gamma_M=\Gamma_M^{\text{sim}}\frac{\gamma^2k_0a+k_1a}{2\pi M\gamma^2}.\tag{30}$$

Now let the electrons pass at a distance $\delta\varepsilon$ from the resonance level $\mathcal{E}_N$ in a weak electric field with frequency $\omega=\omega_{NL}+\delta\omega$, where $\omega_{NL}=(\mathcal{E}_N-\mathcal{E}_L)/\hbar$. Then, from the fact that for small devaiations from resonance mainly the determinant of the system (4) or (16) changes and the determinants for finding the coefficients of the wave function remain practically unchanged, we can write for the conductivity of a monoenergetic electron flux

$$\begin{aligned}\sigma(\mathcal{E}_N+\delta\varepsilon,\omega_{NL}+\delta\omega)\approx{}&\sigma(\mathcal{E}_N,\omega_{NL})\\&\times\left|\frac{\Delta(\mathcal{E}_N)}{\Delta(\mathcal{E}_N+\delta\varepsilon)}\,\frac{\Delta(\mathcal{E}_L)}{\Delta(\mathcal{E}_L+\delta\varepsilon-\hbar\,\delta\omega)}\right|^2\\&=\sigma(\mathcal{E}_N,\omega_{NL})/F_{NL},\end{aligned}\tag{31}$$

where

$$\begin{aligned}F_{NL}=1&+\frac{\gamma^4y^4a^2}{(k_1+\gamma^2k_0)^2}\left(\frac{\delta\varepsilon}{2\mathcal{E}_N}\right)^2\\&+\frac{\gamma^4y^4a^2}{(k_{1\pm}+\gamma^2k_{0\pm})^2}\left(\frac{\delta\varepsilon-\hbar\,\delta\omega}{2\mathcal{E}_L}\right)^2\\&+\frac{\gamma^8y^8a^4}{(k_1+\gamma^2k_0)^2(k_{1\pm}+\gamma^2k_{0\pm})^2}\left(\frac{\delta\varepsilon}{2\mathcal{E}_N}\right)^2\left(\frac{\delta\varepsilon-\hbar\,\delta\omega}{2\mathcal{E}_L}\right)^2.\end{aligned}\tag{32}$$

For the case in which the level to which transitions occur lies below the conduction band bottom of the semiconductor on the left–hand side of the structure we obtain, just as for Eq. (30), the following expression from the expressions (16) and (18):

$$\Gamma_M=\Gamma_M^{\text{sim}}\frac{k_{1-}a}{2\pi M\gamma^2}.\tag{33}$$

We see that, as expected, for the same barrier strength ($\gamma=1$) and in the absence of an offset of the conduction bands at the second barrier ($U=U_1$) the width of the level is half that in an analogous symmetric structure.

In the third case, in which the level along which electrons are injected into the structure lies below the conduction band bottom of the material on the right–hand side, we have

$$\Gamma_M=\Gamma_M^{\mathrm{sim}}\frac{k_0 a}{2\pi M}. \tag{34}$$

Here, for nonresonant conductivity in all three cases Eq. (31) reduces to

$$\sigma(\mathcal{E}_N+\delta\varepsilon,\omega_{NL}+\delta\omega)\approx\frac{\sigma(\mathcal{E}_N,\omega_{NL})}{1+4\left(\frac{\delta\varepsilon}{\Gamma_N}\right)^2+4\left(\frac{\delta\varepsilon-\hbar\,\delta\omega}{\Gamma_L}\right)^2+16\left(\frac{\delta\varepsilon}{\Gamma_N}\right)^2\left(\frac{\delta\varepsilon-\hbar\,\delta\omega}{\Gamma_L}\right)^2}. \tag{35}$$

The integrated conductivity G is of greatest interest for device applications. Using Eq. (35) it can be defined as

$$G(\mathcal{E}_N,\omega)=S\int_0^{\infty}\frac{f(\varepsilon)}{a}\sigma[\mathcal{E}_N+(\varepsilon-\mathcal{E}_N),\omega]d\varepsilon, \tag{36}$$

where S is the cross-sectional area of the DBRTS, and $f(\varepsilon)$ is the electron distribution function over the ''transverse'' (pependicular to the barriers) energy ε in the flux incident on the structure. If the levels are sufficiently narrow, if the electron density does not vary strongly over their width, and if the bottom level is much narrower than the top level, then

$$G(\mathcal{E}_N,\omega)\approx S\frac{f(\mathcal{E}_N)}{a}\sigma(\mathcal{E}_N,\omega)\Gamma_L=\zeta\sigma_{NL}\Gamma_L. \tag{37}$$

It is interesting to note that when transitions occur from a level lying above the conduction band bottom to a level lying below the conduction band bottom on the left-hand side (Fig. 1b), it follows from Eq. (20) that as $k_-\to 0$ (the bottom level approaches the conduction band bottom on the right) the low-signal monoenergetic conductivity increases without bound. This can be attributed to an unbounded increase of the one-dimensional electronic density of states near a conduction band bottom. At the same time, the integrated conductivity

$$G\approx\zeta\sigma_{NL}\Gamma_L=\zeta\Gamma_L^{\mathrm{sim}}\sigma_{\mathrm{sim}}\frac{4\gamma^2k_0^2}{(\gamma^2k_0+k_1)^2} \tag{38}$$

does not depend on k_{1-} at all. It is also interesting to note that in this case the integrated conductivity increases monotonically as $\gamma\to\infty$ and approaches a finite value (four times greater than that for an analogous symmetric structure), while $\sigma_{NL}\to\infty$. For $k_1=\gamma^2k_0$, i.e. when the reflection coefficient of such a structure equals zero, the integrated conductivity of the structure equals the conductance of an analogous symmetric structure.

4. CONCLUSIONS

We obtained the following results:

1. The wave functions of electrons which undergo a resonant interaction with an rf electric field in double-barrier structures with thin, high asymmetric barriers and arbitrary height of the conduction band bottom inside and outside the structure were found.

2. The conditions under which the static transmittance of such structures is maximum (equals 1) were found.

3. Analytical expressions were obtained for the monoenergetic, low-signal, resonance conductivity in asymmetric DBRTSs.

4. Analytical expressions for the width of the resonant levels of an asymmetric DBRTS and the monoenergetic conductivity of electrons tunneling through a DBRTS near the centers of the resonances were found for a number of structures.

5. It was shown that the resonant conductivity of a structure with a thick exit barrier (i.e., a structure of the type barrier —<for a number of structures>—<infinite wall>), which is proportional to the intensity of the quantum transitions between the centers of the levels, is eight times higher than the conductance of the analogous symmetric structure.

6. It was shown for a structure in which the electrons pass into a level lying below the conduction band bottom of the semiconductor material on the left-hand side of the structure that the monoenergetic conductivity approaches $-\infty$ when the conduction band bottom of the material on the right-hand side of the structure approaches the level into which the transitions occur. At the same time, the integrated conductivity remains finite because of the decrease in the width of the bottom level.

This work is supported, in part, by the Russian Fund for Fundamental Research (Project No. 94-02-04449) and the Scientific Council as part of the program ''Physics of solid-state nanostructures'' (Project No. 1-050).

[1] J. Faist, F. Capasso, D. L. Sivco, C. Sirtori, A. L. Hutchinson, and A. Y. Cho, Science **264**, 553 (1994).

[2] J. Faist, F. Capasso, C. Sirtori, D. L. Sivco, J. N. Baillargeon, A. L. Hutchinson, S.-N. G. Chy, and A. Y. Cho, Appl. Phys. Lett. **68**, 3680 (1996).

[3] A. Kastalsky, V. J. Goldman, and J. H. Abeles, Appl. Phys. Lett. **59**, 2636 (1991).

[4] E. I. Golant, A. B. Pashkovskiĭ, and A. S. Tager, Pis'ma Zh. Tekh. Fiz. **20**, 74 (1994) [Tech. Phys. Lett. **20**, 886 (1994)].

[5] I. V. Belyaeva, E. I. Golant, and A. B. Pashkovskiĭ, Fiz. Tekh. Poluprovodn. **31**, 201 (1997) [Semiconductors **31**, 103 (1997)].

[6] S. Bending, A. Peck, J. Lee, and K. V. Klitzing, Solid State Electron. **32**, 1161 (1989).

[7] P. England, J. R. Hayes, E. Colas, and M. Helm, Solid State Electron. **32**, 1213 (1989).

[8] A. B. Pashkovskiĭ, Fiz. Tekh. Poluprovodn. **29**, 1712 (1995) [Semiconductors **29**, 893 (1995)].

[9] E. I. Golant and A. B. Pashkovskiĭ, Fiz. Tekh. Poluprovodn. **28**, 954 (1994) [Semiconductors **28**, 553 (1994)].

[10] V. M. Galitskiĭ, B. M. Karnakov, and V. I. Kogan, *Problems in Quantum Mechanics* [in Russian], Nauka, Moscow (1981).

Translated by M. E. Alferieff

Investigation of the heteroexpitaxial structures {*p*-3*C*/*n*-6*H*}-SiC

A. A. Lebedev, N. S. Savkina, A. S. Tregubova, and M. P. Shcheglov

A. F. Ioffe Physicotechnical Institute, Russian Academy of Sciences, 194021 St. Petersburg, Russia

(Submitted December 16, 1996; accepted for publication February 13, 1997)
Fiz. Tekh. Poluprovodn. **31**, 1083–1086 (September 1997)

The parameters of the epitaxial structures {3*C*/6*H*}-SiC have been investigated. The heteroepitaxial growth was conducted by sublimation epitaxy in an open system. The presence of the 3*C* polytype was confirmed by x–ray investigations. The capacitance–voltage and current–voltage characteristics and the electroluminescence spectra of the *p*–*n* structures were investigated. It was found that a thin, slightly doped, defective *p*-6*H*-SiC layer was formed between *p*-3*C*-SiC and *n*-6*H*-SiC in the heteropolytypic structures; this layer detetmined the electrical properties of the diode structures. © *1997 American Institute of Physics.* [S1063-7826(97)01309-4]

1. INTRODUCTION

The existence of a large number of SiC polytypes with the same chemical composition but substantially different electrical properties make silicon carbide a promising material for constructing different heterostructures. It was shown in Ref. 1 that by varying the Si/C ratio in the growth zone or adding definite impurities it is possible to obtain by sublimation epitaxy heteropolytypes of 3*C*–SiC or 4*H*–SiC films deposited on 6*H*-SiC substrates grown by the Lely method. In Ref. 2 a heteroepitaxial structure {6*H/*3*C*}-SiC was grown in a molecular-beam epitaxy system with a gas–phase source. However, the results of the investigations of the properties of the heterojunctions were not presented in Refs. 1 and 2.

2. SAMPLES

In our case, heteroepitaxial growth of *p*-type 3*C*-SiC films was conducted by the method of sublimation epitaxy (SE) on a 6*H*–SiC substrate, obtained by the Lely method, with a SE grown, slightly-doped $[(2-3)\times 10^{16}\ \mathrm{cm}^{-3}]$ *n*-6*H*–SiC layer. The *p*-3*C*-SiC layer, which was 2–5 μm thick, was doped with aluminum during the growth process. The carrier density in the substrate material was $N_d-N_a \approx 10^{18}\ \mathrm{cm}^{-3}$ and the substrates possessed (0001)Si orientation.

3. X-RAY INVESTIGATIONS

The layers grown consisted of 3*C* silicon carbide, as confirmed by x–ray diffractometry. Rocking curves with half–widths of 10 and 24″, corresponding to the reflections (0006)6*H* and (111)3*C* in Cu$K\alpha$ radiation, were obtained. The structural perfection of the layers was assessed according to topograms obtained by x-ray topography methods with different measurement geometries. Figure 1 shows an x-ray topogram of the heteroepitaxial structure {3*C*/6*H*}-SiC. It is evident from this topogram that the growth of 3*C* silicon carbide is of an island character; i.e., growth does not start simultaneously on the entire surface of the substrate. The total area of the islands in this case was equal to 60–70% of the substrate area ($\sim$1 cm^2). Our experiments showed that as the thickness of the 3*C*-SiC layer increases, individual islands expand over the substrate and their boundaries meet when the thicknesses of the layers are $\geqslant 3-5\ \mu$m. In addition, the x–ray investigations showed structural nonuniformity in the distribution of defects in the epitaxial layer. This can lead to a difference in the electrophysical parameters of the *p*–*n* structures formed on the basis of these epitaxial layers.

4. INVESTIGATION OF THE ELECTRICAL PARAMETERS OF THE STRUCTURES

Diode structures were fabricated by the standard technology, including establishment of contacts with *n*– and *p*–type material, masking with aluminum, and plasma-chemical etching. The diodes were 100–500 μm in diameter. Some structures exhibited capacitance–voltage ($C-U$) and current-voltage ($J-U$) characteristics, which are standard for structures based on 6*H*–SiC obtained by SE but with a substantial ohmic resistance. Extraordinary diodes were also observed. The $C-U$ characteristics of these diodes were also linear in $C^{-2}-U$ coordinates but they exhibited a kink at $U\approx 0$ and the cutoff voltage was $\sim$1 V (Fig. 2). The carrier density N_d-N_a, which was determined from this characteristic in the region after the kink was 3–5 times lower than in the region before the kink. The latter value was close to the value of N_d-N_a, which was determined from the $C-U$ characteristic of ordinary diodes, and to the value of N_d-N_a in the *n*-type epitaxial layer before the 3*C*-SiC film was grown.

The current–voltage characteristics[1)] of the extraordinary diodes exhibited the standard exponential form $J=J_0\exp(qU/\beta kT)$ with β of the order of $\beta_1\sim 1.7$ in the low–current region ($J\sim 10^{-9}$ A) and $\beta_2\sim 1.7$ in the high–current region ($J\sim 10^{-5}$ A) (Fig. 3). As the temperature increased, β_2 changed from 1.73 to 1.56.

For forward currents $>10^{-3}$ A an appreciable electroluminescence with a spectrum that was different for both types of samples appeared. In the case of the ordinary diodes the electroluminescence spectrum consisted of a wide band characteristic of SE diodes with a maximum in the yellow–green region of the spectrum. A peak with a maximum near $\sim$450 nm, due to carrier recombination on an Al acceptor level,[3]

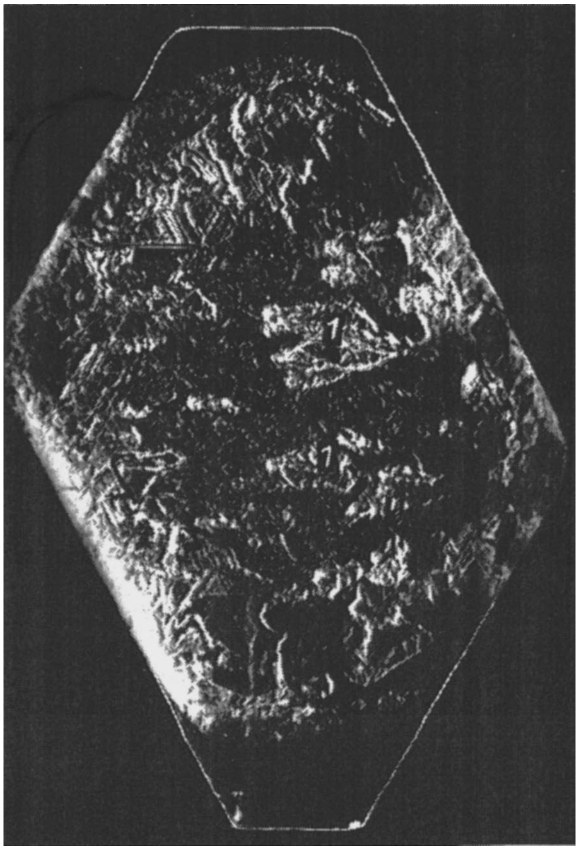

FIG. 1. X-Ray topogram of the {3*C*/6*H*}-SiC sample with a nonuniform distribution of defects in the layer. Lang method, Mo$K\alpha$ radiation. *1* — 3*C*-SiC islands formed at the initial stage of growth. Magnification 8.5^x.

and a maximum near ~425 nm, due to recombination of a free exciton[4] (Fig. 4), predominated in the electroluminescence spectrum of the extraordinary diodes. The electroluminescence spectra of both types of diodes did not contain any maxima which, according to published data, could be attributed to carrier recombination in 3*C*–SiC. Breakdown of the diodes first appeared at voltages $U_{\mathrm{br}}=20-30$ V (which was much less than the value of U_{br} corresponding to densities N_d-N_a determined from the $C-U$ characteristics) and exhibited a sharp and irreversible character.

5. DISCUSSION

The experimental results obtained can be explained from our point of view as follows. A lightly doped *p*-6*H*-SiC layer with a high density of defects formed over the entire area of the substrate between *n*-6*H*-SiC and *p*-3*C*-SiC. In the case of the ordinary diodes, located outside the islands of growth which formed at the initial stage of epitaxy, this defect region was located in the volume of the grown epitaxial layer and increased the ohmic resistance of the diode. In the process, *p*–6*H*–SiC formed directly on *n*–6*H*–SiC and the characteristics of the ordinary diodes are virtually identical to the standard characteristics of *p*–*n* structures based on 6*H*–SiC grown by SE.

In the case of the extraordinary diodes the buffer layer with defects grew directly on the *n*-6*H*-SiC and coincided with the metallurgical boundary of the *p*–*n* junction. When the extraordinary diodes were engaged in the forward direction, electron injection into the defective layer occurred. This resulted in carrier recombination on aluminum acceptor levels and the appearance of blue electroluminescence (as a rule, the background Al concentration in the SE layers is low and such electroluminescence is not observed in pn structures of this type). Because the high compensation in this layer, the Fermi level in it was located close to the center of the band. Since in the *n*–region the Fermi level lies at a depth of 0.2–0.3 eV at room temperature, the contact potential difference of this *p*–*n* structure, which is defined as the difference in the positions of the Fermi levels in the *n*– and *p*–regions of the diode, should equal ~1 V, as was observed experimentally. The high density of defects in this layer also resulted in low breakdown voltages in these structures.

The thickness of the buffer layer evidently corresponds to the thickness of the space charge layer for which a kink was observed in $C-U$ characteristics of the extraordinary

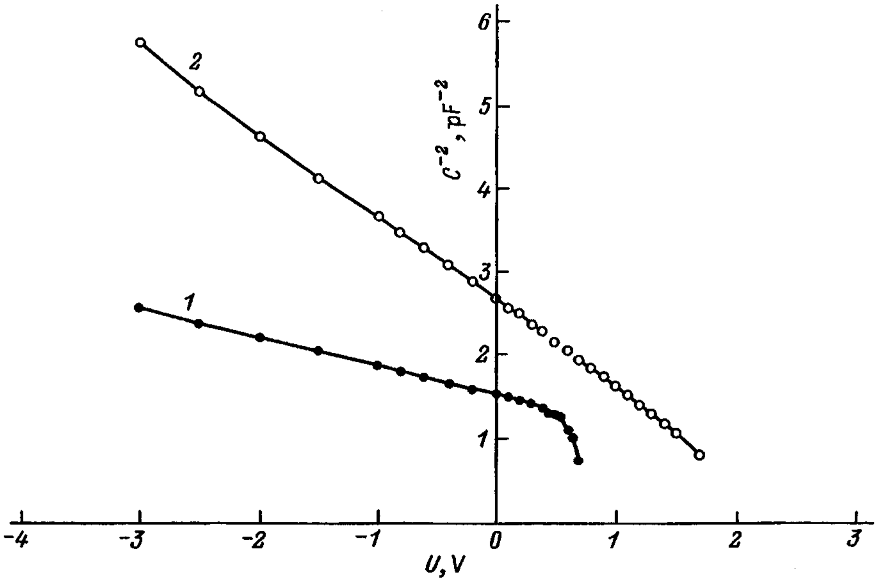

FIG. 2. Capacitance–voltage characteristics of extraordinary (*1*) and ordinary (*2*) diodes at room temperature.

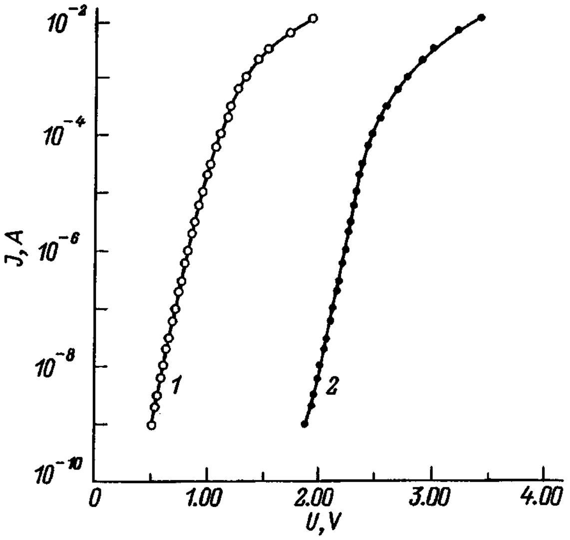

FIG. 3. Current–voltage characteristics of the extraordinary (*1*) and ordinary (*2*) diodes at room temperature.

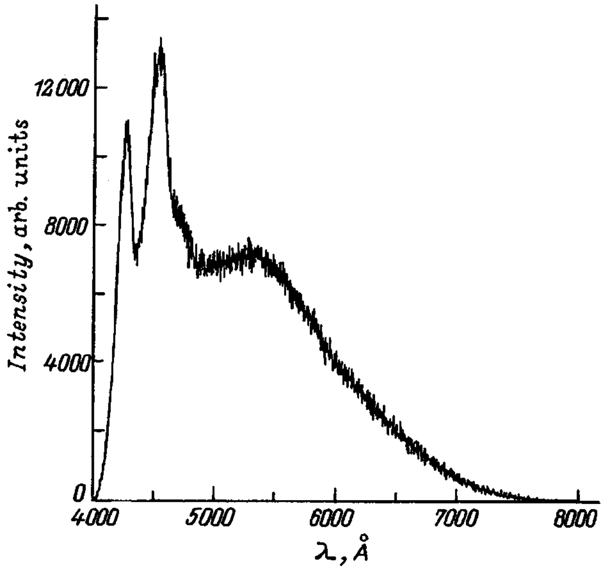

FIG. 4. Electroluminescence spectrum of an extraordinary diode with a forward current density of 40 A/cm^2.

diodes, i.e., several tens of microns. It can therefore be concluded that in the heteropolytypic structures a thin π-6*H*-SiC layer with defects, which determined the electrical properties of the diode structures, formed between *p*-3*C*-SiC and *n*-6*H*-SiC.

In Ref. 5 it was shown that changing the Si/C ratio in the growth cell and increasing the rate of growth in heteroepitaxy of *n*-3*C*-SiC on *n*-6*H*-SiC increases the degree of structural perfection of the transitional region between the 6*H*-SiC substrate and the 3*C*-Sic layer. Therefore, optimization of the technological growth conditions could make it possible to decrease the thickness of the region with defects and to obtain diodes whose electrical properties are determined by the p^+-3*C*/*n*-6*H* heterojunction.

This work was supported by the University of Arizona (USA).

1) The current–voltage investigations of these structures were performed by A. M. Strel'chuk.

---

[1] Yu. A. Vodakov, G. A. Lomakina, and E. N. Mokhina, Fiz. Tekh. Poluprovodn. **24**, 1377 (1982) [Sov. Phys. Semicond. **24**, 883 (1982)].
[2] E. L. Kern, D. W. Hamill, H. W. Dum, and U. D. Shuts, Mater. Res. Bull. **4**, 25 (1989).
[3] W. von Munch and W. Kukzinder, Solid–State Electron. **21**, 1129 (1978).
[4] M. Ikeda, T. Haykava, S. Ymagiva, H. Matsunami, and T. Tanaka, J. Appl. Phys. **50**, 8215 (1979).
[5] A. N. Andreev, A. S. Tregubova, M. P. Scheglov, and V. E. Chelnokov, in *Abstracts E-MRS 1996 Spring Conference*, Strasburg (1996), p. A-5.

Translated by M. E. Alferieff

Radiative recombination rate in quantum-well structures in the model without k-selection

A. A. Afonenko, I. S. Manak, and V. A. Shevtsov

Belarus State University, 220080 Minsk, Belarus

V. K. Kononenko

B. I. Stepanov Institute of Physics, Academy of Sciences of Belarus, 220072 Minsk, Belarus

(Submitted March 20, 1996; accepted for publication February 10, 1997)
Fiz. Tekh. Poluprovodn. **31**, 1087–1091 (September 1997)

The influence of size quantization on the probability of optical transitions without an electron wave-vector selection rule is investigated. It is shown that the inversion current is essentially independent of the thickness of the quantum-well layer in the approximation of a constant injection efficiency. Various approximations for calculating the rate of spontaneous recombination are discussed. © *1997 American Institute of Physics.* [S1063-7826(97)03108-6]

A model for optical transitions without an electron wave-vector selection rule (**k**-selection) has been developed to describe the properties of injection lasers with a doped active region.[1] The model takes into account the bimolecular nature of the recombination process and reflects the influence of imperfections of real laser structures on the emission spectra.[2] It is also used to analyze the threshold and spectral characteristics of quantum-well heterolasers.[3–6]

However, the calculation of the threshold and inversion current in quantum-well lasers using the probability of optical transitions without **k**-selection for bulk semiconductors tends to impart excessive values to these quantities. The rate of spontaneous radiative recombination in a quantum-well layer of thickness d in a model without **k**-selection is calculated in this case as

$$R_{sp}=A\frac{n_1p_1}{d^2}, \tag{1}$$

where A is a constant, and n_1 and p_1 are the surface densities of electrons and holes, respectively.

For given n_1 and p_1 Eq. (1) states that the recombination rate increases as the layer thickness is decreased, in inverse proportion to d^2. This result differs significantly from the behavior of the recombination rate calculated for optical transitions with **k**-selection, where R_{sp} is inversely proportional to d (Ref. 7). The disparity in the predictions of these models is a consequence of the fact that the recombination rate (1) has been derived using the transition probability for a bulk semiconductor,[1] whereas the density of nonequilibrium carriers is calculated as for a quantum well. In this article we analyze the influence of size quantization on the probability of optical transitions without **k**-selection and discuss techniques for calculating the spectra of spontaneous recombination in quantum wells.

By definition, the number of spontaneous transitions per unit time in unit volume within a unit energy interval is calculated as

$$r_{sp}(\hbar\omega)=\frac{1}{V}\sum_i\sum_f\omega_{fi}f_{ei}f_{hf}\delta(E_i-E_f-\hbar\omega). \tag{2}$$

Here the summation is carried out over all initial states in the conduction band (i) and all final states in the valence band (f), and the quantity ω_{fi} gives the transition probability between states. The Fermi-Dirac functions for electrons f_{ei} and holes f_{hf} take the populating of states into account, and V is the volume of the quantum-well layer. The energies of the initial and final states are E_i and E_f, respectively; the δ-function eliminates all transitions except those with energy $\hbar\omega$ from the summation. The probability of direct optical transitions of an electron from the conduction band to the valence band is $\omega_{n_i\mathbf{k}_in_c\mathbf{k}_c}=A_{cv}\delta_{\mathbf{k}_c\mathbf{k}_v}\delta_{n_cn_v}$, where A_{cv} is the Einstein coefficient for band-band transitions, and n_c, $\mathbf{k}_c$ and n_v, $\mathbf{k}_v$ enumerate the subbands and electron wave vectors in the conduction band and in the valence band, respectively.

In quantum-well layers it is often convenient to use the ''surface'' rate of spontaneous recombination (the number of transitions per unit time on unit area and in unit energy interval) r_{sp1}. Here it is assumed that

$$Sr_{sp1}(\hbar\omega)\equiv Vr_{sp}(\hbar\omega), \tag{3}$$

where $S=V/d$ is the area of the quantum-well layer.

The threshold current of the laser can be estimated from the inversion current.[2,7] The inversion current is determined by the degree of excitation of the quantum well when the difference in the Fermi quasilevels for electrons and holes $\Delta F=F_e-F_h$ is equal to the minimum energy of emitted photons $\hbar\omega_{\min}$. Assuming that the injection efficiency and the quantum yield of luminescence are close to unity, we obtain the expression for the inversion current density

$$j_{inv}=edR_{sp}|_{\Delta F=\hbar\omega_{\min}}. \tag{4}$$

We calculate $r_{sp}(\hbar\omega)$ for a doped quantum-well layer. We assume that the wave functions of the states of one of the bands are unperturbed and have the form

$$\psi_{n\mathbf{k}_c}=\sqrt{\frac{2}{V}}\exp[i(k_xx+k_yy)]\sin\left(\frac{\pi nz}{d}+\frac{\pi n}{2}\right),$$

where k_x and k_y are the projections of the wave vector $\mathbf{k}_c$ in the xy plane, and z is the coordinate in the direction of the normal to the quantum-well layer. The approximation of infinite potential barriers is used here for simplicity. The states of the other band ψ_l are localized near impurities.[1,8] The electron transition probability in the quantum well from levels of the *nth* subband to the impurity ground level differs from A_{cv} by the square of the overlap integral of the wave functions:

$$\omega_{lm\mathbf{k}_c}=A_{cv}\left\langle\left|\int_V \psi_l^* \psi_{n\mathbf{k}_c} dV\right|^2\right\rangle, \tag{5}$$

where the averaging signified by the angle brackets $\langle \cdots \rangle$ is carried out over all possible impurity sites in the quantum-well layer $-d/2 \leqslant z_0 \leqslant d/2$. The integration in (5) is carried out over the volume of the quantum-well layer *V*.

We consider two cases below.

1. $d \gg a_0$, where a_0 is the effective Bohr radius of the impurity. In this case we can ignore size quantization in the direction perpendicular to the plane of the layer (*z*-direction) for impurity-localized particles, and the wave function of the state of an impurity with coordinate r_0 has the form

$$\psi_l=\frac{1}{\sqrt{\pi a_0^3}}\exp\left(-\frac{|\mathbf{r}-\mathbf{r}_0|}{a_0}\right). \tag{6}$$

Since the main contribution to the integral (5) is from the immediate region of the impurity, the integration can be extended to infinite volume. We then have

$$\omega_{ln\mathbf{k}_c}(z_0)\approx A_{cv}\frac{64\pi a_0^3}{V[1+a_0^2(k_c^2+\pi^2 n^2/d^2)]^4} \times 2\sin^2\left(\frac{\pi n z_0}{d}+\frac{\pi n}{2}\right). \tag{7}$$

After averaging over z_0 the result acquires the form

$$\omega_{ln\mathbf{k}_c}(z_0)\approx A_{cv}\frac{64\pi a_0^3}{V[1+a_0^2(k_c^2+\pi^2 n^2/d^2)]^4}. \tag{8}$$

This equation is analogous to the transition probability obtained in the plane-wave approximation with *z*-component of the electron wave vector $k_z=\pi n/d$ (Refs. 1 and 8).

Since the transition probability obtained here depends only on the energy of carriers in the subbands $E_c=E_{c0}+\hbar^2(k_c^2+\pi^2 n^2/d^2)/2m_c$, where m_c is the effective electron mass, the transition can be easily made in Eq. (2) from summation over states to integration with respect to energy. Here, according to our analysis, the two-dimensional density of states

$$\rho_{c1}(E)=\frac{m_c}{\pi\hbar^2}\sum_n H(E-E_{c0}-E_{cn}) \tag{9}$$

must be used for the conduction band, whereas for the impurity band, which overlaps the valence band, the density $\rho_v(E)$ must be used as in the case of a semiconductor with bulk properties, because the presence of potential barriers is assumed *a priori* not to influence the hole energy spectrum. Here *E* is the energy of the levels involved in transitions, E_{c0} is the bottom of the conduction band, E_{cn} are the values of the energies of the subband edges numbered $n=1, 2, \ldots$ in the conduction band, and *H* is the Heaviside unit step function [$H(x)=1$ at $x \geqslant 0$, and $H(x)=0$ at $x<0$]. If the tail of the density of states is disregarded, $\rho_v(E)$ can be assumed to be equal to the ordinary volume density

$$\rho_v(E)=\frac{(2m_v)^{3/2}}{2\pi^2\hbar^3}(E_{v0}-E)^{1/2}, \tag{10}$$

where m_v is the effective hole mass for the density of states E_{v0} representing the top of the valence band.

Disregarding the dependence of $\omega_{ln\mathbf{k}_c}$ on the electron wave vector in (8) and restricting it to $n=1$, we write the final expression for the spontaneous transition rates in the form

$$r_{sp}(\hbar\omega)=\frac{A_0}{d}\int_{E_{c0}+E_{c1}}^{E_{v0}+\hbar\omega}\rho_{c1}(E)\rho_v(E-\hbar\omega) \times f_e(E)f_h(E-\hbar\omega)dE. \tag{11}$$

Here $A_0=(1/2)64\pi a_0^3 A_{cv}/(1+\pi^2 a_0^2/d^2)^4$ is the optical transition probability without **k**-selection, and f_e and f_h are the corresponding electron and hole distribution functions. The factor 1/2 appears as a result of taking into account the conservation of electron spin in transitions.

The total recombination rate is obtained by integrating (11) over all possible emitted-photon energies:

$$R_{sp}=A_0\frac{n_1}{d}p, \tag{12}$$

where *p* is the volume density of holes in the quantum-well layer. The optical transition probability without **k**-selection A_0, which coincides with the result for bulk semiconductors[1,8] in the limiting case $d\rightarrow\infty$, begins to drop considerably with decreasing width of the quantum well for $d\simeq 10a_0$.

2. $d<10a_0$. With a further decrease in the width of the quantum well, we need to take into account quantum limitations on impurity-localized carriers in the direction perpendicular to the plane of the layer. In the elementary valence band model we can restrict the discussion strictly to heavy holes.[9] The wave function of the impurity ground state can then be written in the form

$$\psi_l=\frac{1}{\sqrt{N(a,d)}}\exp\left(-\frac{|\mathbf{r}-\mathbf{r}_0|}{a}\right)\cos\left(\frac{\pi z}{d}\right), \tag{13}$$

where the normalization constant is

$$N(a,d) =\frac{\pi a^3}{2}\left\{1+\frac{\cos(2\pi z_0/d)}{[(\pi a/d)^2+1]^2}+\frac{\exp(-d/a)}{1+(d/\pi a)^2} \times\left[\frac{z_0}{a}\sinh\left(\frac{2z_0}{a}\right)\left(1+\frac{d}{2a}+\frac{1}{(\pi a/d)^2+1}\right)\cosh\left(\frac{2z_0}{a}\right)\right]\right\}. \tag{14}$$

Here the characteristic length *a* is evaluated by a variational technique with respect to the state energy.[9] In the approximation $d\rightarrow 0$ this procedure yields $a\rightarrow a_0/2$. The value of *a* rapidly approaches a_0 as the width of the quantum well is

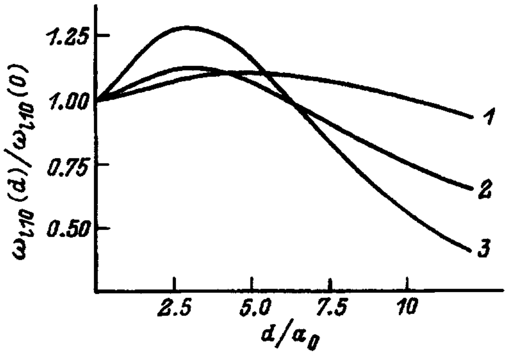

FIG. 1. Normalized transition probability between ground levels of the subbands versus width of the quantum well for various positions of the impurity center. *1* — $z_0=0$; *2* — $z_0=d/4$; *3* — $z_0=d/2$.

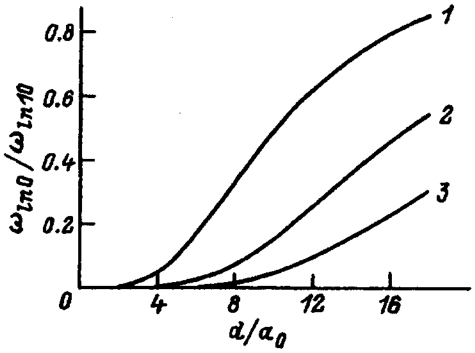

FIG. 3. Ratio of the probability for the transition from conduction subbands with different indices to the impurity ground level to the transition probability between ground levels versus width of the quantum well. *1* — $n=2$; *2* — $n=3$; *3* — $n=4$.

increased: for $d=a_0$ the localization parameter of carriers at impurities situated in the center of the well is $a\approx 0.8a_0$. The approximation (13) ignores the penetration of the wave functions into the barrier layers for potential barriers of finite height, so that a tends to increase. From now on, therefore, we let $a\approx a_0$.

The integration of (5) is elementary in the two-dimensional limit $d=0$:

$$\omega_{ln\mathbf{k}_c}=A_{cv}\frac{8\pi a^2}{S(1+a^2k_c^2)^3}\delta_{n1}. \qquad (15)$$

By analogy with the case of a wide quantum well we assume that to calculate the recombination rate it is sufficient to know the value of (5) for a zero electron wave vector. The transition probability between ground levels of the subbands for arbitrary d can then be found directly by means of (14):

$$\omega_{l10}(d)=A_{cv}\frac{2}{V}\left\langle\frac{N^2(2a,d)}{N(a,d)}\right\rangle, \qquad (16)$$

where $a\approx a_0$. For narrow quantum wells the normalization constant depends linearly on the width, $N(a,d)\approx\pi a^2 d/4$.

Figure 1 shows the transition probability as a function of the width of the quantum well for various positions of the impurity center. As the width of the quantum well is increased, the transition probability averaged over the impurity sites z_0 (Fig. 2) asymptotically approaches the bulk-semiconductor result (8).

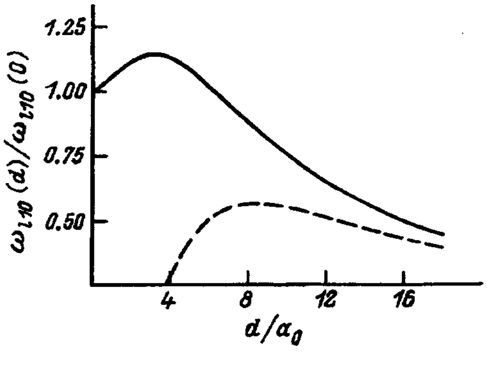

FIG. 2. Normalized transition probability, averaged over the impurity sites z_0, versus width of the quantum well. The dashed curve represents the ratio of the transition probability for the bulk-semiconductor case (8) to the value $\omega_{l10}(0)$ in the two-dimensional limit.

The contribution of transitions with a change in the subband indices to the recombination rate can be estimated from the probability (5) of electron transitions to the impurity ground level. It is evident from Fig. 3 that most rapid growth of the contribution of transitions with increasing width d is exhibited by those with a unit change of the subband index. Assuming that a similar dependence exists for transitions to the next subbands in the valence band, we can then assume that the selection rule for the subband index in radiative transitions begins to be violated when d exceeds a_0 by an order of magnitude or more.

In accordance with the adopted approximation for the wave functions (13), the distribution of carriers in the impurity band must be described by the two-dimensional density of states. For the calculations we use the unperturbed density of states

$$\rho_{v1}(E)=\frac{m_v}{\pi\hbar^2}\sum_n H(E_{v0}-E_{vn}-E), \qquad (17)$$

where E_{vn} are the initial levels of the subbands. Neglecting the weak dependence of the transition probability on d and introducing the ‘‘surface’’ probability of optical transitions without **k**-selection $A_1=(1/2)8\pi a_0^2A_{cv}$, we obtain the final expression for the rate of spontaneous transitions preserving the subband index:

$$r_{sp1}(\hbar\omega)=A_1\frac{m_c m_v}{\pi^2\hbar^4}\sum_n\int_{E_{c0}+E_{cn}}^{E_{v0}-E_{vn}+\hbar\omega}H(\hbar\omega-E_{c0}-E_{cn}+E_{v0}-E_{vn})f_e(E)f_h(E-\hbar\omega)dE. \qquad (18)$$

The total recombination rate is

$$R_{sp}=A_1\sum_n\frac{n_{1n}p_{1n}}{d}, \qquad (19)$$

where n_{1n} and p_{1n} are the surface densities of electrons and holes in the nth subbands. The expression for the recombi-

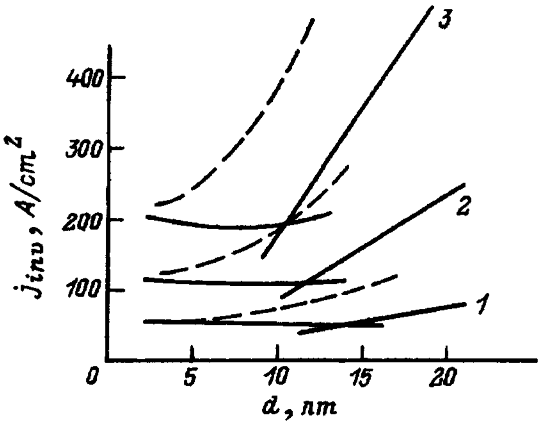

FIG. 4. Inversion current density j_{inv} versus width of the quantum well d in the model without satisfaction of a wave-vector selection rule, calculated for wide quantum wells in the approximation of the volume density of states of the valence band and for narrow quantum wells in the approximation of the two-dimensional density of states for transitions preserving subband indices (solid cures) and without the subband index-selection rule (dashed curves) at various temperatures in the system $Al_{0.3}Ga_{0.7}As$–GaAs–$Al_{0.3}Ga_{0.7}As$, $m_c = 0.07 m_e$, $m_v = 0.40 m_e$, $A_{cv} = 1.5 \times 10^9$ s^{-1}, $a_0 = 17$ Å. *1* — $T = 200$ Å; *2* — $T = 300$ Å; *3* — $T = 400$ Å.

nation rate is simplified for narrow quantum wells, in which the populations of all subbands except the first can be disregarded:

$$R_{sp} = A_1 \frac{n_1 p_1}{d}. \tag{20}$$

For constant surface carrier densities, therefore, the recombination rate is inversely proportional to the thickness of the quantum-well layer.

An expression of the same form as (20) is obtained when the transition probabilities between arbitrary subbands are assumed to be identical; this is applicable to wide quantum wells. However, it follows from the dependence of the transition probability on the width of the quantum well (see Fig. 2) that the use of a constant coefficient A_1 in this case makes the recombination rate too high.

The results of calculations of the inversion current according to Eqs. (12), (19), and (20) are shown in Fig. 4. The use of the two-dimensional density-of-states approximation and the model of subband-index-preserving transitions shows that the inversion current is essentially independent of d for narrow quantum wells. The slight drop in the inversion current, according to (19), is because the number of subbands in the valence band increases more rapidly with d than in the conduction band, and only transitions that preserve the subband indices are taken into account. With a further increase in d, transitions with a change in the subband indices must also be included. In this case the maximum permissible value of the inversion current, which is represented by the dashed curve, can be estimated by using expression (20). The approximation of the volume density of states in the valence band (12) has been used for calculations in the range of wide quantum wells. As in the model with **k**-selection,[7] the increase in the inversion current with the width of the well d is attributable to populating of the upper subbands, which is the most conspicuous at high temperatures.

The electrical neutrality condition $p_1 - n_1 = 10^{12}$ cm^{-3} is used to interrelate the electron and hole densities. This choice of surface density of acceptors is required to satisfy the condition for validity of the model without **k**-selection, i.e., the hole density in the quantum well must not be significantly higher than the impurity concentration.

It is important to note that our analysis of radiative transitions with the transition probability to states in the impurity band regarded as equal to the transition probability from the most localized states has been simplified. Moreover, the hydrogen-like impurity model used here ignores the effects of shielding, dispersion, and anisotropy of the effective carrier masses. The results are therefore useful merely for obtaining a transparent description of the passage to the two-dimensional limit as the width of the quantum well is reduced. From the mathematical standpoint the recombination rate without **k**-selection according to (18), in contrast with the model of direct transitions, is found by replacing the delta-function transition probability $\omega_{n_v \mathbf{k}_v n_c \mathbf{k}_c} = A_{cv} \delta_{\mathbf{k}_c \mathbf{k}_v} \delta_{n_c n_v}$ by a value that is identical for any changes of the wave vector, i.e., the transition probability is averaged over states with different wave vectors in the plane of the quantum-well layer. The value of the transition probability without **k**-selection can be treated as a parameter of the theory and be determined from experiment.

This work has been supported, in part, by a G. Soros International Foundation program in the exact sciences.

[1] G. Lasher and F. Stern, Phys. Rev. A **133**, 553 (1964).
[2] V. P. Gribkovskiĭ, *Theory of Light Absorption and Emission in Semiconductors* [in Russian], Nauka i Tekhnika, Minsk (1975).
[3] P. T. Landsberg, M. S. Abrahams, and M. Osinski, IEEE J. Quantum Electron. **QE-21**, 24 (1985).
[4] B. Saint-Cricq, F. Lozes-Dupuy, and G. Vassilieff, IEEE J. Quantum Electron. **QE-22**, 625 (1986).
[5] V. K. Kononenko and I. S. Zakharova, *Laser Parameters of Quantum-Well Heterostructures*, ICTP Preprint IC/91/63 [in Russian], International Center for Theoretical Physics, Trieste (1991).
[6] G. W. Taylor, J. Appl. Phys. **70**, 2508 (1991).
[7] V. K. Kononenko, Inst. Fiz. Akad. Nauk B. SSR Preprint [in Russian], B. I. Stepanov, Institute of Physics, Academy of Sciences of the Belorussian SSR, Minsk (1987).
[8] H. C. Casey, Jr. and M. B. Panish, *Heterostructure Lasers*, Academic Press, New York (1978) [Russian trans., Mir, Moscow (1981)].
[9] G. Bastard, Phys. Rev. B **24**, 4714 (1981).

Translated by J. Wood

Contact-free determination of the parameters of a 2D electron gas in GaAs/AlGaAs heterostructures

I. L. Drichko[a] and I. Yu. Smirnov[b]

A. F. Ioffe Physicotechnical Institute, Russian Academy of Sciences, 194021 St. Petersburg, Russia

(Submitted April 9, 1997; accepted for publication April 16, 1997)
Fiz. Tekh. Poluprovodn. **31**, 1092–1094 (September 1997)

The parameters of a 2D electron gas in a GaAs/AlGaAs heterostructure — density, conductivity, and mobility in zero magnetic field, transport and quantum (one-particle) relaxation times, Dingle temperature, and spacer width — have been determined by a contact-free (acoustic) method. © *1997 American Institute of Physics.* [S1063-7826(97)01509-3]

To determine the electric parameters of a 2D gas (2DEG) in heterostructures by the standard dc method, it is necessary not only to prepare a sample in the form of a Hall bridge, but also to make electric contacts. In the present paper we report a contact-free method for determining these parameters by an acoustic method that does not require special preparation of the sample — a rectangular plate can serve as the sample.

Acoustic methods are based on the use of surface acoustic waves (SAWs) that propagate along the surface of a piezoelectric substrate in a piezoelectrically active direction. The deformation wave in this case is accompanied by an ac electric field varying with the frequency of the SAW. Therefore, the 2D electrons are in a high–frequency electric field that redistributes the electrons and generates high-frequency currents. This determines the absorption of energy from the wave. In the experiment the SAW absorption coefficient Γ, which decreases as a result of the interaction with the 2DEG, is measured in magnetic fields of up to 30 kOe in the temperature range 4.2–1.4 K. The coefficient Γ is determined by the conductivity of the electronic system.[1] For this reason, the quantization of the electronic spectrum in a magnetic field, which gives rise to Schubnikov–de Haas oscillations, is accompanied by characteristic features in SAW absorption as well. The coefficient Γ oscillates in a magnetic field in a manner similar to the Schubnikov–de Haas oscillations. Such oscillations have been observed in GaAs/AlGaAs[2,3,6] and InGaAs/InP[7] heterostructures. In Ref. 6 it was shown that in the GaAs/AlGaAs structures studied in the present work in magnetic fields not exceeding 30 kOe, the 2D electrons are in a delocalized state, so that the parameters of the 2DEG can be determined reliably by the acoustic method. The experimental procedure employed in the present work is also described in detail in Ref. 6 .

The dependence of the absorption coefficient Γ at 30 MHz on the intensity of the transverse magnetic field at $T=4.2$ K for GaAs/AlGaAs is shown in Fig. 1. It was found that the maxima of Γ are equally spaced as a function of $1/H$. This makes it possible to determine the density of the 2D electron gas $n_s=7\times10^{11}$ cm^{-2} from the oscillation ($n_s=6.75\times10^{11}$ cm^{-2}—from the dc Schubnikov–de Haas oscillations).

The absorption coefficient Γ is determined by the formulas[1]

$$\Gamma=8.68(K^2/2)qA\,\frac{(4\pi\sigma_{xx}/\varepsilon_s v)c(q)}{1+[(4\pi\sigma_{xx}/\varepsilon_s v)c(q)]^2},\qquad(1)$$

$$A=8b(q)(\varepsilon_1+\varepsilon_0)\varepsilon_0^2\varepsilon_s\exp(-2qa),$$

where K^2 is the electromechanical coupling constant of lithium niobate; q and ν are the SAW wave number and velocity, respectively; a is the vacuum gap between the lithium niobate and the specimen; σ_{xx} is the conductivity of the 2DEG; $\varepsilon_1,\varepsilon_0$, and ε_s are the dielectric conductivities of the lithium niobate, vacuum, and GaAs, respectively; and $b(q)$ and $c(q)$ are complex functions of a, q, ε_1, ε_0, and ε_s. As one can see from expression (1), if $(4\pi\sigma_{xx}/\varepsilon_s\nu)c(q)=1$, then Γ reaches its maximum value Γ_M, which does not depend on σ_{xx}.

To calculate σ_{xx} from Γ using Eq. (1), it is necessary to know the value of a. It is impossible to measure this quantity experimentally, since the heterostructure is pressed directly to the surface of the lithium niobate and the gap a is found to be uncontrollable. The value of a can be found from acoustic measurements by investigating the frequency dependence of Γ_M. Here

$$\Gamma_M(q_1)/\Gamma_M(q_2)=\{[q_1b(a,q_1)]/[q_2b(a,q_2)]\}e^{-2a(q_1-q_2)}.\qquad(2)$$

This equation yields $a=0.25$ μm. Knowing a, we can use Eq. (1) to determine $\sigma_{xx}(H)$ from the experimental values of Γ. The function $\sigma_{xx}(H)$, calculated from Eq. (1), is shown in Fig. 1.

In accordance with Ando's theory,[8] σ_{xx} in a magnetic field has the form

$$\sigma_{xx}=\sigma_{xx}^{*}+\sigma_{xx}^{\mathrm{osc}},\qquad(3)$$

where $\sigma_{xx}^{*}=\sigma_0/(1+\omega^2\tau_0^2)$ is the classical Drude conductivity, τ_0 is the transport relaxation time, $\omega_c=eH/m^{*}c$ is the cyclotron frequency, m^{*} is the electron effective mass, σ_0 is the conductivity at $H=0$, and c is the speed of light. The oscillating part can be represented in the form[9]

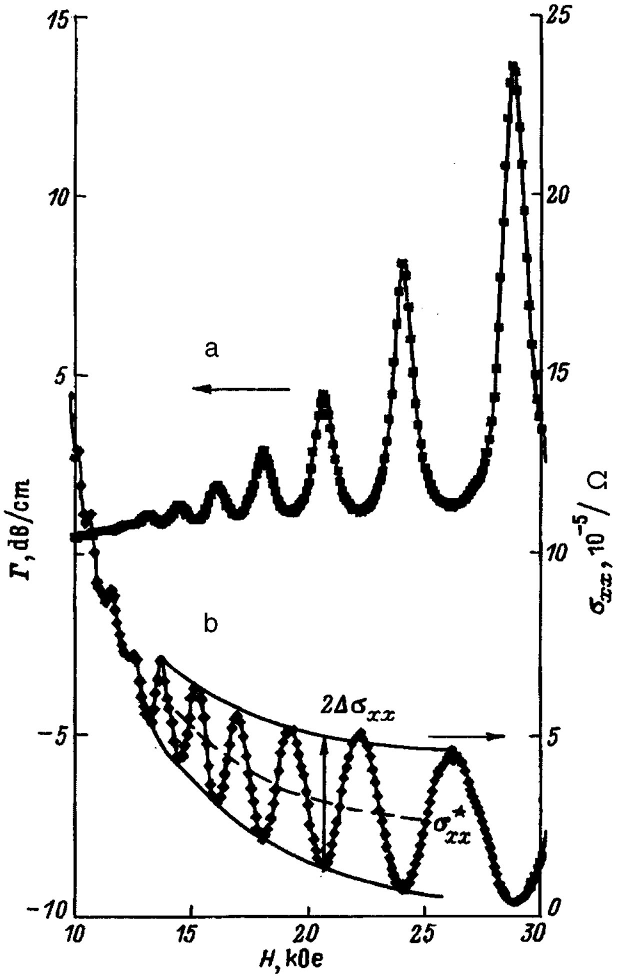

FIG. 1. Experimental curves of the absorption coefficient Γ (curve a) and conductivity σ_{xx} (curve b) versus magnetic field H at a temperature of 4.2 K and 30 MHz.

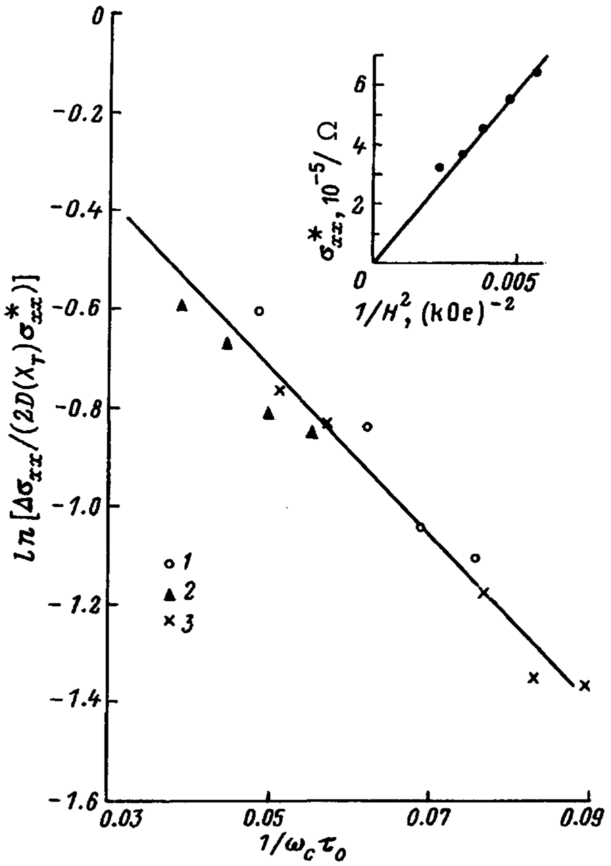

FIG. 2. Normalized oscillation amplitude $\ln[\Delta\sigma_{xx}(2\sigma^*_{xx}D(X_T))]$ versus $1/\omega_c\tau_0$ for different temperatures T, K: *1* — 4.2, *2* — 3.55, *3* — 1.5. Inset: σ^*_{xx} — the nonoscillatory part of the conductivity — versus the reciprocal $1/H^2$ of the squared magnetic field.

$$\sigma_{xx}^{\mathrm{osc}}\sim\sigma_{xx}^{*}D(X_T)\exp(-\pi/\omega_c\tau_q)\cos(2\pi E_F/\hbar\omega_c-\pi), \tag{4}$$

where $D(X_T)=X_T/\sinh X_T$, $X_T=2\pi^2T/\hbar\omega$, E_F is the Fermi energy, τ_q is the quantum (one-particle) relaxation time which determines the collisional broadening of the Landau level by the amount $\gamma=\hbar/2\tau_q$ and which characterizes the damping of the amplitude of the oscillations.

Analysis of the function $\sigma^*_{xx}(1/H^2)$ obtained from our measurements showed that it is linear up to $H\approx 25$ kOe (see the inset in Fig. 2). The mobility $\mu_0=\sigma_{xx}(H=0)/en_s$ at $H=0$ can be determined from the slope, equal to nec^2/μ_0. It was found to be equal to $(1.1\pm0.1)\times10^5$ cm^2/(V·s) [which differs by 15% from the Hall mobility $\mu_H=1.26\times10^5$ cm^2/(V·s)] and does not depend on temperature in the range 1.5–4.2 K. Analysis of the oscillating part $\sigma_{xx}^{\mathrm{osc}}$ yields the quantum (one-particle) relaxation time τ_q and Dingle temperature.

Since the amplitude $\Delta\sigma_{xx}$ of the oscillations is[10,11]

$$\Delta\sigma_{xx}=2\sigma^*_{xx}D(X_T)\exp(-\pi/\omega_c\tau_q), \tag{5}$$

to determine the quantum relaxation time τ_q we constructed a curve of $\ln[\Delta\sigma_{xx}D(X_T))]$ versus $1/\omega_c\tau_0$ for three different temperatures (Fig. 2). As one can see from the figure, this function is linear with a slope $-\pi\tau_0/\tau_q$. This means that the relation (5) is applicable not only for $\omega_c\tau_0<1$ (see Ref. 8), but also when $\omega_c\tau_0\gg1$ if $\Delta\sigma_{xx}/\sigma^*_{xx}<1$. The quantity τ_0/τ_q, calculated from the slope, equals 5.5 ± 0.5; it is temperature-independent in the interval 1.5–4.2 K and corresponds to scattering by charged impurity centers, taking screening into account. The Dingle temperature is $T^*=\hbar/2\pi\tau_q=1.5$ K. The spacer width in the sample can be determined in accordance with Ref. 12 from the known values of τ_0/τ_q and the density n_s. This yields the value 30 Å.

In summary, acoustic methods for investigating a 2D electron gas make it possible to determine by a contact-free method the density n_s, the mobility μ_0 in a zero magnetic field, the conductivity σ_{xx} and its dependence on H, the transport τ_0 and quantum τ_q relaxation times, the Dingle temperature T^*, and the spacer width.

We thank T. A. Polyanskaya for helpful discussions.

This work was supported by the Russian Fund for Fundamental Research grant No. 95-02-04066-a and the International Association grant No. INTAS-1403-93-ext.

---

[a] E-mail: Irina.L.Drichko@shuvpop.ioffe.rssi.ru

[b] E-mail: Ivan.Yu. Smirnov@shuvpop.ioffe.rssi.ru

[1] V. D. Kagan, Fiz. Tekh. Poluprovodn. **31**, 478 (1997) [Semiconductors **31**, 407 (1997)].
[2] A. Wixforth, J. P. Kotthaus, and G. Weimann, Phys. Rev. Lett. **56**, 2104 (1986); A. Wixforth, J. Scriba, M. Wassermeier, J. P. Kotthaus, G. Weimann, W. Schlapp, Phys. Rev. **40**, 7874 (1989).
[3] A. Schenstrom, Y. J. Quan, M. F. Xu, M. P. Baum, M. Levy, and B. K. Sarma, Solid State Commun. **65**, 739 (1988).
[4] V. W. Rampton, K. McEnaney, A. G. Kozorezov, P. J. A. Carter, C. D. W. Wilkinson, M. Henini, and O. H. Hughes, Semicond. Sci. Technol. **7**, 641 (1992).
[5] R. Boulet, P. Coleridge, F. Guillon, M. D. Iorio, and A. Sachrajda, Can. J. Phys. **69**, 461 (1991).
[6] I. L. Drichko, A. M. D'yakonov, A. M. Kreshchuk, T. A. Polyanskaya, I. G. Savel'ev, A. V. Suslov, and I. Yu. Smirnov, Fiz. Tekh. Poluprovodn. **31**, 451 (1997) [Semiconductors **31**, 384 (1997)].
[7] I. L. Drichko, A. M. D'yakonov, V. D. Kagan, A. M. Kreshchuk, G. D. Kipshidze, T. A. Polyanskaya, I. G. Savel'ev, A. V. Suslov, I. Yu. Smirnov, and A. Ya. Shik, Fiz. Tekh. Poluprovodn. **29**, 1306 (1995) [Semiconductors **29**, 677 (1995)].
[8] T. Ando, J. Phys. Soc. Jpn. **37**, 1233 (1974).
[9] A. Isihara and L. Smrčka, J. Phys. C **19**, 6777 (1986).
[10] P. T. Coleridge, R. Stoner, and R. Fletcher, Phys. Rev. B **39**, 1120 (1989).
[11] J. P. Harrang, R. J. Higgins, R. K. Goodall, P. R. Jay, M. Laviron, and P. Delescluse, Phys. Rev. B **32**, 8126 (1985).
[12] S. Das Sarma and F. Stern, Phys. Rev. B **32**, 8442 (1985).

Translated by M. E. Alferieff

Binding energy of Coulomb acceptors in quantum-well systems

V. I. Belyavskiĭ and M. V. Gol'dfarb

Voronezh State Pedagogical University, 394043 Voronezh, Russia

Yu. V. Kopaev

P. N. Lebedev Physics Institute, Russian Academy of Sciences, 117924 Moscow, Russia

(Submitted June 21, 1996; accepted for publication December 19, 1996).
Fiz. Tekh. Poluprovodn. **31**, 1095–1099 (September 1997)

The binding energy of a Coulomb acceptor state in a type–I heterostructure with several tunneling-coupled quantum wells is investigated as a function of the positions of the impurity in the structure. It is shown that the specific features of quantum-well hole states strongly influence the binding energy, especially when subbands with negative effective masses arise. © *1997 American Institute of Physics.* [S1063-7826(97)01609-8]

1. The prospects for building physical devices based on semiconductor nanostructures (NS) are stimulating active investigation of such structures.[1] The possibility of selective doping opens up additional possibilities in the development of NS with prescribed properties.[2] It is obvious that the energy spectrum and envelope functions of impurity states are determined by the specific features of the quantum-well states and the position of the impurity in a given NS. Hydrogen-like states in an isolated, infinitely deep quantum well (QW) have been investigated theoretically in Ref. 3. Later, the theory was refined taking into account the finite height of the barriers, the differences in the permittivities and effective masses in the materials of the QW and barrier layers, and the specific features of the valence-band structure.[4–6] Experimental investigations[7] confirm the conclusion that the binding energy of an acceptor impurity depends on the position of the impurity in the NS. Of interest in this connection are asymmetric systems of QW, in which a relocation of the carrier envelope functions under the action of external fields is most effective,[8] making it possible to employ this structures as elements of integrated circuits in nanoelectronics.[9] The relocation of envelope functions also influences the spectrum of the impurities that are located in the heterostructure and are capable of influencing appreciably the properties of the structure.

The variational method in the effective-mass approximation is used in most studies of the localized states in nanostructures. The results of such calculations depend strongly on the form of the trial variational functions.[10] The present work is devoted to a study of shallow acceptor states in asymmetric nanostructures with QW, such as $\mathrm{Al}_x\mathrm{Ga}_{1-x}\mathrm{As}$–GaAs. We employ a method previously used in Refs. 11 and 12 to describe excitonic states in structures with narrow QW and tunneling-transparent barriers. In application to impurity centers, it consists of expanding the localized envelope functions of an impurity center in a 2D basis in the space of envelope functions of the free carriers in a given NS. It is comparatively easy to take into account the differences in the effective masses and permittivities of the QW and barrier materials and, most importantly, the effects of nonparabolicity of the valence band. The effective-mass method employing ceratin information about the structure of the energy bands of a bulk semiconductor, being applicable to the investigation of localized states in NS, encounters serious difficulties due to the need to take into account the potential which spatially confines the electrons and holes and lowers the symmetry of the system. For this reason it is natural to base the description of localized states on a variant of the effective-mass method that takes directly into account the required information about the structure of the 2D quantum-well subbands in the NS of interest. This makes it possible to allow for the effects which are due to the complex structure of the valence band, specifically, the mixing of the heavy- and light-hole states.[13] An approximation which takes into account only one subband is found to be inadequate for the analysis of acceptor states, since the binding energy of an acceptor (in contrast to shallow donors[3,14]) is comparable, in general, to the characteristic separation between the subbands in the NS. The width of the quantum wells and barriers under consideration is, of course, a factor that determines the accuracy of calculations based on the method of envelope functions in the effective-mass approximation. It is believed[8] that the method is effective if the characteristic sizes of the wells and barriers exceed a value of the order of 10 Å. The characteristic dimensions of the elements of structures which are studied in the numerical examples presented below are of this order of magnitude. In the present paper, we do not consider the problem of calculating the binding energy of an impurity state to spectroscopic accuracy or the problem of determining the qualitative dependence of the binding energy on the position of the impurity in the structure. The method of envelope functions in the effective-mass approximation is most suitable for this purpose.[8]

2. We write the effective Hamiltonian in the form $H=H^{(0)}+U$, where $H^{(0)}$ is the Hamiltonian of free holes in a given NS, and U is an operator describing the Coulomb interaction between a hole and an impurity center. We write the envelope function of the acceptor state as

$$|\rangle=\sum_{\lambda,\beta}|\lambda\beta\rangle\langle\lambda\beta|\rangle, \tag{1}$$

where λ is a combined index which includes the index of the valence band (of heavy HH or light LH holes) and the number n of the quantum-well subband, and β is the 2D radius vector of a unit cell in the plane of the NS. The basis functions $|\lambda\beta\rangle$ can be represented as a linear combination of the functions

$$|\lambda k\rangle = \frac{1}{\sqrt{S}} f_{\lambda k}(z)\exp(ik\rho), \tag{2}$$

which form a basis in which the Hamiltonian operator for the free holes is diagonal. Here S is the area of the heterostructure, and k is the 2D quasiwave number. Since the effective localization radius of the impurity states in semiconductors is greater than the lattice constant a, a relatively small region of quasimomenta near the center of the 2D Brillouin zone makes the main contribution to the formation of the envelope functions $|\rangle$, $ka \ll 1$. Furthermore, the off-diagonal elements of the Luttinger Hamiltonian, which is usually employed for describing hole states in semiconductor NSs,[8], are much smaller than the diagonal elements in the limit $k \rightarrow 0$, so that a simplified classification of hole states, which is associated with their character at $k=0$, is possible for small k. This makes it possible to disregard the dependence of the 1D envelope functions $f_{\lambda k}(z)$ on k, denoting them simply as $f_\lambda(z)$. In this case the basis

$$|\lambda\beta\rangle = \frac{1}{\sqrt{N}} \sum_k |\lambda k\rangle \exp(-ik\beta) \tag{3}$$

degenerates into a point (in the plane of the NS) basis which is modulated by the envelope functions $f_\lambda(z)$; here N is the number of unit cells in the plane of the NS.

The system of equations for the coefficients in the expansion of the envelope function of a localized state in the basis (3) has the form

$$(E - E_\lambda(-i\nabla))\langle\lambda\beta|\rangle = \sum_{\lambda'\beta'} \langle\lambda\beta|U|\lambda'\beta'\rangle\langle\lambda'\beta'|\rangle, \tag{4}$$

where $E_\lambda(k)$ is the 2D dispersion law for holes in a λ subband, and ∇ is the 2D gradient operator. The Coulomb interaction operator is diagonal with respect to β, so that introducing the abbreviated notations $\langle\lambda\beta|U|\lambda'\beta'\rangle \equiv U_{\lambda\lambda'}$ and $U_{\lambda\lambda} \equiv U_\lambda$, the operators $H_\lambda = E_\lambda(-i\nabla) + U_\lambda$ can be determined and Eq. (4) can be rewritten as

$$(E - H_\lambda)\langle\lambda\beta|\rangle = \sum_{\lambda' \neq \lambda} U_{\lambda\lambda'}\langle\lambda'\beta|\rangle. \tag{5}$$

The solution of the system of equations (5) makes it possible to determine the envelope functions and energy spectrum of the NS with an acceptor impurity, taking into account the mixing of states that split-off from all 2D subbands. All information about the profile of the 1D hole potential in a given NS and also about the effective masses of the holes in the QW and barrier materials is contained in the dispersion law $E_n(k)$ and the 1D envelope functions of the holes.

3. Let us examine the case in which the acceptor state is formed exclusively by states of the heavy-hole band, and let us use for simplicity the two-subband approximation; i.e., in Eq. (5) we take into account only two subbands: *HH*1 and *HH*2. In what follows, we drop the index of the *HH* valence band. The subband number $(n=1)$ of the 2D subband, taking into account the influence of the states of the top $(n=2)$ subband, will now play the role of λ. We note that the approximate approach employed here for describing localized states can also be used to take account of the influence of all other subbands. This complication does not change fundamentally the qualitative picture obtained in the two-subband approximation. Using $\psi_n(\beta)$ for $\langle\lambda\beta|$ and defining the Green's operators for the Hamiltonians H_n $(n=1,2)$ as $G_n(E) = (E - H_n)^{-1}$, the system of two equations (5) can be reduced to the single equation

$$(E - H_1)\psi_1 = U_{12}G_2(E)U_{21}\psi_1, \tag{6}$$

which can be regarded as a Schrödinger equation with an energy-dependent potential.

Let $\varphi_{n\nu}(\beta)$ be the eigenfunctions of the operator H_n, where ν is the 2D quantum number enumerating the eigenfunctions of the operator H_n. We represent the Green's function $G_n(E)$ in the form of a Hilbert–Schmidt expansion

$$G_n(E;\beta,\beta') = \sum_\nu \frac{\varphi^*_{n\nu}(\beta')\varphi_{n\nu}(\beta)}{E - E_{n\nu}}, \tag{7}$$

where $E_{n\nu}$ is the spectrum of the operator H_n. The system of functions $\varphi_{n\nu}(\beta)$is complete, so that $\psi n(\beta)$ can be represented as an expansion in this system

$$\psi_n(\beta) = \sum_\nu a_{n\nu}\varphi_{n\nu}(\beta) \tag{8}$$

and Eq. (6) can be put into the form

$$\{E - E_{1\nu} - W_{\nu\nu}(E)\}a_{1\nu} = \sum_{\nu' \neq \nu} W_{\nu\nu'}(E)a_{1\nu'}, \tag{9}$$

where

$$W_{\nu\nu'}(E) \equiv \sum_\mu \frac{u^{12}_{\nu\mu}u^{21}_{\mu\nu'}}{E - E_{2\mu}}, \tag{10}$$

$$\sum_\beta \varphi^*_{1\nu}(\beta)U_{12}(\beta)\varphi_{2\mu}(\beta) \equiv u^{12}_{\nu\mu};$$

$$\sum_{\beta'} \varphi^*_{2\mu}(\beta')U_{12}(\beta')\varphi_{1\nu'}(\beta') \equiv u^{21}_{\mu\nu'}. \tag{11}$$

In determining the Coulomb interaction energy between a hole and an impurity center, the difference in the permittivities of the QWs and barriers could have an appreciable effect. The Coulomb matrix elements can be written as

$$U_{nn'}(\beta,z_0) = \int dz f^*_n(z)G(\beta,z,z_0)f_{n'}(z), \tag{12}$$

where we have introduced the electrostatic Green's function $G(\beta,z,z_0)$, which for the NS considered here is written out explicitly in, for example, Ref. 11 . There are grounds for assuming that the off-diagonal elements (10) are much smaller than the diagonal elements $W_{\nu\nu'} \ll W_{\nu\nu}$, $\mu \neq n'$. This inequality follows from the orthonormality of the 1D envelope functions and is especially valid in the case of asymmetric NS, in which the envelope functions corresponding to different subbands, as a rule, possess maxima in different

QW. For this reason, the energy $E_{1\nu}$ of a level split-off from the bottom subband can be found in the zeroth approximation from the solution of the equation

$$E-E_{1\nu}-W_{\nu\nu}(E)=0. \tag{13}$$

Thus, in this approximation the problem of determining the energy spectrum of a shallow acceptor in a NS reduces to calculating the spectrum of $E_{1\nu}$, taking into account only one bottom subband, and the correction $W_{\nu\nu}$ due to the influence of the states of the neigboring subband.

4. The equation determining the contribution of the *n*th subband to the envelope function of an acceptor, disregarding the states of neighboring subbands, can be written in the form[11]

$$\left[E_n^{(0)}-\frac{\hbar^2}{2m_n}\nabla^2+V_n-U_{nn}(\beta,z_0)-E\right]\psi_n(\beta)=0. \tag{14}$$

Here $E_n^{(0)}$ and m_n are the energy (for $k=0$) and effective mass of a hole in the *n*th subband. The operator V_n, which takes into account (for a small k) the nonparabolicity of the *n*th subband, can be written as[11] $V_n=\hbar^2 b_n^2 k^4/2m_0$, where m_0 is the mass of a free electron, and the typical values of the phenomenological parameter b_n lie between 10 and 100 Å.[11] Equation (14) can be solved by a variational method. In so doing, it is natural to choose the trial envelope function of the ground state in the form of a 2D hydrogen-like orbital

$$\langle n\beta|0\rangle=\sqrt{\frac{2\kappa^2}{\pi}}\exp(-\kappa/\beta) \tag{15}$$

with one variational parameter κ. It should be noted that a different approximate method, used in Ref. 11 and 12 to investigate excitonic states, for calculating the energy spectrum[15] gives similar results.

The method of Ref. 15 is based on a representation of the Hamiltonian Eq. (14) in the form

$$H_n=H_n^{(C)}(\chi)+H_n^{(1)}(\chi), \tag{16}$$

where

$$H_n^{(C)}(\chi)=E_n^{(0)}-\frac{\hbar^2}{2m^*}\nabla^2+\frac{\chi e^2}{\beta}, \tag{17}$$

and the operator $H_n^{(1)}(\chi)$ is the complement of the Hamiltonian (17) with respect to the complete Hamiltonian in Eq. (14). Ordinarily, the parameter χ is determined from the condition that the first correction to the energy due to the operator

$$H_n^{(1)}(\chi)=V_n+U_{nn}(\beta;z_0)-\frac{\chi e^2}{\beta} \tag{18}$$

equals zero. The operator (17) has both continuous and discrete eigenvalues. The latter eigenvalues obviously are the Coulomb series of equations[16] with energies

$$E_n^{(C)}=E_n^{(0)}+\frac{\chi^2\mathrm{Ry}^{(n)}}{\left(n+\dfrac{1}{2}\right)^2}, \tag{19}$$

where $m=0,1,2,\ldots$, and $\mathrm{Ry}^{(n)}=|m_n|e^4/2\hbar^2$. The parameter χ in Eq. (19) is determined from the equation

$$\langle nm|H_n^{(1)}(\chi)|nm\rangle=0, \tag{20}$$

where the eigenfunctions $|nm\rangle$ of the Hamiltonian (17) with a corresponding choice of the parameter χ are, just as in Eq. (15), the standard wave functions of a 2D hydrogen atom. Specifically, the ground-state envelope function has the form (15) if $\kappa a_n=2\chi$, where $a_n=\hbar^2=|m_n|e^2$. The method of Ref. 15 can be somewhat improved,[17] if instead of the condition (20) it is required that the energy of the impurity state calculated in first order in the perturbation (18) have a minimum as a function of the parameter χ. In this case, obviously the result of the calculation of the ground-state energy by the method of Ref. 15 completely agrees with the variational procedure.

To determine the correction due to the effect of the states in a neighboring subband, it can be assumed that the states of the continuous spectrum make the main contribution to $W_{\nu\nu}$. The hydrogen-like series of discrete levels, split-off from the upper subband in the field of the shallow acceptor, cannot appreciably influence the value of W_{nn} provided that the binding energy of these states is less than the splitting between the subbands. In this approximation, μ evidently corresponds to the 2D quasimomentum k. Since $k\ll a^{-1}$ is the main contribution to the formation of the localized state, we can write Eq. (11) approximately in the form

$$u_{\nu k}^{12}=-\frac{2e^2}{\varepsilon}\sqrt{\frac{2\pi}{S}}B_{12}(z_0). \tag{21}$$

Here

$$B_{12}(z_0)=\int dz f_1^*(z)F(\kappa|z-z_0|)f_2(z), \tag{22}$$

and the function $F(\zeta)$ with relatively small differences in the permittivities of the QW and barriers is defined as[11]

$$F(\varsigma)=\varsigma\left\{\frac{\pi}{2}[\mathrm{H}_1(\varsigma)-\mathrm{Y}_1(\varsigma)]-1\right\}, \tag{23}$$

where $\mathrm{Y}_1(\zeta)$ and $\mathrm{H}_1(\zeta)$ are the Bessel and Struve functions, respectively. Therefore, the correction due to the second subband can be estimated as

$$W_{\nu\nu}(E)\Rightarrow\left(\frac{2e^2}{\varepsilon}\right)^2|B_{12}(z_0)|^2\int\frac{kdk}{E-E_2(k)}, \tag{24}$$

where the integration extends over the 2D Brillouin zone.

If the dispersion relation for the second subband has the form

$$E_2(k)=E_2^{(0)}+\frac{\hbar^2k^2}{2m_2}, \tag{25}$$

then

$$W_{\nu\nu}(E)=-4\mathrm{Ry}^{(2)}|B_{12}(z_0)|^2\ \ln\left|1+\frac{\pi^2\hbar^2}{2m_2a^2(E_2^{(0)}-E)}\right|, \tag{26}$$

and Eq. (13) can be easily solved graphically. The energy of the localized state can be estimated roughly as

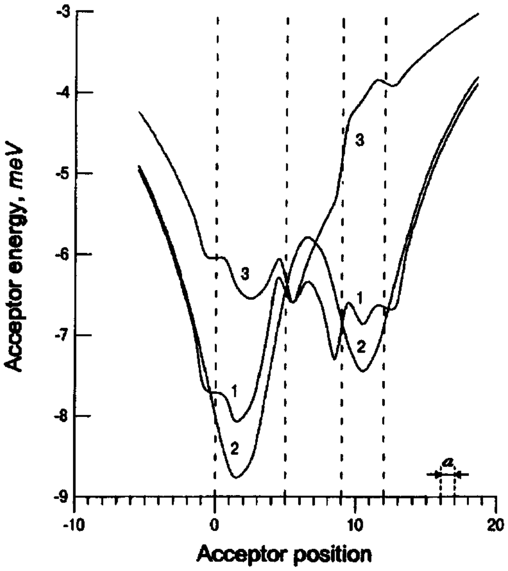

FIG. 1. Ground-state energy of a Coulomb acceptor as a function of the position of the impurity atom in the NS $\mathrm{Al}_{0.3}\mathrm{Ga}_{0.7}\mathrm{As}$–GaAs: *1* — Taking into account of the subbands $HH1$ and $HH2$ and the difference in the permittivities of the QWs and barriers; *2* — same but neglecting the difference in the permittivities; *3* — taking into account only the bottom ($HH1$) subband. One division on the abscissa corresponds to a lattice constant of 5.65 Å.

$$E \approx E_{1\nu} - 4\mathrm{Ry}^{(2)}|B_{12}(z_0)|^2 \ln\left|1+\frac{\pi^2\hbar^2}{2m_2a^2\Delta}\right|, \tag{27}$$

where $\Delta = E_2^{(0)} - E_1^{(0)}$.

The case where the dispersion relation in the second subband corresponds to hole excitations with negative effective mass is of greatest interest:

$$E_2(k) = E_2^{(0)} - \frac{\hbar^2k^2}{2m_2} + \frac{\hbar^2}{2m_0}b_2^2k^4. \tag{28}$$

In this case the integral in Eq. (19) can be expressed in terms of elementary functions

$$W_{\nu\nu}(E) = -4\mathrm{Ry}^{(2)}|B_{12}(z_0)|^2 \frac{1}{\sqrt{\frac{8m_2b_2^2}{\hbar^2}(E_2^{(0)}-E)-1}} \times \left\{\frac{\pi}{2} + \arctan\frac{1}{\sqrt{\frac{8m_2b_2^2}{\hbar^2}(E_2^{(0)}-E)-1}}\right\}, \tag{29}$$

and a rough estimate of the energy of the impurity state can be obtained by solving the transcendental equation

$$E - E_{1\nu} + 4\pi\mathrm{Ry}^{(2)}|B_{12}(z_0)|^2 \times \frac{1}{\sqrt{\frac{8m_2b_2^2}{\hbar^2}(E_2^{(0)}-E)-1}} = 0. \tag{30}$$

5. Figure 1 shows as an example the dependence (curve 1) of the binding energy of the acceptor state on the position of the impurity in a $\mathrm{Al}_{0.3}\mathrm{Ga}_{0.7}\mathrm{As}$–GaAs NS with two QW of width $5a$ and $3a$ and a barrier of width $4a$, where a is the lattice constant. The outer barrier layers are assumed to be semi-infinite. For this NS the splitting between the subbands is equal to 32.1 meV, the effective mass in the second subband is negative and equals in absolute magnitude $0.079m_0$, and the parameter b_n is assumed to be 25 Å. The parameters of the NS correspond to those employed in Ref. 11 . For comparison, Fig. 1 shows (curve *2*) the computational results obtained without regard for the difference in the permittivities in the QW and barrier materials (their average value was used in the calculations). Taking into account only the first subband gives curve *3*, which has a noticeable minimum inside the wider QW where the 1D envelope function of the bottom subband is mainly localized.

The larger the overlapping of the envelope functions of the 2D subbands and the smaller the effective mass in the second subband and the energy gap between the subbands, the greater the dip of the level as a result of the effect of the second subband. The effect of the states in the first subband on the impurity (quasilocal) levels split-off from the second subband can be taken into account similarly. In this case, the first subband has the effect of decreasing the binding energy. The correction is small in the region inside the barrier, where the envelope of the subband possesses a node and is much larger in the wells where the 1D envelope functions are large; in this case the contribution of the second subband can be comparable in order of magnitude to the binding energy of the acceptor state.

It should be noted that contrary to the widely held opinion that the binding energy of a shallow acceptor is always appreciably greater than that of a donor,[4] for common NS such as $\mathrm{Al}_x\mathrm{Ga}_{1-x}\mathrm{As}$–GaAs it is comparatively easy to give examples of structures in which these energies are comparable (see Fig. 1, curve *1*). However, the closely spaced (compared with the conduction subbands) valence subbands and, correspondingly, the more uniform distribution of the 1D envelopes along the axis of growth of the NS have the effect that the dependence of the binding energy on the position of the impurity in the NS is weaker than in the case of deep impurities[18] and shallow donors.[19]

In asymmetric systems of QW the envelope functions in the region of the inner barriers can be comparable in magnitude to their value in the region of the QW. For this reason, taking into account the difference in the permittivities of the QW and barrier materials could appreciably change the binding energy, especially since the difference in the permittivities of the QW and barrier materials in $\mathrm{Al}_x\mathrm{Ga}_{1-x}\mathrm{As}$–GaAs heterostructures with $x \sim 0.1$ equals about 10% and, in general, is not negligible.

This work was supported by the Russian Fund for Fundamental Research and the Russian Ministry of Science and Technology Policy as part of the program ‘‘Physics of solid-state nanostructures.’’

[1] H. Sakaki, *Localization and Confinement of Electrons in Semiconductors,* Springer Ser. Solid State Sci. (1991), Vol. 97, p. 2.
[2] R. Dingle, H. Stoermer, A. C. Gossard, and W. Wiegmann, Appl. Phys. Lett. **33**, 665 (1978).
[3] G. Bastaed, Phys. Rev. B **24**, 1714 (1981).
[4] A. Pasquarello, L. C. Andreani, and R. Buczko, Phys. Rev. B **40**, 5602 (1989).
[5] W. T. Masselink, Y.-C. Chang, and H. Morkoc, Phys. Rev. B **28**, 7373 (1983).
[6] S. Chaudhury and K. K. Bagaj, Phys. Rev. B **29**, 1803 (1984).
[7] G. C. Rune, P. O. Holtz, and M. Sundatam *et al.*, Phys. Rev. B **44**, 4010 (1991).
[8] G. Bastard, J. A. Brum, and R. Ferreira, Solid State Phys. **44**, 229 (1990).
[9] A. A. Gorbatsevich, V. V. Kapaev, Yu. V. Kopaev, and V. Yu. Kremlev, Phys. Low-Dim. Structure **5**, 57 (1994).
[10] F. G. Pikus, Fiz. Tekh. Poluprovodn. **26**, 43 (1992) [Sov. Phys. Semicond. **26**, 26 (1992)].
[11] V. I. Belyavskiĭ, Yu. V. Kopaev, S. T. Pavlov, and S. V. Shevtsov, JETP Lett. **37**, 1743 (1995).
[12] V. I. Belyavskiĭ, Yu. V. Kopaev, S. T. Pavlov, and S. V. Shevtsov, JETP Lett. **61**, 292 (1995).
[13] Y.-C. Chang and J. N. Shulman, Appl. Phys. Lett. **43**, 536 (1983).
[14] E. M. Ivchenko and A. V. Kavokin, Fiz. Tekh. Poluprovodn. **25**, 1780 (1991) [Sov. Phys. Semicond. **25**, 1070 (1991)].
[15] Y. C. Lee, W. N. Mei, and K. C. Lin, J. Phys. C **15**, L469 (1982).
[16] M. Shinada and S. Sugano, J. Phys. Soc. Jpn. **21**, 1936 (1966).
[17] Y. Fu and K. A. Chao, Phys. Rev. B **43**, 12 626 (1991).
[18] V. I. Belyavskiĭ, Yu. V. Kopaev, N. V. Kornyakov, and S. V. Shevtsov, JETP Lett. **61**, 1039 (1995).
[19] V. I. Belyavskiĭ, M. V. Gol'dfarb, Yu. V. Kopaev, and S. V. Shevtsov, Fiz. Tekh. Poluprovodn. **31**, 1095 (1997) [Semiconductors **31**, 936 (1997)].

Translated by M. E. Alferieff

Photoelectric properties of GaAs/InAs heterostructures with quantum dots

B. N. Zvonkov, I. G. Malkina, and E. R. Lin'kova

Scientific Research Physico-Technical Institute, Nizhniĭ Novgorod State University,
603600 Nizhniĭ Novgorod, Russia

V. Ya. Aleshkin

Institute for the Physics of Microstructures, Russian Academy of Sciences,
603600 Nizhniĭ Novgorod, Russia

I. A. Karpovich and D. O. Filatov

N. I. Lobachevsky State University at Nizhniĭ Novgorod, 603600 Nizhniĭ Novgorod, Russia

(Submitted February 27, 1996; accepted for publication January 13, 1997)
Fiz. Tekh. Poluprovodn. **31**, 1100–1105 (September 1997)

The capacitive photovoltage and photoconductivity spectra of GaAs/InAs heterostructures with quantum dots is discussed. For these structures, which were fabricated by metallorganic gas-phase epitaxy, the photosensitivity spectrum has a sawtoothed shape in the wavelength range where absorption by the quantum dots takes place, which is characteristic of a δ-function-like density of states function. The spectra also exhibit photosensitivity bands associated with the formation of single-layer InAs quantum wells in the structure. An expression is obtained for the absorption coefficient of an ensemble of quantum dots with a prespecified size distribution. It is shown that the energy distribution of the joint density of states, the surface density of quantum dots, and the effective cross section for trapping a photon can all be determined by analyzing the photosensitivity spectrum based on this assumption. © *1997 American Institute of Physics.* [S1063-7826(97)01709-2]

Recently, new attention has been focused on GaAs/InAs heterostructures with quantum dots[1–4] since the discovery that interrupting the growth of a layer of InAs at the proper moment causes formation of individual nanocrystals, in which carriers have the typical quantum-dot discrete energy spectrum. These crystals form as a result of self-organization processes based on the Stranski-Krastanov mechanism.[5]

The authors of papers published until now have concentrated primarily on studying the surface morphology of the heterostructure after the growth is interrupted,[6,7] together with the photoluminescence from the quantum-dot structures. Because the density of states in a quantum dot is described by Dirac δ- functions,[8] the photoluminescence spectrum of an individual quantum dot should consist of a narrow line whose natural width is determined by the lifetime of the excited state in the quantum dot as determined by the uncertainty relation. When a sufficiently small number of quantum dots is excited, it is possible to observe several narrow luminescence lines with temperature-independent widths of ~ 0.1 meV.[6,9] When photoluminescence is excited over a relatively large area of the sample, the photoluminescence spectrum has a much broader maximum due to natural scatter in the size distribution of the nanocrystallites.[9] The spectral linewidth is determined by the energy distribution $g(E)$ of the joint density of states in the quantum dot ensemble.

This density of states can be determined in several ways, one of which is to measure the spectral dependence of the optical absorption coefficient.[8] In this paper, we apply the methods of capacitive photovoltage and planar photoconductivity spectroscopy to this problem, methods that have been used previously to study heterostructures with quantum wells.[10–12]

The goal of this paper is to elucidate how features of the photoelectric sensitivity spectra of GaAs/InAs heterostructures with quantum dots evolve as a function of the thickness of the InAs layer, and to develop a methodology for determining certain parameters of the quantum dot ensemble from these spectra: the energy spectrum, the absorption coefficient, the density of states, the surface density of quantum dots, etc.

1. THEORY

In the spectral region where interband transitions occur between the quantum-well levels of a heterostructure containing quantum wells, the mechanism that gives rise to the capacitive photovoltage effect at a surface barrier involves three basic stages:[11] 1) generation of electron-hole pairs in the quantum wells, 2) emission of nonequilibrium carriers from the quantum wells, and 3) separation of pairs in the field of the surface barrier. Small-signal measurements of the capacitive photovoltage photosensitivity in this wavelength range reveal that the absorption $S_W(h\nu)$ is proportional to the absorption coefficient $\beta_W(h\nu)$ of the quantum wells.[12] Since the phenomena listed above will in principle occur for any system dominated by quantum-well effects (well, wire, or dot), we should expect the same mechanism to operate in structures with quantum dots.

Let us find the relation between the absorption coefficient, the joint density of states, and the photosensitivity for an ensemble of quantum dots with a prespecified size distribution.

Since the quantum dots are located in a single plane for the structures under study here, it is convenient to replace the bulk absorption coefficient with a dimensionless absorption coefficient

$$\beta_D(h\nu)=\frac{\Delta I}{I_0}, \tag{1}$$

where $\Delta I=I_0-I_1$, here I_0 and I_1 are the intensities of the incident light and the light passing through the plane containing the quantum dots.

According to Fermi's "golden rule,"

$$\Delta I=\frac{2(eF)^2 h}{m_0^2(h\nu)}\sum_i |P_{eh}^i|^2\delta(E_e^i-E_h^i-h\nu), \tag{2}$$

where F is the electric field intensity of the incident electromagnetic field, m_0 is the free electron mass, e is the elementary charge, E_e^i and E_h^i are quantum-well energy levels for electrons and holes, and P_{eh}^i is the matrix element of the momentum operator for a transition between these levels within the ith quantum dot. The factor of 2 in the numerator takes into account the spin degeneracy of the levels, and the summation runs over the entire quantum dot ensemble.

The matrix element is

$$|P_{eh}^i|^2=|P|^2\int \psi_h^{i*}(\mathbf{r})\psi_e^i(\mathbf{r})d\mathbf{r}=|P|^2|X^i|^2, \tag{3}$$

where $\psi_h^i(\mathbf{r})$ and $\psi_e^i(\mathbf{r})$ are envelope wave functions of holes and electrons in the ith quantum dot, $|X^i|^2$ is the overlap integral of the wave function envelopes, and P is the matrix element of the momentum operator taken over the rapidly oscillating parts of the Bloch functions. In the Kane model[13]

$$\frac{|P|^2}{m_0^2}\approx\frac{E_g}{2m_n}, \tag{4}$$

where m_n is the electron effective mass, and E_g is the width of the band gap of the barrier material (GaAs). These barrier quantities are chosen because of the smallness of the quantum dots (~10 nm), which causes the size-quantized electron and hole levels to lie near the GaAs absorption edge and the envelope wave functions to be localized primarily in the barrier material.

Assuming a weak dependence of the overlap interval X^i on i, and since $I_0=c\sqrt{\varepsilon}F^2/2\pi$, where ϵ is the dielectric constant of the barrier, we obtain from Eqs. (1)–(4)

$$\beta_D(h\nu)=\frac{\pi e^2 h}{cm_n\sqrt{\varepsilon}}|X|^2 g(h\nu), \tag{5}$$

where $g(h\nu)$ is the joint density of states in the ensemble of quantum dots, and $|X|^2\sim 1$.

The stages of emission of carriers from the quantum dot and the appearance of a photovoltage are characterized by a quantum efficiency η_D, which equals the ratio of the number of electron-hole pairs separated by the barrier field to the number of pairs excited in the quantum dot. Let us denote the quantum efficiency for bulk GaAs absorption by η_0, and let S_D denote the ratio of the photosensitivity for absorption by a quantum dot to the photosensitivity at the intrinsic absorption edge of GaAs (the normalized photosensitivity). Then we can write[12]

$$S_D=\beta_D\frac{\eta_D}{\eta_0}. \tag{6}$$

The quantity η_D should be close to unity for a quantum dot in a sufficiently strong surface barrier field; $\eta_0=0.5+0.25$ for a GaAs surface barrier of GaAs, and is only a weak function of the state of the surface.[12] Hence, in our measurement regime we have $S_D(h\nu)\sim g(h\nu)$, implying that capacitive photovoltage spectroscopy is a direct way to determine the joint density of states of the quantum dot ensemble.

Using Eqs. (5) and (6), we can determine the surface concentration of quantum dots N_s by measuring the photosensitivity spectrum $S_D(h\nu)$. If the absorption peak is determined by a single transition in the quantum dot, then

$$N_s=\frac{1}{2}\int g(h\nu)d(h\nu)=\frac{cm_n\sqrt{\varepsilon}}{2\pi e^2 h|X|^2}\int \beta_D(h\nu)dh\nu. \tag{7}$$

The integration extends over that neighborhood of the peak in which the function under the integral sign contributes significantly to the integral.

When we approximate the peak of the absorption by a Gaussian function, Eq. (7) can be written in the form

$$\beta_m=\sigma_D N_s, \tag{8}$$

where the quantity

$$\sigma^{QD}=\frac{2\sqrt{\pi\ln^2}e^2h}{cm_n\sqrt{\varepsilon}\Gamma}|X|^2 \tag{9}$$

can be interpreted as an effective cross section for capture of a photon by a quantum dot, $\beta_m=\beta_D(h\nu_m)$ is the height of the absorption peak, and Γ is the width at half-maximum.

2. EXPERIMENTAL METHOD

GaAs/InAs structures were grown on (001) substrates of GaAs by metallorganic gas-phase epitaxy at atmospheric pressure. In order to obtain wedge-shaped structures, the crystals were grown in a laminar flux without rotating the substrate. Tests indicated that the growth rates of InAs and GaAs in this case fell off linearly with increasing distance from the edge of the substrate and were proportional to one another.

Structure 1, grown on an n^+ substrate at 650 °C, consisted of a buffer layer of GaAs, a layer of InAs with quantum dots, and a covering layer of GaAs. The average thickness of the buffer layer, based on the growth rate, was 0.34 μ, that of the cover layer 0.24 μ; the average nominal thickness of the InAs layer was d = 1.6 monolayers. The structure was doped with Si. Measurement of the dependence of the capacitance on voltage indicated an electron concentration in GaAs of $n_0=(2-4)\times 10^{16}$ cm^{-3}. We investigated the photoluminescence spectra of this structure at 77 K, its capacitive photovoltage at 77 and 300 K, and the capacitance-voltage characteristic ($C-V$) of a Schottky barrier (Al) on it. In order to measure the photoconductivity

TABLE I. Geometric parameters of structure 1

Sample No.	x, mm	L_{bs}, μ	d, monolayers	D, nm
1	0	0.15	1.1	6
2	5	0.18	1.3	9
3	8	0.19	1.4	9
4	14	0.21	1.6	11
5	20	0.23	1.8	12
6	25	0.28	2.1	14

spectrum of a sample grown on a semi-insulating substrate, we grew structure 2 at 550 °C with parameters close to those of structure 1. Structure 2 also had the shape of a wedge. In order to measure the photoconductivity we excised 5×1-mm samples from the structure at specific points along the wedge.

Photoluminescence was excited by a He–Ne laser at a photoexcitation intensity of $\sim 10^{20}$ cm$^{-2}\cdot$s^{-1}. The method of measuring the capacitive photovoltage was described in Ref. 12.

3. RESULT AND DISCUSSION

C-V characteristics. Characteristic plateaus in the *C-V* curves of these structures indicate crossing of the space-charge region boundary of a quantum-size layer in which the motion of carriers is restricted along the direction of growth of the structure.[14] However, the measurement results do not allow us to establish whether or not quantum confinement occurs in the plane of the structure as well.

In Table I we show values of the thickness of the coating layer L_{bs} obtained by the *C-V* method for six samples excised from structure 1 and located a distance x along the wedge. According to these data, we calculated the local nominal thickness of InAs d, taking into account that the growth rates of InAs and GaAs were proportional, which leads us to the relation $d(x) \sim L_{bs}(x)$.

Based on the width of the plateau in the function $C(V)$, we can determine the surface concentration of electrons $n_s = (1.1 \pm 0.2) \times 10^{11}$ cm^{-2} in the quantum-well layer.

Capacitive photovoltage and photoluminescence. Figures 1 and 2 show photosensitivity spectra of the capacitive photovoltage at 30 and 77 K, respectively, measured on samples with various values of d.

The most remarkable feature of these spectra, which distinguishes them from spectra of GaAs/In$_x$Ga$_{1-x}$As quantum-well heterostructures,[10–12] is the presence of a well-defined photosensitivity peak in an energy region smaller than the width of the GaAs band gap. It is natural to assume that this peak is due to the absorption of light in InAs quantum dots, and that its shape reflects the δ-function character of the density of states function in a quantum dot. The regular continuous shift in the absorption maximum $h\nu_m$ toward lower energies with increasing d is explained by the increasing size of the quantum dots. The surface density of these dots and their size dispersion do not change appreciably, because the height of the peak and its width remain nearly constant.

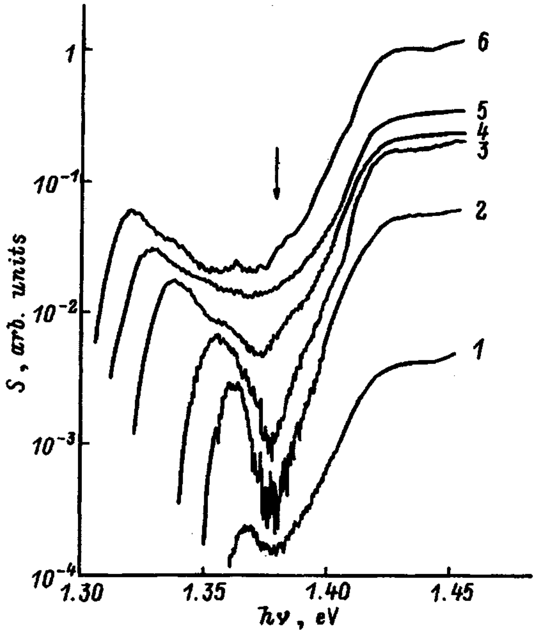

FIG. 1. Capacitive photovoltage spectra for various values of d (300 K). The numbers on the curve correspond to sample numbers in Table I. The arrow shows the theoretical value of the ground-state transition energy in a single-layer InAs quantum well.

At 77 K (Fig. 2) a step-like band is also well resolved with an edge energy of ≈ 1.47 eV. A similar step with edge ≈1.38 eV can also be observed at 300 K (Fig. 1); however, it is less distinct due to temperature-induced blurring of the absorption edge of GaAs. This band is present in all the capacitive photovoltage spectra, with a normalized height and edge position that do not change for $d > 1$ monolayer. The appearance of this band is clearly explained by the for-

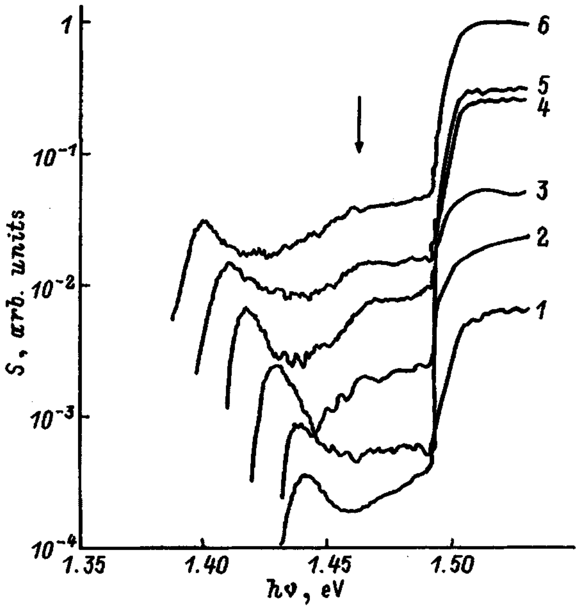

FIG. 2. The same as in Fig. 1 at 77 K. The covering layer is tapered to induce a transition of the quantum-well layer into the space-charge region of the surface barrier.

mation of a wetting layer of InAs with thickness ≈ 1 monolayer. The presence of such a layer has been noted in a number of papers (see, for example, Refs. 1–4,6, and 9). Both values of the edge energy are in agreement with the theoretical estimates calculated for a rectangular InAs quantum well with thickness of 1 monolayer (0.33 nm) according to the model of Ref. 15: 1.464 and 1.374 eV, respectively (indicated by the arrows in Figs. 1 and 2).

Note that the photoluminescence peaks from the GaAs/InAs quantum dots investigated in Refs. 1–4,6, and 7 were shifted rather far into the low-energy region ($h\nu_m \approx 1$ eV at 77 K), whereas a photoluminescence peak is usually observed in the region $h\nu > 1.4$ eV that is assigned to excitons in the wetting layer of InAs. This discrepancy in the values of $h\nu_m$ from the quantum dots, as we will show below, is due to differences in the quantum dot size and shape, which are in turn associated with differences in the technology and growth conditions for the quantum dots.

An alternative assumption, namely that the peaks in the capacitive photovoltage spectra are due to two-dimensional excitons in the wetting layer of InAs, cannot explain a number of features of these spectra: the weak temperature dependence of the normalized height, especially the width, of the peaks in the interval 77–300 K and on the nominal thickness d in the interval 1.1–2.1 monolayers as the function $h\nu_m(d)$ varies continuously, and also the fact that the edge of the stepwise photosensitivity band, which we associate with interband absorption in a quantum-well layer, is independent of d. The latter fact implies that for the technological growth parameters for quantum dots used in this work a transition takes place from layered growth to three-dimensional growth at $d \approx 1$ monolayer, and that further increase in d does not increase the thickness of the wetting layer, but rather supplies the material that goes into creating the quantum dots.

A bulge is observed on the left shoulder of the peaks associated with ground-state transitions with heavy-hole participation $e1-hh1$ in the quantum dot, which can be associated with transitions in which light holes participate, i.e., $e1-lh1$. The shape of the capacitive photovoltage peak is well approximated by a Gaussian function. Analysis shows that the capacitive photovoltage spectra in the range $h\nu < 1.4$ eV can be resolved into two Gaussian peaks from quantum dots with almost the same widths and a band from the quantum well (Fig. 3).

At 77 K (Fig. 4) the photoluminescence spectra exhibit a single peak associated with the transition $e1-hh1$ in the quantum dots. The shape of the peak is also almost Gaussian, with an energy position and width that coincide with the parameters of the corresponding capacitive photovoltage peaks.

Temperature dependence of the capacitive photovoltage and location of the quantum dot relative to the surface barrier. In the original structure, the quantum dots were located in the quasineutral bulk of the GaAs layer. In this case the capacitive photovoltage arises from thermionic emission of holes from the level E_{hh1} into the valence band of GaAs, which subsequently diffuse to the surface of the barrier. In this case the temperature dependence of S_D should have an activation nature, as that in the case of a quantum well: $S_D \sim \exp(-E_a/kT)$, where $E_a = E_{hh1} - E_v$.[11] This temperature dependence of S_D leads to disappearance of the 77 K photosensitivity in the wavelength range where the quantum dots absorb. In order to measure the capacitive photovoltage at 77 K we used layer-by-layer etching of the coating layer, in order to transfer the quantum dots to the barrier region. At a rather strong field of $\sim 10^4$ V/cm, the capacitive photovoltage in the wavelength range where the quantum dots absorb is determined by tunneling emission of electrons through a triangular barrier lowered by the field. The quantum efficiency $\eta_D \approx 1$ ceases to depend on temperature.

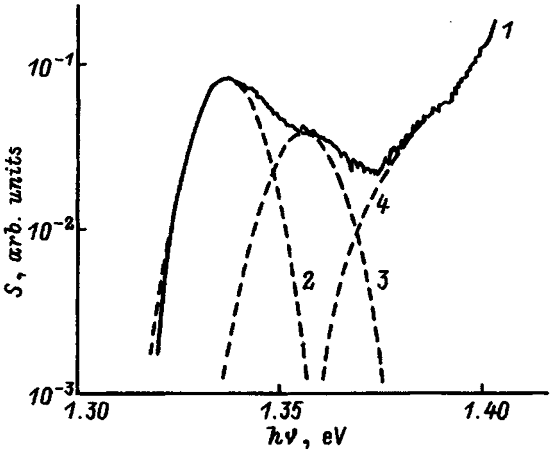

FIG. 3. Approximating the capacitive photovoltage spectra of quantum dots by Gaussian curves for sample 4 (300 K). *1*—capacitive photovoltage spectrum, *2*—photosensitivity peak for the transition *e*1-*hh*1, *3*—the same for the transition *e*1-*lh*1, *4*—capacitive photovoltage spectrum after subtracting curves *2* and *3* from it.

In order for the photosensitivity to appear at 77 K in the wavelength range in which the quantum dots absorb, we found it sufficient to thin L_{bs} by 0.07 μm for samples 1–4 and by 0.14 μm for samples 5 and 6.

When the quantum dots are located in the surface barrier, it is clear from Fig. 2 that S_D does not depend on d within experimental error, i.e., on the size of the quantum

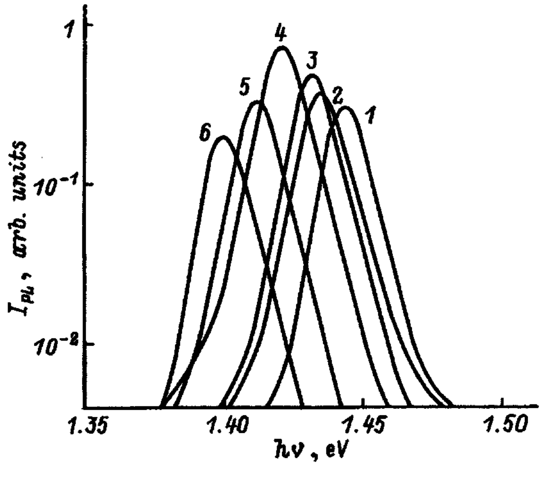

FIG. 4. Photoluminescence spectra for various values of *d* (77 K). The numbers on the curves correspond to sample numbers in Table I.

dot, or on temperature. At 300 K it is also independent of the position of this layer with respect to the barrier. These same regularities have been observed in quantum-well structures,[12] and they imply that $\eta_D \approx 1$. The fact that losses due to recombination do not enter into the capacitive photovoltage effect is attributable to the rather small value of the activated barrier that determines emission of nonequilibrium carriers from the quantum dot. This does not contradict the presence of photoluminescence since the latter is observed at low temperatures and at eight orders of magnitude higher levels of photoexcitation.

The average values of $S_D(h\nu_m)$ for the families of curves, shown in Figs. 1 and 2, are $(4\pm1)\times10^{-2}$ and $(6\pm2)\times10^{-2}$ at 77 and 300 K, respectively. In light of the possible values of η_D in Eq. (6), the absorption coefficient β_m at the maximum is estimated to be 1 to 2×10^{-2}. The presence of a quantum well in the structure under study allows us to determine β_m more precisely, using the quantum well as the absorption standard. The theoretical value $\beta_W \approx 7\times10^{-3}$ is close to that of the absorption edge.[16] It is clear from Figs. 1 and 2 that $S_D(h\nu_m)\approx S_W$, which implies that the corresponding absorption coefficients are almost the same, from which we find by using Eqs. (7)–(9) that $\sigma_D \approx 10\ \text{nm}^2$ and $N_s=(1.2\pm0.3)\times10^{11}\text{cm}^{-2}$. The value of N_s is close to n_s in the quantum-well layer, which indicates a significant equilibrium occupation of the quantum dots by electrons.

Dependence of transition energies on the quantum-dot size. If we assume that the amount of InAs that goes into forming the quantum dots is determined by the thickness d minus one monolayer, we can determine the size of the quantum dot if its shape is known. The latter can be determined by comparing the theoretical dependence of $h\nu_m$ on the quantum dot size, calculated for a given shape of the nanocrystals, with experiment.

The calculations by Grundmann *et al.*[17] were for pyramidal nanocrystals bounded by (110) planes; in Ref. 9 Marzin *et al.* approximated the shape of the nanocrystals by a cone with a base angle of 12.4° resting on a wetting layer one monolayer thick. Our experimental dependences are in better agreement with the latter model.

Figure 5 shows the theoretical function $h\nu_m(D)$ constructed on the basis of the data of Ref. 9. In contrast to Ref. 9, we have plotted along the abscissa not the radius of the cone base under the monolayer r, but rather the diameter of the cone at the monolayer level D. It is clear that the experimental values of $h\nu_m$ for transitions with participation of heavy and light holes are in rather good agreement with the theoretical curves. For our structures the diameter D varied from 6 to 14 nm, depending on d, and the height varied from 0.8 to 1.6 nm for an average distance between quantum dots of $N_s^{-1/2}\approx 30$ nm.

Photoconductivity. In structure 2, whose photoconductivity spectrum we measured, d and the thickness gradient are smaller than in structure 1; therefore, the peaks in the photosensitivity associated with the quantum dots are smaller than the displacement with respect to the intrinsic photosensitivity edge of GaAs (Fig. 6).

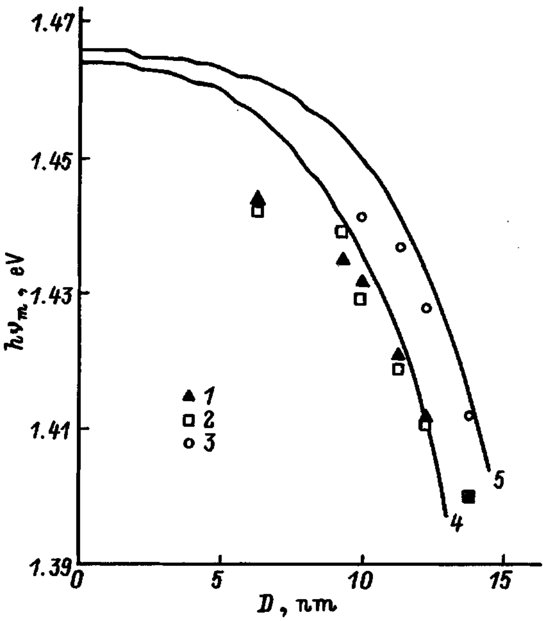

FIG. 5. Dependence of $h\nu_m$ on the size of the quantum dots (77 K): *1*—photoluminescence peak, *2*—primary capacitive photovoltage peak, *3*—secondary peak in the capacitive photovoltage. Theoretical dependences of the transition energies for the model structure of Ref. 9: *4*—*e*1-*hh*1, *5*—*e*1-*lh*1.

With regard to the barrier nature of the photoconductivity of the conducting layers of GaAs, the photoconductivity and capacitive photovoltage phenomena observed in them are closely related, since they are determined by changes in the width and height, respectively, of the surface barrier as a result of exposure to light.[10] In those cases where the contribution to the photoconductivity from the inner barrier at the layer-substrate boundary can be ignored, the small-signal photoconductivity and capacitive photovoltage spectra should coincide, which in fact we observed in our structures.

The regularities in how the photoconductivity spectrum changes as a function of d and temperature were qualitatively analogous to those described above for the capacitive photovoltage. Because of the strong overlap of the quantum-dot

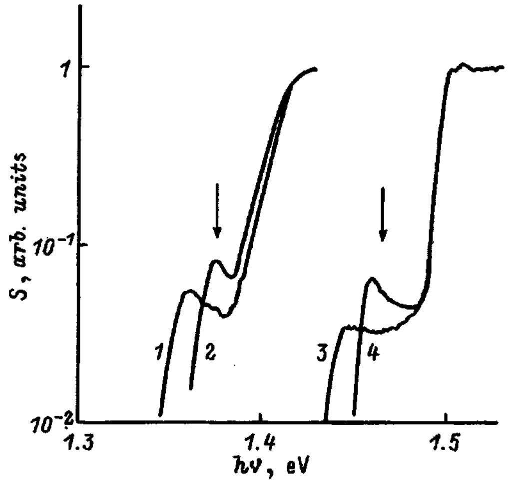

FIG. 6. Photoluminescence spectra of structure 2. *d*, monolayer: *1*,*3*—1.6; *2*,*4*—1.2. *T*, K: *1*,*2*—300 K, *3*,*4*—77 K.

and quantum-well photosensitivity bands, the latter are not resolved in the photoconductivity spectra (the expected position of the edge for these spectra is indicated by an arrow). Indirect evidence of the presence of a quantum well in this structure is the decrease in the value of $S_D(h\nu_m)$ by roughly a factor of 2 for curves *1* and *3*, for which the overlap of the bands is smaller.

This work was supported financially by the Russian Fund for Fundamental Research (95-02-05610 and 95-02-05605), the ''Physics of Solid-State Nanostructures'' Program (2-193), and the Ministry of General and Professional Education (95-0-72-73).

[1] Zh. I. Alferov, D. Bimberg, A. Yu. Egorov, A. E. Zhukov, P. S. Kop'ev, N. N. Ledentsov, S. S. Ruvimov, V. M. Ustinov, and J. Heydenreich, Usp. Fiz. Nauk **165**, 224 (1995).

[2] S. S. Ruvimov, P. Werner, K. Scheerschmidt, J. Heydenreich, U. Richter, N. N. Ledentsov, M. Grundmann, D. Bimberg, V. M. Ustinov, A. Yu. Egorov, P. S. Kop'ev, and Zh. I. Alferov, Phys. Rev. B **51**, 766 (1995).

[3] D. Bimberg, N. N. Ledentsov, M. Grundmann, N. Kirstaedter, O. Schmidt, R. Heitz, J. Bohrer, V. M. Ustinov, A. Yu. Egorov, A. E. Zhukov, P. S. Kop'ev, Zh. I. Alferov, S. S. Ruvimov, P. Werner, U. Gosele, and J. Heydenreich, *Abstracts, Int. Symp. Nanostructures: Physics and Technology* (St. Petersburg, Russia, 1995) p. 167.

[4] G. E. Cirlin, G. M. Guryanov, A. O. Golubok, S. Ya. Tipissev, N. N. Ledentsov, P. S. Kop'ev, M. Grundmann, and D. Bimberg, Appl. Phys. Lett. **67**, 97 (1995).

[5] I. N. Stranski and L. von Krastanov, Sitzungsber. Akad. Wiss. Wien IIb **146**, 797 (1938).

[6] M. Grundmann, J. Christen, N. N. Ledentsov, J. Bohrer, D. Bimberg, S. S. Ruvimov, P. Werner, U. Richter, U. Gosele, J. Heydenreich, V. M. Ustinov, A. Yu. Egorov, A. E. Zhukov, P. S. Kop'ev, and Zh. I. Alferov, Phys. Rev. Lett. **74**, 4043 (1995).

[7] L. N. Bolotov, A. K. Kryganovdkij, I. Kochnev, P. S. Kop'ev, I. V. Makarenko, B. Y. Maltser, A. N. Titkov, M. Fehrenbacher, M. Noeske, H. Rauscher, and P. J. Behm, *Abstracts, Int. Symp. Nanostructures: Physics and Technology* (St. Petersburg, Russia, 1995), p. 193.

[8] C. Weisbuch and B. Vinter, *Quantum Semiconductor Structures: Fundamentals and Applications* (San Diego, Academic Press, 1991).

[9] J.-Y. Marzin, J. M. Gerard, A. Izrael, D. Barrier, and G. Bastard, Phys. Rev. Lett. **73**, 716 (1994).

[10] I. A. Karpovich, V. Ya. Aleshkin, A. V. Anshon, T. S. Babushkina, B. N. Zvonkov, and I. G. Malkina, Fiz. Tekh. Poluprovodn. **24**, 2172 (1990) [Sov. Phys. Semicond. **24**, 1346 (1990)].

[11] I. A. Karpovich, V. Ya. Aleshkin, A. V. Anshon, N. V. Vaĭdus', L. M. Batukova, B. N. Zvonkov, and S. M. Plankina, Fiz. Tekh. Poluprovodn. **26**, 1899 (1992) [Sov. Phys. Semicond. **26**, 1065 (1992)].

[12] I. A. Karpovich and D. O. Filatov, Fiz. Tekh. Poluprovodn. **30**, 959 (1996) [Semiconductors **30**, 961 (1996)].

[13] E. O. Kane, J. Phys. Chem. Solids **1**, 249 (1957).

[14] V. Ya. Aleshkin, E. V. Demidov, B. N. Zvonkov, A. V. Murel', and O. A. Romanov, Fiz. Tekh. Poluprovodn. **25**, 1047 (1991) [Sov. Phys. Semicond. **25**, 631 (1991)].

[15] G. Huang, D. Ji, U. K. Reddy, and T. S. Henderson, J. Appl. Phys. **62**, 3366 (1987).

[16] V. Ya. Aleshkin, A. V. Anshon, and I. A. Karpovich, Fiz. Tekh. Poluprovodn. **27**, 1344 (1993) [Semiconductors **27**, 742 (1993)].

[17] M. Grundmann, O. Stier, and D. Bimberg, Phys. Rev. B **52**, 11 969 (1995).

Translated by F. Crowne

Quantum-dot lasers: Principal components of the threshold current density

S. V. Zaĭtsev, N. Yu. Gordeev, V. I. Kopchatov, A. M. Georgievskiĭ, V. M. Ustinov,
A. E. Zhukov, A. Yu. Egorov, A. R. Kovsh, N. N. Ledentsov, P. S. Kop'ev, and Zh. I. Alfërov

A. F. Ioffe Physicotechnical Institute, Russian Academy of Sciences, 194021 St. Petersburg, Russia

D. Bimberg

Institut für Festkörperphysik, Technische Universität Berlin, D-10623 Berlin, Germany

(Submitted February 4, 1997; accepted for publication February 10, 1997)
Fiz. Tekh. Poluprovodn. **31**, 1106–1108 (September 1997)

Injection heterolasers based on quantum dots grown by molecular-beam epitaxy have been investigated. It is shown that the room-temperature threshold current density can be lowered to 15 A/cm^2 by decreasing the nonradiative recombination and increasing the degree of carrier localization. The density of states in structures with vertically coupled quantum dots was investigated by the electroabsorption method. © *1997 American Institute of Physics.* [S1063-7826(97)01809-7]

Lasers with quantum dots (QDs) in an InAs/GaAs/AlGaAs system are of interest because of their spectral properties. Generation in a single longitudinal mode and a narrow optical gain spectrum have been observed.[1] These lasers also possessed a high temperature stability at low temperatures. At the same time, the threshold current density at room temperature was quite high ($\sim$900 A/cm^2). Electroluminescence investigations of these structures have shown that this is due mainly to strong nonradiative recombination in the active region. Another reason is activational migration of carriers out of the QD states at room temperature. For such structures a transition from lasing via a QD state to lasing via a state of the so-called wetting layer has been observed.[2] By using arrays of vertically coupled (VC) QDs[3] we were able to avoid these effects, but carrier delocalization from the QDs still remained the main obstacle for improving laser characteristics. Using AlGaAs as a QD matrix made it possible to decrease the threshold current density substantially and raise the stimulated emission efficiency.[4] However, estimates show that these parameters can still be substantially improved. In the present work we investigated the main leakage mechanisms that prevent the characteristics of QD lasers from coming close to the theoretical limits.

AlGaAs/GaAs laser structures were grown on a silicon–doped GaAs (100) substrate in a Riber 32P molecular–beam epitaxy system. The active region consisted of three or ten layers of vertically coupled $In_{0.5}Ga_{0.5}As/Al_{0.15}Ga_{0.85}As$ QWs ($N=3$ or 10, respectively).[5] The vertically coupled QDs self-organized during the deposition of several layers of $In_{0.5}Ga_{0.5}As$ QDs (the effective $In_{0.5}Ga_{0.5}As$ was 12 Å thick), the QD layers was separated by a 50-Å-thick GaAs or AlGaAs layer.

Lasers with a closed ring mode were fabricated. The laser characteristics were investigated with a pulsed pump current (pulse duration 3 μs and pulse repetition frequency 5 kHz) in the temperature range 80–300 K. To investigate the mechanisms of internal leaks in QD lasers, we studied the efficiency of the stimulated and spontaneous recombination at different temperatures. To investigate the internal efficiency of spontaneous processes, the radiation was measured through a special window in the top contact of the laser structure. Special attention was devoted to suppressing lasing. This enabled us to estimate the losses to nonradiative recombination of carriers as a function of the pump current density assuming that the maximum efficiency of the spontaneous radiative recombination is close to 100% at 77 K. Similar specimens were used to investigate electroabsorption. The detected radiation passed through the substrate and

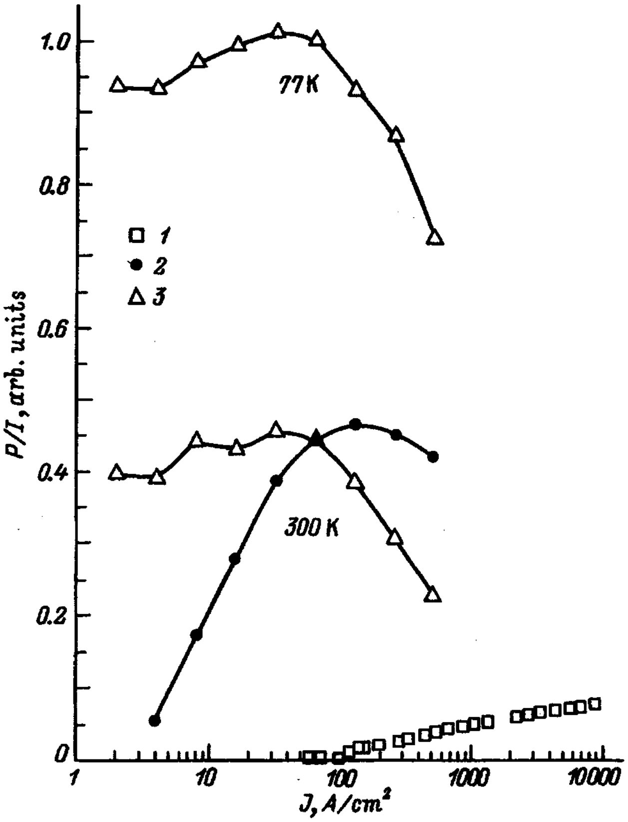

FIG. 1. Internal quantum efficiency P/I versus pump current density J. Structures: InGaAs/GaAs, single-layer; *2* — InGaAs/GaAs, $N=10$; *3* — InGaAs/AlGaAs.

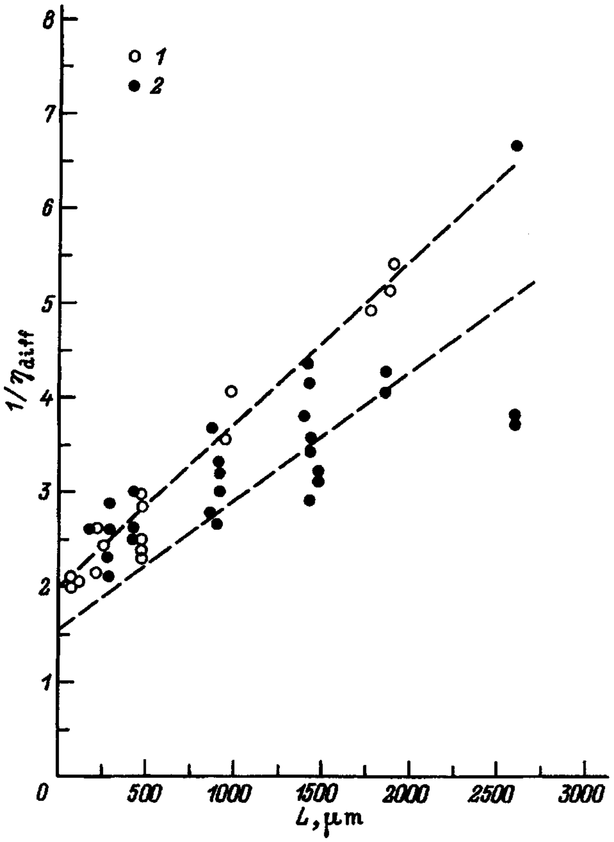

FIG. 2. Reciprocal of the quantum differential efficiency $1/\eta_{\text{diff}}$ of stimulated emission versus cavity length L of InGaAs/GaAs lasers.

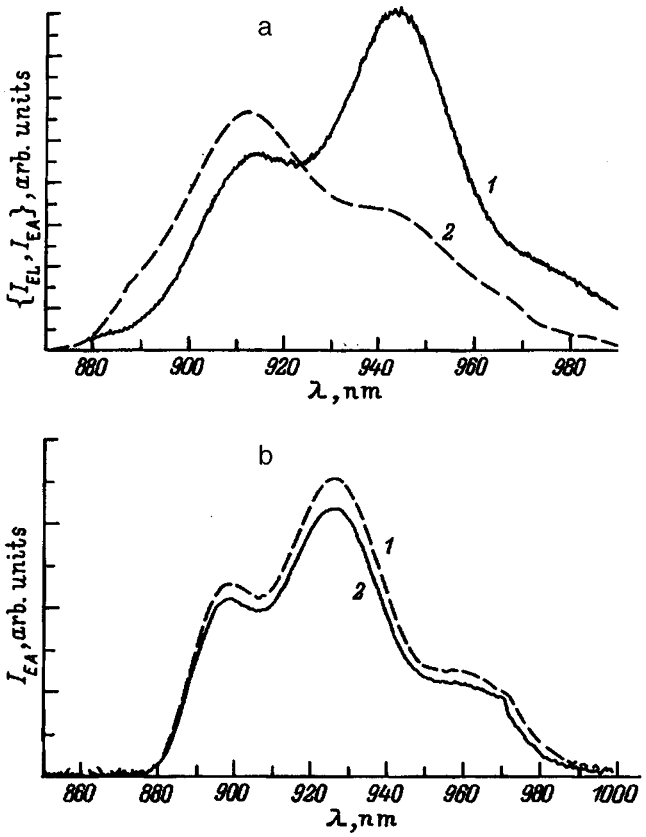

FIG. 3. a — Electroluminescence (*1*) and electroabsorption (*2*) spectra for structures with QDs. b — Electroabsorption spectra with bias voltages 0 (*1*) and 4 V (*2*).

was absorbed in layers with QDs. The electroabsorption spectra adequately represent the distribution of the density of states in the active region. To estimate the quantum efficiency of stimulated recombination, lasers with a strip geometry and different cavity lengths were prepared. Extrapolating to the ordinate the cavity length dependence of the reciprocal of the differential quantum efficiency gives the internal quantum efficiency of lasing.

One can see from Fig. 1 that the internal quantum efficiency of spontaneous radiative recombination in single-layer laser heterostructures based on InAs/GaAs QDs was very low and nonradiative recombination processes did not saturate up to a 10-kA/cm^2 pump current. Optimization of the growth process and the use of several InGaAs/GaAs QD layers enabled us to increase this parameter tenfold at the threshold current density. Although this efficiency at room temperature did not exceed 40% of its value at 77 K, its increase was the main reason for the corresponding decrease of the threshold current density from 1 kA/cm^2 to 100 A/cm^2.

To decrease the thermal activation of the carriers from the QD states $Al_{0.15}Ga_{0.85}As$ was used as the matrix. One can see from Fig. 1 that the spontaneous recombination efficiency with a low excitation level was higher in this case as well. We assume that this increase can be explained by the decrease of the threshold current density to 60 A/cm^2 as a result of stronger carrier localization. Nonetheless, at room temperature again only 40% of the carriers participate in radiative recombination. A characteristic feature of the latter curve is a large decrease in the efficiency with increasing current density for InGaAs/AlGaAs structures, while for InGaAs/GaAs structures with vertically coupled QDs it remained virtually constant above the lasing threshold.

Figure 2 shows the effect of using a matrix of this type with QDs on the differential quantum efficiency of induced emission (η_{diff}). It is evident that the efficiency increases with decreasing cavity length in a wide range (with the exception of relatively short lasers). While for vertically coupled InGaAs/GaAs QDs the limit of the reciprocal of the differential quantum efficiency equals approximately 2 (internal efficiencies of the order of 50%), for vertically coupled InGaAs/GaAs QDs this limit is close to 1.5 (internal efficiency of the order of 65%). Therefore, approximately 35% of the carriers still recombine via the excited states and the states of the wetting layer in the spontaneous regime.

The results of the investigation of electroabsorption are shown in Fig. 3. It can be concluded from the fact that, on the one hand, the electroluminescence spectrum I_{EL} is essentially identical to the electroabsorption spectrum I_{EA} and, on the other hand, the spectrum remains unchanged with increasing bias voltage that the electroabsorption spectrum is due mainly to the distribution of the density of states in the QDs. In any case, the absence of a shift or change in the shape of the absorption edge with increasing reverse-bias voltage is completely atypical for quantum layers. This makes the investigation of the electroabsorption spectra an effective method for studying the size distribution of QDs.

In summary, two principal mechanisms of carrier leakage from the ground states of QDs have been found in structures with vertically coupled QDs. Nonradiative recombination of different types prevents carriers from settling in the ground states of the QDs and excludes them from the amplification process. We estimated the contribution of each mechanism in order to calculate the real current density applied to the QDs at the lasing threshold. Only 65% of the carriers participating in radiative recombination contribute to stimulated emission, and the internal quantum efficiency is of the order of 40%. Therefore, approximately 25% of the current is used to reach the lasing threshold.

The results obtained show that although a very low threshold current density and a high lasing effiiciency have already been obtained, the potential possibilities for laser heterostructures based on vertically coupled QDs are still very high. Actually, it has been shown that a threshold current density of 15 A/cm^2 can be achieved at room temperature without changing the composition and number of QDs. No fundamental mechanisms preventing a further increase in the lasing efficiency have been found. It was proposed that the electroabsorption method be used to investigate the density of states in QDs.

[1] S. V. Zaitsev, N. Yu. Gordeev, M. P. Soshnikov, A. Yu. Egorov, A. E. Zhukov, V. M. Ustinov, N. N. Ledentsov, and P. S. Kop'ev, *SPIE Proceedings on Optical Dimension and Materials (OPDIM) Conference*, Kiev (1995), No. 2648-45, p. 287.

[2] Zh. I. Alferov, N. Yu. Gordeev, S. V. Zaitsev, P. S. Kop'ev, I. V. Kochnev, V. V. Komin, I. L. Krestnikov, N. N. Ledentsov, A. V. Lunev, M. V. Maximov, S. S. Ruvimov, A. V. Sakharov, A. F. Tsatsul'nikov, Yu. M. Shernyakov, and D. Bimberg, Fiz. Tekh. Poluprovodn. **30**, 357 (1996) [Semiconductors **30**, 197 (1996)].

[3] V. M. Ustinov, A. Yu. Egorov, A. E. Zhukov, N. N. Ledentsov, M. V. Maksimov, A. F. Tsatsul'nikov, N. A. Bert, A. A. Kosogov, P. S. Kop'ev, Zh. I. Alferov, and D. Bimberg, in *Proc. Mater. Res. Soc.,* Boston, USA (1995), Vol 417, p. 141.

[4] S. V. Zaitsev, N. Yu. Gordeev, V. M. Ustinov, A. E. Zhukov, A. Yu. Egorov, N. N. Ledentsov, M. V. Maximov, P. S. Kop'ev, Zh. I. Alferov, and D. Bimberg, Superlattices Microstruct. (1997), to be published.

[5] V. M. Ustinov, A. Yu. Egorov, A. E. Zhukov, M. V. Maksimov, A. F. Tsatsul'nikov, N. Yu. Gordeev, S. V. Zaitsev, Yu. M. Shernyakov, N. A. Bert, P. S. Kop'ev, Zh. I. Alferov, N. N. Ledentsov, J. Bohrer, D. Bimberg, A. O. Kosogov, P. Werner, and U. Gosele in *Ninth International Conference on Molecular Beam Epitaxy*, Malibu, CA, USA (1996).

Translated by M. E. Alferieff

The effect of a ‘‘Coulomb well’’ on the absorption and magnetoabsorption spectra of strained InGaAs/GaAs heterostructures

A. V. Kavokin, S. I. Kokhanovskiĭ, A. I. Nesvizhkiĭ, M. É. Sasin, R. P. Seĭsyan,
V. M. Ustinov, A. Yu. Egorov, A. E. Zhukov, and S. V. Gupalov

A. F. Ioffe Physicotechnical Institute, Russian Academy of Sciences, 194021 St. Petersburg, Russia

(Submitted December 5, 1996; accepted for publication February 20, 1997)
Fiz. Tekh. Poluprovodn. **31**, 1109–1120 (September 1997)

The optical and magnetooptical properties of strained InGaAs/GaAs quantum-well heterostructures grown by molecular-beam epitaxy were studied at $T=1.7$ K in magnetic fields $B\leqslant 7.5$ T. The well-resolved oscillatory structure of the magnetoabsorption spectra makes it possible to reproduce the ‘‘fan diagrams’’ for transitions between Landau levels of the $HH1E1$ quantum-confined states, taking into account exciton binding energies calculated variationally. Based on these results, reduced cyclotron masses of carriers were calculated for quantum wells with various indium contents. A self-consistent variational solution to the exciton problem in the structure under study shows that for weak type-II potentials the effect of Coulomb localization of the hole leads to a relative increase in the oscillator strength of the $LH1E1$ exciton transition. In this case the $LH1E1$ and $LH3E1$ exciton transitions remain spatially direct and retain a considerable intensity. The calculated splitting of ~ 9 meV between these two states in zero magnetic field is found to be in agreement with experiment. The significant oscillator strength of light-hole excitons, along with the observed doublet structure, are experimental confirmations that electron-hole attraction can transform a rather low barrier for light holes in a type-II structure into a quantum well with a parabolic ‘‘Coulomb’’ shape near its bottom, i.e., a ‘‘Coulomb well.’’
[S1063-7826(97)01909-1]

1. INTRODUCTION

The usual objects of study in the physics of low-dimensional heterostructures are quantum wells and type-I superlattices, where the carriers are confined in a single layer. In recent years, however, considerable attention has been focused on type-II heterostructures and systems in which a type-I–type-II transition can take place. In such a transition the potential well becomes a barrier to one type of carrier. In these systems, the exciton spectrum differs greatly from that of a type-I quantum well, which allows one to observe unique phenomena. One member of this promising class of heterosystems is InGaAs/GaAs, which belongs to the so-called mixed class with regard to the spatial separation of carriers. Mechanical stress arising from the mismatch of the barrier-layer and well-layer lattice constants causes the quantum wells to have a type-I energy profile for the heavy-hole exciton, whereas for the light-hole exciton the quantum well becomes a rather low barrier corresponding to a weak type-II profile. Accordingly, it is assumed that transitions from the light-hole state are associated with spatially indirect excitons, in which a hole from the ‘‘barrier’’ GaAs layer, which becomes a potential well for light holes, is bound to an electron from the InGaAs quantum well.

However, the spectral feature observed in absorption,[1] photoconductivity,[2] and electroreflectance,[3] which is usually associated with the spatially indirect exciton transition $LH1$ $E1$, does not differ significantly from other spectral lines associated with spatially direct type-I excitons. A theoretical description of the exciton states of this system near the transition point from type-I to type-II must include a ‘‘composite’’ energy profile for the exciton hole arising from both the quantum-well and Coulomb potentials. As far as we know, no previous attempt has been made to do this, which leaves unresolved the question of whether the exciton observed in these spectra is spatially direct or indirect.

In this paper we report the results of an experimental study of the hole energy profile and excitonic states of InGaAs/GaAs quantum-well heterostructures. These investigations are based on examining the absorption and oscillatory magnetoabsorption spectra of the latter. Comparison of experimental data with calculated energies and oscillator strengths for various excitonic states near the type-I–type-II transitions leads us to propose a model in which the $LH1E1$ and $LH3E1$ states of a type-II heterostructure become spatially indirect and direct above-barrier excitonic states, respectively.

2. SAMPLES AND EXPERIMENTAL PROCEDURE

The GaAs heterostructures were grown by molecular beam epitaxy, using GaAs films with (100) oriented surfaces as substrates. The structures consisted of twenty isolated quantum-well $In_xGa_{1-x}As$ layers separated by GaAs barriers ($x=0.15$, 0.2, quantum-well width $L_z=80$ Å, and barrier thicknesses $L_b=400$, 800 Å).

Optical measurements were made at $T=1.7$ K in a pumped-out helium cryostat with a superconducting solenoid, which allowed us to obtain magnetic fields up to 7.5 T. The samples were immersed in liquid helium in free form. Spectra were obtained for left- and right-circularly polarized

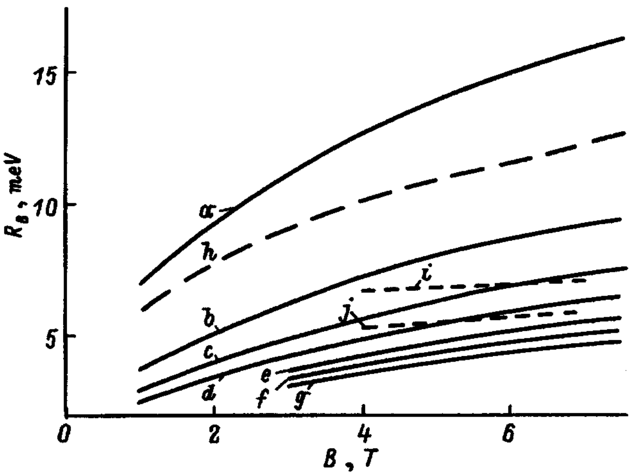

FIG. 1. Binding energy of diamagnetic excitons (R_B) in $In_{0.2}Ga_{0.8}As$/GaAs heterostructures with quantum wells ($L_z = 80$ Å) as a function of magnetic field B for transitions between various Landau subbands with quantum numbers l to various quantum-well levels. $HH1L1$, $l_c = 0$ (a), *1* (b), *2* (c), *3* (d), *4* (e), *5* (f), *6* (g); $HH2E2$, $l_c=0$ (h); LH(n)$E1$, $n=0$ (i), *2* (j). l_c corresponds to the index of the electronic Landau level to which the transition occurs, n is the number of the ''oscillator'' level of the ''Coulomb well.''

light in the Faraday geometry using a high-transmission diffraction monochromator.

3. THEORY

The binding energies of various excitonic states (R_B) of a quantum well placed in an external magnetic field (B) can be obtained by solving the corresponding Schrödinger equation variationally:[4]

$$R_B = \frac{3}{16}\frac{\hbar^2 a_\perp^2}{\mu_\perp L^4} + \frac{\hbar^2}{2\mu_\perp a_\perp^2} + \frac{4}{a_\perp^2}\int \rho d\rho e^{-2\rho/a_\perp} V(\rho) - \hbar\omega_c^e\left(l_e + \frac{1}{2}\right) - \hbar\omega_c^h\left(l_h + \frac{1}{2}\right), \qquad (1)$$

where

$$V(\rho) = -\frac{e^2}{\kappa}\int_{-\infty}^{\infty}\int_{-\infty}^{\infty} dz_e dz_h \frac{U_e^2(z_e)U_h^2(z_h)}{\sqrt{\rho^2 + (z_e - z_h)^2}}. \qquad (1a)$$

Here L is the magnetic length, $a_\perp$ is the Bohr radius of an exciton in the plane of the quantum well, $\mu_\perp$ is the reduced mass of the exciton in the plane of the well, κ is the dielectric permittivity, $U_{e(h)}(z_{e(h)})$ is the electron (hole) wave function normal to the plane of the quantum well, $\omega_c^{e(h)}$ is the electron (hole) cyclotron frequency, and ρ is the electron-hole coordinate for relative motion in the plane of the quantum well. In this paper we let $a_\perp$ be a variational parameter, which we find by minimizing the function $R_B(a_\perp)$. The masses of the heavy and light holes in the plane of the layer are given by the well-known Luttinger parameters for GaAs and InAs. We will use the spherical approximation, along with the assumption that the Luttinger parameters depend linearly on x. The binding energies obtained from Eq. (1) are shown in Fig. 1.

Besides creating excitons, the Coulomb interaction affects optical transitions in size-confined structures in another way: when the motion of a charge carrier is spatially bounded, its electrostatic attraction will modify the shape of the potential seen by a charge carrier of the opposite sign. This leads to warping of the original potential, in general, creating a well with its bottom at the center of the quantum-well structure. In type-I heterostructures this ''Coulomb well'' is present in both the electron and hole wells. However, it is rarely taken into account, because its depth does not exceed one or two dozen meV.

In general, the Coulomb well for the hole band is given by the potential

$$V_h(z_h) = -\frac{e^2}{\kappa}\int_0^{\infty} 2\pi\rho d\rho \int_{-\infty}^{\infty} dz_e \frac{f^2(\rho)U_e^2(z_e)}{\sqrt{\rho^2 + (z_e - z_h)^2}}. \qquad (2)$$

Here $f(\rho)$ is the wave function of the two-dimensional electron-hole relative motion, which in our case is a trial function. It is conveniently chosen in the form $f(\rho) = \sqrt{2/\pi}a_\perp^{-1}\exp(-\rho/a_\perp)$. For the electron potential $V_e(z_e)$ we must replacee $U_e(z_e)$ by $U_h(z_h)$ in Eq. (2) and integrate over z_h. A fully self-consistent variational calculation of the energy levels will take into account electrostatic effects of the Coulomb field automatically. Analytic expressions for Coulomb-well effects were obtained for the first time by Efros in Ref. 5, using perturbation theory. However, his analytic solution required the infinite-barrier approximation, which makes the spectrum of eigenstates arising in an infinite Coulomb well identical to the spectrum of a one-dimensional harmonic oscillator, which consists of equidistant oscillator levels with oscillator quantum numbers $n = 0, 1, \ldots$.

In general, we must superimpose the quantum-well and Coulomb potentials. When the quantum-well energy dominates, the energy of the state in the well adds to the energy of an oscillator state, which puts the total energy outside the parabolic range of the Coulomb potential. This implies that the total shift of the energy levels is insignificant. However, when the height of the barrier equals the depth of the well, and when the well becomes a barrier, $V_{h,e}(z_{h,e})$ will exceed the quantum-well potential. In this case, the role of the Coulomb well becomes dominant, and determines both the energy spectrum of the states and the oscillator strength of the transitions. This situation must inevitably arise in the neighborhood of a type-I to type-II transition.

It is obvious that for our systems, i.e., quantum-well layers made up of $In_xGa_{1-x}As$/GaAs heterojunctions, increasing x leads to a proportional decrease in the width of the band gap E_g(InGaAs). However, this decrease is accompanied by a strain $\varepsilon = -\Delta a/a$ that increases with x, where a is the lattice constant of an unstrained solid solution with indium content x, and Δa is the difference between lattice periods of the solid solution and the base GaAs layer. The behavior of the deformation potential and elastic constants of InGaAs (assuming they vary linearly with x) lead us to conclude that the diagonal component of the strain tensor (the ''hydrostatic'' component of the strain) causes the reverse process, i.e., it tends to make the band gaps equal. The final

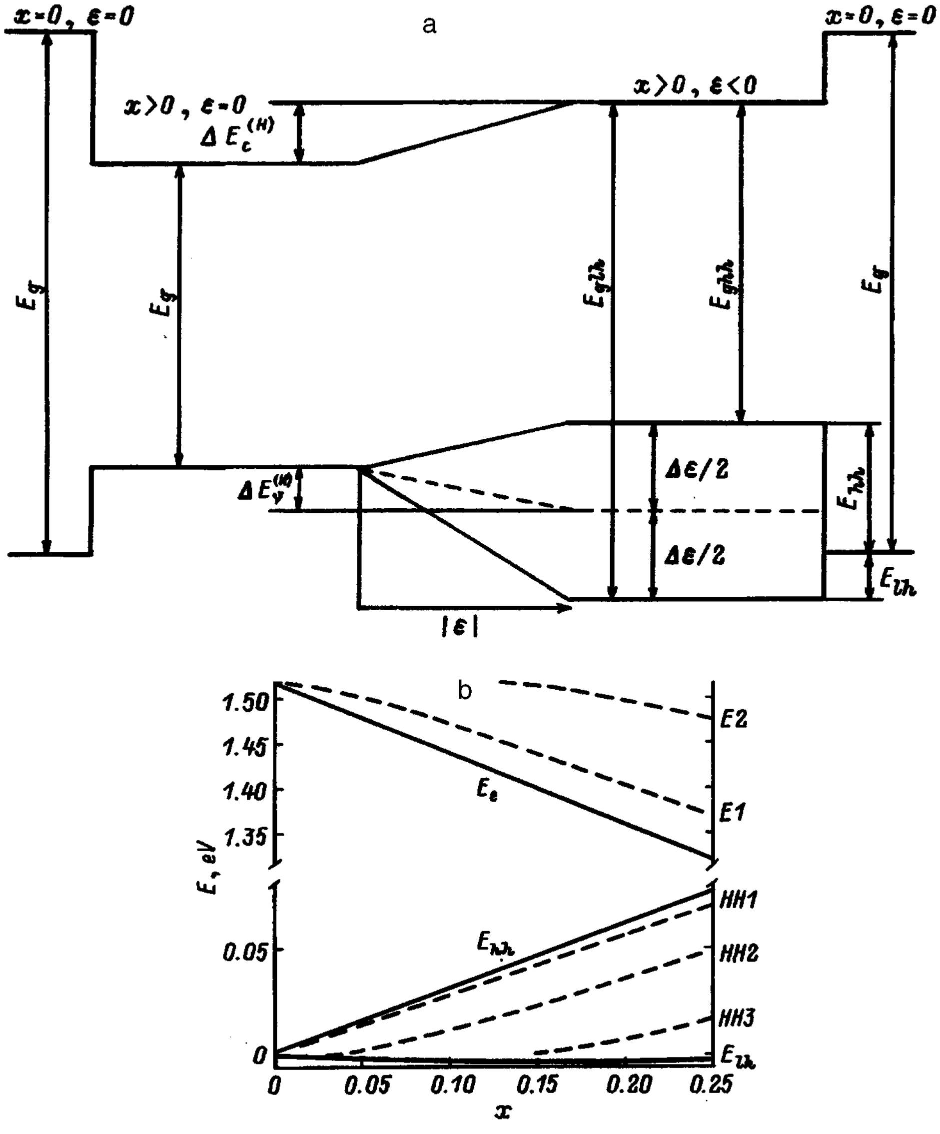

FIG. 2. Energies of quantum-well levels in strained $\mathrm{In}_x\mathrm{Ga}_{1-x}\mathrm{As/GaAs}$ layers. a: energy scheme illustrating the formation of barriers or wells, depending on composition (x) and strain (ε). b: thin solid curves—motion of the edges of the conduction band and valence band with increasing x; the dashed curves show the change with x of the energies of quantum-well states of an electron ($E1$, $E2$) and a heavy hole ($HH1$, $HH2$, $HH3$) for $L_z = 80$ Å; the thick solid curves (lower curve) is $E_{lh}(x)$.

result is found to depend on the axial component, which splits the valence band and drives the heavy holes upward into the band gap. As for the light holes, the top of their band lies above the wells for nearly all compositions of the solid solution in the range $0 \leqslant x \leqslant 0.25$ (Fig. 2). Note that expulsion of the light-hole states from the well is confirmed by a number of direct experiments (see, for example, Ref. 2). Changing the material parameters within the range of possible values has only a slight effect on this result. The ratio of conduction and valence band offsets, $Q = \Delta E_c / \Delta E_v$, turns out to be important. In general, this relation also depends on x. Thus, for the position of the top of the light-hole valence band we may write:

$$E_{lh}(x) = \Delta E_v^0(x) + \Delta E_v^{(H)}(x) - \Delta_\varepsilon(x)/2 - (9/16)\Delta_\varepsilon^2(x)/\Delta_0(x), \qquad (3)$$

where $\Delta E_v^0(x)$ is the fractional change in the width of the band gap as a function of x measured from the valence band, without including strain; $\Delta E_v^{(H)}$ is the fractional change in the width of the bandgap due to hydrostatic strain, measured from the valence band; $\Delta_\varepsilon(x)$ is the strain-induced splitting of the valence band; and $\Delta_0(x)$ is the spin-orbit splitting energy for a given composition. According to Ref. 6, at $T=2$ K we have $E_g(x)[\mathrm{eV}] = 1.5192 - 1.5837x + 0.475x^2$; for the unstrained state we have[7] $Q = 0.85/0.15$. Comparison with the experiments of Ref. 8 lead us to propose that the hydrostatic component, which is proportional to the strain, be distributed in the ratio $Q_\varepsilon^{(H)} = 0.89/0.11$. A more fundamental approach would be to assume for this quantity the corresponding ratio of partial hydrostatic deformation potential constants: $Q_\varepsilon^{(H)}(x) = a_c(x)/a_v(x)$, which also depends on x. For a given composition, an estimate of the value of a_v that is linear in x is $a_v(x)[\mathrm{eV}] = 1.16 - 0.16x$ (Ref. 7). However, the partial parameters are difficult to measure and are not reliably known. Thus, the second term in Eq. (3) is written as follows (see Ref. 9):

$$\Delta E_v^{(H)}(x) = a^*(x)[2 - \lambda(x)]\varepsilon(x), \qquad (4)$$

where $\lambda(x) = 2c_{12}(x)/c_{11}(x)$ for the (100) plane. Invoking Vegard's law, we obtain $\varepsilon(x) = -x/(13.9 + x)$ and write the coefficient $a^*(x)$ in two ways: 1) as $0.11a(x)$, where $a(x) \times [\mathrm{eV}] = -8.68 + 2.77x$ (based on Ref. 8), and 2) as $a_v(x)$,

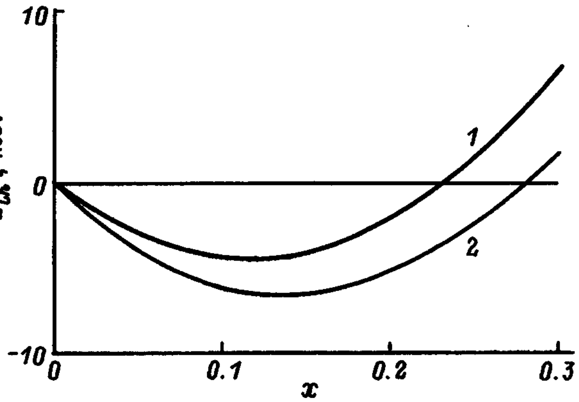

FIG. 3. Change in the position of the top of the valence band for light holes E_{lh} as a function of x. *1,2*—two ways to calculate the hydrostatic component of the strain-induced shift of the top of the valence band $E_v^H(x)$, as explained in the text.

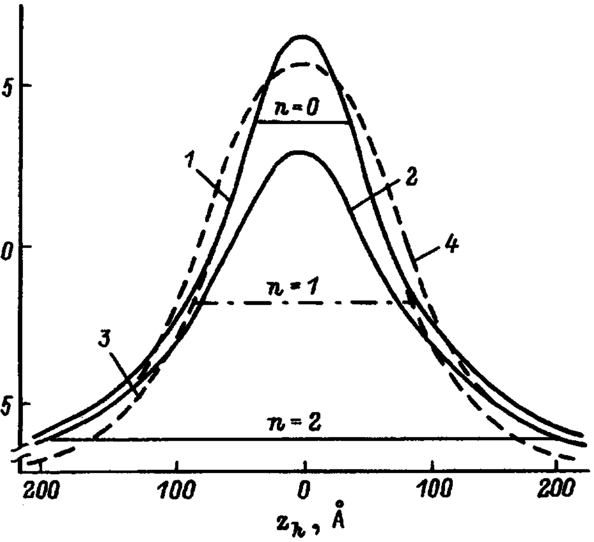

FIG. 4. Real shape of the "Coulomb well" in the $In_xGa_{1-x}As/GaAs$ system with a quantum-well layer of thickness $L_z = 80$ Å(in *1,2*) and its approximation (in *3,4*) for two values of the fitting parameter $a_\perp$. In *1,3*—$a_\perp = 100$ Å, in which case $V_0 =$ 16.7 meV and the first $n=0$ oscillator level is well defined; in *2,4*- $-E_1 =$ 14 meV, in which case $V_0 =$ 13.5 meV, and the third $n=2$ level $E_3 =$ 3 meV is well defined.

i.e., the form given above. The elastic stiffness constants are chosen to equal $c_{12}(x) = 11.26 - 2.93x$ and $c_{11}(x) = 5.71 - 1.18x$ (Ref. 6), and the deformation-potential splitting is defined as in Ref. 9:

$$\Delta_\varepsilon(x) = 2|b(x)|(1 + \lambda(x))|\varepsilon(x)|, \tag{5}$$

where $b(x)[\mathrm{eV}] = -1.7 - 0.1x$ (Ref. 8). Using the expression $\Delta_0(x)[\mathrm{eV}] = 0.341 - 0.09x + 0.40575x^2$ from Ref. 6, we obtain the results shown in Fig. 3. According to these calculations, the value of V_{lh} for light holes is 5 ± 2 meV for compositions in the range $0.05 < x < 0.20$, dropping to zero at $x=0$ and $x = 0.25 \pm 0.03$. It is also necessary to include the renormalization of the barrier height due to the unequal hole effective masses in the well and barrier materials. The origin of this renormalization is the nonzero wave vector of holes in the quantum well, which in turn is a consequence of the Coulomb attraction between the exciton electron and hole. This effect was discussed in detail by one of us in Ref. 10. Using results from that paper, we estimate that the height of the heavy-hole potential barrier is lowered by 3 ± 1 meV for our materials, while the height of the type-II light-hole potential increases by 3 ± 1 meV in a quantum well of width 80 Å. In the end, we have $E_{lh} =$ 7 ± 3 meV. Meanwhile, numerical calculations based on Eq. (2) predict that the Coulomb well for light holes has a depth of $V_{lh}^{(0)} = -15$–20 meV. Consequently, the attractive Coulomb well clearly overwhelms the barrier repulsion for light holes in this case, indicating that its role is decisive.

We can draw no practical inferences from the Coulomb-well picture unless we take into account the finite barrier height. In that case we see that the potential [Eq. (2)] is not parabolic as in Ref. 5, but rather bell-shaped, with a smooth transition to a constant value at large distances from the center of the well. In general form, the problem turns out to be difficult to solve analytically, which motivates us to look for some way to approximate the potential that is maximally close to the real potential [Eq. (2)] and allows a rigorous (variational) fit to the energy levels of interest to us. We choose the well-known hyperbolic function $cosh^2 z$ [see Eq. (11)] for this purpose, which reduces to a constant (flat) potential for large z and to a parabola as $z \to 0$. We can thus approximate the potential in Eq. (2) by the function

$$V_h(z_h) = -\frac{V_0}{\cosh^2 \alpha z_h}, \tag{6}$$

where V_0 and α are fitting parameters chosen in such a way that there is agreement between potentials in Eqs. (2) and (6). The wave functions of the electron and heavy hole depend primarily on the quantum-well phenomenon, and can be viewed as wave functions of an isolated particle in a square well perturbed by the Coulomb potential (see Ref. 4). On the other hand, the wave function of the light hole in a type-II quantum well with a very small band offset is determined by the Coulomb potential Eq. (2).

For comparison, in Fig. 4 we show the "true" shape of the Coulomb well obtained by numerical calculations based on Eq. (2), and its approximation based on Eq. (6). Clearly, it is difficult to choose parameters of this problem such that good agreement is observed over the entire energy interval. Therefore, once we solve the problem self-consistently, we choose these parameters for the energy interval of interest to us. It is especially difficult to obtain a "good" result for oscillator levels with large oscillator quantum numbers n, which bunch together as $n \to \infty$. This forces us to fit the parameters self-consistently for each level individually. The wave functions of particles in the potential [Eq. (6)] are well known:[7]

$$\psi_n = (1 - \xi^2)^{q/2} F\left(-n, 2q + n + 1, q + 1, \frac{1 - \xi}{2}\right), \tag{7}$$

where

$$F(\alpha,\beta,\gamma,\delta)=1+\frac{\alpha\beta\delta}{\gamma}\frac{1}{1!}+\frac{\alpha(\alpha+1)\beta(\beta+1)\delta^2}{\gamma(\gamma+1)}\frac{1}{2!}+\dots.$$

Here $\xi=\tan\,\alpha z_h$, $q=(-2m_hE_h/\hbar^2\alpha^2)^{1/2}$, E_h is the hole energy, and m_h is the mass of a hole in the z direction.

In the present case, where $\alpha=-n$, the expression for ψ_n can easily be found:

$$\psi_0=(1-\xi^2)^{q/2},$$

$$\psi_1=(1-\xi^2)^{q/2}\xi,$$

$$\psi_2=(1-\xi^2)^{q/2}[1-(2\xi+3)(1-\xi^2)/2(\xi+1)], \tag{8}$$

etc. It is worth noting that the functions ψ_n should be normalized by the condition

$$\int_{-\infty}^{\infty}dz_h\psi_n^2(z_h)=1. \tag{9}$$

The wave functions ψ_n are perturbed by the presence of a type-I or type-II quantum-well potential. We first include only the mixing between hole states ψ_0 and ψ_2, since the smooth quantum-well potential ensures mixing of states of the same parity. Therefore, hole states ψ_1, ψ_3 need not be taken into account. On the other hand, the rectangular quantum-well potential for light holes is considerably weaker than $V_h(z_h)$ for light holes, and consequently can be treated as a perturbation. A similar approach was developed in Ref. 12 to describe the Stark effect in a mixed type-I–type-II quantum well. The perturbed wave functions can be written in the following way:

$$\overline{\psi_0}=A(\psi_0+C\psi_2), \tag{10a}$$

$$\overline{\psi_2}=B(\psi_2-C\psi_0), \tag{10b}$$

where

$$C=\frac{V_b}{(E_0-E_2)}\int_{-L_z/2}^{L_z/2}\psi_0(z_h)\psi_2(z_h)dz_h,$$

where A and B are normalization constants, and E_0 and E_2 are eigenenergies of the corresponding unperturbed states,

$$E_n=-\frac{\hbar^2\alpha^2}{8m_{h\|}}\left[-(1-2n)+\sqrt{1+\frac{8m_{h\|}V_0}{\alpha^2\hbar^2}}\right] \tag{11}$$

V_b is the original depth (height) of the quantum well (barrier), which is assumed to be negative for type I and positive for type II (in our case, $V_b\equiv E_{lh}$).

Replacing $U_h(z_h)$ in the potential [Eq. (1a)] by wave functions (10a) and (10b) allows us to compute the binding energy for the two lowest states of the light-hole exciton in a type-II heterostructure. We will calculate this self-consistently in what follows. We first set the Bohr radius of the exciton $a_\perp$ in the plane of the quantum well equal to the Bohr radius of a two- dimensional exciton. This allows us to compute the potential Eq. (2) and the wave functions $\overline{\psi_0}$ and $\overline{\psi_2}$ to first approximation. We then find a refined value of $a_\perp$ by variationally solving the problem of an exciton in a quantum well distorted by the Coulomb potential [Eq. (2)] with the zero-order wave functions $\overline{\psi_0}$ and $\overline{\psi_2}$ (for more detail, see Refs. 4 and 12). We then compute more precise wave functions $\overline{\psi_0}$ and $\overline{\psi_2}$ with the new $a_\perp$, and continue until we have satisfactory accuracy.

This approach allows us to understand how exciton spectra change during a type-I–type-II transition. To this end, we will label the exciton states of a type-II heterostructure as we do the corresponding states of the type-I structure. For example, we refer to the two lowest resolved light-hole exciton transitions as $LH1E1$ and $LH3E1$, in light of the similarity of the oscillator-state wave functions with $n=0$ and 2 to the light-hole quantum-well levels $LH1$ and $LH3$, respectively.

The possible optical transitions in heterostructures with type-I and type-II quantum wells are shown in Fig. 5. In type-I heterostructures direct transitions between hole and electron quantum states dominate. The potential of the Coulomb interaction causes a rather small long-wavelength shift of the lines. This shift δE can be estimated approximately from the ''tail'' of the potential, which remains when the originally rectangular quantum well is superimposed on the ''Coulomb'' well. Thus, the value of the shift δE is larger the smaller the width of the quantum well L_z, but does not exceed V_0 (see Fig. 5a). A problem of current interest is to incorporate δE into type-I quantum well states, primarily as part of attempts to establish an exact correspondence between theoretical and experimental energy spectra of quantum-confined states. Direct transitions also take place in the intermediate case where one of the bands, e.g., the valence band, is originally flat, i.e., neither well nor barrier (Fig. 5b). However, in this case the transitions take place from oscillator levels of the Coulomb well. Furthermore, parity selection rules forbid transitions to the first electronic level from oscillator states of holes with odd numbers $n=1$, 3, ... As the well potential becomes flat, levels of the bell-shaped well with large n, including, e.g., $n=3,\ \dots\ \infty$, bunch together to form a quasicontinuum, along with the true continuum, from which above-barrier transitions are possible. For the InGaAs/GaAs system light-hole states outside the quantum well, i.e., in the GaAs barrier layer, turn out to be higher in energy if the Coulomb well is not included. However, inclusion of the Coulomb well causes a degree of spatial localization of the light hole within the quantum- well layer, and the optical transitions once more become direct. In this case the oscillator strengths of some transitions can turn out to be larger than in the corresponding type-I wells. The resulting spatially direct exciton transitions can play a fundamental role in the absorption spectra of heterostructures that are weakly type- II. The corresponding exciton states are described by the expressions given above. On the other hand, in a structure that is strongly type-II any asymmetric potential fluctuation can lead to the appearance of a spatially indirect exciton (i in Fig. 5). A problem of this kind was solved variationally in Ref. 12. In the same way we can also describe above-barrier resonance states (see Ref. 13), which are in principle present in quantum wells of both types.

We now establish what the energies and oscillator strengths are of the two lowest allowed transitions of a light-hole exciton. Using the method described previously, we can

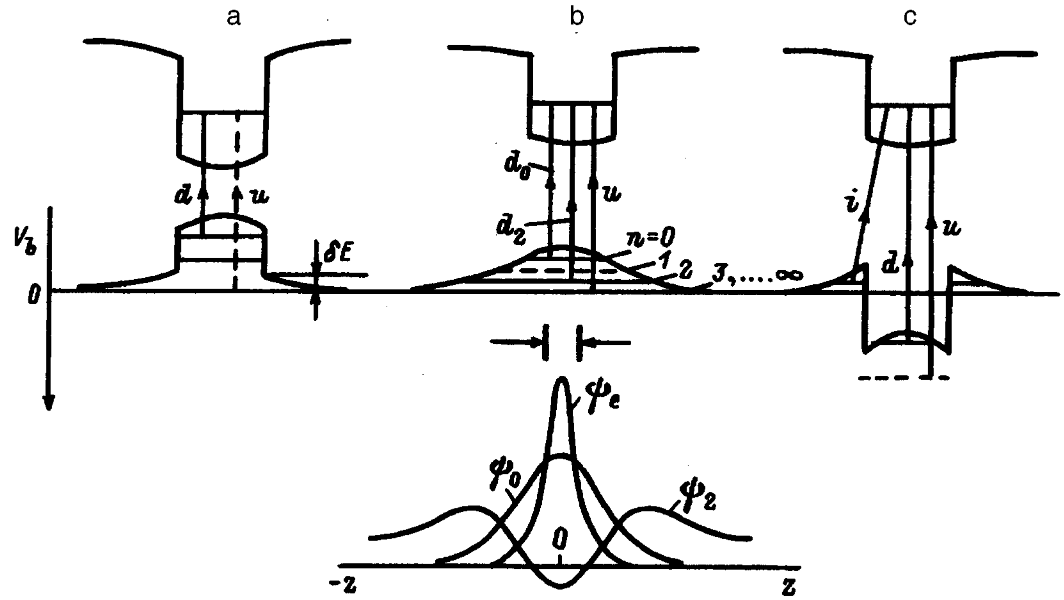

FIG. 5. Energy profiles of type-I (a) and type-II (c) quantum wells, with an intermediate structure with a ''flat'' valence band (b)—sketches. d,u,i are direct, above-barrier, and spatially indirect transitions, respectively. The lower part of the figure shows the shape of the oscillator wave functions ψ_0 and ψ_2, and also the wave function of an electron ψ_e. The corresponding quantum well with $L_z = 80$ Å plotted above these curves is to scale with respect to z.

show that the splitting between states $LH1$ and $LH3$ is determined by the expression

$$\Delta = E_2 - E_0 + V_b \int_{-L_z/2}^{L_z/2} dz[\overline{\psi_2^2}(z) - \overline{\psi_0^2}(z)]. \tag{12}$$

The oscillator strength of the exciton, which is proportional to the longitudinal-transverse splitting ω_{LT}, can now be easily found using the results of Ref. 4:

$$\omega_{LT} = \omega_{LT}^{\text{bulk}} \frac{2a_B^3}{L_z a_\perp^2}\left[\int dz U_e(z_e) U_h(z_h)\right]^2, \tag{13}$$

where $\omega_{LT}^{\text{bulk}}$ and a_B are the longitudinal-transverse splitting and Bohr radius in bulk gallium arsenide, respectively. Here we also replace $U_h(z_h)$ with $\overline{\psi_0}$ or $\overline{\psi_2}$ for the exciton $LH1E1$ or $LH3E1$ transitions, respectively.

This method allows us to find the wave functions of the ground and excited hole states of the composite potential near a type-I–type-II transition analytically. The self-consistent variational solution to the exciton problem can completely describe the Coulomb effects in the system using only one variational parameter. Two advantages to our method of calculating exciton states should be mentioned in comparison with the widely used method of Berroir-Bastard.[14] First of all, we now can use analytic expressions for the hole wave function; the presence of two fitting and variational parameters make this calculation rather precise. Secondly, our method allows us to calculate parameters not only for the ground state, but also for the excited exciton states, which are needed for magnetooptic studies of a system with a type-I–type-II transition.

4. EXPERIMENTAL RESULTS AND DISCUSSION

Figure 6 shows a typical absorption spectrum for these types of heterostructures. It can be regarded as consisting of three basic exciton maxima and at least two plateaus corresponding to absorption continua in type-I quantum-well heterostructures. We interpret the first peak, in order of increasing energy, in the usual way, i.e., as the $HH1E1$ exciton resonance associated with a transition between the lowest quantum-well levels of the heavy hole and electron. The second, as we have already mentioned, is associated with the spatially indirect transition $LH1E1$ for an exciton made up of the first electronic state of the quantum well and a light-hole state in the barrier; the third corresponds to an exciton transition between the first excited quantum-well heavy-hole and electron levels in the well ($HH2E2$). In this figure we illustrate the decomposition of the absorption spectra into its components. This decomposition involves fitting Gaussian curves to the long-wavelength regions of the corresponding absorption maxima, taking into account the fact that the second and third peaks are fitted to reproduce the height of the absorption continua from the previous state. We thus have the ability to compare oscillator strengths of various excitonic states, just as with the reduced density of states in the continua.

The optical interband absorption coefficient in type-I quantum wells in the absence of excitonic effects is well-known.[15] For convenience of comparison, we write this quantity as follows:

$$\alpha(\omega) = (A/\eta) f_{cv}^0 I_{eh}^2 N_{2D}(\omega) \sim (A/\eta) \times (E_p/\hbar\omega) a_p \mu_\perp I_{eh}^2 \Theta(\hbar\omega - E_{ij}). \tag{14}$$

Here $A = 2\pi^2 e^2 \hbar / m_0 c$, η is the refractive index, $f_{cv}^0 = 2|P_{cv}|^2 / m_0 \hbar\omega$ is the oscillator strength of interband three-dimensional transitions, $|P_{cv}|$ is the modulus of the dipole interband transition matrix element, and I_{eh}^2 is the squared integral for overlap of hole and electron wave functions. $N_{2D}(\omega) = (\mu_\perp / \pi\hbar^2)\Theta(\hbar\omega - E_{ij})$ is the interband joint density of states, $\mu_\perp$ is the reduced effective mass of an

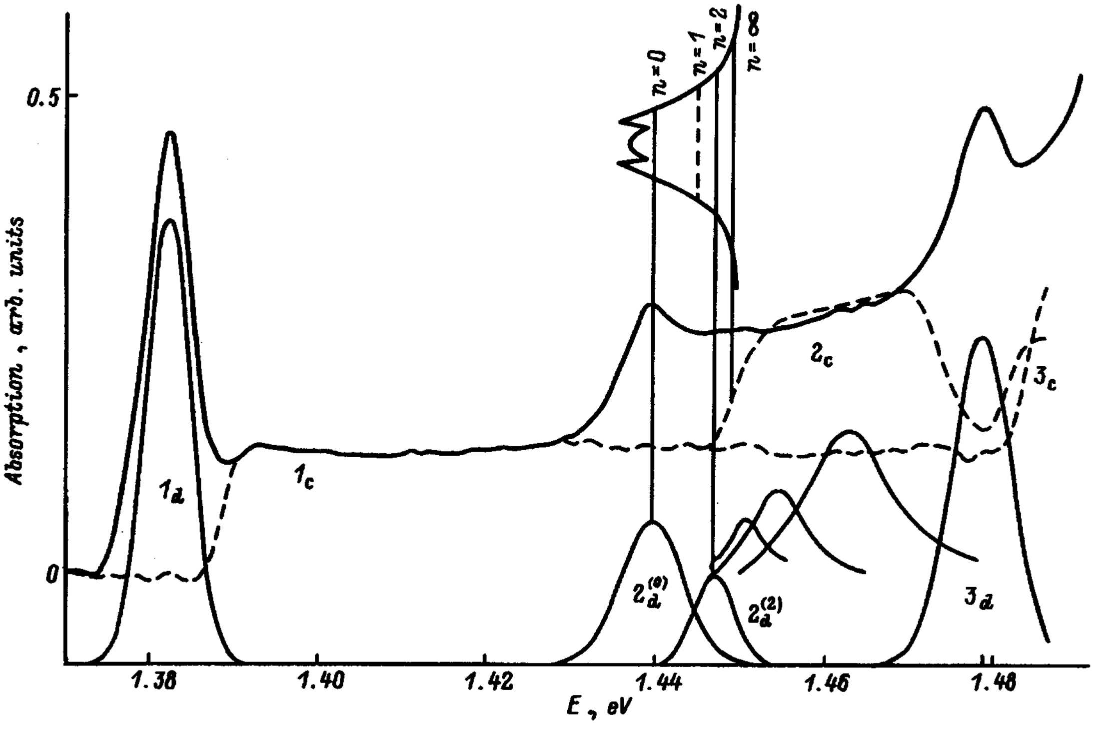

FIG. 6. Experimental absorption spectrum of $In_{0.15}Ga_{0.85}As/GaAs$ (solid thick curve) and its decomposition. $T=1.7$ K, $L_z=80$ Å. 1_d, $2_d^{(0)}$, $2_d^{(2)}$, 3_d—Gaussian lineshapes corresponding (in order) to the discrete exciton maxima $HH1E1$, $LH1E1$ ($n=0$), $LH3E1$ ($n=2$), $HH2E2$. 1_c, 2_c and 3_c are continua of states for $HH1E1$, $LH1E1$, and $HH2E2$, respectively. The inset shows the postulated shape of the ‘‘Coulomb well’’ which is combined with the spectral lines of the light-hole transitions.

electron and hole in the plane of the layer, $E_p=(2m/\hbar^2)|P_{cv}|^2$, $\Theta(\omega)$ is the (Heaviside) unit step function, and E_{ij} is the energy of the absorption edge for a pair of subbands i and j; the coefficient a_p depends on the polarization of the light and the magnetic quantum numbers of states i and j ($M=\pm 1/2$, $\pm 3/2$ for light and heavy holes, respectively). In the case of interband absorption in type-II heterostructures, for one of the states (initial or final) we should include the three-dimensional density of states. In our case this turns out to be the light-hole density of states N_{lh}, which can be written as

$$N_{lh}(E)=\frac{\sqrt{2}}{\pi}\frac{m_{lh}^{\perp}\sqrt{m_{lh}^{\parallel}}D^2L}{\hbar^3}\sqrt{E}, \tag{15}$$

where D and L are the dimensions of the samples parallel and perpendicular to the layers, respectively. The overlap integral I_{ij} for each state in a type-II quantum-well heterostructure is small by a factor of L_z/L; however, it disappears when we calculate the absorption coefficient, due to the integration over $\overline{k_{\parallel}}$. To compute I_{ij}, we write the hole wave function in the form of a linear combination of even and odd components, and take into account that the parity of the ith electronic function allows only one of these components to contribute to I_{ij}. For definiteness let us consider a transition to the first electronic level from even wave functions. Thus, we will look for an even hole state with energy E above a barrier of height V and width L_z. It is not difficult to show that the wave functions of such an above-barrier state can be written as follows:

$$U_{lh}(z)=\frac{1}{\sqrt{L}(1+r^2)}\times\begin{cases}\exp[ik_2(z+L_z/2)]\\ \quad +r\ \exp[-ik_2(z+L_z/2)], z<-L_z/2,\\ \exp[-ik_2(z-L_z/2)]\\ \quad +r\ \exp[ik_2(z-L_z/2)], z>L_z/2,\\ A\cos k_1 z, -L_z/2<z<L_z/2,\end{cases} \tag{16}$$

where

$$r=\frac{1+i(k_1/k_2)\tan(k_1L_z/2)}{1-i(k_1/k_2)\tan(k_1L_z/2)},\quad A=\frac{1+r}{\cos(k_1L_z/2)},$$

$$k_1=\sqrt{\frac{2m_{lh}^{\parallel}(E-V)}{\hbar^2}},\ k_2=\sqrt{\frac{2m_{lh}^{\parallel}E}{\hbar^2}}.$$

Once we have calculated the values of the overlap integrals in this way, we can find the relative contribution of light and heavy hole transitions in type-II heterostructures to the spectral continuum absorption:

$$\frac{\alpha_{LH1E1}^{(\infty)}}{\alpha_{HH1E1}^{(\infty)}}=\frac{\sqrt{2}}{3\pi}\frac{E_{hh}^{\infty}}{E_{lh}^{\infty}}\frac{m_{lh}^{\perp}(m_e+m_{hh}^{\perp})}{m_{hh}^{\perp}(m_e+m_{lh}^{\perp})}\times\frac{\sqrt{m_{lh}^{\parallel}}L}{\hbar}\frac{I_{LH1E1}^2(\omega)}{I_{HH1E1}^2}\sqrt{\hbar\omega-E_{lh}^{\infty}}, \tag{17}$$

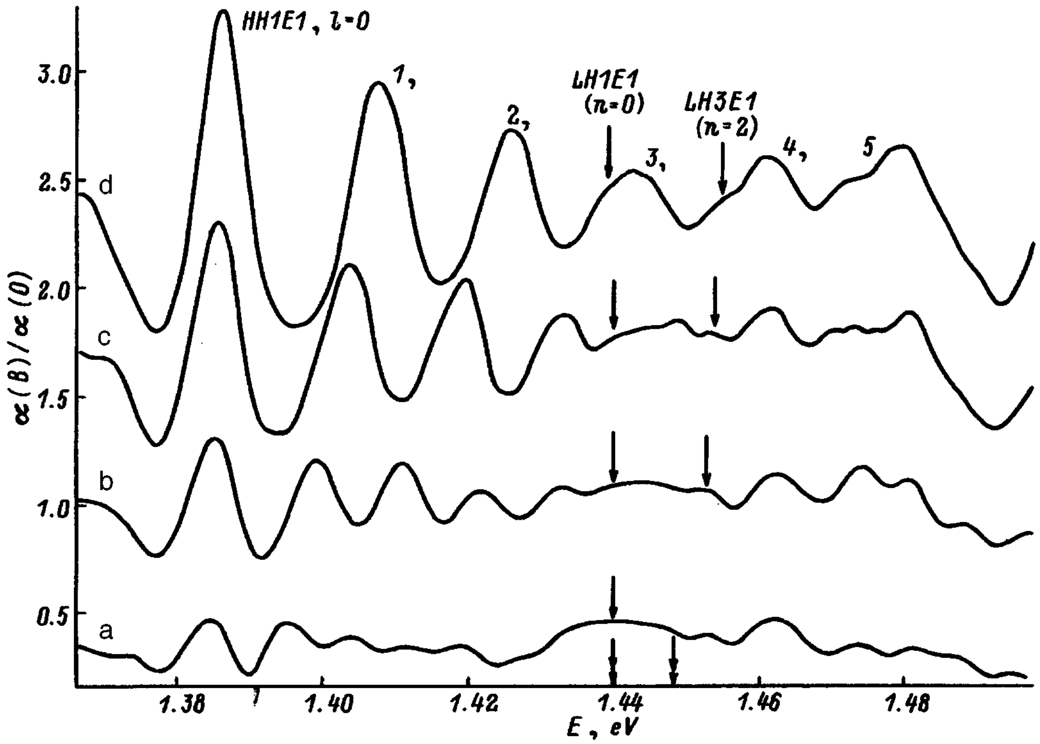

FIG. 7. Plots of the magnetoabsorption spectrum in units $\alpha(B)/\alpha(0)$ for $In_{0.15}Ga_{0.85}As/GaAs$ sample 1-166. $T=1.7$ K. B, T: a— 3.0, b—4.5, c— 6.0, d— 7.5. The arrows indicate the positions of the exciton maxima $LH1E1$ and $LH3E1$. The double arrows are the same at $B=0$.

where E_{hh}^{∞} and E_{lh}^{∞} are the long-wavelength edges of the continuum for the transitions $HH1E1$ and $LH1E1$, respectively; the L cancels when we substitute in the explicit form of I_{LH1E1}^2. Calculations using Eq. (17) do not predict a plateau, as for a two-dimensional type-I system with quantum wells; rather, they yield a function with a peak located 12 meV above E_{lh}^{∞}. This peak corresponds to the maximum value of the overlap integral, which is reached at an energy that corresponds to a quasistationary above-barrier state of the light hole, for which $U_{lh}(\pm L_z/2)=0$. The shape of the continuum is in satisfactory agreement with the experimental data if we postulate the presence of both a quasicontinuum and a true continuum modified by the Sommerfeld factor, along with a somewhat larger oscillator strength for the exciton $HH2E2$ than would follow from the assumption of a flat $LH1E1$ continuum (the latter could be correct only for a type-I heterostructure, which is ruled out by the calculations of Sec. 3). Furthermore, in comparing with the experimental data shown in Fig. 6 we have approximately included inhomogeneous broadening by assuming that it is a quantity of the same order of magnitude as the half-width of the exciton state for the transition $LH1E1$.

The form of the excitonic absorption coefficient in quantum wells of a type-I heterostructure is well known. For $HH1E1$ and $HH2E2$ (in the case of correspondence Q with type-I) we can write it as

$$\alpha_{\exp}(\omega)\sim(A/\eta)(P_{cv}^2/\hbar\omega)a_p(1/a_\perp^2)I_{eh}^2\delta(\omega). \tag{18}$$

Here $\delta(\omega)$ is a function that describes the shape of the discrete line. In the approximation of a two-dimensional structure it follows from Eq. (18) that

$$\alpha_{\exp}(\omega)\sim(A/\eta)(E_p/\hbar\omega)a_p\mu_\perp^2\mu_\parallel I_{eh}^2L_z^{-1}\times\exp\left[-\frac{(\hbar\omega-E_{NM})^2}{H^2}\right]. \tag{19}$$

Equation (19) allows us to compare the integrated absorption coefficients for transitions to ground exciton states for different quantum-well levels with quantum numbers N and M. Here we fit the discrete exciton lines to a Gaussian shape with a half-width H, in light of the dominant role of inhomogeneous broadening in generating these lineshapes. The integrated absorption coefficient can be defined as $K=\sqrt{\pi}H\alpha^{\max}$ or determined by direct numerical integration (where $\alpha^{\max}$ is the amplitude of the absorption coefficient).

For transitions from $LH1E1$ states of the Coulomb well we can use Eq. (13) with the wave functions $\overline{\psi}_0$. For $V=10$ meV these calculations give $\omega_{LT}^{LH1E1}/\omega_{LT}^{\text{bulk}}=1.8$. If we estimate that $\omega_{LT}^{HH1E1}/\omega_{LT}^{\text{bulk}}=(2a_B^3/a_\perp^2L_z)I_{HH1E1}^2\simeq5.6$ for the $HH1E1$ transition of a type-I quantum well with $L_z=80$ Å, we obtain $\omega_{LT}^{LH1E1}/\omega_{LT}^{HH1E1}\simeq0.32$. Analogously, $\omega_{LT}^{LH3E1}/\omega_{LT}^{\text{bulk}}=0.9$, which gives $\omega_{LT}^{LH3E1}/\omega_{LT}^{HH1E1}\simeq0.16$.

The decomposition into spectral components illustrated in Fig. 6 was based on fundamental physical considerations regarding the nature of the lines. The fact that subtracting this theoretical set of spectral features from the experimental spectra leaves only an insignificant remainder is an indication of how good the agreement with experiment is when this procedure is used. The segment between $LH1E1$ and the continuum without including the Coulomb interaction can probably be filled in by quasicontinuum excitonic transitions

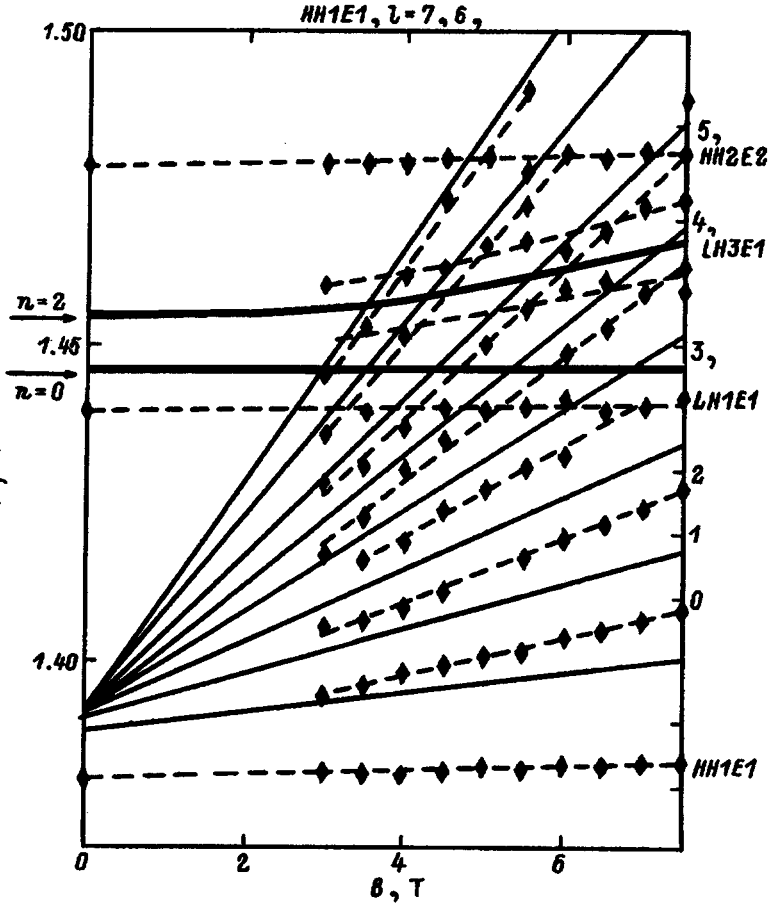

FIG. 8. Fan diagram for $In_{0.15}Ga_{0.85}As$/GaAs sample 1-166 in right-circular polarization. The dashed curves are drawn through the experimental points. The solid curves are computed transition energies between Landau levels, and also ''oscillator'' light-hole levels and the zero Landau level of an electron (the heavy curves) obtained by adding the binding energy of diamagnetic excitons R_B to the experimental positions of the maxima (see Fig. 1). The numbers to the right indicate the label of the electronic Landau level for transitions between the quantum-well levels $HH1E1$. The postulated positions of transitions from the oscillator states $n=0$, 2 at $B=0$ are indicated by arrows on the energy axis.

constructed out of higher even-parity oscillator states of the light hole ($n \geqslant 2$) from the Coulomb well. A certain arbitrariness can be tolerated when including the ''crawl'' of the relatively ''powerful'' absorption edge of the quasibulk barrier layer of GaAs toward the high energy states. Note that the slight deviation of $HH1E1$ from Gaussian behavior can be explained by a possible error of ± 3 monolayers in L_z.

Magnetic fields higher than 2 to 3 T cause oscillations in the absorption spectrum. In Fig. 7 we plot the transmission spectra of one of our samples measured in a field B divided by the transmission when the magnetic field is switched off. A considerable number of absorption maxima are recorded, sometimes more than 20 peaks. The fact that such a large number of strong oscillations is observed in the magnetoabsorption attests to the rather high quality of the quantum-well layers, despite the relatively large half-width of the lines. Accordingly, we can assert that the intrinsic half-width Γ^0_{hh} of the exciton absorption lines for heavy holes is relatively small, and that the observed half-width is determined primarily by an inhomogeneous broadening $\delta\Gamma$, whose effect on the quality of the magnetooptic spectrum is insignificant when $\delta\Gamma \ll \hbar\Omega$, where Ω is the sum of cyclotron frequencies of electrons and holes. The ''fan diagram'' shown in Fig. 8, which is typical of the structures under study, consists of lines that are almost independent of field and lines that are strongly affected by the field.

This oscillatory behavior of the magnetoabsorption maxima, which is characteristic of the interband magnetooptics of quantum wells, has been observed previously in the GaAs/(AlGaAs system.[16] It appears when the strong-field criterion $\beta = \hbar\Omega/2R^* \gg 1$ (where R^* is the binding energy of an exciton for $B=0$) is not satisfied by the excitonic ground state, and is observed only when excited states of the exciton participate in the absorption. Note, however, that these excited states need not be clearly distinguishable when $B=0$, although the lifetime of an exciton in these states must be long enough that the states can be detected in a magnetic field. The corresponding inhomogeneous broadening $\delta\Gamma_{n\geqslant 2}$ can easily mask the absorption lines of excited states when $B = 0$, and yet be insignificant in the regime where the oscillations are observed if $\delta\Gamma_{n\geqslant 2} < \hbar\Omega$.

We calculated the heavy-hole and electron energy levels as functions of the quantum-well width L_z and indium content x, taking into account the effect of strain on the energy structure, while the binding energies of the exciton states $HH1E1$, $HH2E2$, and $LH1E1$ were once more calculated as a function of N and magnetic field.

From the fan diagram shown in Fig. 8 it is clear that the ''dynamic behavior'' of Landau levels of the excitonic states $HH1E1$ and $HH2E2$ is strongly distorted if we disregard the exciton binding energy R_B. Extrapolating the positions of the spectral lines to the $B=0$ axis gives a considerable discrepancy between the energies of the ground state and the excited state. This discrepancy disappears completely if we take R_B into account. In this case (see the solid curves in Fig. 8) all the curves for transitions between Landau subbands,

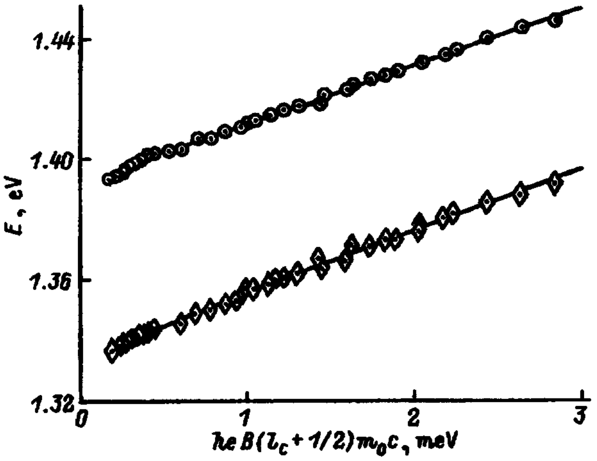

FIG. 9. Positions of maxima in the magnetoabsorption corrected for the binding energy of diamagnetic excitons plotted as a function of the cyclotron energy of a free exciton and the Landau number $(l_c+1/2)$ for $\mathrm{In}_x\mathrm{Ga}_{1-x}\mathrm{As}/\mathrm{GaAs}$ sample 1-166 ($x=0.15$) (upper) and 1- 159 ($x=0.2$) (lower).

including the first Landau subband with $l=0$, converge to a single energy at $B=0$ with insignificant discrepancies.

The fan diagram for $E^{\max}(B)$ corrected in this way allows us to estimate the reduced effective mass μ of an electron and hole in the plane of the quantum well, from the slope of the reconstructed straight line for the transition between Landau subbands $\Delta E/\Delta B$. These estimates give $\mu^{-1}m_0=$ 20.2 and 18.18 for $x=$ 0.2 and 0.15, respectively (Fig. 9). Using the corresponding heavy-hole masses in bulk material, we can estimate the electron masses to first approximation. They turn out to be $m_e=0.056$ and $0.059m_0$, respectively. These estimates do not contradict the results obtained from calculations based on known dependences of m^* on x for bulk material [for example, $m^*(x)=0.0660-0.0537x+0.0116x^2$; see Ref. 17]. Note that the functions shown in Fig. 9 reveal a certain nonparabolicity of the electronic spectrum $E_c(k)$ at large energies, associated with a tendency for the function $E_l^{\max}(B)$ to follow a sublinear relation.

We now return to analysis of the fan diagrams, taking into account the structure of the light-hole magnetoabsorption transitions $LH1E1$ (see Fig. 8). Unfortunately, the magneto-oscillations of a heavy-hole exciton are difficult to distinguish from the background of the family of relatively strong lines belonging to $HH1E1$. Nevertheless, in fields $B>$ 3 T the method of elimination can be used to separate out weak transitions that are stimulated by the magnetic field. These can be associated with excitonic transitions from ''oscillatory'' light-hole states. The shift in the value of the energy towards higher energies (see the computed data in Fig. 1) and the extrapolation to $B=0$ give the position of the absorption maximum, which is found to be above the position of the $LH1E1$ ground state by 9 meV (see the arrows in Figs. 7 and 8). We can interpret this maximum as a second even-parity oscillator state in the Coulomb well ($n=2$). In this case the value 9 meV is found to be in good agreement with the calculated gap between levels $n=0$ and 2 obtained by using Eq. (9), i.e., 8 meV. Analysis of the fan diagram allows us to regard as likely the observation of a third ($n=4$) oscillatory state.

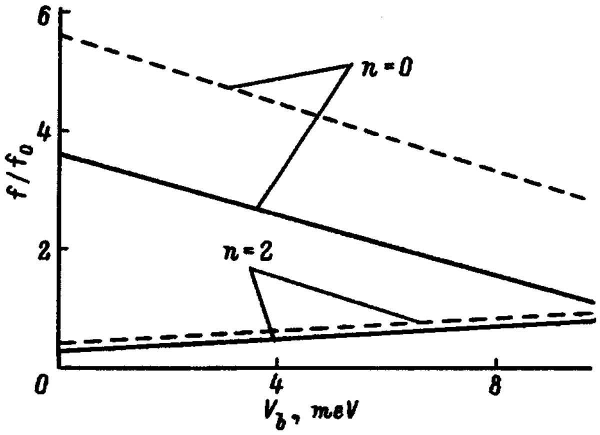

FIG. 10. Dependence of the oscillator strength f/f_0 of transitions from the Coulomb well on the height of the barrier V_b for states $LH1E1$ ($n=0$) and $LH3E1$ ($n=2$) at $B=4$ T (solid curves) and 7 T (dashed curves).

Figure 10 shows the dependence of the oscillator strength for $LH1E1$ and $LH3E1$ excitons ($n=0$ and 2) on the barrier height near the transition from type-I to type-II for a $\mathrm{In}_{0.2}\mathrm{Ga}_{0.8}\mathrm{As}/\mathrm{GaAs}$ quantum well of width 80 Å, calculated using Eq. (10). The oscillator strength of the $LH1E1$ state ($n=0$) decreases markedly as V_b increases, i.e., as the type-I band structure converts into a type-II structure. At the same time, we observed an increase in the oscillator strength of state $LH3E1$ ($n=2$). (We calculated the oscillator strengths for a switched-on magnetic field for reasons of convenience, since perturbation theory can be used. Otherwise, tedious numerical calculations would be necessary.) Important also is the fact that near a type-I-to- type-II transition the oscillator strengths of states $LH1E1$, $LH3E1$ are quite large. The positions of spectral lines associated with these resonances are shown in the inset to Fig. 6; their intensity, which is comparable to the intensity of lines corresponding to exciton transitions in a type-II quantum well, includes the area bounded by the discrete lines $LH1E1$ and $LH3E1$ in Fig. 6. The shapes of the corresponding wave functions ψ_0 and ψ_2 in a type-II quantum well are shown in Fig. 5b.

The overall results of our spectroscopic studies and computations reveal the following tendencies. As the system becomes a stronger type-I system, the state $LH1E1$ evolves into a spatially indirect exciton with its electron and hole localized in different layers. However, the oscillator strength of this excitonic state should be rather low due to the low value of the electron-hole overlap integral. On the other hand, the state $LH3E1$, which does not contribute significantly to the spectra of type-I quantum wells due to the smallness of the electron-hole overlap integral, becomes more visible in the spectra as the system quantum wells become type-II wells.[18] In the strong type-II limit, this state probably becomes a spatially direct quasistationary above-barrier exciton state similar to that described in Refs. 19 and 20. The splitting between the two hole states $LH1$ and $LH3$ is minimal near the transition point, and increases in type-I and type-II regions. In the approximation of treating the system as a strong type-II system, this splitting is approximately equal to the discontinuity in the valence band $V_0^{lh}=V_b$. The observed doublet (triplet) structure can be explained using the model described in Sec. 3. In conclusion, we would like to mention that recent papers have reported seeing a doublet structure for heavy-hole excitons in reflectance spectra of CdTe/CdMnTe heterosystems near the type-I-type–II transition.[21]

5. CONCLUSIONS

We have investigated the absorption coefficient and fan diagrams of InGaAs/GaAs quantum-well structures experimentally and theoretically. Analysis of the absorption spectrum by decomposing it into spectral components corresponding to discrete and continuum states has allowed us to obtain satisfactory quantitative and qualitative agreement with experiment at $B=0$. Using the computed dependences of the binding energy of various excitonic states on magnetic field, we have reconstructed the true ''dynamic behavior'' of the Landau levels and found the effective masses of carriers in these structures. Our theoretical investigations of light-hole states in type-II quantum wells lead us to conclude that the observed light-hole exciton is spatially direct. The high value of the oscillator strength for the $LH1E1$ exciton and the appearance of a doublet structure near the light-hole exciton resonance are in good agreement with our theoretical predictions. General considerations suggest that our model of the behavior of this spectrum is likely to work for more significant excursions of the heterostructure towards type-II as well.

We wish to express our gratitude to E. L. Ivchenko for useful discussions. The studies described in this paper were made possible, in part, by grant No. R58300 of the International Science Fund. This paper was also supported by the Russian Fund for Fundamental Research, Project No. 96-02-17935.

[1] J.-P. Reithmaier, R. Hoger, H. Riechert, A. Heberle, G. Abstreiter, and G. Weimann, Appl. Phys. Lett. **56**, 536 (1990).

[2] X. M. Fang, X. C. Shen, H. Q. Hou, W. Feng, J. M. Zhou, and F. Koch, Surf. Sci. **228**, 351 (1990).

[3] Y. S. Huang, H. Qiang, F. H. Pollak, G. D. Pettit, P. D. Kirchner, J. M. Woodall, H. Stiagier, and L. B. Sorensen, J. Appl. Phys. **70**, 7537 (1991).

[4] A. V. Kavokin, A. I. Nesvizhskiĭ, and R. P. Seĭsyan, Fiz. Tekh. Poluprovodn. **27**, 977 (1993) [Semiconductors **27**, 530 (1993)].

[5] Al. L. Efros, Fiz. Tekh. Poluprovodn. **20**, 1281 (1986) [Sov. Phys. Semicond. **20**, 808 (1986)].

[6] Landolt-Bornstein (Springer-Verlag, Berlin, 1987) V. 22, III, 22a.

[7] M. P. C. M. Krijn, Semicond. Sci. Technol. **6**, 27 (1991).

[8] D. J. Arent, K. Deneffe, C. van Hoof, G. de Boeck, and G. Bords, J. Appl. Phys. **66**, 1739 (1989).

[9] R. P. Seĭsyan, *Spectroscopy of Diamagnetic Excitons* [in Russian], Nauka, Moscow (1984).

[10] R. P. Seisyan, A. V. Kavokin, S. I. Kokhanovskii, A. I. Nesvizhskii, M. E. Sasin, M. A. Sinitzin, and B. S. Yavich, Semicond. Sci. Technol. **10**, 611 (1995).

[11] L. D. Landau and I. M. Lifshits, *Quantum Mechanics: Non-Relativistic Theory* (Pergamon Press, Oxford, 1977) [Russian original, Nauka, Moscow, 1974].

[12] A. V. Kavokin and A. I. Nesvizhskii, Phys. Rev. B **49**, 17055 (1994).

[13] G. Peter, E. Delepotre, G. Bastard, J. M. Berroir, C. Delalande, B. Gil, J. M. Hong, and L. L. Chang, J. Luminesc. **52**, 147 (1992).

[14] G. Peter, E. Delepotre, G. Bastard, J. M. Berroir, C. Delalande, B. Gil, J. M. Hong, and L. L. Chang, Phys. Rev. B **42**, 5891 (1990).

[15] E. L. Ivchenko and G. E. Pikus, *Superlattices and Other Heterostructures. Symmetry and Optical Phenomena*. Springer Ser. Sol. St. Sci. (Springer-Verlag, 1995), v. 110.

[16] N. D. Il'inskiĭ, S. I. Kokhanovskiĭ, and R. P. Seĭsyan, Fiz. Tekh. Poluprovodn. **27**, 108 (1993) [Semiconductors **27**, 57 (1993)].

[17] S. I. Kokhanovskiĭ, Yu. M. Makushenko, R. P. Seĭsyan, Al. L. Efros, T. V. Yazeva, and M. A. Abdullaev, Fiz. Tekh. Poluprovodn. **25**, 493 (1991) [Sov. Phys. Semicond. **25**, 298 (1991)].

[18] R. P. Seisyan, A. V. Kavokin, S. I. Kokhanovskii, A. I. Nesvizhskii, M. E. Sasin, M. A. Sinitzin, and B. S. Yavich, Semicond. Sci. Technol. **10**, 611 (1995).

[19] F. S. Zhang, H. Luo, N. Dai, N. Samarth, M. Dobrowolska, and J. K. Furdyna, Phys. Rev. B **47**, 3806 (1993).

[20] R. P. Seisyan, M. E. Sasin, S. I. Kokhanovskii, M. R. Vladimirova, A. V. Kavokin, M. A. Kaliteevskii, and V. M. Ustinov, in *Proceedings of the 23rd International Conference on the Physics of Semiconductors* (Berlin, 1996).

[21] A. Ribayrol, D. Coquillat, A. V. Kavokin, J. P. Lascaray, H. P. Zhou, C. M. Sotomayor-Torres, B. Lunn, and D. E. Ashenford, in *Proceedings of the 3rd International Conference on Optics of Excitons in Confined Systems* (Montpellier, France, 1993).

Translated by Frank J. Crowne

The effect of a longitudinal magnetic field on electronic intersubband transitions in asymmetric heterostructures

F. T. Vas'ko and G. Ya. Kis

Institute of Semiconductor Physics, Ukraine National Academy of Sciences, 252650 Kiev, Ukraine

(Submitted April 4, 1996; accepted for publication March 14, 1997)
Fiz. Tekh. Poluprovodn. **31**, 1121–1125 (September 1997)

Infrared absorption spectra are calculated for electronic intersubband transitions in asymmetric heterostructures subjected to a longitudinal magnetic field. The systems discussed include a single quantum well in a transverse electric field, a ''stepped'' quantum well, and a double well with tunnel-coupled excited levels. The longitudinal magnetic field causes collisionless broadening of the absorption peaks (because the effect of the magnetic field on the dispersion law of an electronic state varies from state to state, which modifies the transitions between them) and absorption of normally incident light (due to changes in the selection rules). © *1997 American Institute of Physics.* [S1063-7826(97)02009-7]

1. INTRODUCTION

1. The excitation of intersubband transitions of $2D$ electrons by infrared light in heterostructures has been actively studied in recent years (see Refs. 1–3). In Ref. 4, Petrov and Shik discussed the effect of a longitudinal magnetic field on transitions excited by incident light, whose electric field has a component perpendicular to the plane of the heterostructure. Such a magnetic field changes the size-quantized electronic states considerably,[5–7] leading not only to a shift in the levels (i.e., to a change in the frequency of the intersubband transitions), but also to anisotropy in the dispersion law ε_{jp} (where $\mathbf{p}$ is the longitudinal momentum, and j is the subband index). The character of this anisotropy is qualitatively different for symmetric and asymmetric structures: whereas in the first case the field simply makes the effective mass anisotropic [by an amount that is small with respect to the parameter $(d/l_H)^2$, where d is the characteristic thickness of the structure, and l_H is the magnetic length], the asymmetry gives rise to contributions to ε_{jp} that are proportional to the magnetic field and to $\mathbf{p}$. These contributions give rise to a substantial amount of collisionless broadening of the absorption peaks, since the functions ε_{jp} are different for different j, and to breaking of the selection rules for intersubband transitions.1) A mechanism of this kind was discussed previously for inversion layers in a longitudinal magnetic field, in which the transitions were excited by microwave radiation.[6] Various mechanisms for optically induced interband transitions in electric fields parallel to the $2D$ layer have been discussed in a number of papers (for citations see Ref. 8) so that transitions excited by the component of the electric field of the infrared light parallel to the $2D$ layer are now allowed.

In this paper we calculate the spectral dependence of the infrared absorption. Our treatment differs from that of Ref. 4 in that we include the asymmetry of the heterostructures. The following structures are considered (see Fig. 1): a single quantum well in a transverse electric field, a ''stepped'' quantum well, and a double quantum well with tunnel-coupled excited levels. We obtain the relative absorptions for light polarized perpendicular and parallel to the $2D$ layer, and also compare the collisional broadening of the absorption peak with the broadening arising from the collisionless mechanism discussed here.

Let us define the ratio of the absorbed power to the incident flux of infrared light as the relative absorption $\xi(\omega)$. For strongly degenerate electrons and transitions from the ground state ($j = 0$) to an excited level with label j the quantity $\xi(\omega)$ is determined by the usual quantum-mechanical expression

$$\xi(\omega)=2\frac{(2\pi e/L)^2}{\omega\sqrt{\epsilon}}\sum_{i,p}|\langle 0\mathbf{p}|\mathbf{e}\hat{\mathbf{v}}|j\mathbf{p}\rangle|^2 \times\theta(\varepsilon_F-\varepsilon_{0\mathbf{p}})\delta_\Gamma(\varepsilon_{0\mathbf{p}}-\varepsilon_{j\mathbf{p}}+\hbar\omega). \tag{1}$$

in which $\theta(\varepsilon_F-\varepsilon_{0p})$ is the Fermi distribution for electrons, L^2 is the normalized area, ϵ is the uniform dielectric permittivity of the heterostructure, $\hat{\mathbf{v}}$ is the velocity operator, which takes into account the longitudinal magnetic field, $\mathbf{e}$ is the polarization vector, and $\hbar\omega$ is the energy of an infrared quantum. The collisional broadening is taken into account phenomenologically through the replacement of the δ function with a Gaussian function, i.e., $\delta\_\Gamma(\varepsilon)=\exp[-(\varepsilon/\Gamma)^2]/\sqrt{\pi}\Gamma$ with a characteristic half-width Γ. The Fermi energy ε_F is connected with the $2D$ electron concentration by the usual normalization condition (the spin splitting of levels in a magnetic field is ignored, assuming that the g-factor is small). The energy ε_{jp} and electronic states $|j\mathbf{p}\rangle$ in Eq. (1) are found by solving the eigenvalue problem $\hat{H}|j\mathbf{p}\rangle=\varepsilon_{ip}|j\mathbf{p}\rangle$ with the Hamiltonian of an asymmetric heterostructure in a longitudinal magnetic field H (using the $\mathbf{p},z$ representation):

$$\hat{H}=\frac{p^2}{2m}+\frac{\hat{p}_z^2}{2m}+U(z)-\omega_c p_y(z-z_H)+\frac{m\omega_c^2}{2}(z-z_H)^2. \tag{2}$$

Here $U(z)$ is the potential energy localizing an electron along the direction of growth of the heterostructure (i.e., the Z axis; the direction of the X axis is chosen to be along H), $\hat{p}_z=-i\hbar d/dz$, $\mathbf{p}=(p_x,p_y)$, m is the effective mass and $\omega_c=|e|H/mc$ is the cyclotron frequency. The constant z_H is arbitrary due to the gauge invariance of the problem.

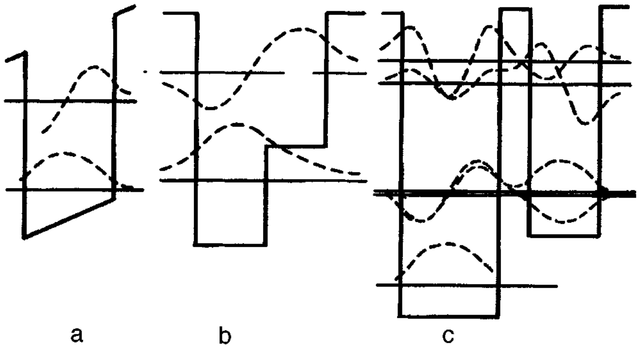

FIG. 1. Energy band diagrams for the heterostructures discussed in Secs. *2-4* (also shown are the positions of levels and wave-function shapes): a—a quantum well in a transverse electric field, b—a ''stepped'' quantum well, and c—a double quantum well (the electric field corresponds to the absorption curves shown in Fig. 4b).

Making the polarization dependence of the absorption explicit in Eq. (1), we have

$$\xi(\omega)=e_z^2\xi_\perp(\omega)+e_y^2\xi_\parallel(\omega), \tag{3}$$

where

$$\xi_{\perp,\parallel}(\omega)=\frac{2\alpha}{\hbar\omega}\sum_j\int d\mathbf{p}\,\theta(\varepsilon_F-\varepsilon_{0\mathbf{p}})\delta_\Gamma(\varepsilon_{0\mathbf{p}}-\varepsilon_{j\mathbf{p}}+\hbar\omega)\times\begin{cases}|\langle 0\mathbf{p}|\hat{v}_z|j\mathbf{p}\rangle|^2, & \perp\\ \omega_c^2|\langle 0\mathbf{p}|z|j\mathbf{p}\rangle|^2, & \parallel\end{cases}. \tag{4}$$

Here we use the expression for the y-component of the velocity operator $\hat{v}_y=\hat{p}_y/m-\omega_c(z-z_H)$ and introduce the effective fine structure constant $\alpha=e^2/(\hbar c\sqrt{\epsilon})$. Equations (3) and (4) describe the absorption of incident infrared light with electric fields both transverse (along *Z*) and longitudinal (along *Y*) to the growth direction. Next we use the connection between the matrix elements of the *z*-component of the velocity and the *z*-coordinate, i.e., $\langle 0\mathbf{p}|v_z|j\mathbf{p}\rangle=i(\varepsilon_{0\mathbf{p}}-\varepsilon_{j\mathbf{p}})\times\langle 0\mathbf{p}|z|j\mathbf{p}\rangle/\hbar$ to obtain the relation[9]

$$\xi_\parallel(\omega)\approx(\omega_c/\omega)^2\xi_\perp(\omega). \tag{5}$$

This result implies that in the infrared region of the spectrum the longitudinal absorption $\xi_\parallel(\omega)$ repeats the features of the transverse absorption $\xi_\perp(\omega)$, only with smaller amplitude. Therefore, we will discuss only the behavior of $\xi_\perp(\omega)$ in what follows.

The calculations given below depend on the specific form of the dispersion relation and the matrix elements of the velocity operator, both of which enter into the spectral functions $\xi_\perp(\omega)$. They are carried out below for the heterostructure shown in Fig. 1.

2. Let us begin our discussion of the spectral dependences with the case of an isolated quantum well of width d in a transverse electric field F (Fig. 1a). When the condition $d/\pi l_H<1$ holds, we may consider the magnetic field to be a small perturbation[7] and the dispersion relations have the form [2)]

$$\varepsilon_{jp}=\varepsilon_j+p^2/2m+\omega_c p_y\langle j|z-z_H|j\rangle+\frac{\omega_c^2 m}{2}\langle j|(z-z_H)^2|j\rangle, \tag{6}$$

where the unperturbed energy levels ε_j are determined from the equation $\hat{H}_0|j\rangle=\varepsilon_j|j\rangle$, and $\hat{H}_0$ is the Hamiltonian (2) for $H=0$ and $\mathbf{p}=0$. We will discuss only transitions between the two lowest subbands, so that $\xi_\perp(\omega)$ is given by the expression

$$\begin{aligned}\xi_\perp(\omega)&=\frac{2\alpha}{\hbar\omega}v_{01}^2\int d\mathbf{p}\,\delta_\Gamma(E_{01}+V_Hp_y-\hbar\omega)\,\theta(\varepsilon_F-\varepsilon_{0\mathbf{p}})\\&=\frac{4\alpha}{\hbar\omega}v_{01}^2\int_{-p_F}^{p_F}dp_y\sqrt{p_F^2-p_y^2}\,\delta_\Gamma\\&\quad\times(E_{01}+V_Hp_y-\hbar\omega).\end{aligned} \tag{7}$$

Here $p_F=\sqrt{2m(\varepsilon_F-\varepsilon_0)}$. The transition energy $E_{01}=\varepsilon_0-\varepsilon_1+\Delta\varepsilon_H$ is determined not only by the distance between levels at $H=0$, but also by a term $\Delta\varepsilon_H$ that is quadratic in the magnetic field from the next term in Eq. (6): $\Delta\varepsilon_H=A(\hbar\omega_c)^2/\varepsilon_0$, where $A\approx0.12$ for the case of a square quantum well and $F=0$. As F increases, the coefficient A increases slowly and almost linearly, reaching a value of 0.3 for $F=$ 100 kV/cm. The transition matrix element v_{01} and characteristic velocity V_H are introduced as follows:

$$v_{01}=\langle 0|v_z|1\rangle, V_H=\omega_c(\langle 1|z|1\rangle-\langle 0|z|0\rangle). \tag{8}$$

In the collisionless limit, i.e., $\Gamma=0$, the integration in Eq. (7) leads to a ''semielliptic'' spectral dependence:

$$\begin{aligned}\xi_\perp(\omega)&=4\alpha\frac{p_Fv_{01}^2}{\hbar\omega V_H}D\left(\frac{\hbar\omega-E_{01}}{V_Hp_F}\right),\\ D(x)&=\sqrt{1-x^2}\,\theta(1-x^2).\end{aligned} \tag{9}$$

It is clear that the magnetoinduced broadening of the absorption peak is characterized by a width $|V_H|p_F$. When $H=0$ (or for a symmetric structure when $V_H=0$ and in a magnetic field) the spectral dependence Eq. (9) becomes a δ-function-like peak, which is broadened only by collisions.

In order to include collision-induced broadening when $V_H\neq0$, we must do the integration in Eq. (7) numerically. The characteristic velocity Eq. (8) and transition energy E_{01} must also be determined numerically for the potential profile shown in Fig. 1a. The results we present here are for a GaAs/Al$_{0.45}$Ga$_{0.55}$As heterojunction quantum well of width 9.5 nm for $\Gamma=$ 1 meV and an electron concentration $n=4\times10^{11}$ cm^{-2}. The spectral dependences plotted in Fig. 2 illustrate the broadening of the peak as we increase both the magnetic and electric fields. For the parameters used here, the characteristic collisionless broadening $|V_H|p_F$ reaches 1.9 meV in the largest fields ($F=$ 150 kV/cm and $H=$ 6 T).

3. The collisionless broadening is larger in a stepped quantum well, since the heterostructures can be highly asymmetric. This calculation differs from that described above only in the calculation of v_{01}, V_H and E_{01} for the potential profile shown in Fig. 1b. Figure 3 shows the spectral dependences of the relative absorption for a stepped quantum well consisting of layers of GaAs and Ga$_{0.85}$Al$_{0.15}$As with widths

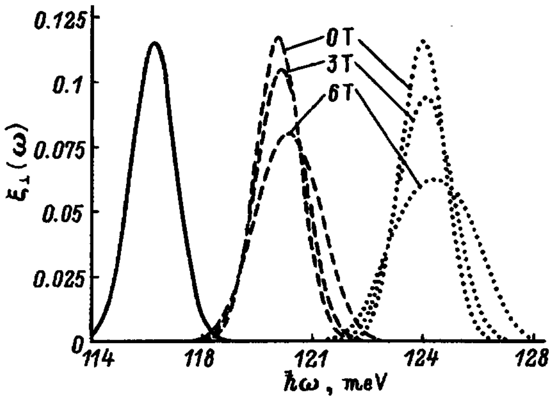

FIG. 2. Spectral dependences $\xi_\perp(\omega)$ for an isolated quantum well. Solid curve—$F = 0$, dashed curve—$F = 100$ kV/cm, dotted curve—$F = 150$ kV/cm (the values of magnetic field in T are shown in the figure).

5 and 4.3 nm for the deep and shallow portions of the well, respectively, and barriers made of $Ga_{0.65}Al_{0.35}As$ (a structure with similar parameters was discussed in Ref. 10) for $\Gamma = 1$ meV and $n = 4\times10^{11}$ cm^{-2}. The spectra shown there illustrate the transition to the collisionless absorption regime at magnetic fields larger than 5 T, for which the curve changes from a Gaussian to a ''semielliptic'' shape as in Eq. (9), since the value $|V_H|p_F = 4$ meV (for $H = 6$ T) exceeds Γ considerably.

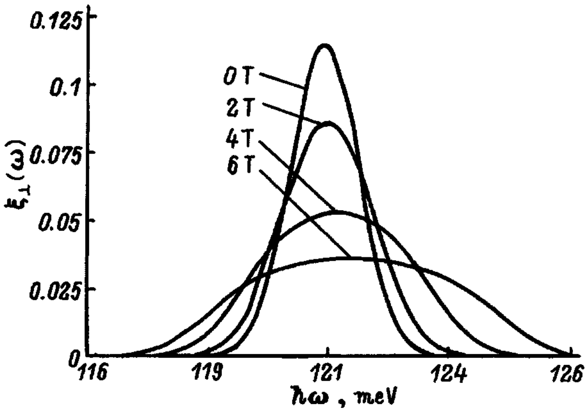

FIG. 3. Spectral dependence $\xi_\perp(\omega)$ for a stepped quantum well (values of the magnetic field in T are given in the figure).

4. For double quantum wells the spectral dependences turn out to be more complicated and sensitive to magnetic field, since the intersubband absorption peak is split by the tunnel coupling of the levels, which in turn is strongly influenced by the magnetic field.[11–13] Here we restrict the discussion to the case of a double quantum well in which electrons occupy the ground state of the deeper left-hand (l) well [such a state can be described by analogy with that in Sec. 2, and the dispersion relation ε^l_{0p} is given by Eq. (6)]. The tunneling resonance occurs between the first excited state of this well and the ground state of the right-hand (r) well, which have the dispersion laws ε^l_{1p} and ε^r_{0p}. Mixing of these states gives rise to excited ± states of the double quantum well. Double wells were investigated in Ref. 14 (see Fig. 1c). In the approximation of weak interwell tunnel coupling, these states can be described by a superposition of wave functions based on orbitals of the l- and r- quantum wells ϕ^l_z and ϕ^r_z (see Ref. 13) $\psi^\pm_l\phi^l_z + \psi^\pm_r\phi^r_z$, where the coefficients $\psi^\pm_{l,r}$ turn out to depend on p_y:

$$\psi^\pm_l = \pm\sqrt{(1\pm\Delta_H/\Delta_T)/2}, \quad \psi^\pm_T = \sqrt{(1\mp\Delta_H/\Delta_T)/2},$$

$$\Delta_H(p_y) = \varepsilon^l_{1\mathbf{p}} - \varepsilon^r_{0\mathbf{p}} = \Delta - \widetilde{V}_H p_y,$$

$$\Delta_T(p_y) = \sqrt{\Delta_H^2 + (2T)^2}. \tag{10}$$

Here Δ is the splitting of the resonance levels at $p_y = 0$, which takes into account the corrections quadratic in the magnetic field, Δ_H and Δ_T determine the splitting of levels for finite p_y in the absence of tunneling and taking tunneling into account, and T is the tunneling matrix element. The characteristic velocity $\widetilde{V}_H = \omega_c\Delta z$ now can be expressed in terms of the distance between centers of the l- and r-orbitals Δz. For the dispersion relations of the ± states we have[13]

$$\varepsilon_{\pm\mathbf{p}} = (\varepsilon^l_{1\mathbf{p}} + \varepsilon^r_{0\mathbf{p}})/2 \pm \Delta_T(p_y)/2. \tag{11}$$

The spectral dependences $\xi_\perp(\omega)$, including transitions to the ± state, are given by analogy with Eq. (7) by the expression

$$\xi_\perp(\omega) = \frac{2\alpha}{\hbar\omega} v_{01}^2 \sum_\pm \int d\mathbf{p} |\psi^\pm_l|^2 \delta_\Gamma \times (\varepsilon_{\pm\mathbf{p}} - \varepsilon^l_{0\mathbf{p}} - \hbar\omega)\,\theta(\varepsilon_F - \varepsilon^l_{0\mathbf{p}}), \tag{12}$$

in which the matrix element v_{01} is computed for states of the l-well ignoring tunneling, and the factor $|\psi^\pm_l|^2$ determines the oscillator strengths for transitions from the ground state to the ± states. In the collisionless limit we also obtain the following expression, which is analogous to Eq. (8):

$$\xi_\perp(\omega) = 4\alpha \frac{p_F v_{01}^2}{\hbar\omega\widetilde{V}_H} \left(\frac{T}{\delta\varepsilon_\omega}\right)^2 D\left(\frac{\delta\varepsilon_\omega - \Delta - \dfrac{T^2}{\delta\varepsilon_\omega}}{\widetilde{V}_H p_F}\right), \tag{13}$$

where we introduce the frequency detuning $\delta\varepsilon_\omega = \hbar\omega - E^l_{01}$, where E^l_{01} is the distance between the ground level and the excited level of the l-well at $\mathbf{p} = 0$ (see Sec. 2). An additional hyperbolic dependence on $\delta\varepsilon_\omega$ appears in the argument of the D-function, which is attributable to the fact that the energy conservation law in Eq. (12) depends on p_y. Because of this dependence, a bandgap appears at the center of the peak ($\delta\varepsilon_\omega = 0$), which divides it into two semielliptic peaks that merge together as $T \to 0$. The factors $|\psi^\pm_l|^2$ give rise to an additional amplitude factor that is proportional to T^2.

In order to include collisions, it is necessary to calculate the following integral numerically:

$$\xi_\perp(\omega) = \frac{2\alpha}{\hbar\omega} v_{01}^2 \sum_\pm \int_{-p_F}^{p_F} dp_y \sqrt{p_F^2 - p_y^2} \times (1 \pm \Delta_H/\Delta_T)\,\delta_\Gamma\left(\frac{-\Delta_H \pm \Delta_T}{2} - E^l_{01} - \hbar\omega\right). \tag{14}$$

This was done for a half-width of $\Gamma = 1$ meV as a function of longitudinal magnetic field H and transverse electric field

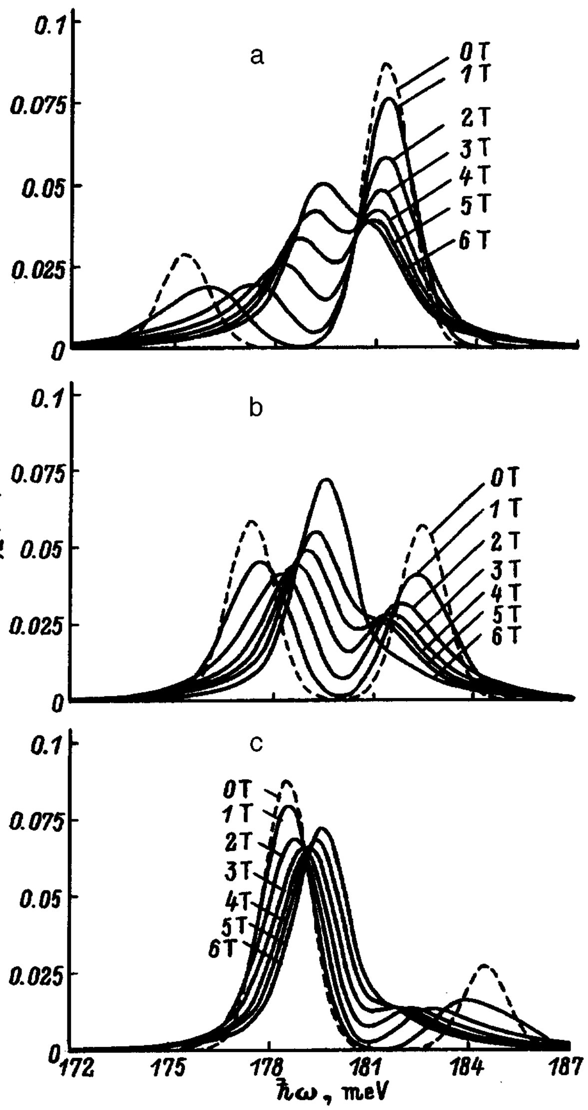

FIG. 4. Spectral dependences $\xi_\perp(\omega)$ of a double quantum well for the following F, kV/cm: a—6.9, b—8.4, c—9.9 (values of the magnetic field in T are shown in the figure; the dashed curve corresponds to $H=0$).

F, which gives the energy splitting Δ between the coupled levels. The structure we investigated was one with parameters close to those used in Ref. 14: the deep well was a layer of GaAs of width 8 nm with electron concentration $n=4\times10^{11}$ cm^{-2}, the shallow well was an undoped layer of $Ga_{0.8}Al_{0.2}As$ with width 5.6 nm, and the interwell barrier was a layer of $Ga_{0.2}Al_{0.8}As$ with thickness 2.5 nm. The external barriers were also $Ga_{0.2}Al_{0.8}As$. The compositions were chosen so that the conditions for applicability of the tunneling approximation were satisfied (see Ref. 13). Figure 4 shows the spectral dependences of the absorption for various splitting energies. For $H=0$ (the dashed curves) case *a* corresponds to $\Delta>0$, case *b* corresponds to resonance ($\Delta=0$), and *c* corresponds to $\Delta<0$. For zero splitting energies Δ and small tunnel coupling, the $\pm$ wave functions are essentially localized in one of the wells (l or r, depending on the sign of Δ); intrawell transitions corresponds to higher absorption peaks, while the peak that corresponds to tunneling is small. Plots of the absorption for $H=0$ exhibit a characteristic redistribution of the peak amplitudes, depending on the mutual positions of levels in the l- and r-wells.[14] For small magnetic fields, as in the cases discussed previously, the peaks are broadened and suppressed. However, when the broadening is large enough, the coherence factor is switched on [see Eq. (13) for the collisionless case], and the amplitude of the peaks begins to increase again, while the peaks themselves are already fused into a single peak at 6 T. For strong tunnel coupling, where the levels are far separated, this effect is not observed. The assymmetry in the behavior of the peaks shown in Fig. 4b is explained by the presence of a correction $\Delta\varepsilon_H$ in Δ that is quadratic in magnetic field, which causes the levels to separate from one another by a few meV.

5. Thus, a longitudinal magnetic field gives rise to a new mechanism for broadening of absorption lines, which is a strong function of the magnitude of this field and of the degree of asymmetry of the structure. We have demonstrated this fact by numerical calculations for several simple types of heterostructures (more exact self-consistent calculations of the energy levels and inclusion of the depolarization effect did not appreciably change the shape of the spectra on the parameters at which the transition from collisional to collisionless broadening mechanisms takes place). Moreover, imposing a longitudinal magnetic field changes the selection rules for intersubband transitions, which leads to a weak absorption of the field component polarized along the $2D$ layer. The extreme sensitivity of the absorption spectrum of double quantum wells with weak tunnel coupling, which is apparent for sufficiently weak electric and magnetic fields, is also noteworthy. For these reasons, the use of infrared spectroscopy in a longitudinal magnetic field to determine the parameters of the energy spectrum and the character of electronic relaxation in asymmetric heterostructures is of considerable interest.

1) For $(d/\pi l_H)^2 \ll 1$ the anisotropy of the effective mass considered in Ref. 5 can be omitted from Eq. (6). Including this contribution would lead to an additional broadening of order $\epsilon_F(\hbar\omega_c/silon_0)^2$, which for the values of parameters used in this paper turns out to be of order 0.1 meV.

2) For $(d/\pi l_H)^2 \ll 1$ the anisotropy of the effective mass considered in Ref. 5 can be omitted from Eq. (6). Including this contribution would lead to an additional broadening of order $\varepsilon_F(\hbar\omega_c/\varepsilon_0)^2$, which for the values of parameters used in this paper turns out to be of order 0.1 meV.

---

[1] E. Rosencher, B. Vinter, and B. Levine, *Intersubband Transitions in Quantum Wells* (N. Y., Plenum Press, 1992).
[2] *Quantum Well Intersubband Transitions: Physics and Devices*, H. C. Liu, B. F. Levine, and J. Y. Anderson, Eds. (Kluwer Academic, Dordrecht, 1994).
[3] C. Sitori, F. Capasso, J. Faist, and S. Scandolo. Phys. Rev. B **50**, 8663 (1994).
[4] A. G. Petrov and A. Ya. Shik, Fiz. Tekh. Poluprovodn. **27**, 1047 (1993) [Semiconductors **27**, 570 (1993)].
[5] A. I. Lukanin and Z. N. Uritskiĭ, Fiz. Tekh. Poluprovodn. **13**, 2286 (1979) [Sov. Phys. Semicond. **13**, 1337 (1979)].
[6] T. Ando, A. Fowler, and F. Stern, Rev. Mod. Phys. **54**, 437 (1982) (Russ. trans., entitled *Electronic Properties of Two-Dimensional Systems*, Mir, Moscow, 1985).
[7] T. Jungwirth and L. Smrka, J. Phys. C **5**, L217 (1993); W. Xu, Phys. Rev. B **51**, 9770 (1995).
[8] R. Q. Yang, Appl. Phys. Lett. **66**, 959 (1995).
[9] J. Dempsey and B. I. Halperin, Phys. Rev. B **47**, 4674 (1993).

[10] P. Boucaud, F. H. Julien, D. D. Yang, J.-M. Lourtioz, E. Rosencher, P. Bois, and J. Nagle, Appl. Phys. Lett. **57**, 215 (1990).

[11] G. S. Boebinger, A. Passener, L. N. Pfeiffer, and K. W. West, Phys. Rev. B **43**, 673 (1991).

[12] S. K. Lyo, Phys. Rev. B **50**, 4965 (1994).

[13] O. E. Raichev and F. T. Vasko, Phys. Rev. B **53**, 1522 (1996).

[14] E. Dupont, D. Delacourt, and M. Papuchon, Appl. Phys. Lett. **63**, 2514 (1993).

Radiation hardness of porous silicon

V. V. Ushakov,[1)] V. A. Dravin, and N. N. Mel'nik

P. N. Lebedev Physics Institute, Russian Academy of Sciences, 117924 Moscow, Russia

V. A. Karavanskiĭ

Institute of General Physics, Russian Academy of Sciences, 11794 Moscow, Russia

E. A. Konstantinova and V. Yu. Timoshenko

Physics Faculty, M. V. Lomonosov Moscow State University, 119899 Moscow, Russia

(Submitted December 20, 1996; accepted for publication February 27, 1997)
Fiz. Tekh. Poluprovodn. **31**, 1126–1129 (September 1997)

The effect of irradiation by 300-keV Ar^+ ions on the properties of electrochemically produced porous silicon is studied at doses of $5\times10^{14}-1\times10^{16}$ cm^{-2}. Raman scattering and photoluminescence data are used to show that the radiation hardness of porous silicon layers is substantially greater than that of single crystal silicon. © *1997 American Institute of Physics.* [S1063-7826(97)02109-1]

INTRODUCTION

Because of its intense luminescence, its relative ease of production, and the possibility of ''introducing'' it into an already highly developed silicon technology, porous silicon is extremely attractive as a material for optoelectronics, such as the fabrication of combination highly integrated opto-microelectronic circuits. Various properties of this material,[1] especially those which are important from the standpoint of the reaction of porous layers to various kinds of chemical and thermal processing,[2–6] have been studied in many recent papers. Another major factor determining the technological applications of semiconducting materials is their radiation hardness. In the past, radiative interactions (ion implantation) have been used either as a step in the fabrication of porous layers[7,8] or for introducing specified impurities into previously prepared layers.[8,9]

In this paper we study the effect of ion bombardment on the intrinsic structural and luminescence properties of porous silicon (*por*-Si). Information on changes in the properties of *por*-Si layers following ion bombardment has been obtained by measuring optical Raman scattering and photoluminescence.

EXPERIMENTAL TECHNIQUE

The initial material was a single crystal slab (100) of *p*-type silicon with a resistivity of 0.5 $\Omega\cdot$cm. Porous layers were prepared in an electrochemical cell with an HF(49%): $C_2H_5OH=1:1$ electrolyte at a current density of 30 $mA\cdot cm^{-2}$ for 4 min. The thickness of the resulting layers was 4–5 μm and their porosity was 70%.

Samples with layers of *por*-Si, as well as single crystal *c*-Si substrates for comparison, were irradiated in a High Voltage Engineering Europa ion accelerator by 300-keV Ar^+ ions at doses of 5×10^{14}, 2×10^{15}, and 1×10^{16} cm^{-2} at room temperature. Raman scattering spectra were obtained on a U-1000 spectrometer using an ILA-120 argon ion laser as a pump (wavelength $\lambda=488$ nm). Photoluminescence measurements were made on an SDL-2 spectrometer with an LGI-503 argon laser as a pump ($\lambda=488$ nm) at an intensity of 0.5 $W\cdot cm^{-2}$. These studies were conducted at room temperature.

In order to estimate the path length of the Ar^+ ions in the porous silicon, Monte Carlo model calculations were done. Figure 1 shows the calculated spatial distributions of implanted Ar in samples of metallic silicon with the actual (curve *1*) and reduced to 30% (in accordance with the porosity mentioned above; curve *2*) densities. These data show that Ar^+ ions penetrate the surface region of single crystal slabs to a depth on the order of 0.5 μm, and that in *por*-Si the penetration region was less than 2 μm deep. This latter value can obviously be regarded as an estimate of the depth for possible defect formation in these experiments.

RESULTS AND DISCUSSION

Figure 2 shows data from the optical Raman scattering experiments. A line corresponding to scattering on bulk phonons (520 cm^{-1}) can be seen for the initial sample of single crystal silicon. After implantation to a dose of 2×10^{15}, this line vanishes because of the complete amorphization of the surface layer.[10]

The Raman scattering spectra for the *por*-Si layers consist of a superposition of scattering lines from bulk phonons and from vibrations in nanocrystals and in the amorphous phase.[11] This can be explained by the composite structure of *por*-Si, which is made up of parts with rather large characteristic dimensions and have essentially bulk properties, as well as structural elements with transverse dimensions on the order of a few nanometers or less. After ion implantation there is a reduction in the Raman scattering signal, but even at an implantation dose of 1×10^{16} cm^{-2} lines associated with bulk phonons and vibrations in nanostructures can be

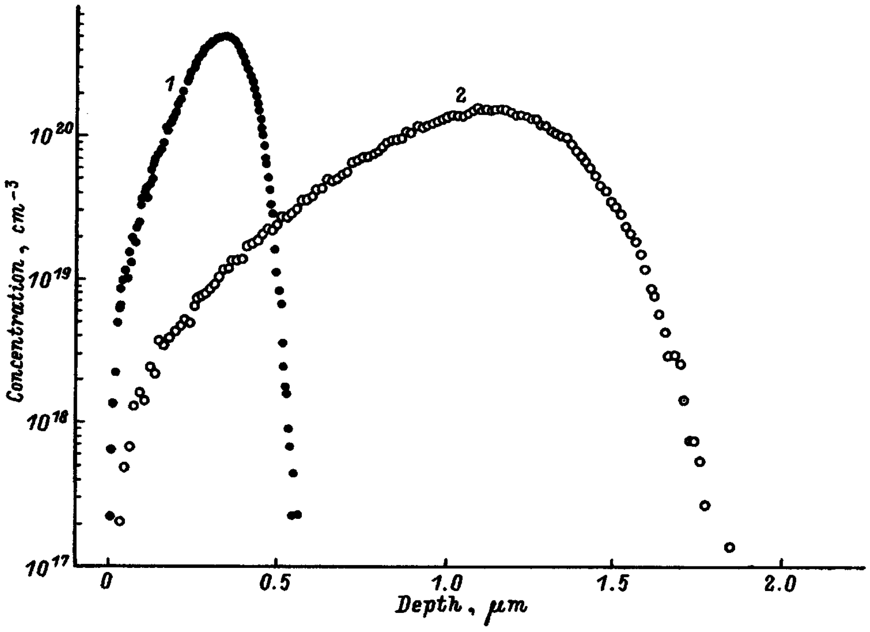

FIG. 1. Calculated variation in the spatial distribution of the concentration of implanted Ar in the surface layers of *c*-Si (*1*) and *por*-Si (*2*) for 300-keV Ar^+ ions at an irradiation dose of 1×10^{16} cm^{-2}.

seen. These data indicate that the destructive effect of the ion beam is less in *por*-Si layers than in single crystal samples.

The luminescence of these samples was studied in parallel with the Raman measurements. As can be seen from Fig. 3, the emission intensity falls off relatively smoothly as the irradiation dose is raised while the luminescence spectra change little (Fig. 4). However, even at a dose of 1×10^{16} cm^{-2}, well beyond that customarily used in ion beam semiconductor technology, a fairly intense emission band can be seen in the luminescence spectra of porous silicon.

As for the causes of the greater radiation hardness of porous layers, first of all it is evident that the extremely developed surface of porous silicon (up to 600 m^2/cm^3)[12] can serve as an efficient sink region for radiation defects which are subsequently annihilated. In addition, it may be noticed that during the interaction of high energy ions with

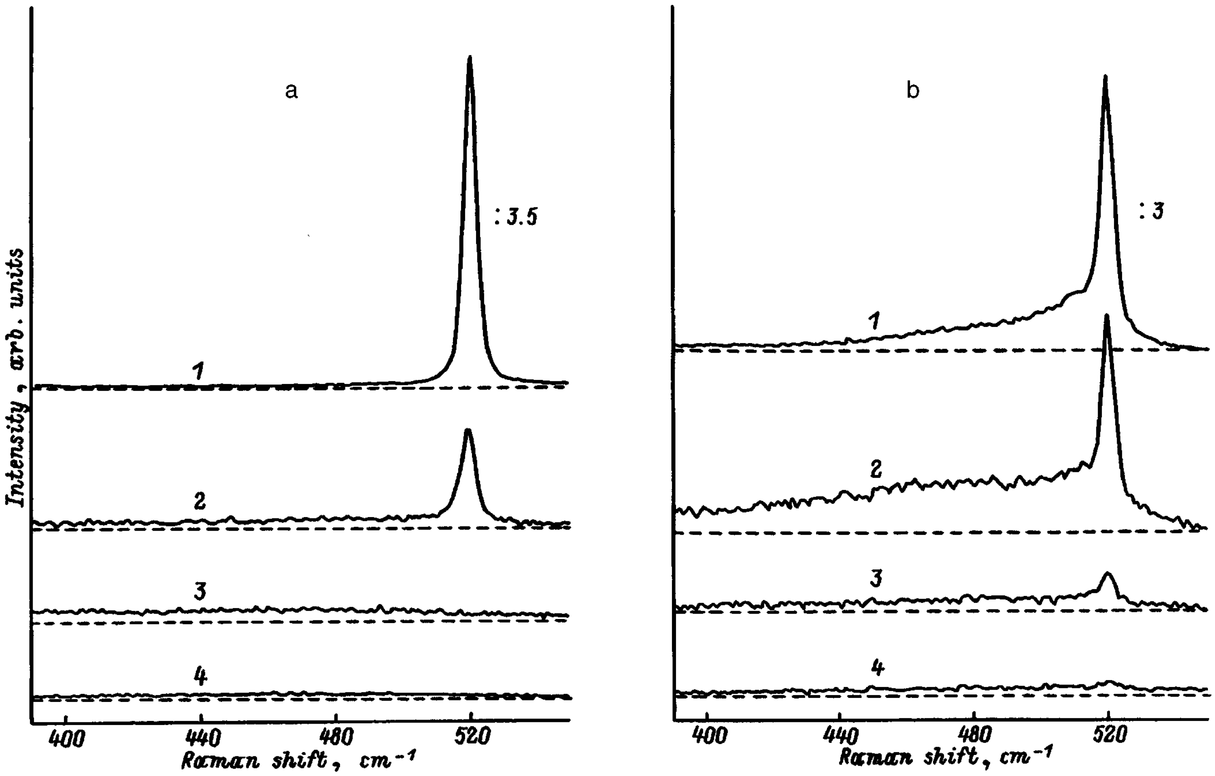

FIG. 2. Raman scattering spectra for *c*-Si (a) and *por*-Si (b): (*1*) initial samples; (*2–4*) after irradiation to doses of 5×10^{14}, 2×10^{15}, and 1×10^{16} cm^{-2}, respectively.

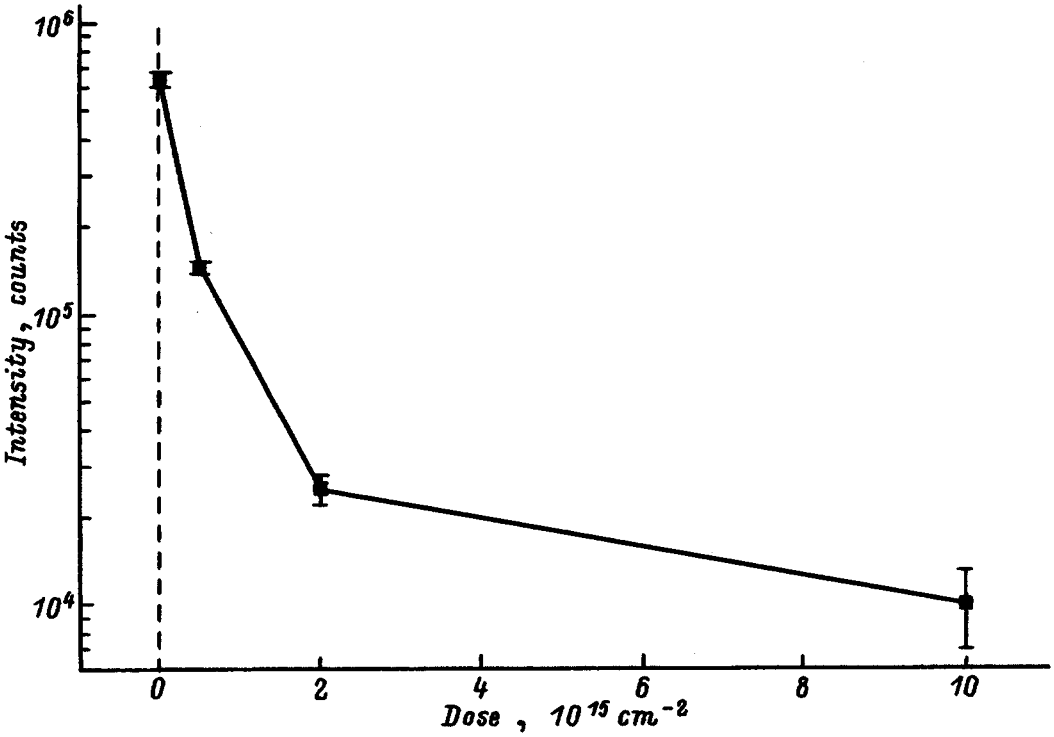

FIG. 3. Photoluminescence intensity of *por*-Si as a function of Ar$^+$ ion irradiation dose.

the elements of a porous structure energy may be transferred not only to individual atoms, but also to clusters or parts of ''silicon filaments.'' This sort of ''collective'' energy acceptance is possible because of the changes in the phonon spectrum in nanometer silicon structures.[11] The energy gained by groups of atoms in *por*-Si nanostructures will evidently be less than the amount acquired by individual atoms and this reduces the damage from the ion beam.

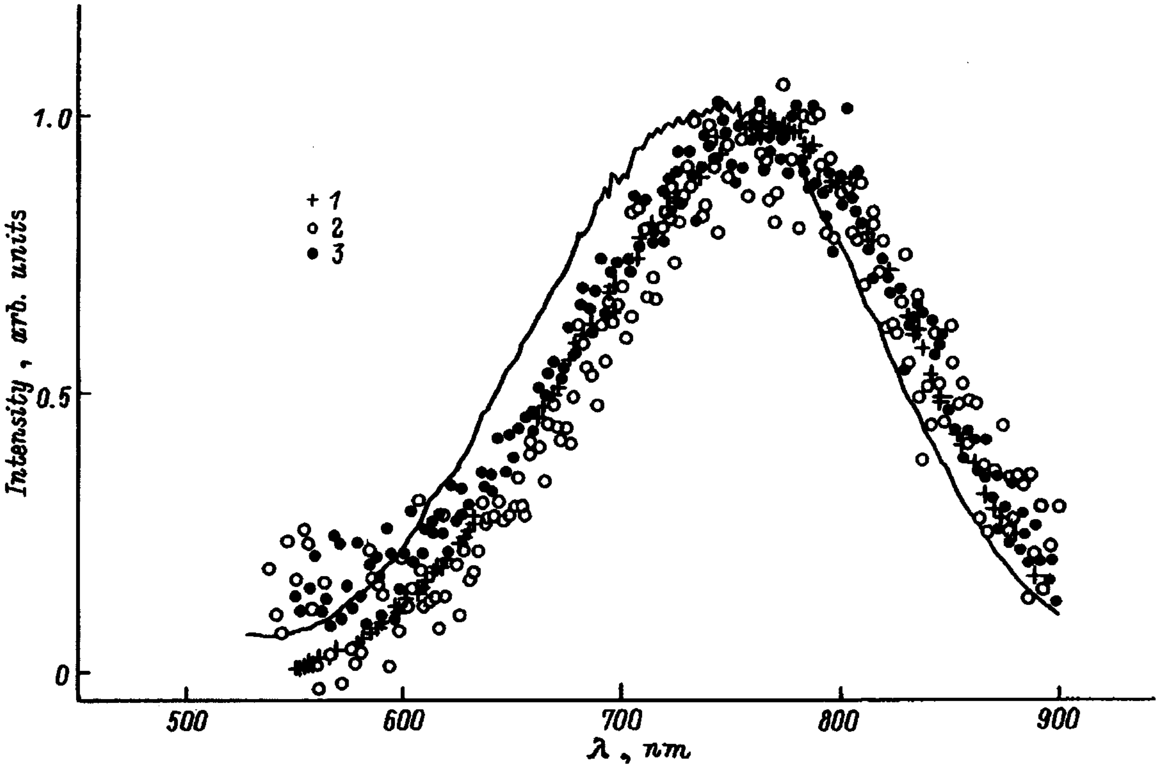

FIG. 4. Normalized photoluminescence spectra for the initial *por*-Si (smooth curve) and *por*-Si implanted with Ar$^+$ ions to doses of 5×10^{14} (*1*), 2×10^{15} (*2*), and 1×10^{16} cm^{-2} (*3*).

The results presented here indicate that optoelectronic emitting structures made of porous silicon will continue to operate under high radiation conditions. Furthermore, ion-beam technology can be used directly in fabricating these structures without the risk of major damage to the emitting layer.

This work was carried out as a project of the Russian Fund for Fundamental Research.

1)E-mail: ushakov@sci.fian.ms.su(Ushakov)

---

[1] Y. Kanemitsu, Phys. Reports **203**, 3 (1995).
[2] Th. Dittrich and V. Yu. Timoshenko, J. Appl. Phys. **75** , 5436 (1994).
[3] A. Roy, K. Jayaram, and A. K. Sood, Solid State Commun. **89**, 229 (1994).
[4] S. M. Prokes, W. E. Carlos, and V. M. Bermudez, Appl. Phys. Lett. **61**, 1447 (1992).
[5] K.-H. Li, S. Tse, J. C. Campbell, B. K. Hance, and J. M. White, Appl. Phys. Lett. **62**, 3501 (1993).
[6] Chi-Huei Lin, Si-Chen Lee, and Yang-Fang Chen, J. Appl. Phys. **75**, 7728 (1994).
[7] D. A. Redman, D. M. Follstaedt, T. R. Guilinger, and M. J. Kelly, Appl. Phys. Lett. **65**, 2386 (1994).
[8] L. Pavesti, G. Giebel, F. Ziglio, G. Mariotto, F. Priolo, S. V. Campisano, and C. Spinella, Appl. Phys. Lett. **65**, 2182 (1994).
[9] F. Namavar, Feng Lu, C. H. Perry, and R. A. Siref, J. Appl. Phys. **77**, 4813 (1995).
[10] H. Ryssel and I. Ruget, *Ionenimplantation*, Teubner, Stuttgart (1978).
[11] I. I. Reshina and E. G. Guk, Fiz. Tekh. Poluprovodn. **27**, 732 (1993). [Semiconductors **27**, 401 (1993)].
[12] G. Bomchil, A. Halimaoui, and R. Herrino, Appl. Surf. Sci. **41/42**, 604 (1989).

Translated by D. H. McNeill

Study of porous silicon obtained by krypton ion implantation and laser annealing

M. F. Galyautdinov,* N. V. Kurbatova, É. Yu. Buĭnova, E. I. Shtyrkov,
and A. A. Bukharaev

Kazan Physical-technical Institute, Russian Academy of Sciences,
420029 Kazan, Russia

(Submitted August 20, 1996; accepted for publication October 25, 1996)
Fiz. Tekh. Poluprovodn. **31**, 1130–1134 (September 1997)

An ellipsometric technique is used to study the formation of a finely porous layer saturated with atoms of an inert gas in a crystalline silicon lattice that has been doped by high doses of krypton and then irradiated by nanosecond laser pulses. The changes in the complex refractive index of this layer induced by laser pulses at different powers are studied. A scanning field ion microscope is used to follow the transformation of the pores, as the energy per unit area of the annealing laser light is varied, and to estimate their sizes. © *1997 American Institute of Physics.* [S1063-7826(97)02209-6]

INTRODUCTION

Over the last five years many papers have been published on porous silicon produced by electrochemical etching of single crystal Si.[1–5] A reaction in the original single crystal Si causes the formation of a branched system of voids with sizes ranging from 2 to 50 nm, which are directed into the depth of the crystal.[5,6] Interest in porous silicon has been stimulated by one of its unique properties: an intense photoluminescence in the visible, which makes it especially valuable for optoelectronics.[1–3,5,7] Despite a large number of papers devoted to exploring the microscopic nature of the photoluminescence in porous silicon, this question remains open.[8] Most researchers believe that the unusual properties of porous silicon are caused by size quantization effects. Others believe that the photoluminescence in porous silicon is caused by siloxene and its derivatives formed during anode etching. From the latter standpoint the porous silicon which we have obtained by implanting Kr^+ inert gas ions in single crystal substrates and then annealing with a laser[9] is of interest for study because it differs significantly from porous silicon prepared in the traditional way.

In this paper studies are made using ellipsometry and scanning field microscopy techniques on porous silicon obtained in different implantation and laser annealing regimes.

EXPERIMENT

We have studied p-type single crystal silicon doped with $E=40$ keV Kr^+ ions at doses $D=6\times10^{14}$, 1.08×10^{15}, 4.8×10^{15}, 6×10^{15}, 1.08×10^{16}, 6×10^{16}, 2.4×10^{17} cm^2 with ion current densities ranging from 2 to 5 μA/cm^2. Discrete segments on each of the seven implantation samples were annealed by pulsed ruby laser light (wavelength $\lambda=0.69$ μm, pulse duration $\tau=50$ ns) passed through a diaphragm at different energy densities $W=0.1-2.0$ J/cm^2. Thus, on each sample there were several simultaneously existing segments with different degrees of disordering of the crystalline lattice ranging from complete amorphization at $W=0$ to complete recrystallization at a threshold value of W that was characteristic of each sample, as well as a control segment of silicon which had not been subjected to implantation.

A type LÉF 3M-1 laser ellipsometer was used to study the change in the polarization of a monochromatic light beam ($\lambda=0.63$ μm) on reflection from each annealed segment, and from the control, for all the samples, which differed in the amount of implanted Kr atoms. The measurements were made at room temperature and atmospheric pressure with the probe light incident on the sample at an angle of 70°, which is optimal for silicon.[9] The measured polarization parameters of the reflected light, Δ and Ψ, depend on the angle of incidence of the light on the sample and on the thickness of the natural SiO_2 oxide layer and its refractive index, as well as on the distribution of the refractive index n and extinction coefficient k over the depth of the sample. The parameters Δ and Ψ are integral, since they contain information on the properties of the entire test volume of the sample, whose dimensions are determined, in turn, by the penetration depth of the light. In highly disordered silicon samples the probe light ($\lambda=0.63$ nm) does not penetrate further than 100 nm because of strong absorption.

The implanted part of the substrate was removed layer by layer using anode oxidation followed by etching of the oxide in dilute acid. In our experiment, the thickness d of the etched layer was 10 nm in each step. The ellipsometric parameters Δ and Ψ were measured after each layer removal step.

The ellipsometric parameters are related to the optical constants n and k of the test surface by the basic equation of ellipsometry,[10]

$$\tan\Psi\,\exp i\Delta=f\,(n,k,\ldots). \qquad (1)$$

When n and k are determined from the experimental ellipsometric parameters, the specific form of the function on the right hand side of this equation depends on the model chosen for the surface. In order to obtain the unknown optical constants n and k, the inverse ellipsometry problem was solved for each etching step using a ''clean surface'' (''air/implanted layer'') model in a special program for analyzing ellipsometric measurements.[11] The choice of this particular model is based on the fact that in these samples the probe light did not penetrate to a depth greater than the thickness of the implanted layer because of high absorption. The effective

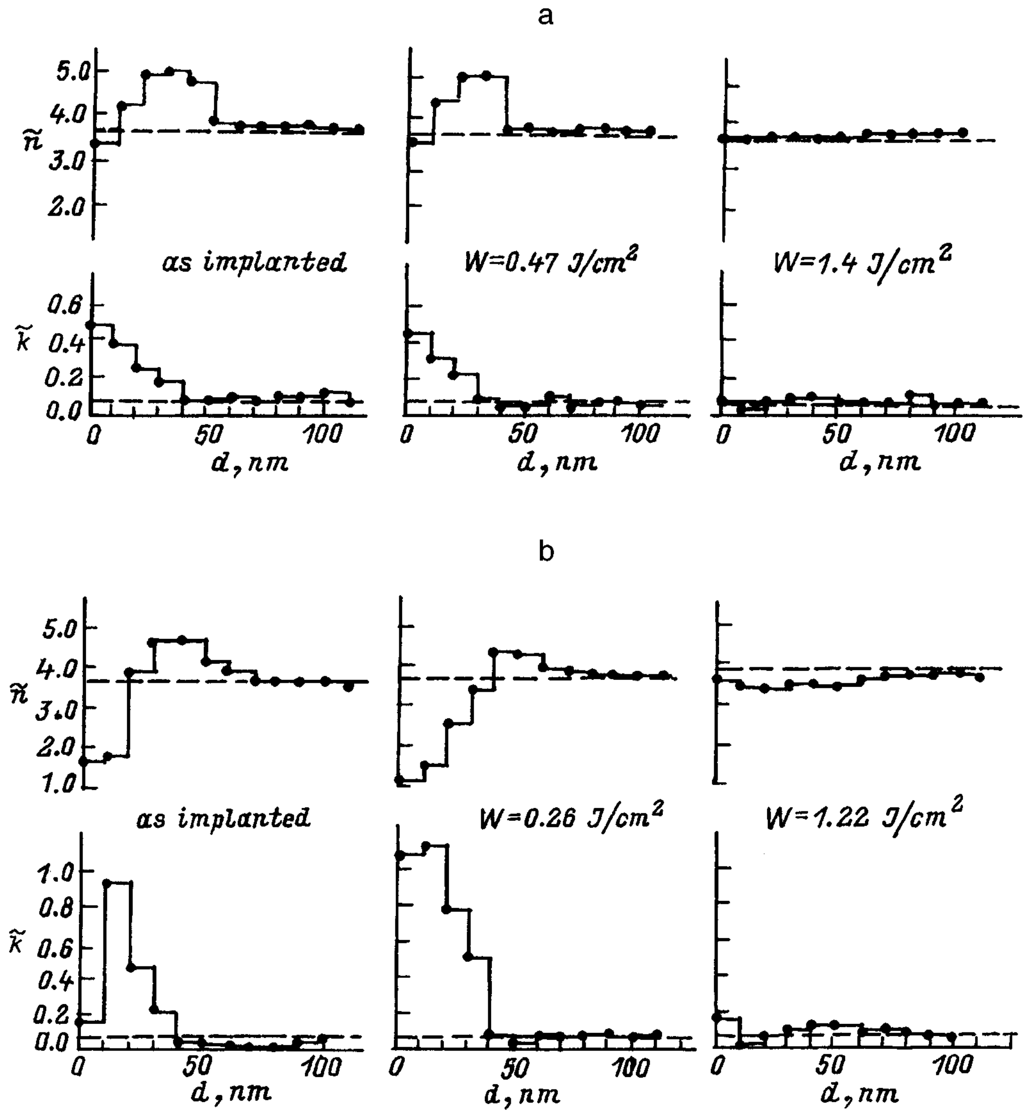

FIG. 1. The change in the effective optical constants $\tilde{n}$ and $\tilde{k}$ (real and imaginary parts of the complex refractive index) in the surface layer of silicon doped with high doses of krypton ions after nanosecond laser annealing: (a) $E=40$ keV, $D=6\times10^{14}$ cm^{-2}; (b) $E=40$ keV, $D=2.4\times10^{17}$ cm^{-2}.

optical constants $\tilde{n}$ and $\tilde{k}$ were calculated for the entire remaining part of the implanted layer after each etching step. This operation was performed ten times, until the layer containing the Kr$^+$ ions had been completely etched ($d\simeq100$ nm). The differential values $n(d)$ and $k(d)$ were not calculated for each thin layer, since we were only interested in the behavior of the optical constants within the implanted part of the substrate, and not in their absolute values within each thin layer. Thus, we have studied the variation in the effective constants $\tilde{n}$ and $\tilde{k}$ in the surface layer which contains atoms of the inert gas krypton. Similar layer-by-layer ellipsometric studies of silicon doped with Ar$^+$ ions ($E=40$ keV, $D=10^{15}$ cm^{-2})[12] have shown that the behavior of the effective optical constants $\tilde{n}$ and $\tilde{k}$ in the implanted layer is consistent with the behavior of $n(d)$ and $k(d)$ calculated for each thin layer.

As a result, for each test sample we obtained profiles characterizing the variation in the refractive index and extinction coefficient (i.e., the real and imaginary parts of the complex refractive index $N=n-ik$) over the entire layer containing the implanted impurity for segments annealed by pulses of laser light at different energies W per unit area. The curves for two of the samples are shown in Figs. 1a and 1b. The broken line joining the calculated points only indicates that the measurements were discrete, taken after the sample had been etched by a 10-nm thickness. The dashed horizontal lines in all the graphs in Fig. 1 correspond to $\tilde{n}_c$ and $\tilde{k}_c$, the optical constants of the original single crystal. They were measured on the control segment of the silicon sample which had not been subjected to implantation. These measurements were also made layer-by-layer, in 10 nm steps. The constancy of $\tilde{n}_c$ and $\tilde{k}_c$ over the entire 100-nm-thick layer is an indication of the perfection of the crystal lattice of the original silicon, since the complex refractive index is known to be sensitive to the slightest changes in the structure of the material.

The microscopy studies were conducted using a P4-SPM-MDT scanning field microscope developed by the Nanotekhnologiya-MDT Company (of Zelenograd, Russia). The measurements were made in a contact mode.

DISCUSSION OF RESULTS

It can be seen from Fig. 1a that implanting Kr^+ ions to a dose of 6×10^{14} cm^{-2} in a perfect Si crystal lattice with

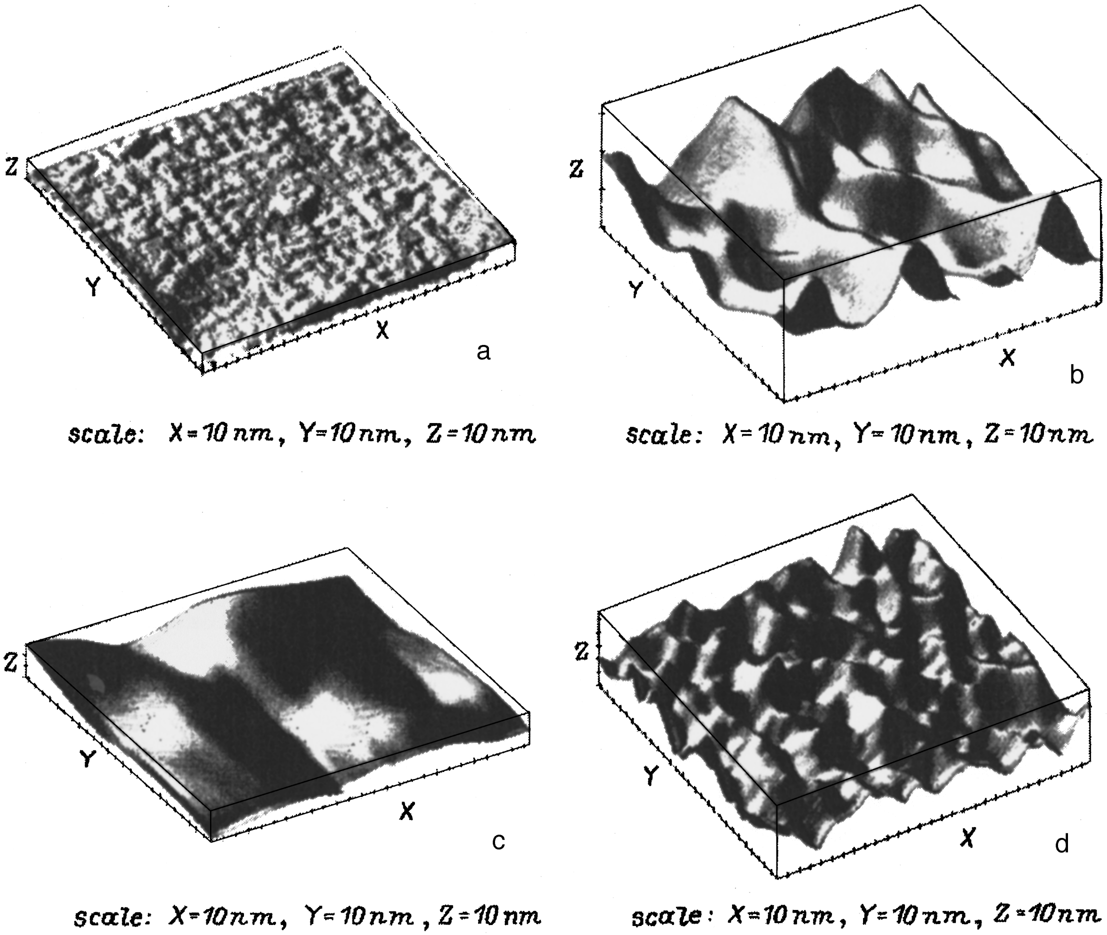

FIG. 2. Scanning field microscope images of silicon surfaces doped with Kr^+ ions ($E=40$ keV, $D=2.4\times10^{17}$ cm^{-2}): (a) initial single crystal KDB-1 Si (111); (b) amorphous segment; (c) after laser annealing, $\lambda=0.69$ nm, $\tau=50$ ns, $W=0.19$ J/cm^2; (d) after laser annealing, $\lambda=0.69$ nm, $\tau=50$ ns, $W=1.1$ J/cm^2.

fixed optical constants $\tilde{n}_c=3.85$ and $\tilde{k}_c=0.02$ over the entire depth does cause a substantial increase in $\tilde{n}$ and $\tilde{k}$ within the layer where the measurements were made. This indicates that the crystal structure of the material has been damaged significantly; the layer with the highest $\tilde{n}=5$ lies at a depth of 30 nm in the sample, while the maximum of $\tilde{k}=0.5$ occurs at the surface. The difference in the depths of these maxima is explained by the fact that the $\tilde{n}(d)$ profile is determined by the defect distribution, as well as by the distribution of the implanted ions, while the $\tilde{k}(d)$ profile is determined only by the defects.[9,12] Laser annealing of this kind of sample at a fixed energy W per unit area restores the damaged crystal lattice, along with the $\tilde{n}(d)$ and $\tilde{k}(d)$ profiles (Fig. 1a, $W=1.4$ J/cm^2).

When the Kr^+ ion dose is raised by almost a factor of 10, recrystallization during laser annealing has a distinct feature that we have pointed out previously.[9] Specifically, irradiating an amorphous sample with a single nanosecond laser pulse having an energy per unit area below the threshold for epitaxial recrystallization causes formation of a layer of thickness ~30 nm near the surface with an effective refractive index $\tilde{n}\simeq3$ that corresponds neither to crystalline nor to amorphous silicon. This can be explained by the formation of micropores saturated with the inert gas. As such, the formation of gas ''bubbles'' in semiconductors doped with high doses of inert gases ($>10^{17}$ cm^{-2}) is a known effect.[13] Here, however, the main point of interest is the possibility of controlling the properties of porous silicon by laser annealing.

Void formation in samples heavily doped with krypton ($>10^{16}$ cm^{-2}) and their transformation as a result of pulsed laser irradiation is traced in Fig. 1b. A porous layer can be formed immediately as a result of implantation with an efficiency that is higher when more inert gas ions are implanted. (The reduction in $\tilde{n}$ in the surface layer compared to $\tilde{n}_c$ is greater in the sample with a maximum dose of inert gas atoms.) An interaction with a single weak nanosecond pulse appears to cause a transformation of the voids, since we can see a substantial drop in the effective refractive index and an increase in the effective extinction coefficient by more than a factor of 50 compared to $\tilde{k}_c$ (Fig. 1b for $W=0.26$ J/cm^2). With this absorption, the thickness of the probed layer is less than 20 nm and the small value of $\tilde{n}$ indicates that the main contribution to the refractive index is from voids filled with the inert gas concentrated in this surface layer.

Irradiating this kind of porous silicon with a single nanosecond laser pulse with an energy per unit area of $W>1$

J/cm^2 causes epitaxial recrystallization, with the bulk of the implanted impurity krypton being expelled to the surface and then released as a gas.[14] The result is a finer grained porous material with a refractive index close to $\tilde{n}_c$ (Fig. 1b for $W = 1.22$ J/cm^2).

These conclusions regarding the formation of porous silicon and its modification by nanosecond laser pulses based on our ellipsometric studies have been confirmed by studies with a scanning field microscope. Unexpectedly, however, this was not a simple task. The scanning field microscope was used to study a sample with the maximum inert gas dose, Si←Kr$^+$ ($E = 40$ keV, $D = 2.4 \times 10^{17}$ cm^{-2}), which the ellipsometric measurements had shown should clearly have a porous structure near the surface. But this structure could only be observed after electrochemical etching of a 10-nm-thick layer beneath which the porous silicon was buried (Figs. 2a–2d).

The initial single crystal KDB-1 Si, with a (111) orientation, has a flat surface (Fig. 2a) with negligible roughness of height ~1 nm and transverse dimensions of ~10 nm.

In the implanted Si (Fig. 2b), one can see pores with sizes of ~100 nm and depths of up to 150 nm. After annealing by a weak laser pulse ($\lambda = 0.69$ nm, $\tau = 50$ nm, $W = 0.19$ J/cm^2), the transverse dimensions of the pores increased to ~150 nm, while the depth decreased to ~30 nm (Fig. 2c). After irradiation by a single pulse with $W = 1.1$ J/cm^2, we obtained a finely porous silicon with pore sizes of 30–50 nm (Fig. 2d).

CONCLUSIONS

These ellipsometric and microscopic studies of krypton ion doped silicon have shown that implanting inert gas atoms to levels of $10^{15} - 10^{17}$ cm^{-2} with subsequent annealing by single nanosecond laser pulses transforms perfect Si single crystals with optical constants $\tilde{n}_c = 3.85$ and $\tilde{k}_c = 0.02$ into a material which contains a porous layer near its surface, ''buried'' under a 10-nm-thick film of silicon. These voids are filled with the inert gas and this causes a reduction in the effective refractive index of the sample by a factor of 3 compared to $\tilde{n}_c$, while the effective extinction coefficient increases by a factor of 50 compared to $\tilde{k}_c$. Here the void dimensions can be controlled over a range from 10 to 150 nm by varying the energy per unit area of the annealing laser pulse from 0.1 to 1.5 J/cm^2.

This work was supported in part, by the Russian Fund for Fundamental Research (No. 96-02-18245) and the State Scientific-Technical Program on the Physics of Solid State Nanostructures.

*Fax: 7(8432)76-50-75; E-mail: mansur@ksc.iasnet.ru

---

[1] L. T. Canham, Appl. Phys. Lett. **57**, 1046 (1990).

[2] N. Koshida and H. Koyama, Appl. Phys. Lett. **60**, 347 (1992).

[3] R. Tsu, H. Shen, and M. Dutta, Appl. Phys. Lett. **60**, 112 (1992).

[4] Y. M. Weng, Zh. N. Fan, and X. F. Zhong, Appl. Phys. Lett. **63**, 168 (1993).

[5] X. Zhao, O. Schoenfeld, Y. Aoyagi, and T. Sugano, Appl. Phys. Lett. **65**, 1290 (1994).

[6] A. V. Mel'nikov, Yu. N. Moiseev, and T. V. Murzina, Zh. Éksp. Teor. Fiz. **108**, 669 (1995) [JETP **107**, 363 (1995)].

[7] V. A. Karavanskiĭ and A. N. Obraztsov, Fiz. Tekh. Poluprovodn. **29**, 582 (1995) [Semiconductors **29**, 302 (1995)].

[8] V. M. Dubin, F. Ozaham, and J. N. Chazalviev, Phys. Rev. B **50**, 14867 (1994).

[9] M. F. Galyautdinov, É. Yu. Karas', N. V. Kurbatova, and E. I. Shtyrkov, Opt. Spektrosk. **73**, 344 (1992) [Opt. Spectrosc. **73**, 200 (1992)].

[10] V. I. Pshenitsyn, M. I. Abaev, and I. Yu. Lyzlov, *Ellipsometry in Physical and Chemical Research* [in Russian], Leningrad (1986).

[11] L. Frank and F. L. McCrackin, *A Fortran Program for Analysis of Ellipsometer Measurements*, NBS Technical Note 479 (April 1969).

[12] L. F. Bakhturova, V. V. Bakovets, I. P. Domovesova, and B. M. Ayupov, Fiz. Tekh. Poluprovodn. **27**, 588 (1993) [Semiconductors **27**, 327 (1993)].

[13] G. G. Zakirov and E. A. Nikitina, in *Abstracts of Talks at the All-union Conference on Ion-beam Modification of Materials* [in Russian], Kaunas (1989), p. 189.

[14] C. Jech and R. Kelly, J. Phys. Chem. Solids **30**, 465 (1969), edited by L. V. Sharonova.

Translated by D. H. McNeill

Photoluminescence and photoexcitation spectra of porous silicon subjected to anodic oxidation and etching

V. V. Filippov[1)] and P. P. Pershukevich

Institute of Physics, Academy of Sciences of Belarus, 220072 Minsk, Belarus

V. P. Bondarenko

Belarus State University of Information Technology and Electronics, 220027 Minsk, Belarus

(Submitted January 18, 1996; accepted for publication March 18, 1997)
Fiz. Tekh. Poluprovodn. **31**, 1135–1141 (September 1997)

The photoluminescence and photoexcitation spectra of porous silicon films with an initial porosity of 50–60%, produced on single crystals of *p*-type silicon and subjected to anodic oxidation and chemical etching, are studied. The existence of an amorphous phase in the etched porous silicon is found not to affect the photoluminescence spectrum of porous silicon. Features of the photoexcitation spectra before and after etching, as well as the evolution of the photoluminescence and photoexcitation spectra after etching, can be interpreted in terms of a uniform quantization model that includes elastic stresses in the silicon crystals of the porous silicon. © *1997 American Institute of Physics.* [S1063-7826(97)02309-0]

INTRODUCTION

The mechanism for the visible photoluminescence of porous silicon continues to be the subject of intense discussion. In many cases, the size quantization effect first proposed by Canham[1] fully describes the observed features of luminescence in porous silicon films which contain nanometer sized crystallites (silicon cores). The emission of light from porous silicon is undoubtedly also affected by its extended (textured) surface with dangling silicon bonds on which chemical compounds are formed. Thus, the character of the passivation of porous silicon surfaces and the role of silicon-hydrogen compounds on the crystallite surfaces, including polysilanes, continue to be discussed widely in the literature.[2–6]

In this paper we study the evolution of the photoluminescence and photoexcitation spectra during oxidation of porous silicon samples in air at room temperature after they have been etched in highly dilute hydrofluoric acid. Similar studies of just the photoluminescence spectrum have been carried out previously,[6] using freshly prepared samples of porous silicon with a substantial concentration of $\mathrm{Si-H}_x$ ($x=1,2,3$) compounds on the surface of the silicon crystallites. During the oxidation process, these compounds were replaced by $\mathrm{Si-O}$ bonds and this determined the nonunique variations in the photoluminescence spectrum (vanishing of SiH and $\mathrm{SiH_2}$ groups and the appearance of $\mathrm{SiO_2}$) observed in the earlier work.[6] In order to eliminate this ambiguity, in the present work the porous silicon samples were subjected to anodic electrochemical oxidation. Then the anodic oxide was etched in a water solution of HF, which, according to our data and earlier papers,[7–9] does not lead to the appearance of silicon-hydrogen bonds on the surface. Thus, the only factor which determines the evolution of the photoluminescence and photoexcitation spectra in the present experiments was oxide formation on the surface of silicon crystallites. As will be shown below, our data support the size-quantization mechanism for luminescence in porous silicon. Silicon oxide is a good pacifier of the crystallite surfaces and increases the emission efficiency of the material. In freshly prepared samples this function is served by silicon-hydrogen structures. This type of porous silicon is not distinguished by stable photoluminescence. Films of anodic-oxidized porous silicon, on the other hand, are highly transparent in the visible and have stable luminescence characteristics which are recovered after repeated etching in a water solution of HF. Furthermore, an oxide shell on the silicon crystallites produces mechanical stresses, one consequence of which is partial polarization of the emission from the porous silicon.[10]

1. EXPERIMENTAL TECHNIQUE

Porous silicon films with a thickness of 5 μm were prepared by electrochemical anodizing on single crystals of boron-doped silicon with a resistivity of 10 $\Omega\cdot$cm and orientation in the (111) plane. The anode currents during electrochemical processing in 36% HF were 10, 20, and 40 mA/cm^2, respectively, for samples 1, 2, and 3. The initial porosities of samples 1, 2, and 3 were 50, 55, and 60%. These samples were then subjected to galvanostatic anodic electrochemical oxidation in an $\mathrm{NH_4NO_3}$-ethylene glycol solution with a current density of 10 mA/cm^2. The initial voltages lay in the range of 6–7 V and the final forming voltage was 30 V for all the samples.

The photoluminescence and photoexcitation spectra were measured on an automated SDL-2 spectrofluorometer based on diffraction grating monochromators for excitation (MDR-12) and detection (MDR-23). The excitation source was a DKSSh-120 xenon arc lamp. In the excitation spectrum measurements the constancy of the excitation spot shape was ensured by introducing a special system of mirrors after the excitation monochromator. The signal was detected with an FÉU-100 photomultiplier operating in a photon counting regime. The spectral widths of the slits of both monochromators were varied over 2.4–3.0 nm. The photoexcitation and photoluminescence spectra were corrected for

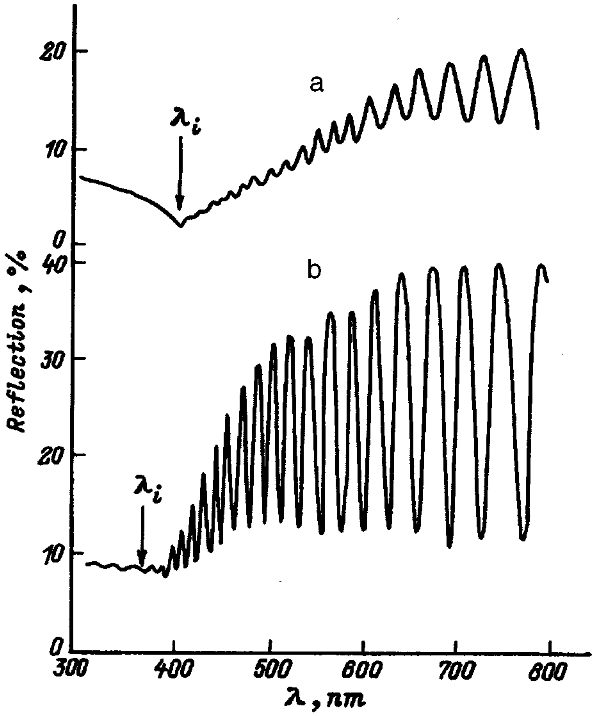

FIG. 1. Reflection spectra of sample 2 before (a) and after (b) anodic oxidation.

sensitivity using standard methods. The error in measuring the luminescence spectra was less than 2–3%. The reflection and transmission spectra were recorded on a Jasko IR-810 spectrometer with a spectral resolution of 2 cm^{-1}.

2. RESULTS AND DISCUSSION

2.1. *Reflection and absorption spectra.* Figure 1 shows reflection spectra for porous silicon samples obtained with an anode current density of 20 mA/cm^2. In the visible the reflection spectra are characterized by a distinct interference pattern which vanishes on approaching the UV region. As can be seen from Fig. 1, the cutoff wavelength λ_i for the interference pattern was 423 nm for the porous silicon sample prior to anodic oxidation. After anodic oxidation of this sample, λ_i fell to 372 nm. An interference pattern was observed for all the porous silicon samples that were tested and the cutoff wavelength λ_i for the interference pattern depended on the conditions under which the samples were prepared and characterized the shift in the edge of the intrinsic absorption band of the porous silicon. This shift can be caused only by a quantum-well effect in nanometer-sized crystallites (silicon cores) of the porous silicon. Another possible reason, a large fraction of the transparent phase in the porous silicon film associated with voids and the oxide, cannot explain the vanishing of the interference pattern near the UV region. Furthermore, it proceeds quite rapidly (as λ decreases), which indicates a rapid rise in the absorption within the film. Thus, the boundary between the transparency and strong absorption regions lies in the region of λ_i. Since the interference falls off when the intensity of the wave reflected off the boundary between the film and the substrate, which participates in the interference, falls by a factor of e, we can estimate the level of absorption corresponding to λ_i.[10] Here $\alpha_{\lambda j}\cdot h=1$, where $\alpha_{\lambda j}$ is the absorption coefficient at wavelength λ_i and h is the thickness of the porous silicon layer. For our films, with a thickness $h=5\times10^{-4}$ cm, we have $\alpha_{\lambda j}=5\times10^{5}$ cm^{-1}. The values of λ_i for all the samples are listed in Table I. Also given there are the wavelengths of the peaks in the photoluminescence spectra. Judging from λ_i, which characterizes the effect of the shift in the edge of the intrinsic absorption band, sample 1 has the smallest silicon crystallites. This conclusion is independent of the position of the photoluminescence peak. As the table shows, however, there is a correlation between photoluminescence and the size of the crystallites: the smaller they are (sample 1), the more strongly the peak of the photoluminescence spectrum will be shifted toward the blue.

TABLE I. Anodizing current density I, cutoff wavelength λ_i for the interference pattern, and peak wavelength λ_m of the photoluminescence spectrum for porous silicon samples subjected to anodic oxidation.

Sample No.	I, mA/cm^2	λ_i, nm	λ_m, nm
1	10	335	645
2	20	372	680
3	40	383	695

The films of anodically oxidized porous silicon were then subjected to etching in a water solution of hydrofluoric acid (H_2O:HF=9:1), washed in distilled water, and dried. 10–15 minutes after etching, their photoluminescence and photoexcitation spectra were taken. The choice of a dilute water solution of hydrofluoric acid for etching was determined by the fact that it yields a flat and perfect boundary on the silicon after the oxide is removed.[11] IR absorption spectra were taken on identically processed samples. These are shown in Fig. 2. The spectral features were identified using data published elsewhere.[12–15] As can be seen from Fig. 2, anodic oxidation of porous silicon causes a large increase in the absorption band at 1100 cm^{-1}, which indicates that the fraction of oxide in the porous silicon samples increases after anodic oxidation. The IR spectra of the anodically oxidized samples contain no absorption bands characteristic of the vibrations of the SiH_2 and SiH_3 groups or clusters of them.[14] We note that a peak at 938 cm^{-1} has been attributed to vibrations of an Si–H group only in two papers[14,15] (935 cm^{-1}) but is absent in the other studies. After etching, weak broad absorption bands appeared at 2160 and 1635 cm^{-1}, which may be evidence of the presence of silicon-hydrogen compounds in the etched samples. However, since the absorption at 2160 and 1635 cm^{-1} is very weak, we have eliminated compounds of the type SiH_x from further consideration as a possible reason for the observed changes in the photoluminescence spectra of the porous silicon films.[4,6,16]

2.2. *Photoluminescence spectra.* Depending on their initial porosity, the porous silicon films had different oxide fractions. This explains the different etching times required for significant changes to show up in the luminescence characteristics. The photoluminescence spectra of samples 1 and 2, which had the smallest size silicon cores and largest oxide

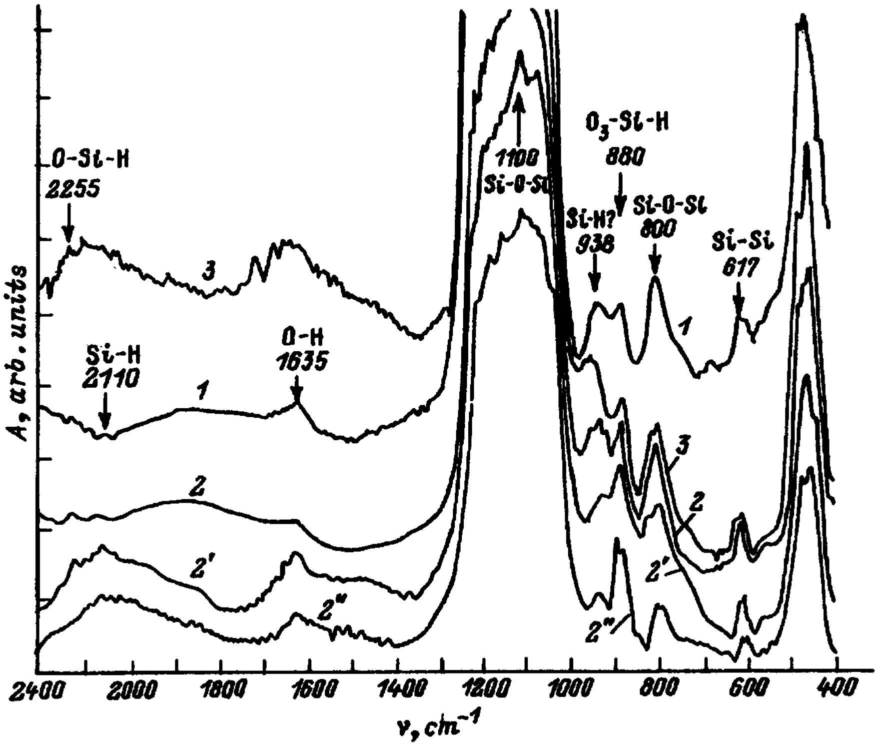

FIG. 2. IR absorption spectra of samples 1 (*1*), 2 (*2*), and 3 (*3*) prior to etching, sample 2 (*2′*) after etching twice for 3 min and sample 2 (2″) prior to anodic oxidation.

fraction, were essentially unchanged after 20 s of etching. At the same time, noticeable changes were observed for sample 3. Its spectrum became narrower and underwent a shift to shorter wavelengths (Fig. 3). This shift continued to increase for up to 19 h after etching, although the width of the spectrum began to increase by 1 h after etching. Afterwards the photoluminescence spectrum began to widen and return back to the red, but measurements made after 14 days showed that the initial position had still not been recovered and the peak was displaced by 18 nm.

The photoluminescence spectrum of sample 2 shifted to shorter wavelengths with an etching time of 3 min. Its subsequent evolution was completely analogous to that of the photoluminescence spectrum of sample 3.

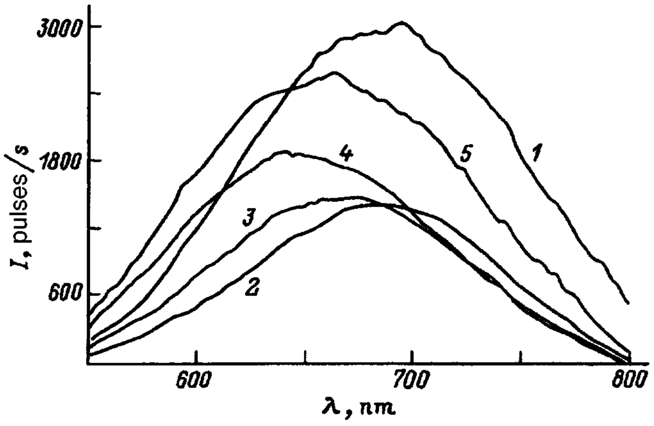

FIG. 3. Time evolution of the photoluminescence spectrum of sample 2 after etching followed by oxidation in air for the following times (h): (*2*) 0.3, (*3*) 1.3, (*4*) 19, (*5*) 336. Curve *1* is the initial spectrum prior to etching.

A blue shift showed up in the photoluminescence spectrum of sample 1 only after the sample had been etched for three minutes with subsequent washing in water, drying, and control measurements, for a total of eight times. The evolution of the photoluminescence spectrum of sample 1 was the same as that of samples 2 and 3. After the photoluminescence spectrum initially became narrower, in all the samples the spectrum underwent broadening, mainly as a result of the long-wavelength wing. In sample 1 the width of the spectrum exceeded that of the control sample (by 17 nm), but because of oxidation in the air after a few days it broadened to its original value and returned to the initial position it had occupied before etching.

These features of the evolution of the photoluminescence spectra can be understood fully if we attribute the observed emission of the porous silicon to a quantum-well effect for carriers in the crystallites of the silicon core of the porous silicon films. In fact, after etching of the oxide shell on the surface of the crystallites in porous silicon, with oxidation in the air there is a reduction in the sizes of the crystallites and, as a consequence, a blue shift in the photoluminescence spectrum. Evidently, a surface layer of the porous silicon undergoes etching to a depth which depends on the etching time. In sample 3, where the crystallites are the largest and the fraction of silicon oxide is relatively small (the interference pattern shows up most weakly), it is etched away more rapidly. In sample 1, where the oxide fraction is large and the crystallites are smallest, however, as natural oxidation proceeds after etching they are reduced to critical sizes where the surface state and surface defects cause the nonradiative recombination channel to become dominant as a result of the small volume of the crystallites. In this regard, a subsequent second etching of the samples is significant. If

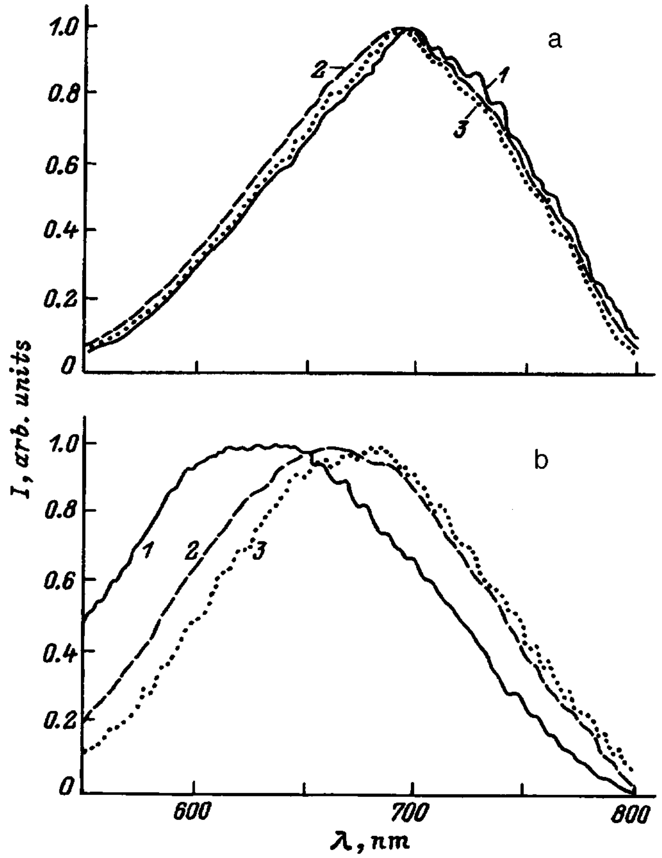

FIG. 4. Photoluminescence spectra of sample 2 before (a) and after (b) etching for different excitation wavelengths (nm): (*1*) 250, (*2*) 350, (*3*) 450. The normalization factors for the spectra are (a) (*1*) 0.7, (*2*) 1.0, (*3*) 6.0; (b) (*1*) 1.5, (*2*) 1.0, (*3*) 4.0.

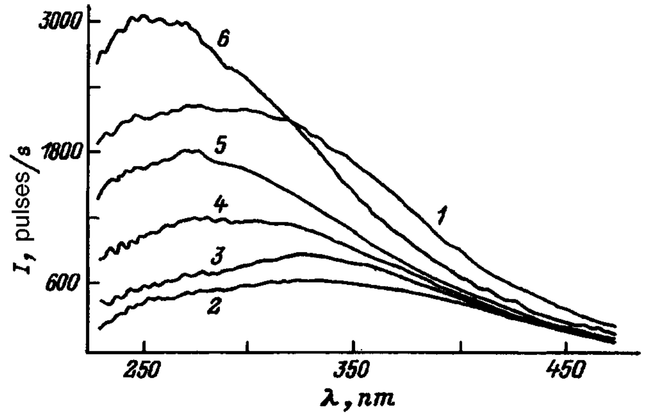

FIG. 5. Time evolution of the photoexcitation spectra of sample 2 after etching with oxidation in air for the following times (h): (*2*) 0.13, (*3*) 1.5, (*4*) 47, (*5*) 144, (*6*) 336. Curve *1* is the initial spectrum before etching.

smaller crystallites are formed in the surface region of the porous silicon after an initial etching (i.e., the photoluminescence spectrum seems shifted to the blue after etching and oxidation in the air), then a subsequent etching would quench their emission for the above reason. Here the photoluminescence spectrum is not shifted to the blue, but to the red (Fig. 3, spectrum 5). We shall discuss the broadening of the photoluminescence spectrum somewhat later.

Figure 4 shows photoluminescence spectra of sample 2 for different excitation wavelengths λ_{ex} before and after etching. We note that the position of the peak in the photoluminescence spectrum is independent of λ_{ex} for the initial sample prior to etching (Fig. 4a). Similar behavior of the photoluminescence spectra of anodized porous silicon has been observed previously.[17] The behavior of these photoluminescence spectra is entirely different for freshly prepared samples of porous silicon with a large content of SiH_x groups,[18,19] as well as in the case of hydrogenated amorphous silicon.[20] In them, the peak of the photoluminescence spectrum is observed to depend monotonically on the excitation energy. A similar dependence exists when porous silicon is anodized after etching (Fig. 4b). This sort of porous silicon, as we have seen, is not a stable system and evolves relatively rapidly (compared to freshly prepared samples) to an equilibrium state that is close to the initial state (Fig. 3).

The half width of the photoluminescence spectra of the unetched samples, however, does depend on λ_{ex}. This dependence results from a change in just the short wavelength wing of the photoluminescence spectrum, while the long wavelength wing is essentially the same for all λ_{ex}. The lack of a definite dependence of the half width of the photoluminescence spectrum on λ_{ex} in different samples is indicative of a difference in the distribution of the high energy part of the carrier photoexcitation. Thus, the spectra of Fig. 4a are evidence of a high level of uniformity in the excitation and emission processes in porous silicon samples subjected to anodic processing.

2.3. *Photoexcitation spectra.* The evolution of the photoexcitation spectra shown in Fig. 5, like that of the photoluminescence spectra, reflects the approach, during the oxidation process, to a stable state that is close to the initial state prior to etching and depends on the size of the silicon crystallites. Photoexcitation spectra for different observation wavelengths are shown in Fig. 6. They all have a smooth extremum in the region 275–280 nm. It correlates with the position of one of the two short wavelength peaks in the imaginary part of the pseudodielectric function ε_2 of single crystal silicon (293 nm),[21] which is shifted to shorter wavelengths as a result of quantum-well effects. The existence of a single peak in ε_2 has been confirmed[22] in porous silicon near the position of the peak corresponding to direct interband E_2 transitions in single crystal silicon. Thus, single-crystal silicon, rather than amorphous silicon, determines the behavior of ε_2 and the absorption spectrum of porous silicon. This conclusion also holds for the photoexcitation spectra of anodized porous silicon shown in Fig. 6. The absorption spectrum and the pseudodielectric function ε_2 have been calculated theoretically on the basis of first principles when quantum-well effects occur.[23,24] Sanders and Chang[23] considered quantum wires of silicon and Buda *et al.*[24] have taken into account the passivation of a surface of wires by hydrogen. The resulting complicated multipeaked spectrum[23] is, as yet, difficult to compare with available experimental data. At the same time, the calculations of Buda *et al.*[24] imply that in the case of quantum wires with a diameter of 0.76–1.14 nm, ε_2 has a distinct maximum in the region 340–366 nm, which depends weakly on the transverse di-

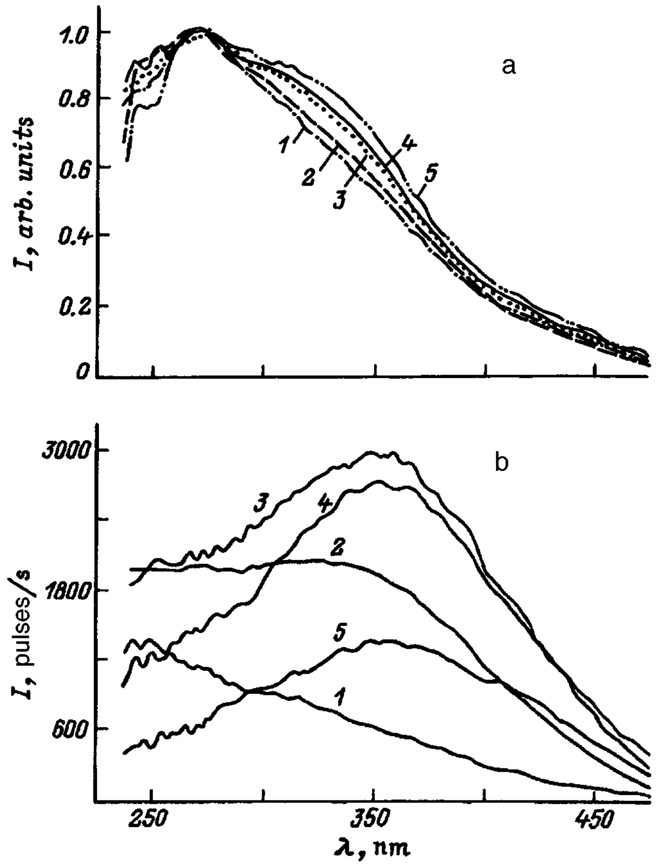

FIG. 6. Photoexcitation spectra of sample 2 before (a) and after (b) etching for different photoluminescence wavelengths (nm): (*1*) 550, (*2*) 600, (*3*) 650, (*4*) 700, (*5*) 750. The normalization factors for the spectra are (a) (*1*) 10, (*2*) 2.5, (*3*) 1.25, (*4*) 1.0, (*5*) 1.5.

mensions of the wires. In single-crystal silicon it corresponds to the direct-band $\Gamma_{15}-\Gamma'_{25}$ (366 nm) transition. However, neither the porous silicon absorption spectra of Ref. 22 nor the photoexcitation spectra shown in Fig. 6 contain this peak, which is attributable to the quantum wire crystalline structure.

The situation is entirely different after etching (Fig. 6b). While the photoexcitation spectra for the short wavelength wing of the photoluminescence spectrum do not change significantly, the photoexcitation spectra for its long wavelength wing have a distinct maximum after etching, precisely in the region where the maximum of ε_2 should lie according to the calculations of Ref. 24. Why does the photoexcitation spectrum not have this maximum at the short wavelengths of the photoluminescence spectrum where it might seem that the quantum-well effect should show up more clearly? We believe that the reason lies in the elastic stresses to which the silicon core, covered with its oxide shell, is subject. They change the symmetry of the crystal lattice (the lattice constant of porous silicon becomes larger in the direction normal to the film boundary[25]), which should affect the characteristics of the photoluminescence process fundamentally. This, in particular, can explain the absence of the above-mentioned peak in the photoexcitation spectra of the initial anodized samples. After etching of the oxide, the stresses in the silicon core (or crystallites) are substantially lowered, i.e., the calculations of Ref. 22 are applicable to it. This, however, is not true of the small-size crystallites, for which the effect of surface stresses remains important because of their low volume-to-surface ratio. Thus, in the short wavelength part of the photoluminescence spectrum, which is caused by small sized crystallites according to the quantum-well mechanism, the influence of structural features on the photoexcitation spectra of single crystal silicon is masked. We have attributed the partial polarization of the emission from porous silicon (which, just as above in the short wavelength part of the photoluminescence spectrum, falls off monotonically with increasing wavelength[10,26]) to these stresses.[10] Yet another argument in favor of this interpretation is a drop in the degree of polarization after etching, followed by a return to a level close that prior to etching.

The cause of the extremum in the photoexcitation spectra of etched porous silicon may be an amorphous phase of silicon. Single crystal silicon surfaces treated in hydrofluoric acid are known to have a surface layer of highly disoriented silicon atoms which form a disordered amorphized phase.[27,28] In a porous silicon layer treated with HF, the fraction of this phase will not be small. Its role in the mechanism for the luminescence of porous silicon has been discussed elsewhere.[29,30] In some papers the photoluminescence of porous silicon films has been attributed directly to the amorphous phase.[31,32] For us here, the important thing is that spectra of the imaginary part of the pseudodielectric function of amorphous silicon have a maximum at $\lambda_{ex}=355$ nm.[33] Evidently, if the porous silicon is photoexcited through an amorphous phase, then the size of the crystallites is unimportant. Hence, if this maximum is caused by the amorphous phase, then it should be present in the photoluminescence spectra for all the photoluminescence wavelengths, but this is not observed. This argument, along with the arguments presented above, imply that the amorphous phase of silicon is unimportant in the photoexcitation processes for porous silicon. Nevertheless, the surface states and the states in the tails of the bands of amorphous silicon are of some significance for photoluminescence processes in porous silicon films. They are responsible for the observed broadening of the long wavelength wing of the photoluminescence spectrum after etching, which was discussed in Sec. 2.2. Their role as centers for the nonradiative relaxation of photoexcited carriers is more important. In fact, after etching of the oxide shell, the photoluminescence intensity falls off, sometimes substantially (see Fig. 3). Then, as an oxide shell forms during the gradual oxidation of the disordered surface layers of the crystallites, the photoluminescence intensity partially recovers and, after the second and subsequent etchings, usually completely.

CONCLUSIONS

We have studied the photoluminescence and photoexcitation spectra of films of anodized porous silicon before and after etching in a water solution of HF, as well as their time evolution. The absence of silicon-hydrogen compounds on the surface of the silicon crystallites in an anodized porous silicon film has made it possible to exclude the polyhydrides as possible contributors to the photoluminescence of porous silicon. Thus, the features of the photoluminescence and photoexcitation spectra and their time evolution after etching are entirely caused by the oxide shell of the silicon crystallites and any changes in it. The observed features of these spectra and their time evolutions cannot all be completely interpreted in terms of a quantum-well model; this is particularly true of the absence of a maximum in the photoexcitation spectra associated with the theoretically predicted[24] peak in the imaginary part of the pseudodielectric function of the porous silicon and its appearance after etching in the long-wavelength wing of the photoluminescence spectrum. Including elastic stresses in this model makes it possible to explain this behavior of the photoexcitation spectra, as well as the previously observed degree of polarization of the photoluminescence of porous silicon and the variations in this polarization owing to etching. The different character of the quantum-well structures considered in Ref. 22 (quantum wires with passivation of the surface by hydrogen) and in this paper makes more rigorous quantitative comparisons, such as cross sections of the wires and crystallites, impossible. However, this difference does not affect the general conclusion that the photoexcitation spectra of porous silicon contain features that are structurally related to absorption by crystalline silicon in the porous silicon core. The amorphous phase of silicon, which forms the surface layers of crystallites with disoriented silicon atoms as a result of etching, is not important in the photoexcitation processes. However, it does have an effect on the photoluminescence of porous silicon which shows up primarily as a drop in the photoluminescence intensity and a broadening of the long wavelength wing of the photoluminescence spectrum.

We thank V. A. Yakovtseva and A. V. Bondarenko for help in preparing this paper for publication.

1)Fax: 0172-39 31 31
E-mail: ifanbel%bas03.basnet.minsk.by@demos.su

---

[1] L. T. Canham, Appl. Phys. Lett. **57**, 1046 (1990).

[2] R. Kumar, Y. Kitochi, and K. Hara, Appl. Phys. Lett. **63**, 3032 (1993).

[3] J. M. Lavine, S. Sawan, Y. T. Shieh, and A. J. Balezza, Appl. Phys. Lett. **62**, 1099 (1993).

[4] K. H. Jung, S. Shin, D. L. Kwong, C. C. Cho, and B. E. Gnade, Appl. Phys. Lett. **61**, 2467 (1992).

[5] S. M. Prokes, W. E. Carlos, and P. M. Burmudez, Appl. Phys. Lett. **61**, 1447 (1992).

[6] Y. M. Weng, Z. M. Fan, and X. F. Zong, Appl. Phys. Lett. **63**, 168 (1993).

[7] S. Shih, K. H. Jung, D. L. Kwong, M. Kovar, and J. M. White, Appl. Phys. Lett. **62**, 1904 (1993).

[8] J. Vial, F. Bsiesy, F. Gaspard, R. Herino, M. Ligeon, F. Muller, R. Romestain, and R. Macfarlane, Phys. Rev. B **45**, 14171 (1992).

[9] M. B. Robinson, A. C. Dilon, and S. M. George, Appl. Phys. Lett. **62**, 1493 (1993).

[10] V. V. Filippov, P. P. Pershukevich, V. P. Bondarenko, and A. M. Dorofeev, Phys. Status Solidi B **184**, 573 (1994).

[11] Y. G. Chabal, G. S. Higashi, N. Raghavachari, and V. A. Burroughs, J. Vac. Sci. Technol. A **7**, 2104 (1989).

[12] W. B. Pollard and G. Lucowski, Phys. Rev. B **26**, 3172 (1982).

[13] M. H. Bordski, M. Cardona, and J. J. Cuomo, Phys. Rev. B **26**, 3356 (1977).

[14] Y. Ogata, H. Niki, T. Sakka, and M. Iwasaki, J. Electrochem. Soc. **42**, 195 (1995).

[15] M. S. Brandt, H. D. Fuchs, M. Stutzmann, J. Weber, and M. Cardona, Solid State Commun. **81**, 307 (1992).

[16] A. Nakajima, T. Itakura, S. Watanabe, and N. Nakayama, Appl. Phys. Lett. **61**, 46 (1992).

[17] T. Motohiro, T. Kachi, F. Miura, Y. Takeda, S. Hyodo, and S. Noda, Japan. J. Appl. Phys. **31**, L207 (1992).

[18] N. Ookubo, J. Appl. Phys. **74**, 6375 (1993).

[19] Y. H. Xie, W. L. Wilson, F. M. Ross, J. A. Mucha, and E. A. Fitzgerald, J. Appl. Phys. **71**, 2403 (1992).

[20] J. Shah, A. Pinczuk, F. B. Alexander, and B. G. Bagley, Solid State Commun. **42**, 717 (1982).

[21] D. E. Aspnes, and A. A. Studnia, Phys. Rev. B **27**, 985 (1983).

[22] N. Koshida, H. Koyama, Y. Yamamoto, and G. J. Collins, Appl. Phys. Lett. **63**, 2655 (1993).

[23] G. D. Sanders and Y. C. Chang, Phys. Rev. B **45**, 9202 (1992).

[24] F. Buda, J. Kohanoff, and M. Parrinello, Phys. Rev. Lett. **69**, 1272 (1992).

[25] L. P. Avakyants, V. M. Avdokhina, and G. B. Demidovich *et al.*, Poverkhnost' 5, 95 (1989).

[26] A. N. Starukhin, A. A. Lebedev, B. S. Razbirin, and L. M. Kapitonova, Pis'ma Zh. Tekh. Fiz. **18**, 80 (1992) [Tech. Phys. Lett. **18**, 160 (1992)].

[27] G. Renand, P. Fuoss, A. Ourmazd, J. Bevk, B. Freer, and P. Hahn, Appl. Phys. Lett. **58**, 1272 (1991).

[28] T. Konishi, K. Uesugi, K. Takoka, S. Kawano, M. Yoshimuta, and T. Yao, Japan. J. Appl. Phys. **32**, 3131 (1993).

[29] N. Noduchi, I. Suemune, and M. Yamanishi, Japan. J. Appl. Phys. **31**, L490 (1992).

[30] F. Koch, Microelectronic Engineering **28**, 237 (1995).

[31] T. George, M. S. Anderson, W. T. Pike, T. L. Lin, R. W. Fathaner, K. Jung, and D. L. Kwong, Appl. Phys. Lett. **60**, 2354 (1992).

[32] J. P. Perez, J. V. Malobes, P. McNeill, J. Prosad, R. Cheek, J. Kelber, J. P. Estrera, P. D. Stevens, and R. Glosser, Appl. Phys. Lett. **61**, 563 (1992).

[33] D. T. Pierce and W. E. Spicer, Phys. Rev. B **5**, 3017 (1972).

Translated by D. H. McNeill

Comparison of equilibrium and nonequilibrium charge carrier mobilities in polycrystalline synthetic diamond and amorphous diamond-like carbon films

Yu. V. Pleskov[1)] and A. R. Tameev

A. N. Frumkin Institute of Electrochemistry, Russian Academy of Sciences, 117071 Moscow, Russia

V. P. Varnin and I. G. Teremetskaya

Institute of Physical Chemistry, Russian Academy of Sciences, 117915 Moscow, Russia

A. M. Baranov

S. A. Vekshinskiĭ Scientific-research Institute of Vacuum Technology,
113105 Moscow, Russia

(Submitted May 12, 1996; accepted for publication April 1, 1997)
Fiz. Tekh. Poluprovodn. **31**, 1142–1145 (September 1997)

Nonequilibrium charge carrier mobilities of 10^{-3} and 3×10^{-8} cm^2/V·s in films of polycrystalline diamond and diamondlike carbon, respectively, are determined from the time of flight of injected carriers through the films. In polycrystalline diamond the nonequilibrium hole mobility is 3 orders of magnitude lower than the equilibrium mobility ($0.1-1$ cm^2/V·s) obtained from the dc electrical conductivity of the films. This can be explained by the effect of trapping of nonequilibrium carriers on their transport. *© 1997 American Institute of Physics.* [S1063-7826(97)02409-5]

Synthetic semiconducting diamond is a promising material for electronics, optics, and a number of other areas.[1] It has recently been studied extensively as a possible material for indestructible electrodes in electrochemistry.[2] In this paper we use a combination of electrical (the time dependence of the transient current when nonequilibrium current carriers are injected into a film) and electrochemical (contact impedance spectroscopy of a diamond film-electrolyte[3]) measurements to determine the hole mobility of diamond, knowledge of which may be useful for describing transport processes in bulk diamond and at interphase boundaries. We have compared the hole mobility of diamond measured under equilibrium and nonequilibrium conditions.

EXPERIMENTAL TECHNIQUE

The samples. We grew the polycrystalline diamond films on a tungsten substrate by chemical gaseous phase deposition from a mixture of methane and hydrogen activated by an incandescent filament, as described previously.[4] For measuring the film conductivities by electrochemical contact impedance spectroscopy, we used highly conducting boron-doped films[4] with a resistivity on the order of 10^4 Ω·cm and a majority carrier concentration of $10^{17}-3\times10^{18}$ cm^{-3}. The time dependence of the transient current was measured on dielectric (undoped) samples with a resistivity of 10^9-10^{10} Ω·cm. All the films were relatively monocrystalline; the average size of the visible crystallites on the film surfaces was as large as 1 μm.

Diamond-like films of *a*-C:H were produced on a molybdenum substrate from gaseous phase cyclohexane in an rf discharge plasma (13.56 MHz).[5] Before the films were deposited the substrate surface was initially processed in a CF_4 plasma. The films about 100 nm in thickness were deposited at room temperature.

Mobility measurements. The transport of nonequilibrium charge carriers in the diamond films was studied by a time-of-flight technique.[6] The time dependence of the transient current owing to unipolar drift of injected nonequilibrium charge carriers in a metal-sample-metal sandwich structure under the influence of an applied dc electric field was recorded. In our case, one of the metal electrodes was the tungsten or molybdenum substrate and the other was a layer of gold evaporated onto the surface of the test film. A packet of charge carriers in the form of a thin layer of width much smaller than the sample thickness was injected into the diamond film being tested.

Excess charge carriers were generated by a light pulse. Since the quantum yield for photogeneration of charge carriers in the intrinsically diamond and diamond-like films at the laser wavelength was not high enough (on the order of 10^{-4} in diamond[7]), the sandwich structure was supplemented by a layer of selenium (between the film surface and the gold electrode), within which photogeneration and separation of charge carriers took place and from which carriers were injected into the test film. The thickness of the selenium layer ($0.2-0.5$ μm) was much less than that of the diamond film, but comparable to that of the *a*-C:H film. Thus, in the first case, we disregarded the voltage drop in the Se layer, while in the second, when determining the field strength in the *a*-C:H film required to calculate the mobility, we introduced an approximate correction for the actual electric field distribution in the sandwich structure.

The light pulse source was an ILGI-503 nitrogen laser ($t_{\text{pulse}}=10$ ns at half-maximum and wavelength 337 nm). The time dependence of the transient current was recorded on an S9-8 storage oscilloscope with a preamplifier (Ya-40 –1102 differential amplifier) combined with a computer for data acquisition and processing. The time constant R_mC_m of the measurement circuit was less than the carrier time of

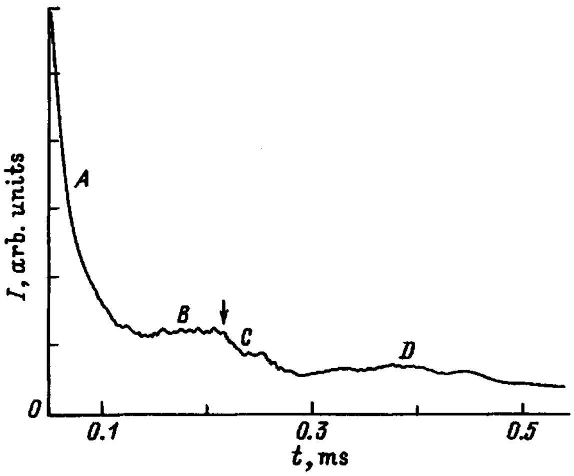

FIG. 1. A plot of the transient current during injection of holes into polycrystalline diamond. Sample 475 (see Table I). The electric field is $F = 1.9\times10^4$ V/cm. The time of flight, t_T, is denoted by an arrow.

flight t_T. A G5-54 pulse generator served to simultaneously trigger the laser pulse and oscilloscope. All the measurements were made at room temperature.

RESULTS AND DISCUSSION

After an initial drop corresponding to charging of the R_mC_m circuit (segment A), the plots of the transition current during injection of electrons into a diamond film as a function of time (a typical curve is shown in Fig 1) have a characteristic plateau (segment B) followed by a relatively rapid drop in current (segment C). The time t_T at which this drop begins (denoted in the figure by an arrow) corresponds to the arrival of the leading edge of the charge carrier packet at the opposite electrode after passing through a diamond film of thickness d.

We calculated the drift mobility μ of the charge carriers using the formula $\mu = d/Ft_T$, where $F = U/d$ is the electric field strength and U is the applied voltage. The mobilities determined in this way are listed in Table I along with the values of the ''equilibrium'' mobility calculated from the conductivity σ of boron-doped films using the formula $\mu = \sigma/pe$. Here

$$p = [(N_AN_v)^{1/2}/\sqrt{2}]\exp(-E_A/2kT)$$

is the majority carrier concentration (holes in B doped diamond, which is a p-type semiconductor), N_A is the acceptor concentration (more precisely, the concentration $N_A - N_D$ of uncompensated acceptors), $N_v \cong 2\times10^{19}$ cm^{-3} is the density of states in the valence band, and $E_A = 0.37$ eV is the ionization energy of the acceptor B. The values of σ and N_A given in the table are taken from Refs. 2 and 3. In those papers we determined the electrical resistance of films by extrapolating the real component of the electrode impedance in the complex plane to an infinite frequency and the uncompensated acceptor concentration, from the slope of Mott–Shottky plots for the diamond-⟨electrolyte solution⟩ contact.

When holes are injected into a diamond film, the shape of the transient current, the time of flight, and the calculated mobility are close to the above case of electron injection. The electric field dependence of the nonequilibrium mobility, if there actually is one, is extremely weak (in the range of fields, $10^3 - 10^4$ V/cm, that we studied). We did not investigate the nature of this dependence.

The current decay curve for an a-C:H film after hole injection qualitatively resembles that shown in the figure. However, the nonequilibrium charge carrier mobility in a-C:H is 4–5 orders of magnitude lower than in polycrystalline diamond, both for holes (see the table) and for electrons, which is substantially lower than that for films[8] grown in a $CH_4 + Ar$ plasma. As in the case of polycrystalline diamond, in a-C:H the mobilities of electrons and holes are roughly the same.

Because of the essentially unipolar nature of the induced conductivity in diamond for the present experimental setup, the injected carriers do not undergo recombination (although the lifetime of electron-hole pairs in diamond is extremely short) since there are practically no carriers of the opposite sign. Nonequilibrium carriers, however, can be trapped. If the time to free them from traps is much greater than the time of flight t_T of the bulk of the injected carriers, then the

TABLE I. Hole mobilities and values of quantities used in the calculations.

Sample No.	d, μm	F, V/cm	t_T, ms	Nonequilibrium mobility μ_m, cm^2/(V·s)	σ, Ω^{-1}/(V·s)	N_A, cm^{-3}	Equilibrium mobility μ_m, cm^2/(V·s)
				Polycrystalline diamond			
475	26	1.4×10^4	0.3	6.2×10^{-4}	7×10^{-10}	–	–
		1.9×10^4	0.16	8.4×10^{-4}			
508	8	0.75×10^4	0.055	1.9×10^{-3}	3×10^{-10}	–	–
354	10	0.09×10^4	1.1	10^{-3}	–	–	–
306	10	–	–	–	0.9×10^{-4}	5×10^{17}	1
559	6	–	–	–	0.5×10^{-4}	3×10^{18}	0.1
419	2.5	–	–	–	0.6×10^{-4}	(0.6×10^{17})	(6)
420	2.3	–	–	–	1.2×10^{-4}	(10^{17})	(7)
				a–C:H			
228	0.1	9	4	3×10^{-8}	–	–	–

Note: Less reliable values are given in parentheses.

observed current signal decreases, but trapping should have no effect on the measured mobility. The tiny residual current in the final, smooth segment *D* of the curve (see the figure) is probably caused by the arrival at the collector electrode of carriers which have been trapped in the volume of the film and then released. If, on the other hand, charge carriers can be trapped and released during the time of flight, then this should slow down the flight of the packet, i.e., reduce the effective mobility.

Our measured mobilities (both equilibrium and nonequilibrium) in polycrystalline diamond films are several orders of magnitude lower than the drift mobility of electrons and holes in single-crystal diamond (2500 and 2100 $cm^2/(V\cdot s)$, respectively[9]). This is not surprising if we note the obstacles to the transport of free carriers created by intercrystallite boundaries, as well as by other defects in the crystal structure of polycrystalline diamond. This is confirmed by the very low charge carrier mobility we have measured in a-C:H, which can serve roughly as a model for the material in the intercrystallite boundaries of polycrystalline diamond.

A comparison of the data in the table shows that the equilibrium hole mobility in the diamond films we have studied is three orders of magnitude higher than the nonequilibrium mobility. This difference can be explained by the fact that equilibrium holes (in boron-doped films) and nonequilibrium holes and electrons injected into undoped (''dielectric'') diamond films are transported by two different mechanisms.

A model of jumps over centers can be applied to carrier transport in a relatively disordered medium such as polycrystalline diamond films. For measurements of the mobility under nonequilibrium conditions, i.e., in the dielectric samples, the carriers injected into the sample fall into capture centers (traps) which lie deeper and which had not been filled until then. The transient currents are determined by charge carriers that have been trapped and then released. Probably this mechanism is predominant for nonequilibrium holes and electrons in undoped diamond films and they correspond to comparatively low values of the mobility. For measurements under ''equilibrium'' conditions– in doped samples– on the other hand, the traps are filled and the conductivity of the film is determined by free charge carriers. This second, parallel, mechanism for conductivity becomes noticeable only for a sufficiently high equilibrium hole concentration, as is provided by introducing B dopant into the diamond. With this mechanism for the conductivity, the mobility is higher.

We thank V. I. Polyakov and A. V. Vannikov for a discussion of the results.

The part of this work related to polycrystalline diamond was supported by the Russian Fund for Fundamental Research (project No. 96-03-34133a).

1) FAX: (095)9520846; E-mail: chrush@elchem.rc.ac.ru

---

[1] J. Field, Ed., *Properties of Natural and Synthetic Diamond*, Academic Press, London–New York (1992).

[2] A. D. Modestov, Yu. V. Pleskov, V. P. Varnin, and I. G. Teremetskaya, Élektrokhimiya **33** (1) (1997).

[3] Yu. V. Pleskov, V. Ya. Mishuk, M. A. Abaturov, V. V. Elkin, M. D. Krotova, V. P. Varmin, and I. G. Teremetskaya, J. Electroanal. Chem. **396**, 227 (1995).

[4] A. Ya. Sakharova, Yu. V. Pleskov, F. Di Quarto, S. P'yatstsa, K. Sunseri, I. G. Teremetskaya, and V. P. Varnin, Élektrokhimiya **31**, 188 (1995).

[5] V. V. Sleptsov, A. A. Kuzin, G. F. Ivanovsky, V. M. Elinsov, S. S. Gerasimovich, A. M. Baranov, and P. E. Kondrashov, J. Non-Cryst. Solids **136**, 53 (1991).

[6] A. V. Vannikov, V. K. Matveev, V. P. Sichkar', and A. P. Tyutnev, *Radiation Effects in Polymers. Electrical Properties* [in Russian] , Nauka, Moscow (1982), Chapter 1.

[7] Yu. V. Pleskov, A. Ya. Sakharova, A. V. Churikov, V. P. Varnin, and I. G. Teremetskaya, Élektrokhimiya **32** (10) (1996).

[8] O. I. Kon'kov, I. N. Trapeznikova, and E. I. Terukov, Fiz. Tekh. Poluprovodn. **28**, 1406 (1994) [Semiconductors **28**, 791 (1994)].

[9] B. S.Vavilov, A. A. Gippius, and E. A. Konorova, *Electronic and Optical Processes in Diamond* [in Russian], Nauka, Moscow (1985). Edited by T. A. Polyanskaya

Translated by D. H. McNeill

Recombination in the space charge region and its effect on the transmittance of bipolar transistors

S. V. Bulyarskiĭ, N. S. Grushko, A. I. Somov, and A. V. Lakalin

M. V. Lomonosov Moscow State University, Ulyanovsk Branch, 432700 Ulyanovsk, Russia

(Submitted December 3, 1995; accepted for publication February 10, 1997)
Fiz. Tekh. Poluprovodn. **31**, 1146–1150 (September 1997)

The effect of recombination in the space charge region of the emitter junction on the transmittance of bipolar transistors is considered. Measurements of the transmittance of several commercial transistors at low injection levels essentially agree with theoretical values given by the expressions obtained here, which take into account deep levels and recombination through them. © *1997 American Institute of Physics.* [S1063-7826(97)02509-X]

For many years after the publication of Shockley, Noyce, and Sah,[1] it was assumed that the principal indication of recombination in the space charge region is a characteristic dependence of the current on voltage of the form $\exp(qU/2kT)$. This dependence overlooked the fact that as the injection level is raised, the stationary population of the deep levels changes, because that the position of the Fermi quasilevel changes. While the current-voltage characteristic is determined by the rates of emission of free carriers in its initial portion, at higher injection levels it is determined by their trapping rate. Thus, charge exchange of the recombination centers takes place at a variable rate; this leads to the observed features of the current-voltage characteristic. The charge-exchange processes have been examined in more detail elsewhere.[2,3]

Our task in this study was to find the limits of applicability of the theory of recombination in the space charge region of a p-n junction[1] and of the method for determining the parameters of the centers from the current-voltage characteristic in this range of variation of the current, as well as to demonstrate the role of recombination in reducing the small-signal efficiency of the emitter in a transistor.

The current-voltage characteristics were measured on an automatic PC-controlled apparatus. The basic current measurement device was a V7-46, which made it possible to average each value of the current and voltage directly in the course of the measurements.

SEPARATION OF THE INDIVIDUAL RECOMBINATION PROCESSES INTO COMPONENTS

According to the Shockley–Read–Hall theory, the rate of recombination through a simple two-charge center is given by[1]

$$R(x)=\frac{c_n c_p N_t[n(x)p(x)-n_i^2]}{c_n[n(x)+n_1]+c_p[p(x)+p_1]}, \tag{1}$$

where $n_1=N_c\exp(-E_{tn}/kT)$, $p_1=N_v\exp(-E_{tp}/kT)$, c_n and c_p are the capture coefficients for electrons and holes at a given center averaged over all states, N_t is the concentration of deep centers, and E_t is the location of the deep centers in the band gap. $E_c-E_v=(E_c-E_t)+(E_t-E_v)=E_{tn}+E_{tp}=E_g$.

Usually, one considers recombination in quasineutral regions. But, as experiments show, in silicon and other wider-gap semiconductors, in the initial portion (at low injection levels) the recombination currents in the space charge region are comparable to or greater than the diffusion currents. Thus, recombination in the space charge region of p-n junctions at low injection levels must also be considered in order to understand the processes occurring in microwave transistors operating as small-signal amplifiers.

If the bending of the bands in the space charge region of a p-n junction is described by the potential $\Psi(x)$ (Fig. 1), whose reference point is the bottom of the conduction band in the n-region, then the distributions of the electron $n(x)$ and hole $p(x)$ concentrations in the space charge region are given by[2]

$$\begin{aligned} n(x)&=n_n\exp\left(-\frac{\Psi(x)}{kT}\right),\\ p(x)&=p_p\exp\left[-\frac{q(U_{\mathrm{dif}}-U)-\Psi(x)}{kT}\right]. \end{aligned} \tag{2}$$

Substituting Eq. (2) in Eq. (1), we obtain

$$R(x)=\frac{c_n c_p N_t N_i^2\left(\exp\frac{qU}{kT}-1\right)}{c_n[n_n\exp(-\varphi_1)+n_1]+c_p[p_p\exp(-\varphi_2)+p_1]}, \tag{3}$$

where $\varphi_1=\Psi(x)/kT$ and $\varphi_2=q(U_{\mathrm{dif}}-U)-\Psi(x)/kT$.

The recombination current can be found by integrating the recombination rate $R(x)$ over the volume of the space charge region:[2]

$$i_r=qS\int_{-x_p}^{x_n}R(x)dx, \tag{4}$$

where S is the area of the p-n junction. However, since the function $R(x)=R(\Psi(x))$ is determined by the specific shape of the p-n junction, in general, the integral (4) is not solved

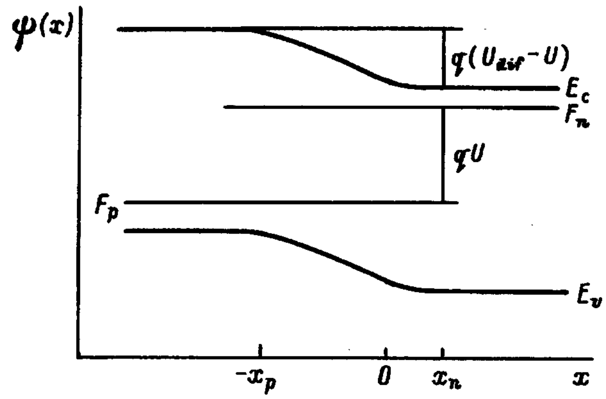

FIG. 1. Band diagram of a forward biased p-n-junction. The bending of the band is described by a potential $\Psi(x)$ such that $\Psi(x=x_n)=0$, $\Psi(x=-x_p)=q(U_{\text{dif}}-U)$.

simply by substituting Eq. (3) in Eq. (4). The integral (4) can be estimated. In fact, the recombination rate in the space charge region is localized and has the form of a bell shaped curve with exponential wings.[2,3] The maximum recombination rate occurs at the potential

$$\Psi_{\text{max}}=\frac{q(U_{\text{dif}}-U)}{2}+\frac{kT}{2}\ln\left(\frac{c_n n_n}{c_p p_p}\right), \tag{5}$$

and the recombination rate at this point is

$$R_{\text{max}}=\frac{c_n c_p n_i^2 N_t\left[\exp\left(\frac{qU}{kT}\right)-1\right]}{2n_i\sqrt{c_n c_p}\exp\left(\frac{qU}{2kT}\right)+c_n n_1+c_p p_1}. \tag{6}$$

We now find the increment in the coordinate [relative to the position of the center of the distribution $R(x)$ in the space charge region] for which the recombination rate drops by a factor of 2.73,

$$\exp\left(-\frac{\Delta\Psi}{kT}\right)=\exp(-1);\quad \Delta\Psi=\frac{\partial\Psi}{\partial x}\Delta x=-E\Delta x.$$

This implies that

$$\int_{-x_p}^{x_n} R(x)dx\approx 2R_{\text{max}}\Delta x=\frac{2kT}{qE}R_{\text{max}},$$

where E is the average field strength in the $p-n$ junction,

$$E=\frac{w(U)}{q(U_{\text{dif}}-U)}.$$

For the current we then obtain

$$i_r(U)=qSw(U)\frac{c_n c_p n_i^2 N_t(e^{qU/kT}-1)}{2n_i\sqrt{c_n c_p}e^{qU/2kT}+c_n n_1+c_p p_1}\times\frac{2kT}{q(U_{\text{dif}}-U)}. \tag{7}$$

In the case of several deep centers the resulting current is the sum of the currents due to recombination through each of the deep centers:

$$i_r=\sum_{m=1}^{p}\frac{qSw(U)c_{nm}c_{pm}n_i^2(e^{qU/kT}-1)N_{tm}}{2n_i\sqrt{c_{nm}c_{pm}}e^{qU/2kT}+c_{nm}n_{1m}+c_{pm}p_{1m}}\times\frac{2kT}{q(U_{\text{dif}}-U)}, \tag{8}$$

where w is the width of the space charge region, and p is the number of deep centers.

Equation (8) is valid as long as the maximum recombination rate does not lie on the edge of the space charge region. The voltage U at which this occurs is the limit of applicability of the Shockley–Noyce–Sah theory: $qU=E_g-kT\ln(c_p N_c N_v/c_n n_n^2)$ if the p-region of the $p-n$ junction is more heavily doped, $qU=E_g-kT\ln(c_p N_c N_v/c_n p_p^2)$ if the n-region of the p-n junction is more heavily doped, and $U=U_{\text{dif}}-(kT/q)\ln(c_n/c_p)$ is the $p-n$ junction is symmetric.

We now analyze the recombination currents for low injection levels and examine in more detail the recombination method which allows us to obtain the parameters of the deep levels from the current-voltage characteristics when the width of the space charge region of a p-n junction is known.[2] Let us examine Eq. (7). For concreteness we assume that the deep level lies above the middle of the band gap, i.e., $c_n n_1 \gg c_p p_1$. Depending on the applied voltage, the conditions for populating the center will vary. Two cases are possible:

1. Let

$$2n_i\sqrt{c_n c_p}\exp\left(\frac{qU}{2kT}\right)\ll c_n n_1. \tag{9}$$

Then

$$i_r(U)\approx qSw(U)N_t c_p\frac{n_i^2}{n_1}\exp\left(\frac{qU}{kT}\right)\times\frac{2kT}{q(U_{\text{dif}}-U)}\propto\exp\left(\frac{qU}{kT}\right). \tag{10}$$

2. Let

$$2n_i\sqrt{c_n c_p}\exp\left(\frac{qU}{2kT}\right)\gg c_n n_1. \tag{11}$$

Then

$$i_r(U)\approx qSw(U)N_t n_i\sqrt{c_n c_p}\exp\left(\frac{dU}{2kT}\right)\times\frac{2kT}{q(U_{\text{diff}}-U)}\propto\exp\left(\frac{qU}{2kT}\right). \tag{12}$$

The change in the current-voltage characteristic is attributable to the charge exchange of the deep level. Equations (10) and (12) can be used to calculate the parameters of the deep level. For analyzing the current-voltage characteristic, however, it is more convenient to introduce another physical quantity, the reduced recombination rate R_{np}, which is defined as

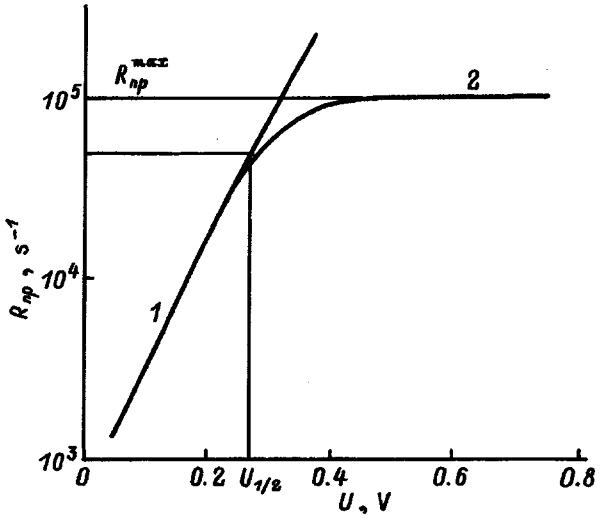

FIG. 2. An $R_{np}=f(U)$ curve for the case of recombination through a single deep center.

$$R_{np}(U)=\frac{i_r(U)}{qSw(U)n_i\left[\exp\left(\frac{qU}{2kT}\right)-1\right]}\cdot\frac{q(U_{\text{dif}}-U)}{2kT}, \quad (13)$$

where i_r is the current flowing through the p-n junction.

The relationship of this quantity to the deep-center parameters is evident from Eqs. (7) and (13):

$$R_{np}(U)=\frac{c_nc_pn_iN_t\left[\exp\left(\frac{qU}{2kT}+1\right)\right]}{2n_i\sqrt{c_nc_p}\,\exp\left(\frac{qU}{2kT}\right)+n_1c_n+p_1c_p}. \quad (14)$$

In the first case [Eq. (9)] (segment 1 in Fig. 2), we have

$$R_{np}=\text{ const }\cdot\exp(qU/2kT),$$

and in the second [Eq. (11)] (segment 2 in Fig. 2), we have

$$R_{np}=R_{np}^{\max}=\sqrt{c_nc_p}N_t/2. \quad (15)$$

If we consider the voltage $U_{1/2}$ at which the condition $R_{np}=R_{np}^{\max}/2$ is satisfied, then $c_nn_1+c_pp_1=2n_i\sqrt{c_nc_p}\exp(qU_{1/2}/2kT)$. Assuming that the deep center lies above the middle of the band gap (i.e., $c_pp_1\ll c_nn_1$), we find

$$E_{tn}=\frac{(E_g-qU_{1/2})}{2}+\delta, \quad (16)$$

where $\delta=\frac{kT}{2}\ln(\frac{1}{4}c_nN_c/4c_pN_v)$.

There are often a number of deep centers in the space charge layer, however, and recombination takes place in parallel through these centers. Thus, the recombination currents corresponding to each deep center add up to the total current in accordance with the superposition principle. Thus, the actual function $R_{np}=f(U)$ is the sum of several ''shelves'' (Fig. 3).

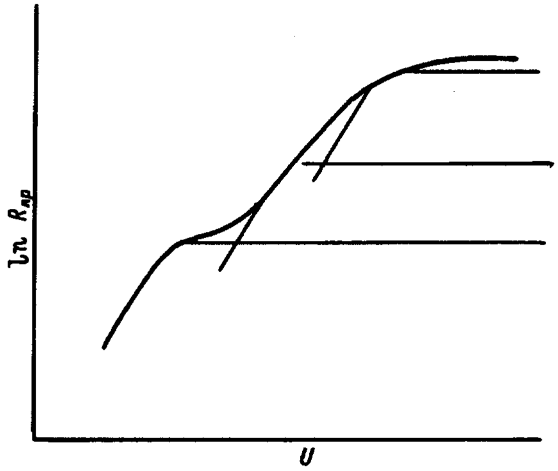

FIG. 3. The separation of complex recombination processes into components.

The algorithm for separating the experimental R_{np} curve into components relies on the conditions (15) and consists of the following:

1. The current-voltage characteristic of the forward biased p-n junction is measured at voltages below U_{dif} (there should be quite a few points). R_{np} is evaluated for each point using Eq. (13). The quantities $w(U)$ and U_{dif} are determined from capacitance measurements.

2. The resulting $\ln R_{np}(U)$ is decomposed into components by graphical separation. According to Eq. (15), each of the shelves which form it should have an initial slope given by $q/2kT$ and be constant in the final segment (Figs. 2 and 3).

3. For each of the shelves found in this way we find $U_{1/2}$ such that $R_{np}(U_{1/2})=R_{np}^{\max}/2$ and estimate the activation energy of the corresponding deep center using Eq. (16), neglecting the term δ there. The systematic error associated with disregard of δ is determined by the ratio of the trapping coefficients c_n/c_p (16) and is $\cong 0.05$ eV for $T=300$ K.

4. If the ratio c_n/c_p of the trapping coefficients is known (from other experiments or by calculation), then it is possible to calculate the lifetimes in highly doped n-type materials, τ_{p0}, and p-type materials, τ_{n0} using the formulas[3]

$$\begin{aligned}\tau_{p0}&=(c_pN_t)^{-1}=\frac{1}{2}\sqrt{\frac{c_n}{c_p}}(R_{np}^{\max})^{-1},\\ \tau_{n0}&=(c_nN_t)^{-1}=\frac{1}{2}\sqrt{\frac{c_p}{c_n}}(R_{np}^{\max})^{-1}.\end{aligned} \quad (17)$$

Thus, it is possible to determine the deep-level parameters approximately from current-voltage characteristics and capacitance measurements, without resorting to temperature measurements.

EFFECT OF RECOMBINATION PROCESSES ON THE AMPLIFYING PROPERTIES OF TRANSISTORS

The analytic models of bipolar transistors used to calculate the emitter i_e, base i_b, and collector i_k currents[4,5] neglect the field of the mobile charge in the emitter and collec-

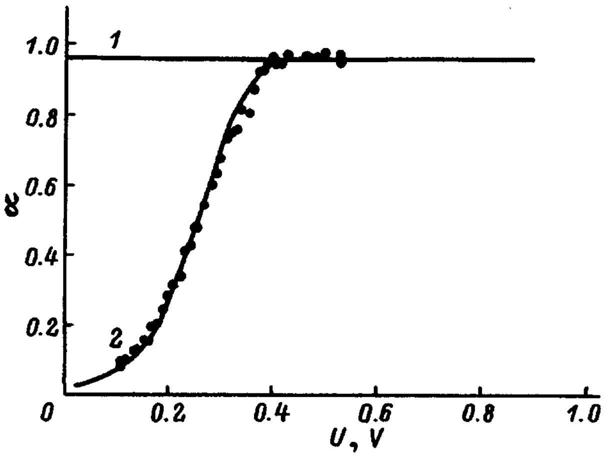

FIG. 4. The transmittance of a transistor. (1) The $\alpha=f(U_{eb})$ curve of a bipolar transistor calculated in accordance with Refs. 4 and 5; (2) a calculation using Eqs. (21) and (22) when two deep recombination centers are present. The points are experimental data.

tor p-n junctions and in the base, the resistance of the input regions of the emitter, collector, and base, and recombination in the space charge region of the emitter junction.

The transmittance α can be regarded as the product of three coefficients:

$$\alpha=\gamma_1\gamma_2\gamma_3,$$
$$\gamma_1=di_{ne}/di_e=di_{ne}/d(i_{ne}+i_{pe}), \qquad (18)$$
$$\gamma_2\mp di_{nk}/di_{ne},\qquad \gamma_3=di_k/di_{nk},$$

where γ_1 is the efficiency of the emitter junction, γ_2 is the transmittance through the base, γ_3 is the efficiency of the collector junction, i_{ne} is the diffusion current of electrons injected from the emitter junction (here and below it is assumed that the transistor is of n-p-n-type), i_{nk} is the current of electrons through the collector junction, and i_{pe} is the diffusion current of holes injected into the emitter. The coefficient γ_3 equals unity in the absence of generation and avalanche processes.

In practice, at low injection levels there is almost always a segment of the form $\alpha=f(U_{eb})$, in contrast with Ref. 4, where $\alpha=$ const (Fig. 4). This effect is explained by nonradiative recombination in the emitter junction, but it has not been discussed analytically in the literature. Thus, it is important to obtain the transmittance of the transistor as a function of the injection level.

The difference in the approach described below is that the effect of the recombination current in the space charge region of the emitter junction on the coefficient γ_1 is taken into account explicitly. Including the recombination current, the efficiency (18) of the emitter junction is given by

$$\gamma_1=\frac{di_{ne}}{di_e}=\frac{di_{ne}}{d(i_{ne}+i_{pe}+i_r)}=\left(1+\frac{di_{pe}}{di_{ne}}+\frac{di_r}{di_{ne}}\right)^{-1}. \qquad (19)$$

Compared to Eq. (18) this expression contains a new term di_r/di_{ne}, which is attributable to the fact that for a low injection level the recombination current can be much greater than the diffusion and drift currents. Let us calculate di_r/di_{ne}. Using an expression for the electron component of the current in the base for an ideal drift-free transistor[4] together with Eqs. (8) and (19), we find

$$\frac{di_r}{di_{ne}}=\sum_{m=1}^{p}\frac{w(U_{eb})c_{nm}c_{pm}N_{tm}N_bL_n}{D_n\coth(w_b/L_n)}\times\frac{[n_i\sqrt{c_{nm}c_{pm}}e^u(e^u+1)+e^u(c_{nm}n_{1m}+c_{pm}p_{1m})]2kT}{e^u(2n_i\sqrt{c_{nm}c_{pm}}e^{u/2}+c_{nm}n_{1m}+c_{pm}p_{1m})^2q(U_{\rm dif}-U_{eb})}, \qquad (20)$$

where $u=qU_{eb}/kT$, w is the width of the space charge region of the emitter junction, w_b is the width of the quasineutral part of the base, L_n is the electron diffusion length in the p-base, N_0 is the concentration of the shallow acceptor impurity in the base, and U_{eb} is the voltage across the emitter junction. In the derivation, if this expression $w(U)/(U_{\rm dif}-U)$ as a function of the voltage is ignored in contrast with the exponential factor, setting $w(U)/(U_{\rm dif}-U)\approx$ const. For γ_1 we obtain

$$\gamma_1=\left(1+\frac{D_pN_bL_n\,{\rm th}(w_b/L_n)}{D_nN_eL_p(w_e/L_p)}+\frac{2kT}{q(U_{\rm diff}-U_{eb})}\times\frac{w(U_{eb})N_eL_n}{D_n\coth(w_b/L_n)e^u}\times\sum_{m=1}^{p}\frac{c_{nm}c_{pm}N_{tm}[n_iAe^{u/2}(e^u+1)+Be^u]}{(2n_iAe^{u/2}B)^2}\right)^{-1}, \qquad (21)$$

where $A=\sqrt{c_{nm}c_{pm}}$, $B=c_{nm}n_{1m}+c_{pm}p_{1m}$, p is the number of deep levels, m indicates the corresponding center, N_e is the concentration of the shallow donor impurity in the emitter, L_p is the hole diffusion length in the n-emitter, and w_e is the width of the quasineutral part of the emitter. As before, the coefficient γ_2 is given by the expression

$$\gamma_2=\frac{1}{\cosh(w_b/L_n)}. \qquad (22)$$

Thus, the presence of deep recombination centers in the space charge region of the emitter junction causes a reduction in the efficiency γ_1 of the emitter junction and in its dependence on the voltage U_{eb} across the emitter junction. As the voltage is raised, γ_1 approaches a constant value.

Measurements were made on an 808AM-GM transistor. The current-voltage characteristic of the emitter p-n junction was analyzed by the method described above and the parameters of the deep levels were determined from the $R_{np}(U)$ curve. It was found that the recombination currents in the emitter junction are caused by deep centers with activation energies $E_{t1}=0.52$ eV ($R_{np}^{\rm max}=3.5\times10^5$ s^{-1}) and $E_{t2}=0.37$ eV ($R_{np}^{\rm max}=2.0\times10^6$ s^{-1}). These values were then used for calculating the transmittance α using Eqs. (21) and (22) with γ_3 assumed equal to unity. Figure 4 shows the results of the calculation and some experimental measurements of the transmittance α. The experimental and calculated values of α are in good agreement.

Auger recombination may reduce the transmittance of bipolar transistors.[5] Calculations show that the lifetime, including Auger recombination, is 10^{-3} s for a voltage of 0.8 V. In our case, however, this form of recombination has no effect on α at low injection levels, since the variation in α is observed at voltages where Auger recombination is unimportant. Thus, recombination in the space charge region of the emitter junction is mainly responsible for the reduction of the emitter efficiency at low injection levels.

[1] C. T. Sah, R. N. Noyce, and W. Shockley, Proc. IRE **45**, 1228 (1957).

[2] S. V. Bulyarskiĭ and N. S. Grushko, *Physical Principles of the Functional Diagnostics of Defective p−n transitions* [in Russian], Shtiintsa, Kishinev (1992), p. 236.

[3] S. V. Bulyarskiĭ and N. S. Grushko, *Generation-recombination Processes in Active Elements* [in Russian], MGU, Moscow (1995), p. 399.

[4] N. S. Sviridov, *Elements of Transistor Theory* [in Russian], Tekhnika, Kiev (1969), p. 225.

[5] S. M. Sze, *Physics of Semiconductor Devices*, Wiley, New York (1969).

Translated by D. H. McNeill